Investigation of Corrosion Under Insulation (CUI) using microelectrodes

Mahmoud B Shwaib Saeed

Submitted in accordance with the requirements for the degree of

Doctor of Philosophy

The University of Leeds
Institute of Functional Surfaces (iFS)
School of Mechanical Engineering
October 2023

The candidate confirms that the work submitted is his own and that appropriate credit has been given where reference has been made to the work of others.

Acknowledgements

I would like to express my heartfelt gratitude and appreciation to all those who have contributed to the successful completion of this PhD thesis.

First and foremost, I extend my deepest gratitude to my supervisor, Professor Rick, for his invaluable guidance, unwavering support, and mentorship throughout this research journey. His expertise, dedication, and insightful feedback have been instrumental in shaping the direction and quality of this thesis.

I am grateful for the support and guidance of Dr. Wassim, who provided valuable input, constructive discussions, and assistance in refining the research methodology. His expertise and mentorship have greatly enhanced the scholarly contributions of this work.

I would also like to acknowledge Professor Anne Neville, who unfortunately passed away during the course of this research. Her profound impact on the field of study and her contributions to the initial stages of this research will always be remembered and cherished. Professor Neville's passion for the subject matter and her remarkable voice when discussing scientific concepts resonated deeply with me and played a significant role in my decision to pursue my PhD at the University of Leeds.

To my beloved wife, Barga, I am forever grateful for your unwavering love, patience, and encouragement. Your support and understanding during the challenging phases of this journey have been a constant source of strength for me.

I would like to thank my children, Areen and Abdulrahman, for their understanding. Your presence has brought joy and inspiration to my life, and I am grateful for your unwavering support.

I would like to express my deep appreciation to my mother, whose unconditional love, sacrifices, and unwavering belief in my abilities have been a constant source of inspiration. I am forever grateful for your endless support and encouragement throughout this academic endeavour.

I would also like to acknowledge my brother, Shwaib, for his continuous encouragement, motivation, and belief in my capabilities. Your support and guidance have been invaluable throughout this journey. I still remember what you told me when I was in grade 7.

I extend my gratitude to the rest of my family, friends, and colleagues who have supported me during this undertaking. Your encouragement, understanding, and belief in my abilities have been greatly appreciated.

Lastly, I would like to sincerely thank the Libyan Ministry of Higher Education and Scientific Research for providing the financial support that made this research possible.

In conclusion, I am profoundly grateful to all those mentioned above and anyone else who has supported me in any way throughout this journey. Your contributions, guidance, and encouragement have been invaluable, and I am truly thankful for your unwavering belief in my abilities.

Abstract

Corrosion under insulation (CUI) presents a substantial and pervasive challenge in a wide range of industrial sectors, both onshore and offshore. The severity and prevalence of CUI exhibit geographical dependencies, with heightened risks associated with facilities situated in proximity to coastal regions. The potential consequences of CUI are profound, encompassing significant structural damage to insulated pipes and tanks, thereby posing threats to both personnel safety and uninterrupted production processes. Despite its significance, the evaluation of CUI through electrochemical techniques remains an area that has yet to reach its full potential in terms of development and application.

This research initiative is focused on assessing the CUI rates, with particular emphasis on the top (12 o'clock) and bottom (6 o'clock) positions of ASTM A 106Gr B. This effort employs an innovative approach that involves the use of three microelectrodes in conjunction with the Linear Polarisation Resistance technique (LPR).

The electrochemical analyses performed in this study have unveiled noteworthy disparities in corrosion rates between the top and bottom samples, as determined by LPR. The corrosion rate estimates obtained through mass loss measurements consistently surpass those obtained via LPR. This trend holds regardless of the specific environmental conditions, including temperature, pH levels, or the analytic technique employed. This observed trend may be affected by the Stern-Geary coefficient (β) value, which is approximated to be 26 mV/decade in this research.

Moreover, this research examining of surface morphology and the underlying corrosion mechanisms. This examination leverages advanced analytical tools such as scanning electron microscopy, X-ray diffraction (XRD), and Raman spectroscopy. The data collected from the XRD was used to evaluate the Protective Ability Index (PAI) of the corrosion layer formed under thermal insulation. The results showed a good correlation between the CUI rate and the PAI.

Table of Contents

List of Figures

List of Tables

List of units

$	American dollars
A	ampere
Å	angstrom
C	Columbus
cm	centimetre
°C	degrees Celsius
g	gram
J	joule
K	degrees Kelvin
m	meter
mm	millimetre
mm/year	millimetre per year
µm	micrometer
MPa	Mega Pascal
ppm	parts per million
s	second
V	volt
W	watt
wt %	weight percentage

List of chemicals

$\mathbf{Al_2O_3}$	Aluminium oxide
$\boldsymbol{\alpha - \mathrm{FeOOH}}$	Goethite
$\boldsymbol{\beta - \mathrm{FeOOH}}$	Akaganeite
$\mathbf{C}$	Carbon
$\mathbf{Cl}$	Chloride
$\mathbf{Cr}$	Chrome
$\mathbf{Cu}$	Copper
$\mathbf{Fe}$ - $\mathbf{Fe^{2+}}$ - $\mathbf{Fe^{3+}}$	Iron, ferrous iron and ferric iron
$\mathbf{Fe_2O_3}$ - $\mathbf{Fe_3O_4}$	Hematite - magnetite
$\boldsymbol{\gamma - \mathrm{FeOOH}}$	Lepidocrocite
$\mathbf{H_2S}$	Hydrogen sulphide
$\mathbf{HCl}$	Hydrogen chloride
$\mathbf{K_2O}$	Potassium oxide
$\mathbf{MgO}$	Magnesium oxide
$\mathbf{Mn}$	Manganese
$\mathbf{Mo}$	Molybdenum
$\mathbf{Na_2O}$	Sodium oxide
$\mathbf{NaCl}$	Sodium chloride
$\mathbf{Ni}$	Nickle
$\mathbf{P}$	Phosphorus
$\mathbf{P_2O_5}$	Phosphorus pentoxide
$\mathbf{S}$	Sulphur
$\mathbf{Sb_2O_3}$	Antimony trioxide
$\mathbf{Si}$	Silicon
$\mathbf{SiC}$	Silicon carbide
$\mathbf{SiO_2}$	Silica
$\mathbf{SnCl_2}$	stannous chloride
$\mathbf{TiO_2}$	Titanium dioxide
$\mathbf{V}$	Vanadium
$\mathbf{ZrO_2}$	Zirconium dioxide

List of abbreviations

AC	Alternating Current
AMPP	Association for Materials Protection and Performance
API	American Petroleum Institute
ASTM	American Society for Testing and Materials
BP	British Petroleum
CSCC	Chloride Stress Corrosion Cracking
CUI	Corrosion Under Insulation
DC	Direct Current
DECC	Department of Energy and Climate Change
EAS	Electrochemically Active Species
EDL	Electrical Double Layer
EDL	Electric Double Layer
EDX	Energy dispersive X-ray analysis
GPD	Gross Domestic Product
IC	Ion chromatography
IMPACT	International Measures of Prevention, Application and Economics of Corrosion Technology
MIC	Microbial Induced Corrosion
NACE	National Association of Corrosion Engineers
O&G	Oil and Gas
OCP	Open Circuit Potential
OGTC	Oil & Gas Technology Centre
PIR	polyisocyanurate or rigid polyiso foam
PSA	Petroleum Safety Authority Norway
PUR	Polyurethane rigid foam
PVC	Polyvinyl Chloride
PVDC	Polyvinylidene Chloride
SEM	Scanning electron microscopy
STET	Scanning Reference Electrode Technique
SVET	Scanning Vibrating Electrode Technique
TSA	Thermal Spray Aluminium
WCO	World Corrosion Organization
XRD	X-ray diffraction

Chapter 1: Introduction

1.1 Definition of Corrosion

Corrosion is an inevitable process by which metals return to their natural state of stability. A consequence of the extraction processes that separate most pure metals from their ores is that these metals become thermodynamically unstable by increasing their energy [1-3]. The only exception is gold, silver, and platinum, all of which are found in their metallic state when they are found as minerals [4]. The Oil and Gas industry (O&G) heavily relies on a diverse range of metals and alloys, among which carbon steel and mild steel play pivotal roles. These metals are characterized by their thermodynamic instability [5]. The unstable metals with high energy will react with the surrounding environment to produce a thermodynamically more stable system; this process is known as corrosion [1]. During the process of metal corrosion, electrons and charges are transferred to the surrounding environments in a system of electron and charge transfer, resulting from an electrochemical interaction between these unstable metals and their environments [6]. Anodic material (corroded), corrosion solution, and cathodic reaction determine the complexity of the electrochemical reaction. The electrochemical reactions can be divided into two or more reduction and oxidation reactions, where the oxidation is corrosion and reduction is the cathodic part of the reaction [4].

Corrosion in pipes or tanks can manifest both internally and externally as depicted in Figure 1-1. Internal corrosion specifically pertains to the deterioration or damage that transpires on the inner surface of a pipe due to chemical or electrochemical reactions between the transported substance and the material comprising the pipe wall. Several types of internal corrosion can be encountered in pipes. For instance, carbon dioxide (CO_2) corrosion , Microbial Induced Corrosion (MIC), flow-induced corrosion, pitting and uniform corrosion [7]. However, external corrosion is an electrochemical degradation mechanism that occurs on the surface of metals. It is primarily caused by environmental factors such as soil, water, and air. External corrosion encompasses various types of corrosion, including atmospheric corrosion, uniform corrosion, pitting corrosion, Stress Corrosion Cracking (SCC) and corrosion under insulation. These examples illustrate the different manifestations of corrosion that occur on the surface of metals in response to environmental factors [8].

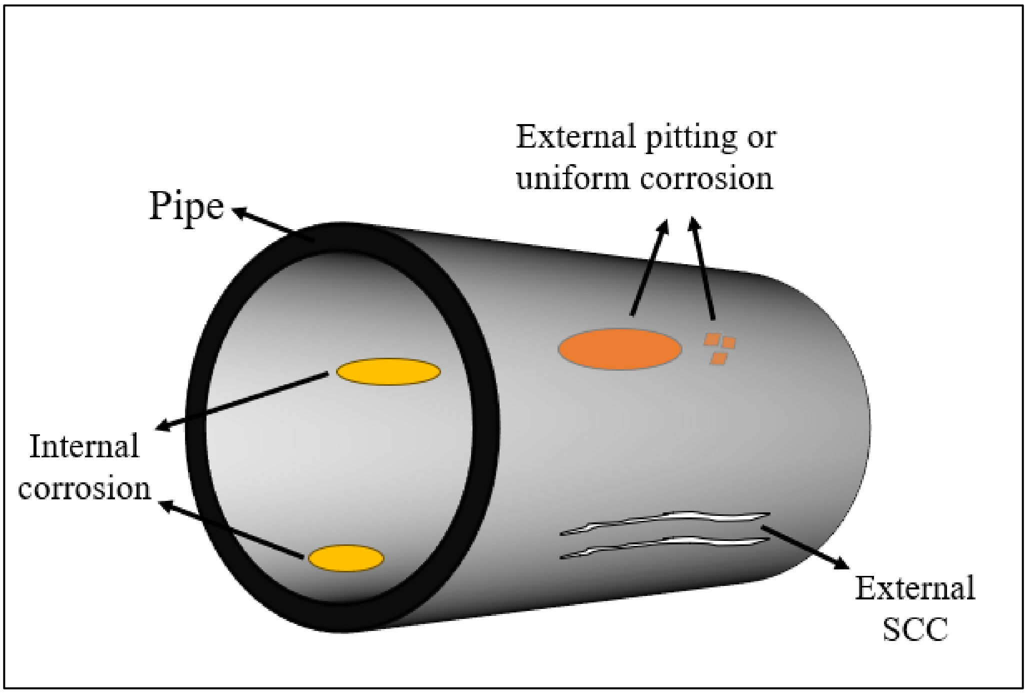

Figure 1-1: Illustrates internal and external corrosion of a pipe, adapted from [9]

The corrosion failure that is observed between a metal surface and the thermal insulation on that surface is termed Corrosion Under Insulation (CUI). The CUI is caused by water and moisture trapping between a metal surface and the insulation on the metal surface, as shown in Figure 1-2 [10-12]. There are several ways in which moisture, in its many forms, can find its way under an insulation system, such as rainwater, leaks, wash water, or even sweating due to temperature cycling or low-temperature operation [13].

Although CUI is not a new issue in the O&G industry, it still poses a serious threat to the entire sector. The problem of CUI does not exclusively affect the O&G industry. It can also affect any insulated pipework or equipment in any other sector, such as those used in power plants, chemical processing facilities and public sectors [12, 14, 15]. CUI is responsible for 20% of significant incidents in the European oil and gas sector, according to the Oil & Gas Technology Centre (OGTC). Approximately 50% of leaks registered from hydrocarbon systems that the Petroleum Safety Authority Norway (PSA) reported were caused by CUI [16].

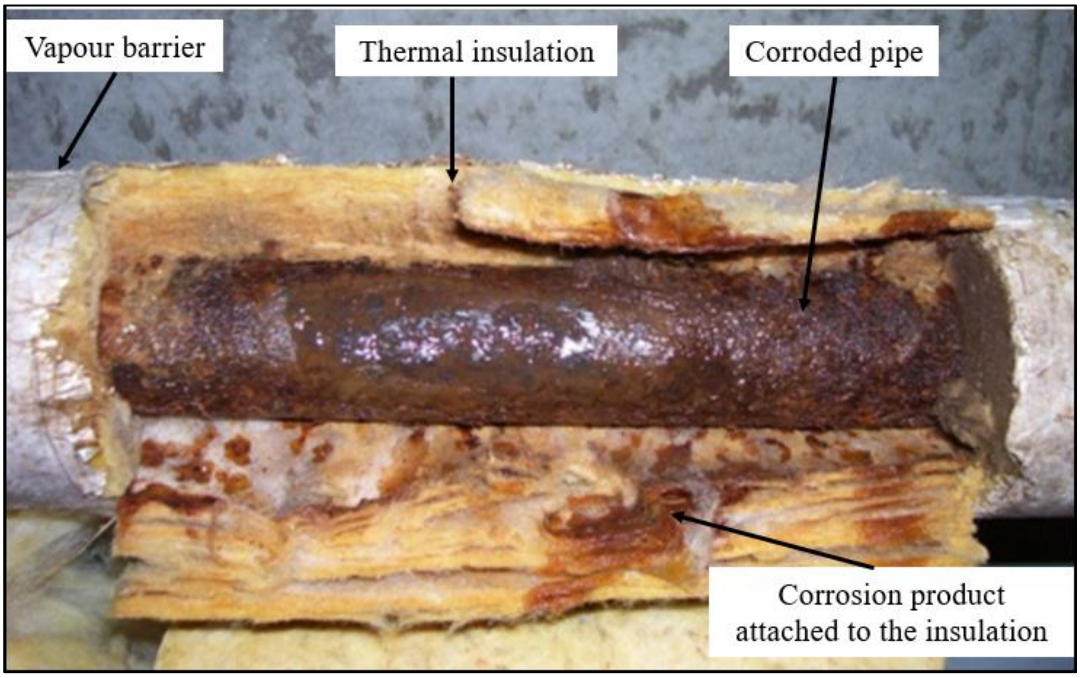

Figure 1-2: Corroded pipe due to Corrosion under insulation (CUI), adapted from [17]

1.2 Cost of Corrosion

Corrosion is a costly and pervasive problem that affects various industries that rely on metallic components, including oil and gas, transportation, construction, and manufacturing. According to estimates, corrosion represents a significant economic burden for industrialized nations, with an average annual cost of 3 to 4% of their total Gross Domestic Product (GDP) as shown in Figure 1-3 [18]. A 2-year study (International Measures of Prevention, Application and Economics of Corrosion Technology "IMPACT") released by NACE international in 2016 showed that corrosion is estimated to cost the global $2,5 trillion, equivalent to approximately 3.4% of the global (GDP) [19].

The comparison illustrates variations in corrosion costs as a percentage of GDP across different regions and countries. The Arab world faces the highest corrosion cost as a percentage of GDP, standing at 5.0%. While the United States (US) has the lowest among the provided data at 2.7% of GDP. Meanwhile, China, Russia, and India fall within a similar cost range at 4,2%, 4.0% and 4.2% respectively. These findings emphasize the importance of proactive corrosion management to minimize financial burdens and promote sustainable economic growth.

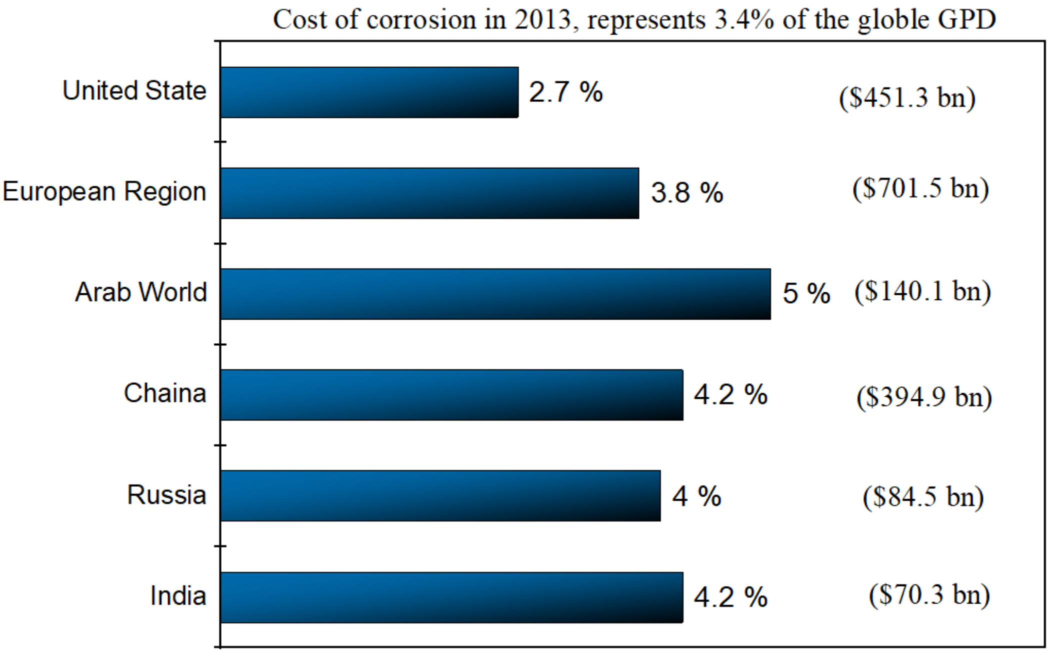

Figure 1-3: The global cost of corrosion in 2013 as a percentage of the national GDP (bn is billion), adapted from [18]

Corrosion costs encompass a range of detrimental effects that can have significant implications in various aspects. These costs can be classified into three major categories: waste of energy and material, economic loss, and environmental impact, per Figure 1-4 [17].

One significant aspect of corrosion costs is the waste of energy and material. Corrosion can lead to the degradation and deterioration of equipment and structures, resulting in the loss of valuable resources. The energy that is consumed in the manufacturing, operation, and maintenance of these assets is wasted as corrosion accelerates their deterioration. Additionally, the materials used in these structures and equipment are gradually degraded, necessitating replacement, and leading to further material waste.

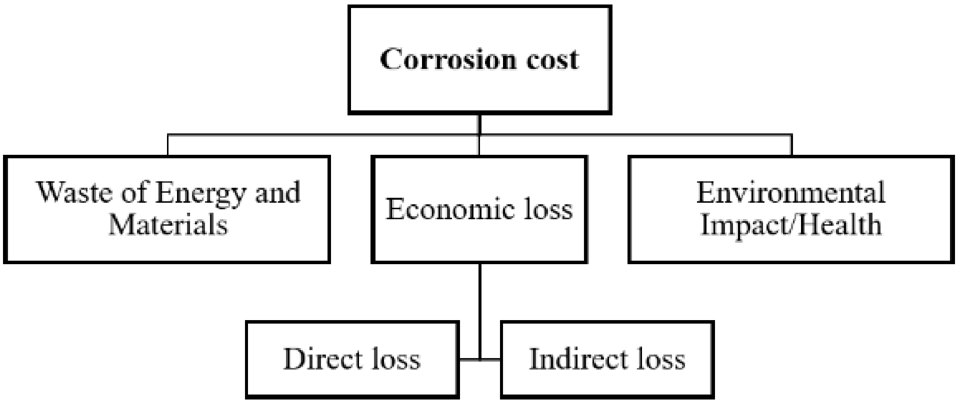

Figure 1-4: The classification of corrosion costs involves categorizing the various expenses associated with corrosion-related issues [20]

The economic loss associated with corrosion extends far beyond the direct financial costs of repairing and maintaining corroded assets. While the expenses incurred for repairing or replacing corroded equipment can be substantial, there are also indirect costs to consider. Corrosion can result in reduced productivity and efficiency as equipment malfunctions or fails. Downtime and production interruptions can lead to delays, decreased output, and lost revenue. Furthermore, there may be additional expenses related to safety measures, inspections, and insurance premiums to mitigate the risks associated with corrosion.

In addition to the financial impacts, corrosion has significant environmental consequences. When materials corrode, they can release harmful substances into the environment. These substances can contaminate soil, water, and air, posing risks to human health and ecosystems. The environmental impact of corrosion extends to the depletion of natural resources as additional materials are required to replace corroded components [21].

According to the World Corrosion Organization (WCO), almost 45% of corrosion costs occur in the O&G industry affecting both onshore and offshore operations [22]. In 2014, the cost of corrosion in China was 3.34% of its GDP, around $176 billion. However, this figure was slightly lower than IMPACT estimated [23]. It is projected that corrosion costs $17.6 billion in the production and manufacturing sector in the USA. This sector comprises oil production, mining, refining, chemical and pharmaceutical production, and agricultural and food production. The USA oil and gas industry is expected to incur a cost of $1.4 billion due to corrosion (about

8% of the total cost of corrosion in the production and manufacturing sectors of the country's economy), as shown in Figure 1-5 [24].

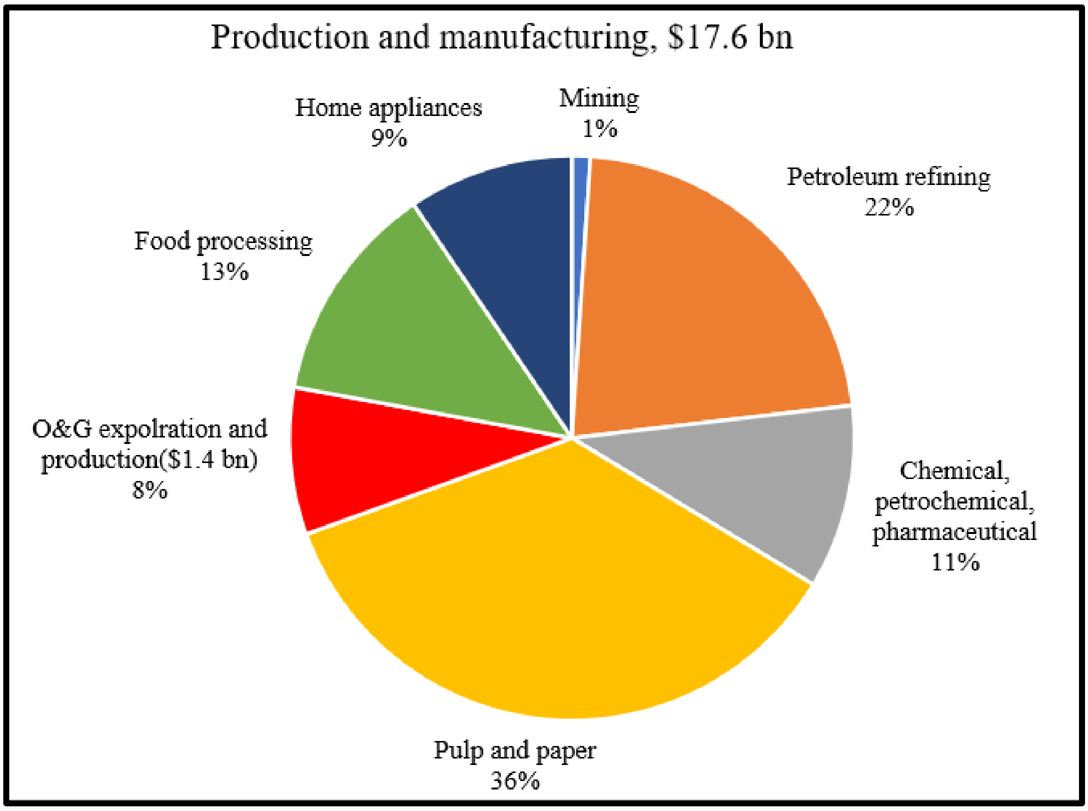

Figure 1-5: Annual corrosion costs in the USA's production and manufacturing sector, adapted from [24]

1.2.1 Cost of Corrosion Under Insulation (CUI)

Globally, it is estimated that the CUI is responsible for approximately £1 trillion in costs annually across the globe. The UK economy is estimated to be impacted by £28 billion in costs per year [25]. CUI can have multiple potential costs and impacts, the most significant being the risk of casualty or severe injury. In addition, CUI-related substance leaks, such as hydrocarbons [26], can cause environmental harm. Corrosion can also lead to production downtime, decreased output, and costly inefficiencies due to the need for expensive maintenance and repairs to industrial assets and pipelines. CUI is believed to account for a significant proportion, estimated to be between 40% to 60%, of pipe maintenance costs, with the repair of CUI damage alone accounting for up to 10% of total annual maintenance costs [14].

As an illustration, in 2002, a sum exceeding $5 million was assigned for the restoration of 304 stainless steel machinery that had malfunctioned as a result of Chloride Stress Corrosion Cracking (CSCC) occurring beneath thermal insulation [27]. In 2006, a leak in a 4-inch hydrocarbon pipe in a petrochemical facility located near the Gulf Coast caused an explosion that cost the company $50 million. The failure occurred due to pipe degradation caused by years of exposure to CUI [28]. These events highlight the importance of regular inspection and maintenance of ageing pipelines and equipment, as well as the need to implement effective CUI prevention and mitigation strategies to prevent similar catastrophic failures in the future. CUI inspection is complex and time-consuming, and lack of proper inspection could affect the insulated equipment integrity and cause catastrophic consequences such as major equipment outages and unexpected maintenance cost, thus raising the CUI cost [10, 29, 30].

1.3 Research objectives

The objective of this study is to examine CUI through the implementation of a three-cell microelectrode arrangement positioned at the top and bottom (12 and 6 o'clock positions) of a pipe, this includes:

- Design and manufacture a rig to evaluate CUI by implementing the use of the three microelectrode cells.
- Design mass loss and post-analysis coupons that cover only the 6 and 12 o'clock positions (bottom and top samples, respectively)
- Understand the effect of variation in the environmental factors such as temperature and pH on CUI rate.
- Evaluate the corrosion rate under thermal insulation by mass loss and linear polarisation techniques.
- Analysis of the chemical composition of the corrosion layer grown on the surface of the top and the bottom samples.

The implementation of a unique three-cell microelectrode configuration represents a pioneering step in the study of CUI. This technique has been utilized to assess top-of-the-line corrosion phenomena.

1.4 Outline of thesis

This thesis comprises a total of seven chapters, including the current one.

Chapter 2 presents an overview of important electrochemistry and corrosion theories, along with the kinetics and thermodynamics relevant to understanding the corrosion behaviour of metal substrates in active environments.

Chapter 3 is the literature review and focuses on corrosion under insulation and covers the typical thermal insulation system, the theoretical mechanisms of corrosion, the common forms of corrosion damages, factors influencing corrosion, and the expected corrosion products. The review provides a comprehensive understanding of the corrosion processes occurring under insulation and offers insights into effective corrosion prevention strategies in industrial settings.

Chapter 4 focuses on the materials used and the experimental procedure employed in the study. The chapter will detail the microelectrodes' material, the type of heating oil used, the insulation material applied, and the specific chemical composition of the electrolyte utilized for the experiments.

Chapter 5 will highlight on presenting the 3D CAD design of the experimental rig, which includes the assembly of the entire setup, including the three microelectrodes configuration. The chapter will provide detailed illustrations and descriptions of the rig's components, their spatial arrangement, and how the microelectrodes are strategically positioned within the system.

Chapter 6 will focus on presenting the results and the discussion of the thermal insulation experiments. This includes detailed analysis and documentation of the findings from images and EDX mapping. Additionally, the chapter will focus on showcasing the results of corrosion under insulation at different temperatures and pH levels. The primary goal will be to establish a correlation between the corrosion rate at the top and bottom sections of the pipe and the formation of corrosion products on the metal surface.

Chapter 7, the conclusions, and recommendations for future research directions are presented.

Chapter 2: Theory of aqueous corrosion: Thermodynamic vs Kinetics

According to NACE/ASTM G193, corrosion is a natural process that leads to the gradual deterioration of a material, often a metal, due to its interaction with the surrounding environment. This interaction is typically initiated by a chemical or electrochemical reaction between the metal and substances present in its environment, such as oxygen, water, or acids. As the reaction proceeds, the metal undergoes a series of physical and chemical changes that ultimately result in mechanical degradation [31].

This chapter presents a review of some critical theoretical and scientific concepts that govern electrochemical aqueous corrosion reactions of metallic substrates. The focus is on both the thermodynamics and kinetics of corrosion. Furthermore, this chapter discusses relevant electrochemical techniques that contribute to an understanding of the corrosion behaviour of materials.

2.1 The electrochemical nature of corrosion

Corrosion represents an electrochemical phenomenon, manifesting only when four essential components combine, represented by the acronym ACME. These components are an Anode, a Cathode, a Metal, and an Electrolyte, collectively forming what is known as a corrosion cell. In this cell, the metal acts as a conductor, facilitating a connection or pathway between the anode and cathode, as illustrated in Figure 2-1.

The Anode and the Cathode are the two primary regions within the corrosion cell. The Anode is the site where metal oxidation occurs, releasing metal ions and electrons into the surrounding environment. On the other hand, the Cathode is where reduction reactions happen, involving the consumption of electrons and the discharge of substances like oxygen or hydrogen.

The metal itself becomes an essential part of the corrosion cell. It acts as the conductor that connects the anode and the cathode, allowing the flow of electrons between these regions. As the metal oxidizes at the anode, it tends to create an electron-deficient area, while at the cathode, it becomes electron-rich due to reduction reactions. This electron flow helps sustain the corrosion process.

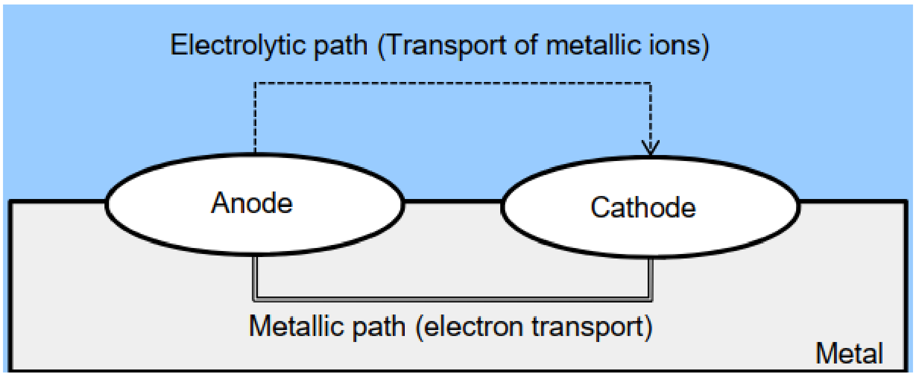

Figure 2-1: The fundamental components in an electrochemical corrosion cell, anode, cathode, metallic path and electrolyte (ACME) [32]

The electrolyte in the corrosion cell is an electrical conductor medium, usually in the form of a liquid or moist environment. Electrolytes facilitate the movement of charged particles, such as metal ions and electrons, between anode and cathode. Among the most common electrolytes are saltwater, acidic solutions, and atmospheric moisture [33].

In the realm of corrosion, its electrochemical nature signifies that the corrosion mechanism does not commence with a direct reaction between the material under investigation and its environment. Instead, it operates through electrochemical half-cells. Equations 2-1 to 2-4 define these half cells, wherein electrons are either generated or consumed as indicated in the respective equations. These half-cells play a crucial role in the overall corrosion process. Equation 2-1 is a general anodic reaction, whereas equations 2-2 to 2-4 are the hydrogen reduction, oxygen reduction in an acid environment and oxygen reduction in a neutral environment, respectively.

The loss of metal occurs as an anodic process, wherein metal oxidation takes place at the anode, resulting in the release of metal ions and electrons into the surrounding environment. In contrast, cathodic reactions involve species being reduced through the consumption of the electrons produced during the anodic process [34].

$$Fe \rightarrow Fe^{2+} + 2e^- \qquad (2\text{-}1)$$

$$2H^+ + 2e^- \rightarrow H_2 \qquad (2\text{-}2)$$

$$O_2 + 4H^+ + 4e^- \rightarrow 2H_2O \qquad (2\text{-}3)$$

$$O_2 + 2H_2O + 4e^- \rightarrow 4OH^- \qquad (2\text{-}4)$$

In many instances, as illustrated by equations 2-2 to 2-4, the solution surrounding the corrosion cell contains various species that could potentially undergo the reduction process, rather than the metal ions produced at the anode. The pH level of the environment plays a pivotal role in determining which specific reduction reaction is more likely to occur. For instance, acidic conditions may favour hydrogen evolution, while basic environments may promote hydroxide creation [35].

However, it is important to emphasize that in real-world scenarios, both cathode and anode may be located on the same metal surface. Due to these localized conditions and the availability of reactants, different regions of the metal may undergo corrosion simultaneously.

2.2 Thermodynamic of corrosion

As with all natural processes, corrosion occurs when conditions are favourable for the reaction. A corrosion reaction is governed by thermodynamic principles, in which every element involved in the reaction seeks to minimize its state of energy. To initiate the conversion of iron ore into iron metal, energy is typically introduced through diverse techniques, including the application of high temperatures generated through combustion or electrical heat sources. During this transformative process, the iron ore absorbs energy via thermal input, thereby facilitating the reduction reactions that culminate in the conversion of iron oxide to metallic iron. Upon successful formation of the iron metal, its exposure to the surrounding environment marks the onset of a natural energy dissipation process. Through the phenomenon of corrosion, the iron metal gradually relinquishes the previously gained energy. Iron begins to react with oxygen and moisture in the presence of moisture, primarily by oxidizing. The corrosion process produces corrosion products with lower energy states and higher stability than the original iron metal, including iron oxides such as rust [36].

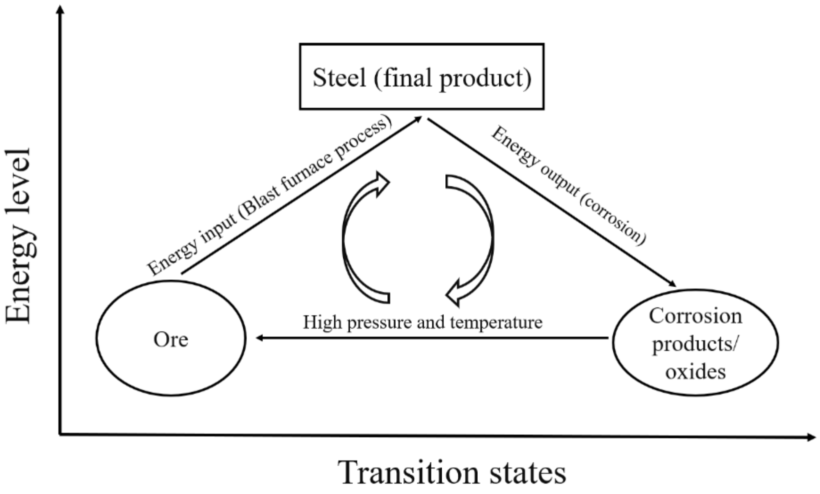

Figure 2-2: Different forms of metal in terms of their energy state, adapted from [37]

The process of corrosion in electrochemical systems is influenced by both chemical and electrochemical reactions taking place on the surface, as well as the interfacial energy of the material, making the thermodynamics of corrosion quite complex [38]. To determine whether corrosion will occur spontaneously, it is essential to obtain the Gibbs free energy changes (ΔG) associated with the reaction. If the Gibbs free energy change linked with the corrosion reaction is negative, corrosion can occur under favourable thermodynamic conditions. This implies that the reaction is energetically favourable and, therefore, more likely to proceed. When all the reactants and products are in their standard states, with the temperature at 25°C and the pressure is 1 bar the standard free energy change, ΔG^{o} is given by equation2-5.

$$\Delta G^{o} = -nFE_{cell}^{o} \tag{2-5}$$

Where;

n is the number of electrons participating in the chemical reaction

F is the Faraday constant (96485 s.A.mol^{-1})

E_{cell}^{o} is the standard potential of the reaction (V)

In Equilibrium conditions, E_{cell}^{o} is given by equation 2-6 [39]

$$E_{cell}^{o} = E_{cathode}^{o} - E_{anode}^{o} \qquad 2\text{-}6$$

The electromotive force series for selected elements, representing the standard half-cell electrode potentials against the standard hydrogen electrode (SHE), is provided in Table 2-1. The reactions listed in this table are presented as reduction reactions, moving from left to right at a temperature of 25°C. Yet, they provide information regarding the relative reactivity of metals, while Gibb's free energy is a valuable tool for assessing the spontaneity of a chemical reaction [40].

Table 2-1: Standard potentials series vs (SHE) in volts (V), at 25°C [39]

Electrode reaction	E° (V SHE)
$\mathbf{Au^{+} + 3e^{-} \rightarrow Au}$	+1.5
$\mathbf{Pt^{2+} + 3e^{-} \rightarrow Pt}$	+1.19
$\mathbf{Ag^{+} + e^{-} \rightarrow Ag}$	+0.8
$\mathbf{Fe^{3+} + e^{-} \rightarrow Fe^{2+}}$	+0.77
$\mathbf{2H^{+} + 2e^{-} \rightarrow H_2}$	0.0
$\mathbf{Ni^{2+} + 2e^{-} \rightarrow Ni}$	-0.25
$\mathbf{Fe^{2+} + 2e^{-} \rightarrow Fe}$	-0.44
$\mathbf{Mn^{2+} + 2e^{-} \rightarrow Mn}$	-0.18

Electrochemical reactions seldom occur under standard conditions (temperature 25°C, pressure 1 bar and the reaction quotient equal to 1), as the activity of various species can differ greatly from unity and the temperature can vary significantly from ambient conditions. To understand the underlying mechanisms of corrosion reactions, the transition state theory plays a crucial role. This theory can be mathematically expressed through the redox reaction as illustrated in equation 2-7 [39].

$$aA + bB \rightarrow cC + dD \qquad 2\text{-}7$$

Where;

A and B are the reactants substance

C and D are the product substances

a and b are the moles of the reactant’s substances

c and d are moles of the products

Equation 2-7 describes the reaction mechanism in which two reactants, A and B, combine to form two new products, C and D. The reaction requires the physical interaction of the reactants to form an intermediate species, AB. The formation of AB is a brief process that requires a sufficient amount of energy and proper orientation. This intermediate state, AB, is known as the transition state, which is a crucial step in the reaction mechanism.

As per the transition state theory, an intermediate state, known as the transition state, exists between the initial state, where the molecules are reactants, and the final state, where the molecules have become products. The transition state forms at the maximum energy level, and the reaction requires a specific amount of energy to surpass the energy barrier and reach the transition state. Once the energy barrier is surpassed, the reaction proceeds and the products are formed [35, 38, 41, 42].

Figure 2-3 displays the variations in free energy that occur throughout a reaction, with the y-axis representing energy and the x-axis representing the progression of the reaction process.

Corrosion often occurs in non-equilibrium (non-standard) conditions, where one or more standard parameters such as temperature, pressure, or chemical composition deviate from their equilibrium values. In these cases, the calculation of the free energy of a system using standard thermodynamic relationships, equation 2-5, will not be valid. Hence, to ensure an accurate description of the thermodynamics of the system, using equation 2-8 may become necessary [33].

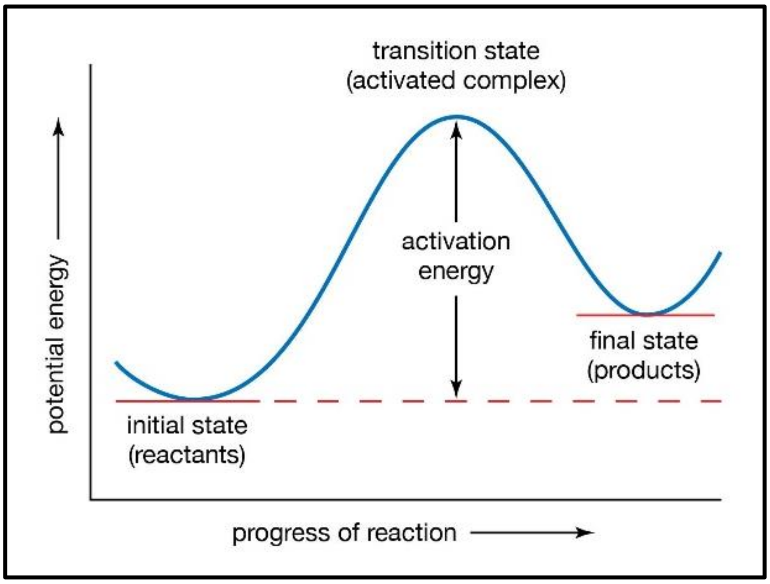

Figure 2-3: Transition state theory [43]

$$\Delta G = -nFE_{cell} \tag{2-8}$$

Where;

E_{cell} is the cell potential in a non-equilibrium state (V) and is obtained by using equation 2-9, which is known as the Nernst equation.

$$E_{cell} = E^{\circ}_{cell} - \frac{RT}{nF} lnQ \tag{2-9}$$

Where, T is the reaction temperature in kelvins (K), R represents the universal ideal gas constant (8.3145 $JK^{-1}mol^{-1}$) and Q is the reaction activity quotient corresponding to Gibb's free energy of the system, and it is the ratio between the activities of product species over the reactant species.

Meanwhile, by using equation 2-7, further simplification of the activity quotient is given by equation 2-10.

$$Q = \frac{[C]^c[D]^d}{[A]^a[B]^b} \tag{2-10}$$

Thus, the appropriate expression of the Nernst equation under non-equilibrium conditions is presented in equation 2-11.

$$E_{cell} = E^{o}_{cell} - \frac{RT}{nF} ln \frac{[C]^{c}[D]^{d}}{[A]^{a}[B]^{b}} \qquad 2\text{-}11$$

Nernst's equation relates the equilibrium potential of an electrochemical cell to the concentrations of reactants and products involved in the cell reaction. The equation shows that the cell potential depends on the concentration of the electroactive species, temperature, and the standard potential of the reaction. The logarithmic term in the equation reflects the effect of the solution composition, or activity, on the cell potential. This means that changes in the concentration of reactants or products have a relatively weak effect on the cell potential, as the logarithmic relationship dampens the effect of concentration changes [38, 44].

Thus, electrochemical corrosion can occur under the following thermodynamic conditions:

If E_{cell} is > 0, then $\Delta G< 0$ and loss of ions and corrosion becomes spontaneous.

If E_{cell} is = 0, then ΔG= 0, the corrosion is at equilibrium, and therefore there is no tendency for corrosion to occur.
If Ecell is < 0, then ΔG > 0 and the loss of electron and corrosion becomes nonspontaneous under these conditions [38, 45, 46].

2.2.1.1 The Pourbaix (E-pH) diagram for Fe-H_2O

Marcel Pourbaix created a novel and concise potential-pH diagram in 1945 to evaluate the comparative stability of a specific metal. This diagram has come to be recognised as the Pourbaix diagram or (E-pH diagram) [39]. Pourbaix diagrams illustrate the thermodynamic stability of various phases that may exist for a given metal under different potential and pH conditions under the standard conditions (temperature 25°C, pressure 1 bar, concentrations of ions 10^{-6}M). In this diagram, the redox potential, in the y-axis, of a metal is plotted as a function of solution pH, x-axis. The Pourbaix diagram provides a visual representation of the regions where the metal is thermodynamically stable, unstable, or immune to corrosion based on Nernst equations. Figure 2-4 depicts the typical E-pH diagram for the Fe-H_2O system at 25°C. The stability of metallic iron is dependent on its environment, as it can corrode in regions where hydrated forms of Fe^{+2}, Fe^{+3}, and $FeOH^{-}$ remain stable. In contrast, when metallic iron is stable and has a higher negative potential, it is immune to corrosion. The presence of stable metallic oxide regions also contributes to the protection of iron against corrosion, which is known as a passive region. In the last region, iron is considered to be in a thermodynamically stable phase, which means that under normal conditions, it is resistant to corrosion [47].

In the presence of atmospheric oxygen, iron can undergo corrosion at potentials below the Oxygen Equilibrium Potential (OEP). Furthermore, in aqueous phases, hydrogen ions may cause corrosion at potentials that are below the Hydrogen Equilibrium Potential (HEP) [48].

The horizontal lines (A-B and D-E) on the diagram represent pure electron transfer (redox) reactions, which depend solely on potential but are independent of pH levels as shown in equations 2-12 and 2-13.

$$Fe(s) \rightarrow Fe^{+2}(aq) + 2e^{-} \qquad 2\text{-}12$$

$$Fe^{+2}(aq) + \rightarrow Fe^{+3}(aq) + e^{-} \qquad 2\text{-}13$$

There are vertical lines, such as K-E, that represent reactions that are not involved in electron transfer (potential independent) but are pH dependent. The following equation is an example of such reactions.

$$Fe^{+3} + 3H_2O \rightarrow Fe(OH)_{3+} + 3H^{+} \qquad 2\text{-}14$$

The sloping lines in the E-pH diagram represent a combination of redox and acid-base reactions involving H^{+} or OH^{-}. These reactions are shown in equations 2-15 and 2-16. The $Fe(OH)_2$ is a prevalent iron (II) oxyhydroxide compound typically observed within the iron oxide layer that forms on carbon steel during atmospheric corrosion [49]. This iron oxyhydroxide has been reported in corrosion layers resulting from CUI conditions [50].

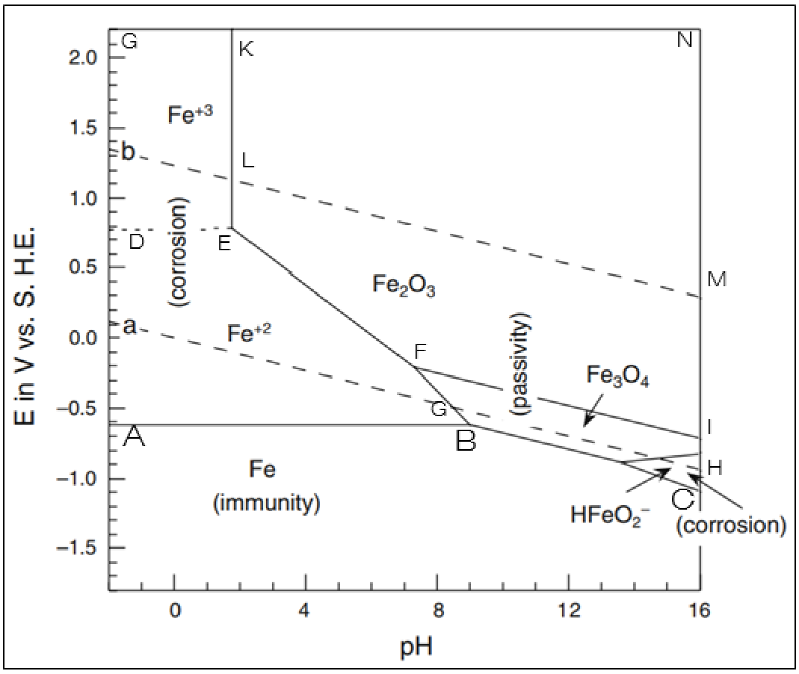

Figure 2-4:Pourbaix diagram for iron-water at 25°C [41]

$$Fe + 2H_2O \rightarrow Fe(OH)_2 + 2H^+ + 2e^- \qquad 2\text{-}15$$

$$Fe + 2H_2O \rightarrow HFeO_2^- + 3H^+ + 2e^- \qquad 2\text{-}16$$

A thermodynamic analysis of corrosion processes, including those using Pourbaix diagrams, can only indicate the feasibility of the corrosion process and may have many limitations. Determining the kinetic parameters of the corrosion reactions from the charts is unachievable. These diagrams are based on aqueous solutions and pure metals at standard conditions, even though actual conditions may differ significantly from equilibrium. Since corrosion products (oxides, hydroxides, etc.) may not always precipitate on the surface of the metal, the implicit assumption that corrosion products lead to passivity is not necessarily valid. A corrosion prediction based on the solution's bulk pH may be inaccurate because the pH at the metal surface may vary dramatically due to side reactions [34, 37].

2.3 Corrosion kinetics

Material lifetimes are primarily determined by the corrosion rate of a metal or alloy in its environment [41]. The importance of corrosion kinetics over corrosion thermodynamics is that; some metals with a high tendency to react (e.g., aluminium) can react at such a slow rate that they can meet the requirements for a structural metal and may also tend to react with media more reactively than metals that have a naturally less reactive tendency. Several approaches can evaluate the corrosion rate, such as mass loss, thickness measurements or electrochemical techniques [38, 51]. There are different types of corrosion rate expressions that can be used depending on both the technical system and the type of corrosion. The typical way to represent this is by measuring the penetration rate in millimetres per year (mm/year). However, it is also possible to express it in terms of mass loss, penetration, or corrosion current densities. These different aspects can be determined using various methods such as direct mass loss, thickness measurements, or commonly used electrochemical techniques.

The corrosion rate correlates with the rate of electron transfer and, therefore, with the current flow associated with it. It is usually referred to as corrosion current density and is dependent upon the surface area of the element that is corroding. Mixed potential theory and the Butler-Volmer equation are two theories used to explain the relation between corrosion rate and corrosion current density.

2.3.1 The Electrochemical nature of corrosion

In aqueous systems, metallic corrosion is an electrochemical process in nature, for this reason, it can be effectively studied using electrochemistry techniques. For a corrosion reaction to take place on a metal or alloy, it must have four essential components: anodic and cathodic sites, an electrical conductor and an electrolyte as shown in Figure 2-5 [52].

Therefore, an electrochemical cell model for corrosion should be constructed using two electrodes composed of distinct half-cell reactions interacting across an electrolyte conducting current. In corrosion reactions, oxidations and reductions are involved, and the redox couples (reduction-oxidation pairs) of these reactions differ.

In the oxidation half-cell, electrons are released from the substrate metal into electrochemically active species in the electrolyte, whereas electrons are gained or consumed in reduction half-cells. During half-cell, anodic reactions, the steel, Fe, is directly oxidised to produce Fe^{+2} ions and a number of electrons, $2e^-$. This means that the number of electrons released equals the state of the valence of the metal ion created by the reaction demonstrated in equation 2-12 [54, 55].

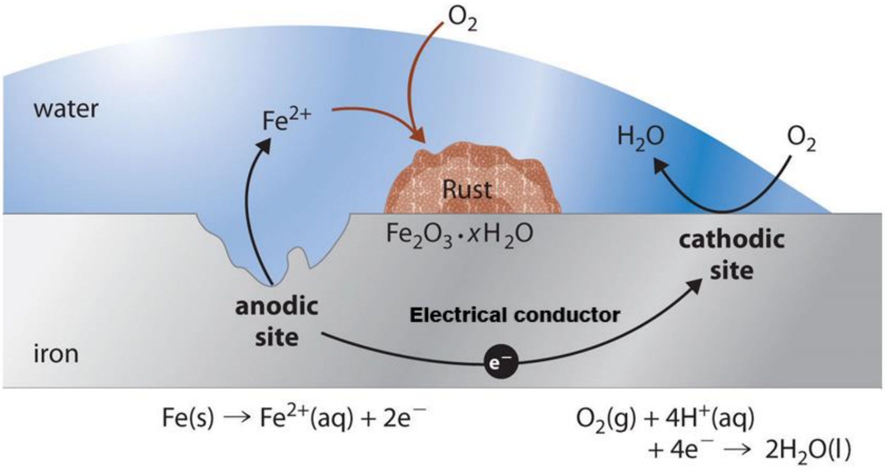

Figure 2-5: The four components of the corrosion cell [53]

In different environments, half-cell cathodic reactions can take on a variety of forms depending on the pH and the availability of dissolved oxygen in the solution. The cathodic reaction can be the oxygen reduction in neutral, acid environments and hydrogen evolution as shown in equations 2-17 to 2-19, respectively.

$$O_2 + 2H_2O + 4e^- \rightarrow 4OH^- \qquad 2\text{-}17$$

$$O_2 + 4H^+ + 4e^- \rightarrow 4OH^- \qquad 2\text{-}18$$

$$2H^+ + 2e^- \rightarrow H_2 \qquad 2\text{-}19$$

2.4 Study of corrosion: Electrochemical methods

Corrosion of metallic materials in aqueous environments is fundamentally an electrochemical process. Therefore, electrochemical techniques would be appropriate for the investigation and understanding of these phenomena. Among the many applications of electrochemistry are the reduction of metal ions into atoms on an electrode surface, which can be achieved both chemically and electrochemically. The flow of current is only associated with the electrochemical approach, which initiates metal reduction at the nanoscale, resulting in the formation of atom agglomerates or nanoparticles [44].

2.4.1 Three electrode cell setup

The direct measurement of the potential of a common metal immersed in a solution is not feasible, nevertheless certain techniques have been developed to overcome this limitation such as the three-electrode setup. This setup comprises three electrodes: the working electrode (WE), a reference electrode (RE), and a counter electrode (CE). The reference electrode provides a stable reference potential against which the working electrode potential can be measured. The counter electrode, on the other hand, is used to facilitate the flow of electrical current. By monitoring the potential of the working electrode as a function of the reference electrode, the behaviour of the electrochemical system can be studied. It should be noted that in both Alternating Current (AC) and Direct Current (DC) electrochemical techniques,

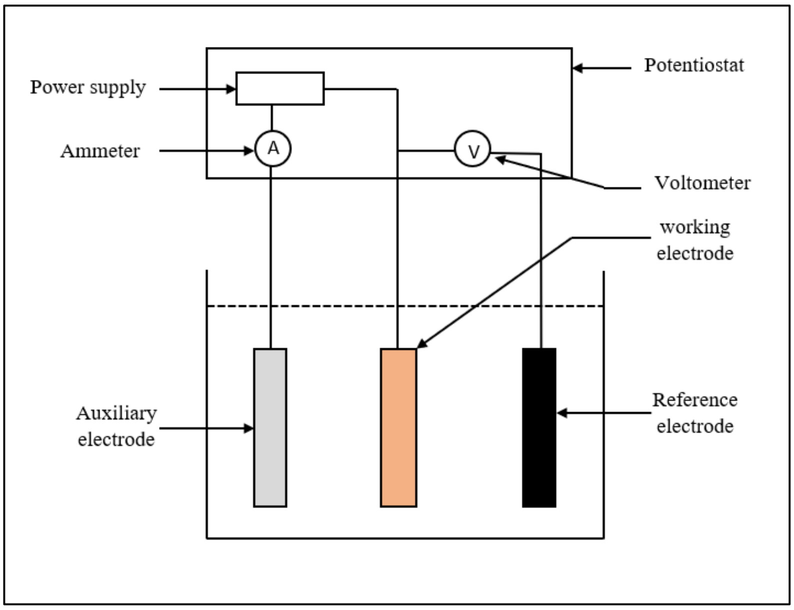

Figure 2-6: Schematic diagram of a three electrodes cell, adapted from [33]

a separate auxiliary electrode is required to complete the electrical circuit, as shown in Figure 2-6 [33].

In essence, the WE is the site where the reaction of interest occurs and the corrosion rate is measured. In an ideal scenario, the CE should be made of a material that can support electrochemical oxidation and reduction reactions with the reactant present in the electrolyte without corroding or contaminating the electrolyte [38]. In general, CEs are commonly fabricated using noble metals like platinum, but this is not mandatory. On the other hand, the RE within a three-electrode setup should be composed of a material that can consistently maintain its potential throughout the entire experimental process[56]. There are various commercially available types of reference electrodes, including the standard hydrogen electrode, silver/silver chloride electrode, and calomel electrode. Typically, counter electrodes and reference electrodes are obtainable in the form of integrated platinum wires with silver-silver chloride electrodes or saturated calomel electrodes [33].

As shown in Figure 2-6, a high-impedance voltmeter is used to measure the voltage between the working electrode (WE) and the reference electrode (RE) using a potentiostat. At the same time, an ammeter calculates the amount of current flowing between the counter electrode (CE) and the work electrode (WE). This configuration is intended to minimize the amount of current passing through the RE, while simultaneously allowing the desired current or potential to be applied through the WE via the CE [56].

2.4.2 Open Circuit Potential (OCP)

When a metal is exposed to a corrosive electrolyte, both anodic (oxidation) and cathodic (reduction) reactions occur simultaneously on its surface. As these reactions progress, the rates of anodic and cathodic reactions reach a state of equilibrium, which is referred to as the open circuit potential (OCP) [57]. In electrochemistry, the OCP is determined experimentally during periods of no electrical current flow and is subject to alteration as the conditions of the electrochemical cell are modified. To measure the OCP, a reference electrode equipped with a high-impedance voltmeter is used to prevent current flow between the test electrode and the reference electrode [38, 48, 57].

2.4.3 Polarisation and corrosion kinetics

The concept of polarisation is intricately connected to the kinetics of electrochemical corrosion. The term polarisation refers to the deviation from the equilibrium potential caused by a current flow or a net charge flow during the corrosion process. The magnitude of deviation in electrode potential difference from equilibrium condition is termed as over-potential (η) and is expressed in equation 2-20.

$$\eta = E - E^{\circ} \qquad 2\text{-}20$$

Where, E and E^{o} are final potential and equilibrium potential respectively.

Figure 2-7 illustrates a schematic representation of a polarisation diagram for the reduction-oxidation (RedOx) in iron (Fe). Anodic polarisation refers to the positive overpotential, denoted as (η_a), which causes a deviation in the electrode potential from its equilibrium value in the positive direction. While cathodic polarisation refers to the negative overpotential, known as (η_c), which causes a deviation in the electrode potential from its equilibrium value in the negative direction.

There are three types of polarisation phenomena occurring independently or simultaneously when a metal substrate interacts with its environment. Activation-controlled polarisation (η_{act}), occurs when the rate of metal supply at the metal surface is higher than the rate at which metal ions are deposited. This type of polarisation is primarily influenced by factors such as the activation energy required for the electrochemical reactions to occur at the electrode-electrolyte interface and the availability of metal ions for deposition. Concentration polarisation (η_{con}), also known as diffusion-controlled polarisation, occurs when the metal deposition rate is greater than the diffusion rate of metal ions through the bulk solution. There is an association between concentration polarisation and the availability of cations around the cathode. As ionic species are eliminated around the cathode, polarisation is controlled by mass transport (diffusion). Resistance polarisation (iR) is also known as ohmic polarisation when the electrode-electrolyte interface has a significant resistance to current flow. Due to this resistance, a voltage drop can occur, which can lead to a deviation in the electrode potential from the equilibrium potential [33, 38].

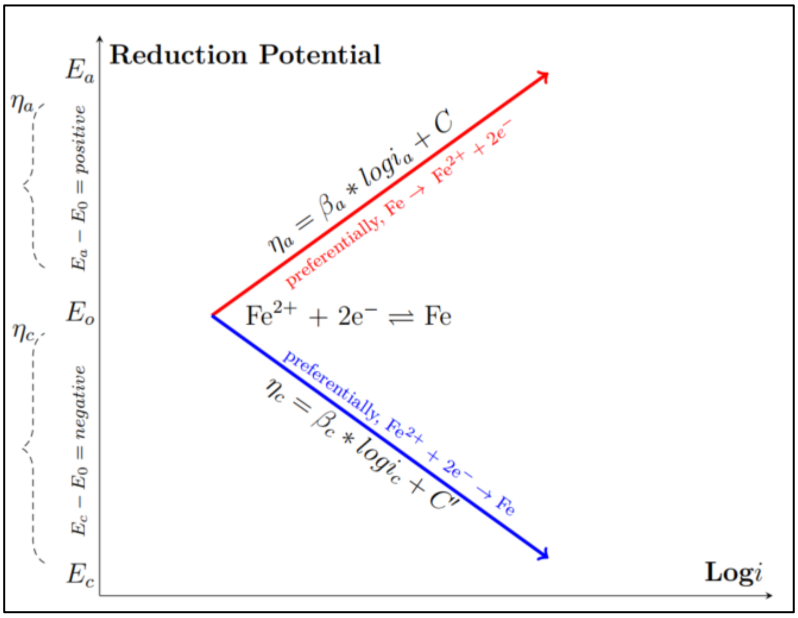

Figure 2-7: Polarisation Diagram for Redox in Fe [58]

Thus, the combined effect of activation polarisation, concentration polarisation, and resistance polarisation contributes to the overall polarisation that impacts the kinetics of corrosion as given by equation 2-21

$$Total\ polarization\ (\eta_{total}) = \eta_{act} + \eta_{con} + iR \qquad 2\text{-}21$$

However, in most cases, ohmic resistances are not considered unless the reaction itself or an associated reaction generates films on the electrode surface.

2.4.4 Electrical double layer (EDL)

In the presence of a corrosive electrolyte, metal (M) undergoes corrosion, resulting in the formation of M^{n+} ions, as shown in equation 2-22. Along with the formation of Mn^+ ions, free electrons are also released. Cations dissolved in water become hydrated and move freely away from the metal, which causes the metal to become negatively charged.

$$M \rightarrow M^{n+} + ne^{-} \qquad 2\text{-}22$$

The metal surface, which is now negatively charged, attracts positively charged ions present in the solution. This interaction creates a potential difference between the bulk solution and the metal surface, which establishes a dynamic equilibrium [75]. Although a significant proportion of the cations accumulate close to the metal surface, they are unable to reach the excess electrons due to the presence of water layers acting as barriers. The cations would be reduced to metal atoms if they were to come into contact with the surface electrons. This means that the bulk electrolyte, cations, and water molecules form the interface between the electrolyte and the metal. A thin layer of electrically charged material is formed at the metal-electrolyte interface as a result of this phenomenon. This layer is referred to as the Electric Double Layer (EDL). This is shown schematically in Figure 2-8.

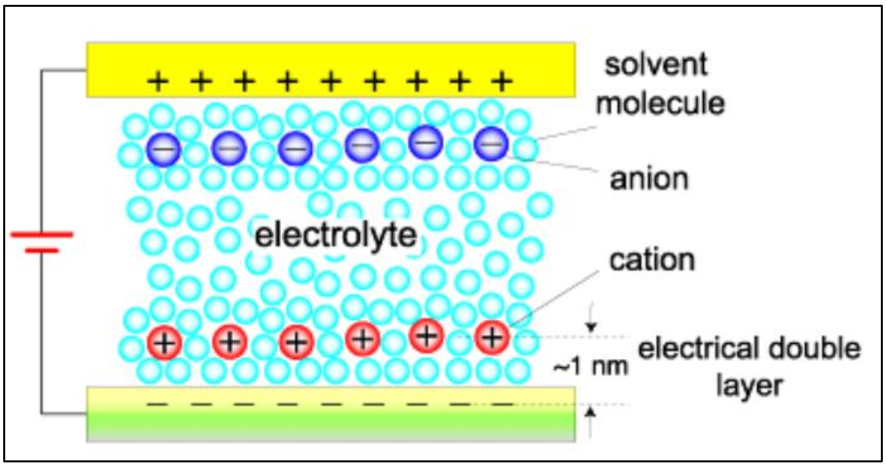

Figure 2-8: Diagram depicting the Electric Double Layer (EDL) [59].

However, when a metal corrodes, the system is not in equilibrium since cations continue to migrate from the EDL. This is due to the presence of Electrochemically Active Species (EAS), such as cathodic hydrogen. In this case, EAS diffuses to the steel surface and is reduced by excess electrons in the EDL, which creates an imbalance which is neutralized by anodic dissolution. The corrosion process will proceed as long as excess electrons released by anodic dissolution are available to be consumed by EAS [48].

EDLs also take into account potential differences observed when metals are immersed in electrolytes [48]. With regard to electron transfer in corrosion processes, the existence of this electrical potential has led to studies of the relationship between voltage, current, and EDL composition [51, 60].

2.4.5 Butler-Volmer equation

The Butler-Volmer equation relates electrical current to changes in metal potential caused by an external power source as shown in equation 2-23 [61]. The $e(\alpha Fn\eta/RT)$ component is for the cathodic current, while $e((1-\alpha)Fn\eta/RT)$ is for the anodic current. When a clean and pure metal is placed in a solution containing one of its salts, it reaches a dynamic equilibrium state where the rates of cathodic and anodic reactions are balanced, and the flowing currents correspond to the exchange current. The equation comprises two components, one representing the oxidation (forward reaction) and the other the reduction (reverse reaction).

$$i = i_{ex}[e^{\frac{\alpha Fn\eta}{RT}} - e^{-\frac{(1-\alpha)Fn\eta}{RT}}] \qquad \text{2-23}$$

Where i is the net current passing through the electrode in A/m^2

i_{ex} is the exchange current density in A/m^2

α is the symmetry coefficient for the anodic or cathodic reaction in a dimensionless unit and it is close to 0.5.

η is the activation over-potential (E-E_o) in V

R is the universal gas constant (8.314) J/Kmol

T is the absolute temperature in K

F is the Faraday constant (96485) C/mol

n is the number of participating electrons

At a state of equilibrium, where activation over potential (η) is equal to 0, the exchange current density characterizes the rates of oxidation and reduction. Specifically, it represents the current density at which the oxidation and reduction processes are balanced and equal as described in equation 2-24 [35].

$$i_{ex} = i_a = i_c \qquad 2\text{-}24$$

When even a slight deviation from the equilibrium potential occurs, the anodic and cathodic currents will no longer be balanced, and the net current will respond to the introduced potential disturbance. The magnitude of the exchange current plays a crucial role in this behaviour. If the exchange current has a large value, even a small change in potential will lead to a substantial alteration in the net current. Conversely, when the exchange current is small, significant deviations in potential from the equilibrium will result in only minor net restoring currents.

When an anodic overpotential is induced through a potentiostat, the exponential term for the anodic reaction (forward reaction) becomes dominant, and conversely, if a cathodic overpotential is applied, the exponential term for the reduction reaction becomes dominant(reverse reaction) [6].

However, during a cathodic potential shift, the net current experiences a change, resulting in a negative overpotential (η). Consequently, the current density is expressed using equation 2-25.

$$i = i_c - i_a \qquad 2\text{-}25$$

Conversely, when an anodic potential shift occurs, the net current changes, leading to a positive overpotential (η). In such cases, the current density is also represented by using equation 2-26.

$$i = i_a - i_c \qquad 2\text{-}26$$

2.4.6 Tafel Polarisation

The Tafel polarisation technique, also called the Tafel extrapolation technique, is an electrochemical method used to record the non-equilibrium potential and current response of a corrosion cell in a potential-current plot. The current response is typically represented on a logarithmic scale. Moreover, the Tafel polarisation technique is employed to estimate the Tafel slopes (β_a and β_c) from a single polarisation curve as illustrated in Figure 2-9. This curve is commonly referred to as the Stern diagram, which is derived from equation 2-23, and represents non-linear polarisation behaviour. Additionally, the Evans diagram, representing linear polarisation, is included in the figure to demonstrate the existence of a common point such as E_{corr} and i_{corr} between both diagrams. The Stern diagram and the Evans diagram provide valuable insights into the anodic and cathodic processes, facilitating a comprehensive understanding of the electrochemical behaviour of the metal in a given corrosive environment [35].

The Tafel involves polarising a working electrode (the substrate metal) in both the anodic and cathodic directions over an over-potential range of ±300 mV around the open circuit potential (OCP) of the substrate metal in an electrolyte. To estimate the Tafel slopes, a narrower over-potential range of ±5-10mV off E_{corr} is typically considered to capture the linear regions of the anodic and cathodic processes. These Tafel slopes are then utilized to calculate the Stern-Geary constant (β) according to equation 2-27 [6].

$$\beta = \frac{\beta_a \left| \beta_c \right|}{2.303(\beta_a + \left| \beta_c \right|)} \qquad \text{2-27}$$

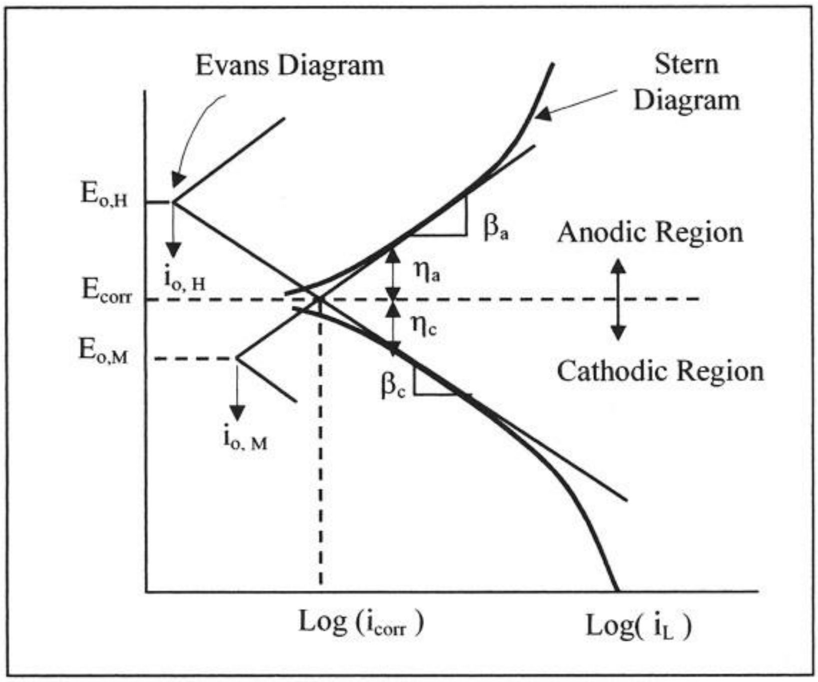

Figure 2-9: A polarisation curve showing Tafel extrapolation [35]

2.4.7 Linear polarisation resistance

The linear polarisation resistance (LPR) is defined as the polarisation resistance of a material, which is obtained by calculating the slope of the potential-current density ($\Delta E/\Delta i$) curve at the free corrosion potential as shown in Figure 2-10. Since the working electrode is polarized by only ± 15mV from the OCP, the LPR technique is regarded as a non-destructive method for monitoring corrosion. This yields the value of polarisation resistance (R_p), which can be further related to the corrosion current density (i_{corr}) by using Stern- Geary equation 2-28 [62].

$$i_{corr} = \frac{\beta}{R_p} \tag{2-28}$$

Where β is the empirical polarisation resistance composed of the anodic (β_a) and cathodic (β_c) Tafel constants in mV/decade and can be determined by using the Tafel polarisation curve and equation 2-27.

Figure 2-10 demonstrates the test procedure, which initiates at a potential 15 mV lower than E_{corr} (owing to cathodic polarisation) and then proceeds by shifting 15 mV in the positive direction through anodic polarisation. The data presented in this test were obtained from a CUI laboratory experiment rig conducted on ASTM A 106 Gr B carbon steel with an 800-grit finish using SiC paper. The test was conducted at a pH of 7 and room temperature, with the solution containing a salt concentration of 3.5% sodium chloride. Thus, by considering a uniform current distribution across the working electrode and analysing the slope Rp from Figure 2-10, it becomes possible to derive a more simplified expression of the Stern-Geary equation, which is presented in equation 2-29.

$$i_{corr} = \frac{\beta_a |\beta_c|}{2.303(\beta_a + |\beta_c|)R_p} \quad \text{2-29}$$

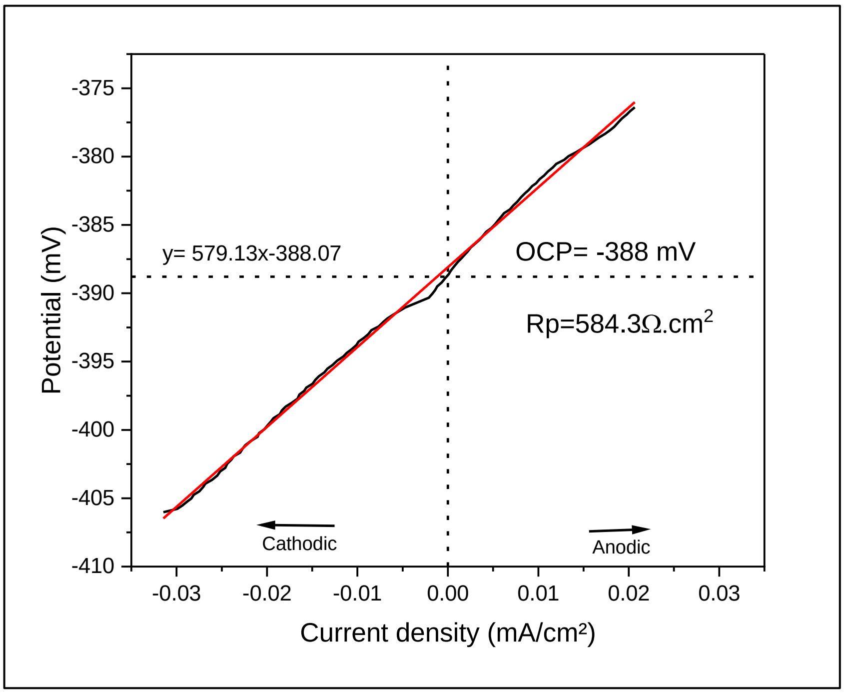

Figure 2-10: Example of LPR curve measured from CUI rig by using three microelectrode cell

The corrosion rate in millimetres per year (mm/year) can be correlated to the corrosion current density i_{corr} in milliamperes per square centimetres (mA/cm²) as shown in equation 2-30 [6]. This equation provides a quantitative relationship between the observed slope and the corrosion rate, offering valuable insights into the corrosion behaviour of the tested material under specified experimental conditions.

$$Corrosion\ rate\ (mmpy) = 3.27x10^{-3}\frac{i_{corr}E_w}{\rho} \qquad \text{2-30}$$

Where $3.27x10^{-3}$ is a conversion constant in mm. g/μA/cm/year

i_{corr} is corrosion current density in μA/cm^2,

E_W is the material equivalent weight described as the atomic weight divided by the number of transported charges for pure elements.

ρ is the metal density in g/cm^3

2.4.8 Mass loss

Mass loss analysis is a quantitative method for monitoring and measuring corrosion in metallic structures. The process will involve the introduction of a weighed sample of the metal or alloy under consideration into the test environment, and its removal after a reasonable time. Since time and weight are the only indicators used to monitor corrosion, this may be the simplest corrosion monitoring method available. In order to determine the accuracy of the corrosion rate, the coupon is first cleaned of all corrosion products by chemical means before being weighed. The mass loss is then converted to corrosion rate (CR) by the given equation 2-31.

$$CR = K\frac{w}{At\rho} \qquad \text{2-31}$$

Where; K is a constant ($8.76x10^4$), w is the mass loss (g), A is the surface area in (cm^2), t is the exposure time in (hour) and ρ is the metal or alloy density in (g.cm^{-3}).

Chapter 3: CUI literature review

Despite the first failure due to CUI being reported in 1965, over half a century ago, there has been limited literature published on this subject. In 1971, ASTM published the first standard relevant to CUI, ASTM C691-1971 ”*Evaluating the influence of wicking type thermal insulations on the stress corrosion cracking tendency of austenitic stainless steels*” [63]. Since then, other institutes such as NACE (currently known as AMPP) and API have conducted investigations and gathered information to create a clear understanding of CUI. Currently, the literature on CUI can be categorized into standards, control measures, inspection techniques, recommended practices, scientific publications and reviews.

In refineries, thermal insulation plays a critical role in energy saving, process efficiency, and overall operational sustainability. Figure 3-1 depicts a visual representation of thermally insulated pipes and vessels within an oil refinery.

Figure 3-1: Thermally insulated pipe and vessel in an oil refinery [64]

Moreover, insulation exhibits applications that surpass its utilization within the realm of refineries, as it finds relevance across a diverse array of industries and even extends to domestic contexts. This versatility is aptly demonstrated through the depiction in Figure 3-2 where insulated pipes are prominently employed within the

School of Mechanical Engineering at the University of Leeds. This illustration effectively underscores the profound significance of insulation technologies within the landscape of universities.

Figure 3-2: Insulated piping system at the University of Leeds

3.1 Thermal insulation system

An insulated pipe is a complex system that typically consists of multiple layers working together to maintain the desired temperature of the fluid or gas being transported. These layers include the pipe itself, which is also called the substrate, a protective coating, an insulation layer, and the cladding, as shown in Figure 3-3.

3.1.1 Substrate

In the context of CUI, the term "substrate" refers to the material constituting the external surface of equipment that interacts with the thermal insulation material. This interaction occurs whether there is a protective coating present or not. The substrate is the surface where CUI takes place, as depicted in Figure 3-3 indicated by number 1.

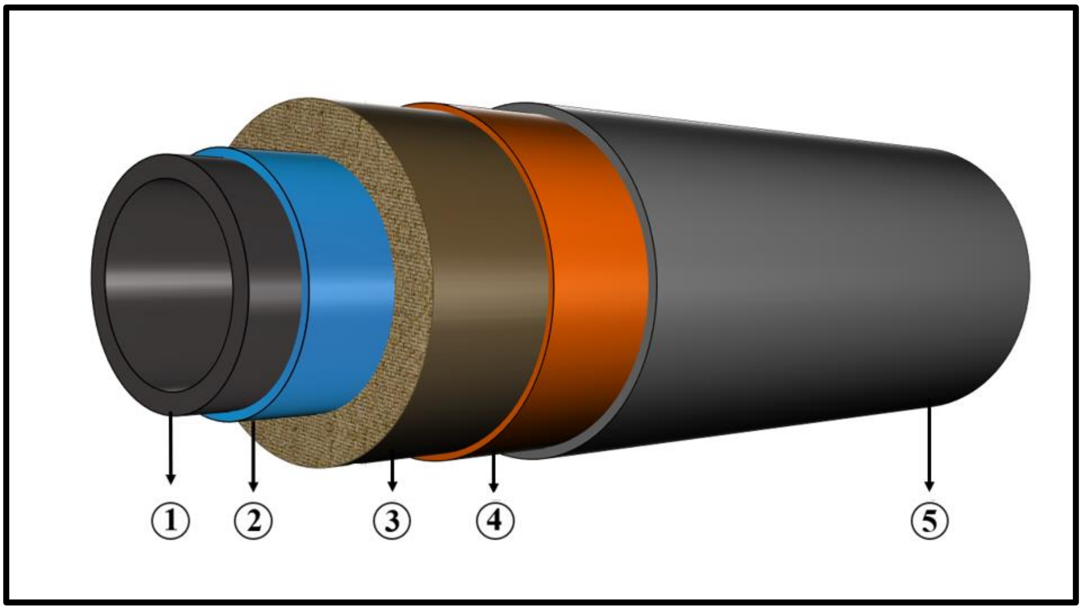

Figure 3-3: A schematic diagram of a typical insulated pipe consists of (1) substrate (pipe), (2) protective coating, (3) thermal insulation, (4) vapour barrier, (5) cladding

Within the oil and gas industry, a range of metals and alloys are utilized as substrates for equipment exposed to potential CUI. Among these materials, carbon and low-alloy steel, such as ASTM A106 Gr B and X65, are commonly employed. Additionally, stainless steel, particularly grades 304 and 316, is frequently utilized. These materials are favoured for their desirable properties, including strength, durability, and cost-effectiveness [32, 65].

3.1.2 Coating

Protective coatings, as illustrated in Figure 3-3 indicated by number 2, are located between the substrate and the thermal insulation. The coating plays a critical role in preventing CUI and is considered the last line of defence. Therefore, their suitability and durability are of utmost importance. There are various types of coatings available, and the application method depends on several factors, such as cost, service temperature, cyclic condition, and lifetime. Figure 3-4 shows the temperature limit for four common types of coatings used in CUI mitigation according to NACE TG 425, NACE SP0198-2010 and NORSOK M501, Ed, 6. These coatings are epoxy novolac, thermal spray aluminium (TSA), high-build silicon and epoxy phenolic. Among them, the TSA is the most effective and can withstand very high temperatures (up to 650°C). In addition, high build silicon can stand a high temperature (above 400°C). Extensive research has been conducted on different types of coatings, and the results can be found in the literature [29, 66-71]. In a study conducted by Kane and Chauviere [66], a comparison was made between the rate of CUI on a coated ASTM A106 Gr B steel with TSA under cyclic conditions (82°C-110°C), and bare steel. The findings revealed that the corrosion rate of the bare steel was approximately 10 times higher than that of the coated steel (0.03 mm/year and <0.003 mm/year respectively). This highlights the significant protective effect of the coating, as it substantially reduced the susceptibility of the steel to corrosion in the given temperature range.

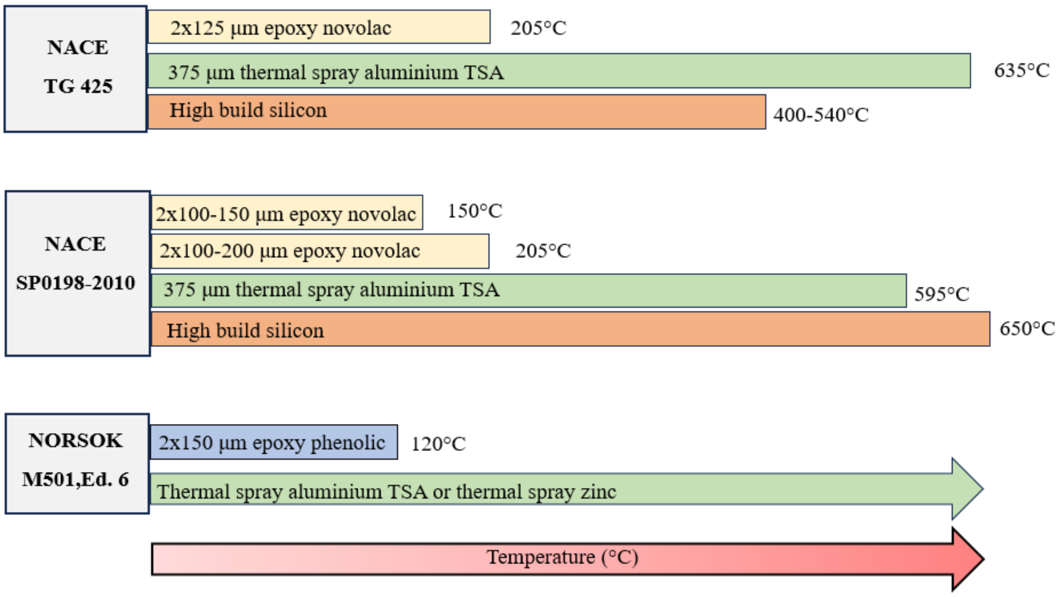

Figure 3-4: Provides an overview of the upper-temperature limits for different coating types (epoxy novolac, TSA, high build silicon and epoxy phenolic as specified by authoritative sources NORSOK M 501, NACE SP0198, and NACE TG 425, adapted from [68]

3.1.3 Thermal insulation materials

Thermal insulation materials, as shown in Figure 3-3 indicated by number 3, are utilized to minimize heat transfer between equipment and its surrounding environment. The primary objectives of thermal insulation materials include conserving energy, ensuring personal safety, controlling condensation, and reducing noise and vibration levels. By minimizing the amount of heat lost or gained, thermal insulation materials assist in maintaining a stable temperature environment, while also providing additional benefits such as cost savings, improved process efficiency, and reduced environmental impact [72-74]. The significance of thermal insulation in offshore, which is known as marine insulation, operations is undeniable, considering the frequent exposure to harsh environmental conditions, including extreme temperatures that can lead to equipment malfunction or damage. Thermal insulation plays a pivotal role in maintaining the temperature of equipment and other components, preventing them from overheating or getting too cold, which can adversely affect their performance [75]. Consider the steam line or chimney, serving as conduits to exhaust high-temperature air emitted by the engine. These vital components are often fabricated using stainless steel, renowned for its superior capacity to withstand elevated temperatures. Furthermore, to augment their insulation capabilities, mineral wool can be meticulously applied to the ducts and vents, effectively bolstering their thermal efficiency [76].

Within the literature, there are multiple classification schemes available for insulation materials. A frequently utilized method of categorisation for thermal insulation materials is grounded on their specific properties, which involve thermal conductivity, acoustic properties, water vapour permeability, hydrophobicity, and fire resistance. Being aware of these distinct properties and their impact on insulation performance is crucial in the process of selecting the most suitable insulation material for a particular use. By choosing the correct insulation, energy efficiency can be improved, while condensation and corrosion can be prevented. Additionally, acoustic performance can be enhanced, and fire safety can be increased [65]. Figure 3-5 shows the classification of thermal insulations according to cell geometry, operating temperature, and chemical composition. Thermal insulations come in various shapes, including preformed pipes, slabs, or rolls.

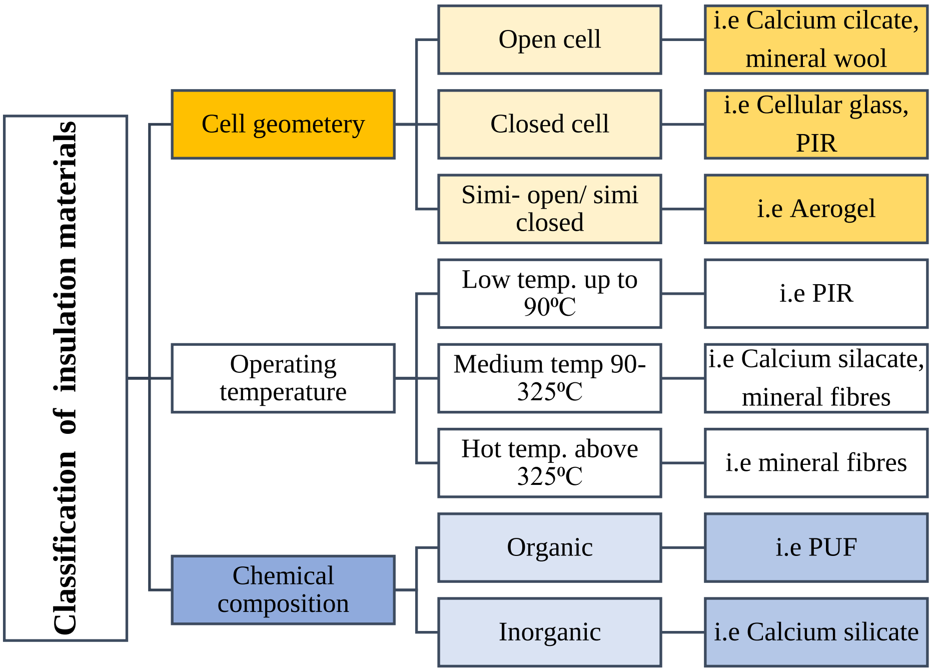

Figure 3-5: Classification of thermal insulation materials based on the chemical composition, operating temperature and cell geometry, adapted from [29, 73]

While corrosion risk is an important factor to consider when selecting thermal insulation materials, it is not the only characteristic to consider during the selection process. Other crucial factors to consider include thermal conductivity, compatibility with the system, density, health hazards, fire resistance, degradation resistance, and dimensional stability. Proper consideration of these characteristics is necessary to select the optimal insulation material that can meet the application's requirements while also providing long-term durability and safety [29, 73].

Table 3-1 presents the prevalent thermal insulation materials extensively employed in the O&G industry. These materials have gained widespread recognition and utilization due to their exceptional thermal properties and compatibility with the demanding conditions prevalent in the industry.

Table 3-1: Common thermal insulation material used in the O&G industry

Material ***Characteristics***	**Calcium silicate**	**Cellular glass**	**Mineral wool**	**Expanded perlite**	**PUR & PIR**
Cell geometry	Open cell	Closed cell	Open cell	Open cell	Closed cell
Service temperature ºC	High Temp. 121-540 Recommended for hot system	-268 – 270 Recommended for cold to medium system	20 – 1000 Recommended for hot system	20 – 175 Recommended for cold to medium system	Below freezing to 120 Recommended for cold system
Thermal conductivity (W/mK)	0.039-0.093 50 to 350ºC	0.038-0.045 -20 to 20ºC	0.037-0.111 50 to 400ºC	0.037-0.039 20 to 40ºC	0.018-0.023 -100 to 20ºC
Bulk density kg/m^3	190-240	112-152	60-155	30-35	Min 40
Compressive strength KN/m^2	Min 1300	Min 490	Min 48	Min 550	Min 160
Water adsorption	Max 3% by volume	-	Max 10% by volume	Max 10% by volume	-
Pros	Low thermal conductivity. Different shapes and sizes are available. Low Cl^-	Stable thermal conductive. No water adsorption.	Non-combustible High temperature Different shapes and sizes are available	Water resistance (up to 205 ºC) Good mechanical performance Various shapes and sizes	Low permeability Different shapes and sizes Seamless seal
Cons	Easily adsorb water. Brittle	Expensive Crack above 150 ºC Crack in vibration conditions	Skin allergies Low compression stress Easily adsorb water	Fragile more than calcium silicate, High thermal conductivity	Sensitive to sunlight Long-time water retention High Cl^- Leaches toxic gases when burns
Manufacturing standards	ASTM C533, EN 14306, BS 3958	ASTM C552, EN 14305	ASTM C547, EN 143030	ASTM C610	ASTM C591

3.1.4 Water vapour barrier

A vapour barrier, also referred to as a vapour retarder, plays a crucial role in managing moisture and preventing the migration of water vapour through the insulation layers. The vapour barrier is positioned between the thermal insulation and the cladding, securely attached to the insulation material as shown in Figure 3-3 indicated by number 4.

Insulation materials with closed cells, such as PUR, are impermeable to water vapour, whereas those made of open cells, like mineral fibre, allow water vapour to pass through easily. During cold weather conditions, a water vapour barrier is necessary for thermal insulation and is constructed using materials that possess low permeability to water vapour, such as polyethene, glass foam, plastic, or foil sheet. This barrier slows down and prevents the diffusion of water vapour into the metal surface and is placed between the exterior surface of the thermal insulation and the cladding. Therefore, a vapour barrier layer is required to protect all insulation used in facilities operating at sub-ambient temperatures, below 15°C [22, 74, 77].

3.1.5 Cladding/ jacketing

Cladding is used to maintain the thermal insulation's integrity and protect it against the weather as shown in Figure 3-3 indicated by number 5. It is inevitable that at some point during the life span of an insulation system, water and water vapour will be able to penetrate it. Several reasons for this include poor design, improper installation, and external mechanical damage, such as scaffolding or footprints. Therefore, materials selection for the cladding should be characterised by their durability against mechanical factors, UV degradation, water, and water vapour ingress [78]. The two main types of cladding include metallic cladding and non-metallic cladding.

Metallic cladding is commonly used in the oil and gas industry. The most common metals used to produce metallic jacketing are aluminium (AA 3103- comply with ASTM B209B), zinc galvanised steel (according to ASTM A653 and ASTM 1924), and stainless steel (304L or 316L-2B finish according to ASTM A167) [30, 79].

Aluminium is the most widely used metal in cladding manufacturing due to its excellent formability, high corrosion resistance, and low density [22].

However, the disadvantages of aluminium jackets include their vulnerability to pitting corrosion and their inability to withstand elevated temperatures [80-82]. Galvanized steel is known for its high durability, and this is largely attributed to its favourable mechanical properties. Limiting the use of galvanized steel cladding in proximity to austenitic stainless steel or nickel base alloy is advisable. This is due to the high risk of corrosion associated with galvanized sheeting, especially in coastal and arid regions. In corrosive and high-temperature environments, stainless steel is a superior choice compared to aluminium and zinc galvanized steel [65, 77].

Non-metallic cladding is typically composed of thermoplastic materials such as Polyvinyl Chloride (PVC) and Polyvinylidene Chloride (PVDC). These materials are characterized by unique properties that make them suitable for specific applications. However, non-metallic cladding is not suitable for high-temperature environments due to its low-temperature threshold. Furthermore, these materials are not fire-resistant, which significantly limits their use in industries such as oil and gas. Therefore, non-metallic cladding is typically reserved for low-temperature applications where fire resistance is not a primary concern [79, 83].

3.1.6 Caulking

Caulking materials are utilized to seal the joints and terminations of jacketing, serving as a preventive measure against water infiltration. However, these caulks have a tendency to dry out and shrink as time passes, which causes them to lose their effectiveness as sealants [84]. Consequently, corrosive water from the external environment can infiltrate the degraded sealing materials and dampen the insulation, leading to CUI [65].

3.1.7 Spacers

Historically, spacers have not been incorporated into the insulation systems as per the standards set by NACE or API standards. However, there has been a recent surge of interest from the O&G companies in the inclusion of spacers as a novel addition to insulation systems to minimise the CUI rate. A contact-free insulation system has been introduced as a novel approach to tackle CUI. This system involves the deployment of a non-metallic spacers distributed around the circumference of the pipe to create a consistent and unified air gap between the insulation and process pipe. The air gap effectively separates the insulation system, a common source of water infiltration, from the process pipe, preventing moisture from directly contacting the pipe and mitigating the risk of CUI. Compared to traditional insulation systems, the contact-free insulation system offers benefits such as ease of installation, reduced maintenance costs, and improved efficiency. In a study by Rana et al. [85], the impact of different insulation configurations on CUI was explored, including closed contacting insulation, point contact spacer with a drain, and Teflon spacers membrane spacers with a drain as shown in Figure 3-6. The results of the study showed that the use of point contact spacers reduced CUI by 31%, while Teflon spacers membrane spacers decreased CUI by an impressive 90.2% when compared to closed contacting insulation. These findings suggest that the selection of appropriate spacer configurations can have a significant impact on CUI prevention and mitigation, potentially resulting in improved equipment performance and increased operational safety.

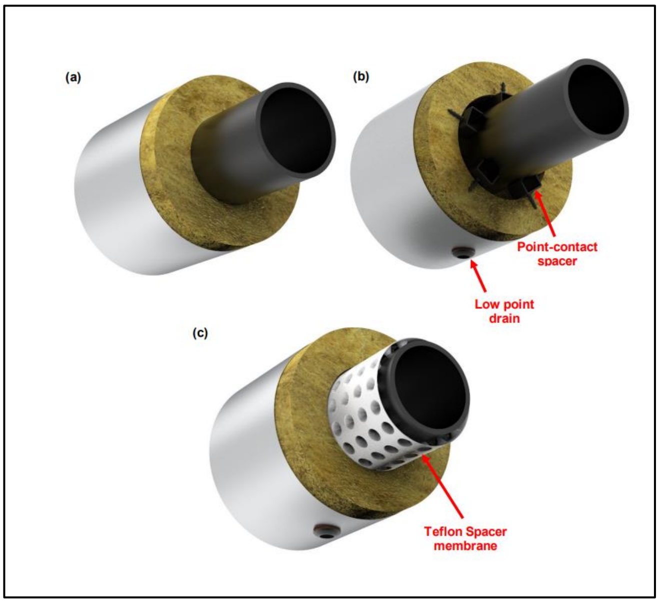

Figure 3-6: Insulation configurations (a) closed-contacting insulation, (b) point contact spacer and (c) Teflon spacer membrane [85]

3.2 Mechanism of CUI

CUI is an electrochemical phenomenon that requires the simultaneous presence of four essential components: an anode, a cathode, an electrolyte, and an electrical circuit or pathway. In the context of CUI, the electrolyte typically takes the form of oxygenated water, which can be further influenced by the inclusion of various contaminants that have the potential to accelerate the corrosion process. The intricate interplay of these elements and their chemical reactions contribute to the complex nature of CUI.

Figure 3-7 offers a concise overview of the electrochemical reaction for CUI, illustrating the fundamental processes involved in various electrochemical systems. This diagram provides a visual representation of the key components and transformations that occur during an electrochemical reaction.

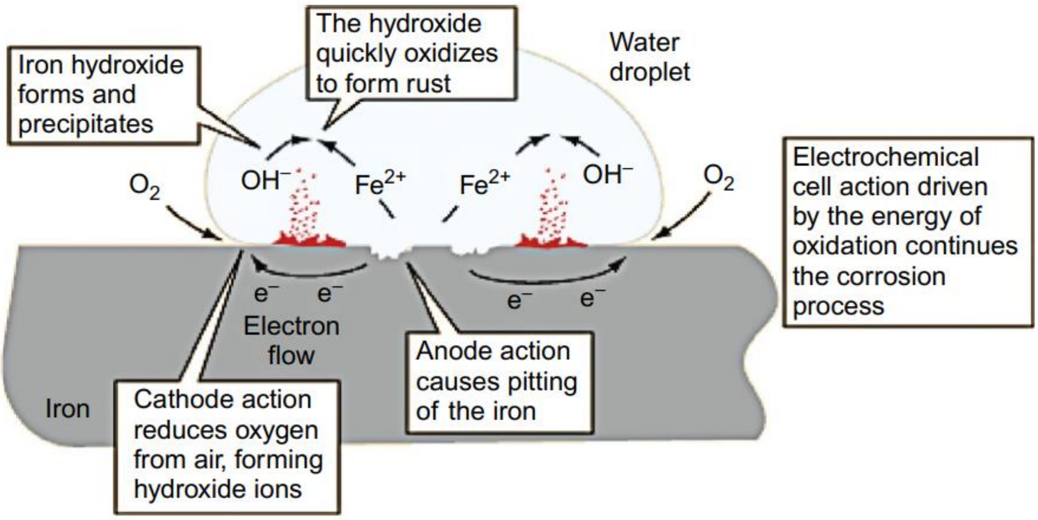

Figure 3-7: Electrochemical of CUI of carbon steel [30]

The anode represents the site where oxidation occurs, leading to the release of electrons as shown in equations 3-1 and 3-2.

$$Fe \rightarrow Fe^{2+} + 2e^{-} \qquad 3\text{-}1$$

$$Fe \rightarrow Fe^{3+} + 3e^{-} \qquad 3\text{-}2$$

The cathode represents the site where reduction takes place, resulting in the consumption of electrons as shown in equation3-3.

$$O_2 + 2H_2O + 4e^{-} \rightarrow 4OH^{-} \qquad 3\text{-}3$$

The hydroxide ions (OH^{-}) engage in a reaction with both ferrous ions (Fe^{2+}) and ferric ions (Fe^{3+}) ions, resulting in the formation of $Fe(OH)_2$ or $Fe(OH)_3$ compounds. Concurrently, the precipitation of Fe_2O_3 occurs as a byproduct of this chemical process as shown in equation 3-4.

$$4Fe + 6H_2O + 3O_2 \rightarrow Fe(OH)_3 \rightarrow 6H_2O + 2Fe_2O_3 \qquad 3\text{-}4$$

In an aqueous environment with increased acidity, the cathodic reaction involves the reduction of oxygen in an acidic condition, as expressed in equation 3-5.

$$O_2 + 4H^{+} + 4e^{-} \rightarrow 2H_2O \qquad 3\text{-}5$$

The overall corrosion process is shown in 3-6. Ferric ions (Fe^{3+}), originating from the dissolution of iron, per equation 3-2.

$$Fe^{3+} + 3H_2O \rightleftarrows Fe(OH)_3 + 3H^{+} \qquad 3\text{-}6$$

The mechanism of CUI in a hot environment involves a series of processes influenced by elevated temperatures as demonstrated in Figure 3-8. In such conditions, water or moisture can infiltrate the insulation system, and due to the high temperatures, various phenomena occur.

Initially, the water or moisture enters the insulation and may be absorbed or trapped within its structure. Over time, the heat from the equipment's surface causes the water to evaporate, transforming it into water vapour. This vapour then migrates through the insulation material towards the outer surface.

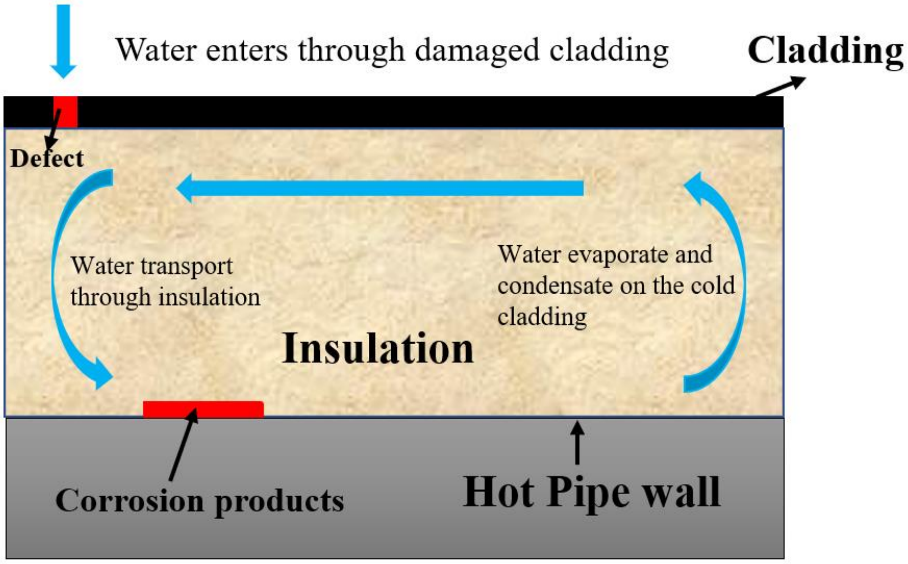

Figure 3-8: Proposed CUI mechanism in a hot environment, adapted from [86]

As the water vapour reaches the outer surface of the insulation, it encounters colder temperatures, leading to condensation. The water vapour condenses into liquid water, creating a moist environment. This moisture, in contact with the hot metal surface, creates a conducive environment for corrosion to occur.

The presence of moisture and oxygen initiates an electrochemical reaction on the metal surface. The moisture serves as an electrolyte, allowing the transfer of ions, while the oxygen acts as the oxidizing agent. This reaction leads to the formation of corrosion products, such as metal oxides or hydroxides, and the degradation of the metal surface.

The cyclic nature of the evaporation and condensation process further exacerbates CUI. During each cycle, the concentration of contaminants within the moisture may increase, potentially accelerating corrosion rates. Additionally, the continuous wetting and drying of the insulation system can cause mechanical stress and thermal expansion/contraction, leading to insulation degradation and reduced effectiveness.

Furthermore, the presence of damaged or inadequate barrier coatings on the equipment surface can exacerbate CUI in a hot environment. If the coating is compromised, direct contact between water and the metal surface is facilitated, accelerating the corrosion process [86].

3.3 Susceptible areas to CUI

The significance of equipment and piping design in relation to their vulnerability to CUI is widely acknowledged [29]. Besides, the design of equipment attachments such as ladder support and platform brackets should also be considered, as they can impact CUI. Improperly shaped or positioned attachments can create paths for moisture or water to seep into the insulation, causing corrosion on the underlying substrate and increasing the risk of CUI. Therefore, it is critical to meticulously design and install all attachments to prevent moisture infiltration and minimize the likelihood of CUI. Figure 3-9 depicts the susceptible area to CUI.

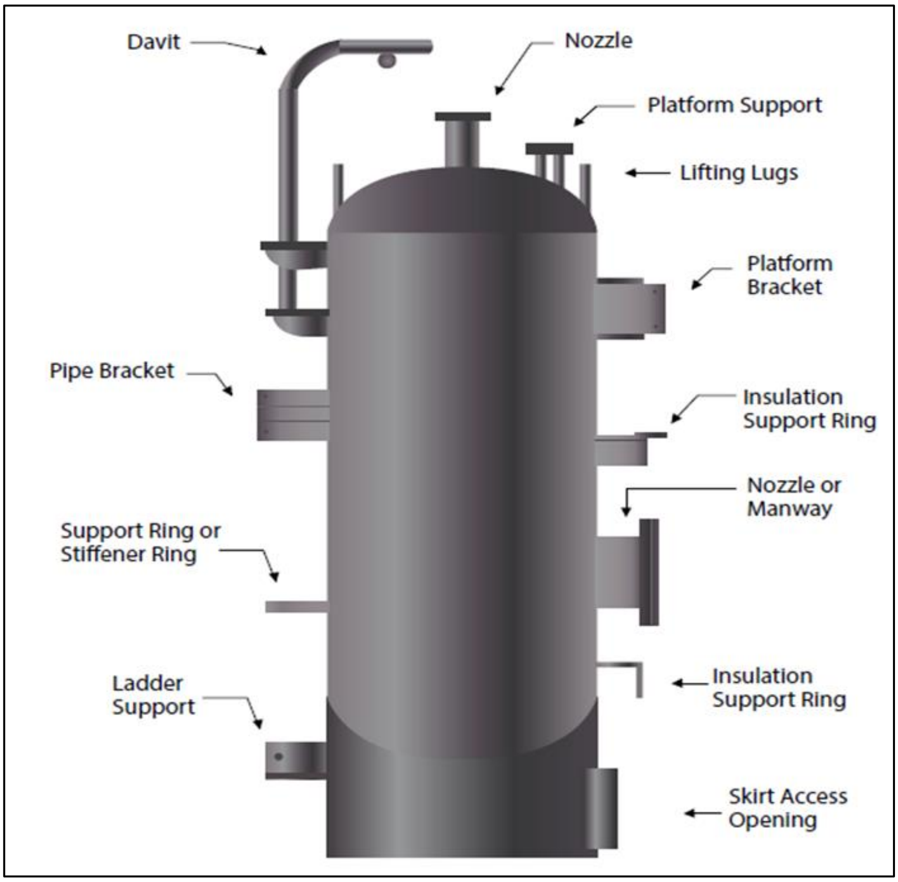

Figure 3-9: Susceptible areas to CUI in a typical column and pressure vessel [22]

As the result of an investigation conducted by Geary [87], a catastrophic failure occurred in a process column in a refinery. The severity of the failure was further exacerbated by an ensuing explosion, causing extensive damage as depicted in Figure 3-10. The investigation determined that the primary cause of this failure was traced back to an incorrect design of the intervention system involving pipe supports located between brackets and insulated pipes. These findings were corroborated by BP (British Petroleum) document No S/UTG/309/01 from 2001. The inadequate design of the intervention system resulted in the pipe being exposed to moisture, leading to the occurrence of CUI. As moisture infiltrated the insulation material, it facilitated the corrosion process, gradually deteriorating the integrity of the pipe. Ultimately, this corrosion-induced weakening of the pipe's structure played a pivotal role in the occurrence of the subsequent explosion. The CUI-related damage significantly compromised the pipe's integrity, creating a hazardous environment.

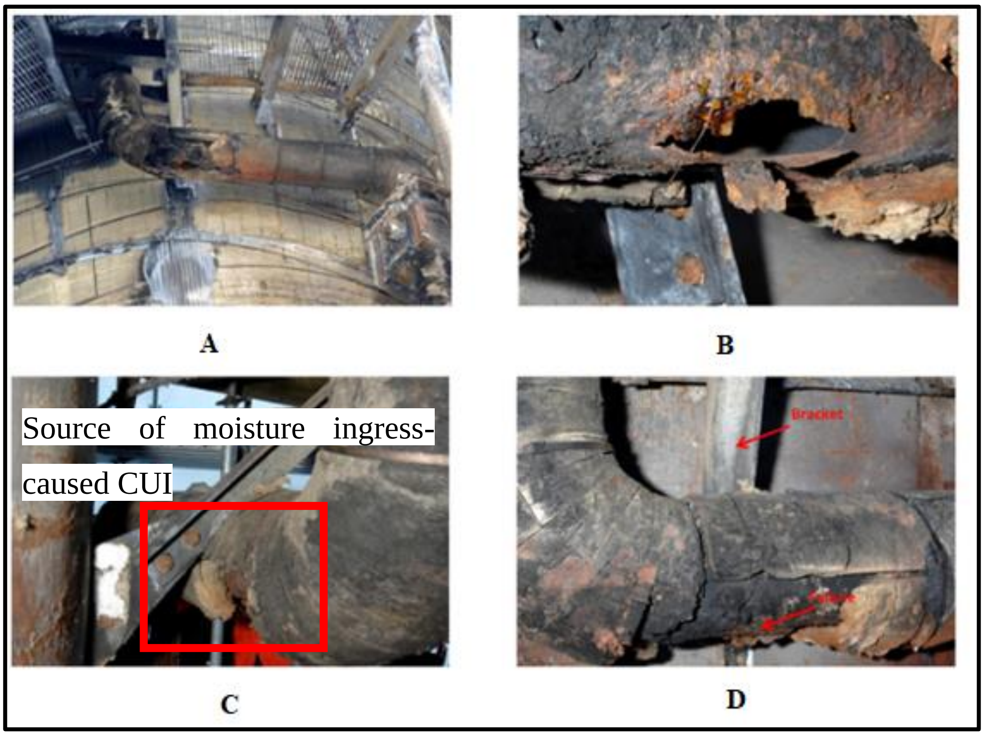

Figure 3-10: A failure pipework due to CUI caused by improper attachment design (bracket) led to moisture ingress [87]

The insights gained from this investigation and the associated BP document emphasized the need for improved design practices and reinforced the significance of comprehensive inspections, maintenance, and adherence to safety protocols in preventing similar incidents in the future. The lessons learned from this case study underscored the critical role of effective intervention system design in ensuring the integrity and safety of industrial processes.

3.4 Factors influencing CUI

For CUI to occur, two crucial elements must be present: moisture (water) and a warm environment. When it comes to cracking iron products like carbon steel piping and equipment, the presence of oxygen is necessary, whereas chloride ions are necessary for cracking stainless steel 300 series products [3].

Moisture and heat are the primary contributors to CUI, as the combination of these two elements creates an environment that promotes corrosion. When water infiltrates insulation, it is trapped and held against the underlying metal surface, leading to prolonged exposure to moisture. This is especially true in warm environments, where the heat can cause the water to evaporate and condense repeatedly, further increasing the exposure to moisture [30].

In addition to moisture and heat, the presence of corrodents like oxygen, chloride ions, acids, acid gases, strong bases, and salts can accelerate the corrosion process. These corrodents can react with the metal surface, causing it to deteriorate and weaken over time [79].

3.4.1 Water (moisture)

The amount of water present in the atmosphere fluctuates depending on both the temperature and the relative humidity. For instance, if the temperature is 10°C and the relative humidity is 60%, the water content in the air is $5.7 g/m^3$. However, when the temperature rises to 30°C and the relative humidity reaches 100%, the water content in the air increases significantly to $31.4 g/m^3$.

Oil and gas production facilities are often situated in coastal areas due to the close proximity to offshore oil and gas reserves, as well as the convenience of transportation through shipping and pipelines. According to the reports published by the Department of Energy and Climate Change (DECC) in 2014 [88], and the UK fuel market review refining [89], the number of refineries in the UK is 9 and all of them are situated close to port facilities. In the same context, the Libyan oil industry has a significant presence on the Mediterranean coast, with all six of its oil terminals situated along this coastline. These terminals are critical hubs for the export of crude oil [90]. Thus, seawater is one of the most common corrosive mediums, second only to the atmosphere. Most metals, alloys, and construction materials are susceptible to corrosion when exposed to seawater and marine environments due to their corrosive nature. The degree of corrosion is determined by the specific conditions of exposure, with factors such as temperature, salinity, and oxygen content playing a significant role in the corrosion behaviour of different materials [91].

CUI is known to occur and progress beneath wet insulation and is expected to decrease or stop in dry-out conditions. However, in cases where dry-out occurs, it may not always be possible to slow down or halt CUI due to water entrapment caused by the jacketing, leading to an increase in the concentration of corrosive ions within the insulation system [13, 30].

In a study carried out by Pojtanabunyoeng et al. [50], it was observed that corrosion rates at the top section of a pipe increased from 0.14 mm/year without jacketing to 0.25 mm/year with jacketing after 2 weeks of exposure. This increase in corrosion rates was attributed to prolonged wetness caused by water retention.

According to Zwaag and Rasmussen [92], there is no direct correlation between the rate of CUI and the water adsorption capacity of insulation. However, they suggest that the time of wetness is the most crucial factor in determining the CUI rate, which displaces the significance of the thermal insulation water adsorption rate. In atmospheric exposure, the time of wetness denotes the duration for which a metal surface remains wet [93]. It is important to note that water retention, permeability, and wetting ability may vary depending on the insulation used [30].

Cains, et al [10] conducted a study and found that non-insulated systems can dry out in less than a minute. However, when seawater or distilled water is present, the time of wetness for insulated systems can be as long as 14.7 and 12.9 days, respectively. This suggests that the duration of wetness is not solely determined by temperature, but also by the chemical composition of the electrolyte.

Moisture can originate from various external natural sources, including rain, snow, humidity, and condensation. These sources can contribute to the accumulation of water on the surfaces of industrial equipment and piping, creating an environment conducive to corrosion. In addition to natural sources, water can also enter an insulation system through leaks or damaged cladding, exacerbating the potential for

CUI. It is crucial to identify and address these external sources of moisture to prevent the development and progression of CUI [94].

3.4.2 Temperature

Temperature has a significant role in CUI, as highlighted by a NACE SP0198-2010 (*control of corrosion under thermal insulation and fireproofing materials - a systems approach*) and API 583 (*corrosion under insulation and fireproofing*). An increase in operational temperature can have both positive and negative effects on the CUI rate. On the one hand, it may decrease the time of wetness, thereby reducing the corrosion rate. However, on the other hand, higher operational temperatures can increase the concentration of corrosive species due to the evaporation of the brine. Additionally, a high operational temperature can potentially cause the deterioration of the coating and sealant that assist water in reaching the metal surface and promoting corrosion [83, 95].

Figure 3-11 highlights the critical temperatures for the CUI phenomenon to occur which are low risk (green), medium risk (amber) and high risk (red). According to API 583 and NACE SP 0198-20, equipment can be protected against corrosion for most of its lifetime if the service temperature remains below the freezing point. However, when the service temperature is between freezing and ambient temperature, there may be less pitting corrosion and a low general corrosion rate. This could be because lower water temperatures lead to a slower reaction rate, and contaminants are frequently diluted through condensation. On the other hand, in warm and hot conditions, particularly in closed systems with thermal insulation, the corrosion rate can increase due to a rise in reaction rate and acute water ingress dehydration [96]. This eventually results in an increase in contaminants concentration due to water evaporation [97].

According to NACE standards, the high risk of CUI occurrence encompasses a broader temperature range compared to the API standards. NACE identifies a higher risk of CUI within a temperature range of 125°C, which extends from 50°C to 175°C. In contrast, the API standards indicate a high-risk threshold at a narrower temperature range of 33°C, spanning from 77°C to 110°C. This means that NACE recognises a wider temperature range as being susceptible to CUI, indicating a broader spectrum of potential risk compared to the API standards.

The maximum corrosion rate for carbon steel in aerated environments, up to 0.5 mm/year, is typically observed at around 80ºC [83, 95]. However, a study has demonstrated that the worst CUI damage typically occurs at around 93°C for both carbon and stainless steels [99]. This temperature is within the critical range specified by NACE and API standards.

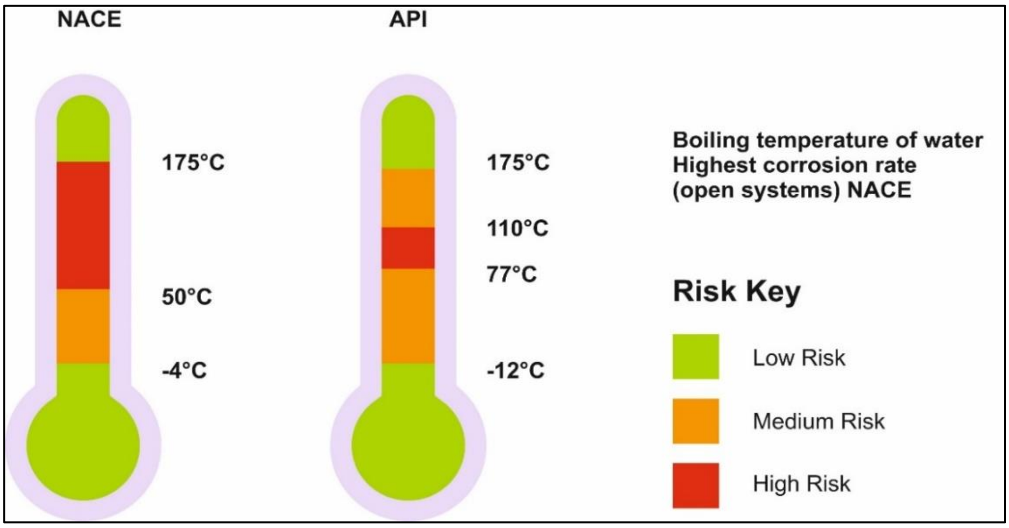

Figure 3-11: The risk of CUI occurrence as a function of temperature, as identified by NACE SP0198 and API 583 standards [98]

3.4.3 Cyclic temperature

Cyclic temperature conditions refer to the recurring fluctuations in temperature that are frequently observed in petroleum facilities due to operational changes or shutdown operations. In the context of this subsection, the term "cyclic temperature" will be replaced with "wet-dry condition" to better reflect the corrosion dynamics.

In the literature, it is well established that the wet-dry condition is more corrosive than an isothermal condition. During the wet phase, the presence of moisture and electrolytes brings them into contact with the metal surface, promoting the occurrence of CUI. As the temperature rises during the subsequent dry phase, the moisture evaporates, leaving behind concentrated corrosive agents that can further accelerate the corrosion rate.

Furthermore, the cyclic wet-dry condition can lead to the concentration of contaminants initially present in the moisture. When water penetrates the insulation during the wet phase, it can carry dissolved salts, acidic compounds, or other corrosive substances. As the moisture evaporates, these contaminants become more concentrated, contributing to localized corrosion and increased corrosion rates during subsequent wet phases.

Moreover, the wet phase provides an opportunity for corrosion products to form on the metal surface. However, as the temperature rises during the dry phase, the moisture evaporates, leading to the dehydration and cracking of these corrosion products. This exposes fresh metal surfaces to subsequent wetting cycles, resulting in the acceleration of corrosion.

Additionally, the cyclic wetting and drying cycles can significantly impact the performance and durability of barrier coatings applied to the metal surface. The moisture and temperature fluctuations can cause coating degradation, such as blistering, cracking, or delamination. Once the coating is compromised, the underlying metal surface becomes vulnerable to direct contact with moisture and corrosive agents, leading to an accelerated corrosion process.

Studies have shown that the rate of CUI increases with cyclic temperature conditions. Yang and Liu [100] reported ~5.1 mm/year of an average corrosion rate of CUI for an X70 carbon steel (CS) sample exposed to 93°C isothermal wet (IW) condition compared to ~8.7 mm/year when exposed to a cyclic wet (CW) condition as shown in Figure 3-12.

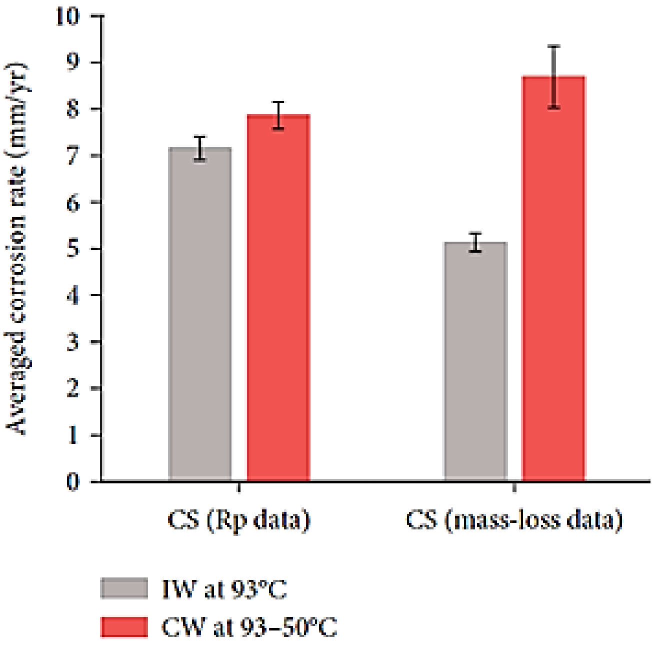

Figure 3-12: Average rate of CUI of carbon steel (CS) X70 under isothermal wet (IW) and cyclic wet (CW) conditions [100]

3.4.4 Insulation material

A crucial component of any insulation system is the insulation material. The type and quality of insulation material can significantly affect the likelihood and severity of CUI. Certain insulation materials may absorb and retain moisture more readily than others, providing a more conducive environment for corrosion. In the context of CUI, it is important to note that the duration of water retention, also known as the time of wetness, holds greater significance than water absorption alone. While water absorption is a contributing factor, the length of time that the insulation or metal surface remains wet has a more pronounced impact on the corrosion process. Even if the insulation material has a low water absorption rate, if it retains moisture for extended periods, it creates an environment conducive to corrosion. Prolonged wetness allows for continuous electrolyte contact with the metal surface, facilitating the electrochemical reactions that drive corrosion. In addition, insulation materials that are not properly installed, damaged, or degraded over time can create gaps or voids where moisture can accumulate, increasing the risk of CUI [101]. However, there have been studies that have demonstrated that different insulation materials can cause varying rates of corrosion under insulation under the same conditions [11, 92, 102]. Table 3-2 provides a comparative analysis of water absorption by weight, estimated affected area (corroded area), and CUI rate for three distinct thermal insulation materials: aerogel blanket, fibreglass, and stone wool insulations. These parameters offer insights into the performance and vulnerability of each material to moisture-related corrosion.

Table 3-2: CUI results for aerogel blanket, fibreglass and stone wool insulations after 21 cycles (21 days) and the cyclic temperature is 60°C-150°C, adapted from [92]

Insulation type	Water absorption by weight (%)	Estimated affected area (%)	Uniform corrosion (mm/year)
Aerogel blanket	79	39	0.17
Fibreglass	836	42	0.05
Stone wool	315	32	0.04

The water absorption by weight reveals that the aerogel blanket exhibits the lowest water absorption rate at 79%, compared to fibreglass and stone wool, which are 836% and 315%, respectively. Fibreglass has the highest water absorption by weight, indicating its greater propensity to retain moisture. On the other hand, stone wool exhibits a lower water absorption rate, suggesting its relatively better resistance to water absorption.

The estimated affected area column indicates the percentage of the insulation surface susceptible to corrosion. Aerogel blanket and fibreglass demonstrate similar estimated affected areas at 39% and 42%, respectively, while stone wool has a slightly lower estimated affected area at 32%. This suggests that all three materials have comparable susceptibility to corrosion, with stone wool showing a slight advantage in terms of potential corrosion coverage.

Considering the CUI rate, the aerogel blanket exhibits the highest uniform corrosion rate at 0.17 mm/year, followed by fibreglass and stone wool. This implies that the aerogel blanket is more prone to uniform corrosion compared to the other two materials, while stone wool shows the slowest uniform corrosion rate. Nevertheless, there is no direct relation between water absorption and corrosion rate.

3.4.5 Contaminants

It is generally accepted that the corrosive action of a non-marine atmosphere is primarily determined by moisture levels and industrial pollutants, whereas the marine atmosphere differs in that it consists of higher concentrations of salt particles conveyed by the wind from the sea spray. Further, the salt aerosols contain hygroscopic components such as calcium and magnesium chlorides that settle on metal surfaces. Consequently, liquid films are formed on metal surfaces, which contain high salt concentrations despite being above the dew point. The average salt content in seawater is not uniform across all oceans and varies significantly. The variation is shown in detail in Table 3-3. The lowest recorded salt content is 8g/kg, found in the Baltic Sea, while the highest recorded salt content is 260g/kg, observed in the Dead Sea.

Under thermal insulation, the primary contaminants that are discovered are chlorides and sulphates. These contaminants may originate (leach) from the insulation materials themselves or external sources such as rain. Chlorides and sulphates are especially harmful due to their metal salt compounds' high solubility in water, resulting in highly conductive aqueous solutions. Additionally, the hydrolysis of these metal salts can cause acidic conditions that lead to localized corrosion.

In marine environments, the Cl^{-} ions are abundant which is carried by air masses to the onshore insulated facilities. Therefore, with an increase in Cl^{-} ions content, not only does the electrolyte solution's electrical conductivity increase, resulting in higher activity of corroding elements but the solution's ability to penetrate protective layers and stabilise anodes locally also increases [91]. However, in general, the mean concentration of Cl^{-} would decrease as the distance from the shoreline increases [103]. This is demonstrated by measuring the atmospheric salinity as a function of the distance from the shoreline as shown in Figure 3-13. Therefore, insulated oil and gas facilities located closer to the shoreline are expected to have a higher rate of CUI compared to those located further away.

Table 3-3: Salt content in gram (g) of different oceanic regions per kilogram (Kg) of seawater [91]

Oceanic region	**Salt content g/kg**
Baltic Sea	8
Black Sea	22
Atlantic Ocean	37
Mediterranean Sea	41
Caspian Sea	13
Dead Sea	260
Irish Sea	33
Red Sea	41
Persian Gulf	39-42

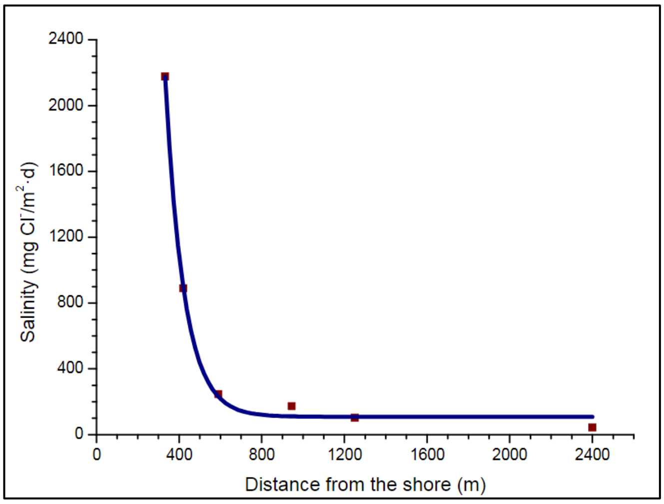

Figure 3-13: Variations in atmospheric salinity as a function of distance from the shoreline [104]

There is no universally recognised standard that defines the precise concentration of chloride ions (Cl^{-}) required to initiate SCC. However, according to the NACE 0198-2010 [29], areas nearby SCC have demonstrated an average concentration of 350 ppm of Cl^{-}. Furthermore, the ASTM C795-08 *Standard Specification for Thermal Insulation for Use in Contact with Austenitic Stainless Steel* [105] has outlined limits on the concentration of Cl^{-} in ppm, based on the concentration levels of sodium(Na) and silicate (SiO_3), as illustrated in Figure 3-14.

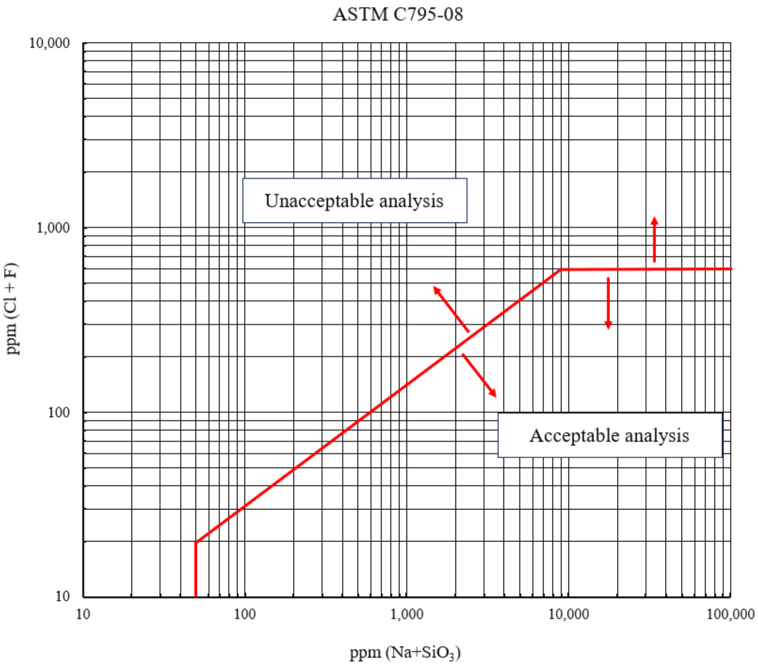

Figure 3-14: Evaluation of insulation material acceptability based on (Cl + F) and (Na + SiO_3) Plot Points [105]

The ASTM C871 *standard test methods for chemical analysis of thermal insulation materials for leachable chloride, fluoride, silicate, and sodium ions* [106] and BS EN ISO 12624: 2022 *Thermal insulating products for building equipment and industrial installations – Determination of trace quantities of water-soluble chloride, fluoride, silicate, sodium ions and pH* [107] are standards provide a test method for the chemical analysis of thermal insulation materials to determine the concentration of leachable chloride, fluoride, silicate, and sodium ions. The results of this test can be compared with the empirical graph shown in Figure 3-14.

3.5 Types of corrosion observed under insulation.

Different forms of external corrosion can occur, such as uniform or galvanic corrosion. However, specific types of corrosion damage caused by CUI are often observed and documented in the literature. A CUI can be manifested in various ways, including uniform corrosion, pitting corrosion, and Stress Corrosion Cracking (SCC) [95]. Additionally, microbiological activities underneath thermal insulation may cause CUI, although no investigation or reporting of it in literature has been done to date[108]. The type of corrosion observed generally depends on the material used in specific applications such as, stainless steel being more susceptible to SCC than carbon steel [83, 95].

3.5.1 Uniform corrosion

Uniform corrosion refers to the even reduction in metal thickness without any localized attack, often resulting in significant mass loss as depicted in Figure 3-15. This type of corrosion is frequently observed in active metals, such as carbon steel [32], and is commonly associated with wet insulation, as reported by various authors [50, 67, 92, 102, 109].

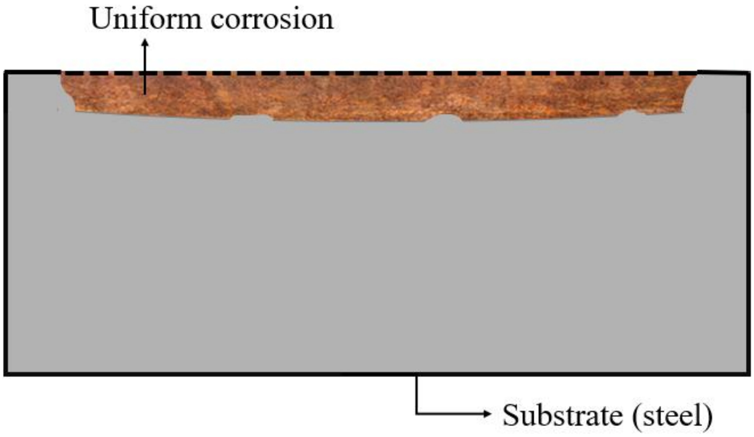

Figure 3-15: Illustrating uniform corrosion, where the loss of material thickness is approximately equal at every point, adapted from [8]

Cain et al. [109] employed a CUI setup based on the ASTM G189-07 standard as shown in Figure 3-16. The setup comprises two distinct compartments, with each compartment containing three steel objects. The process of measuring mass loss was carried out for all the electrodes, following the guidelines outlined in NACE 0775. The results indicated a mass loss increase of almost threefold, from 2.01 to 5.67 g/m^2 after around 5 hours of exposure, when applying thermal insulation and using distilled water as an electrolyte and this was described as dominantly being caused by a general corrosion phenomenon. The observed corrosion in the presence of distilled water is likely caused by the ions leached from the insulation material. However, when seawater was utilized instead of distilled water, a corrosion rate increase of more than twofold, from 7.92 to 16.68 g/m^2, was observed in a similar experiment. These outcomes highlight the substantial influence of insulation and solution corrosiveness on CUI.

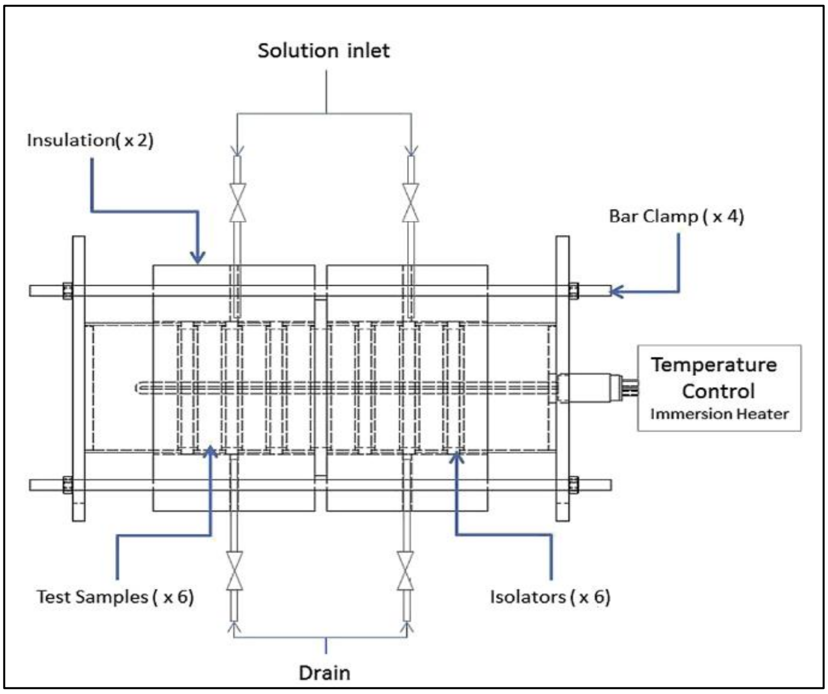

Figure 3-16: A schematic of ASTM G189-07 CUI rig [10, 110]

Zwaag and Rasmussen [92], studied the effect of cyclic conditions and insulation material on CUI using a setup similar to ASTM G189-07, per Figure 3-17. Six different types of insulation were tested under cyclic conditions at temperatures of 60 ºC and 150 ºC for wet and dry conditions, respectively. The selection process for insulation materials considered the maximum acceptable heat loss of 40 W/m, which led to variations in insulation thickness among the different materials due to differences in their thermal conductivity.

The authors found that the general corrosion rate for carbon steel coupons varied depending on the insulation material. The PIR insulation material had the highest corrosion rate at 0.45 mm/year, whereas calcium silicate had the lowest rate at 0.03 mm/year. Interestingly, the closed and semi-closed insulation types showed higher corrosion compared to the open cell insulation, as demonstrated in Figure 3-18. In the case of closed cell insulations such as cellular glass and PIR, the estimated affected area was higher, with values of 70% and 100% respectively. On the other hand, open and semi-closed insulations like stone wool and aerogel blankets had lower estimated affected areas of 32% and 39% respectively. The difference in the affected area may be due to the water adsorption and spread behaviour of each insulation. The closed-cell insulation may be readily saturated by the distilled water pumped into the insulation system at a flow rate of 40ml/hr, while the open-cell insulation may not be fully saturated. However, there may not be a straightforward relationship between the affected area and the corrosion rate.

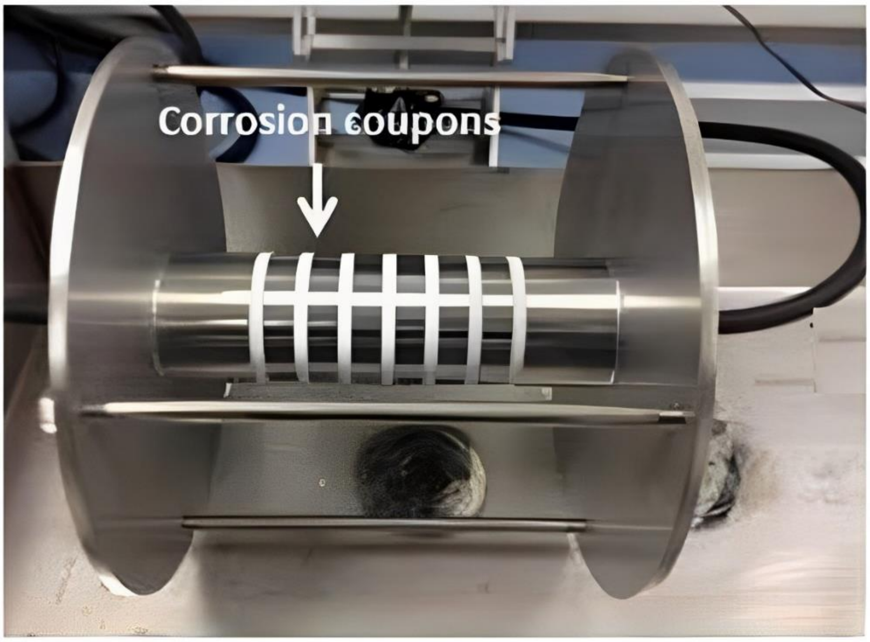

Figure 3-17: CUI investigation rig, where the white ring are insulators made by Teflon, adapted from [92]

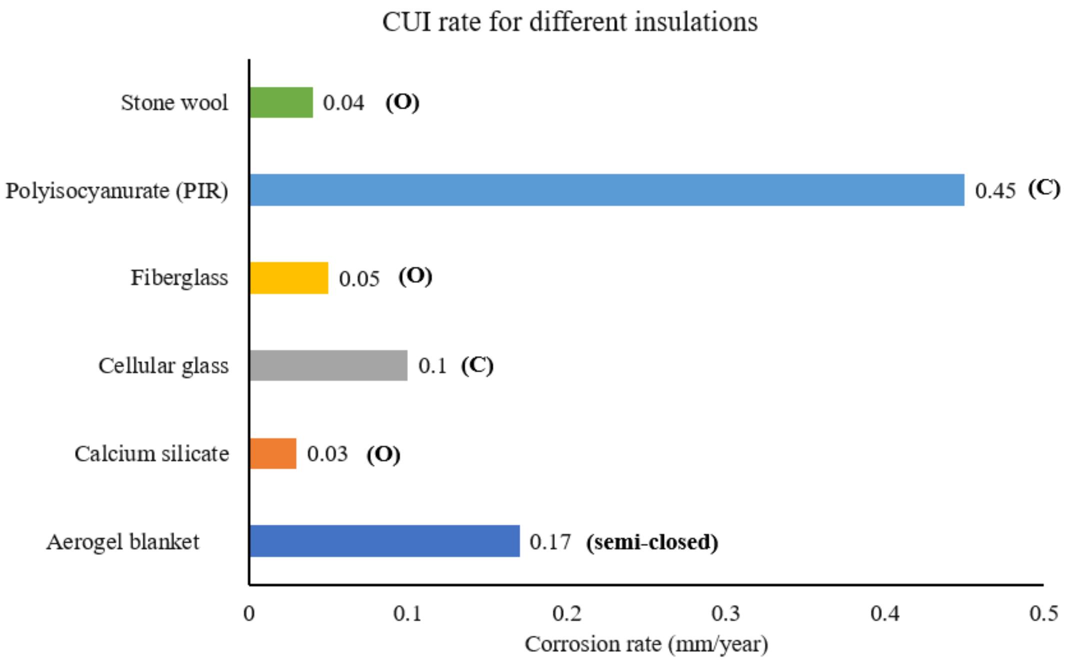

Figure 3-18: CUI rate for different insulation by mass loss after 21 days, (O) is open cell insulation, (C) is closed cell insulation, adapted from [92]

In addition, Pojtanabuntoeng et al. [102] reported that the general corrosion rate varied at different sections of the insulated system. The top sample was a semi-circle arc between 9 and 3 o’clock and had a corrosion rate of 1.0mm/year, while the bottom of the sample, at 6 o'clock, had a rate of 0.6mm/year. Therefore, it can be inferred that the corrosion rate of an insulated system will vary from point to point, even when the same insulation system is used. This variation will depend on the availability and duration of the electrolyte at each specific point, which may be affected by factors such as insulation thickness, surface geometry, and environmental conditions leading to different corrosion layers developing.

3.5.2 Pitting corrosion

This type of corrosion is characterized by a localized disintegration of metal, while the bulk metal remains unaffected. This leads to the growth of pits and graves [33]. Under thermal insulation, pitting corrosion is another common type of corrosion. The first stage of the formation of a pit may be surface heterogeneity, the formation of aeration or concentration cells [108]. Although active-passive metals like stainless steel alloys are typically more susceptible to pitting corrosion than active metals like carbon steel, severe pitting corrosion has also been reported in carbon steel pipes [102]. The shape of pitting corrosion can vary, as shown in Figure 3-19.

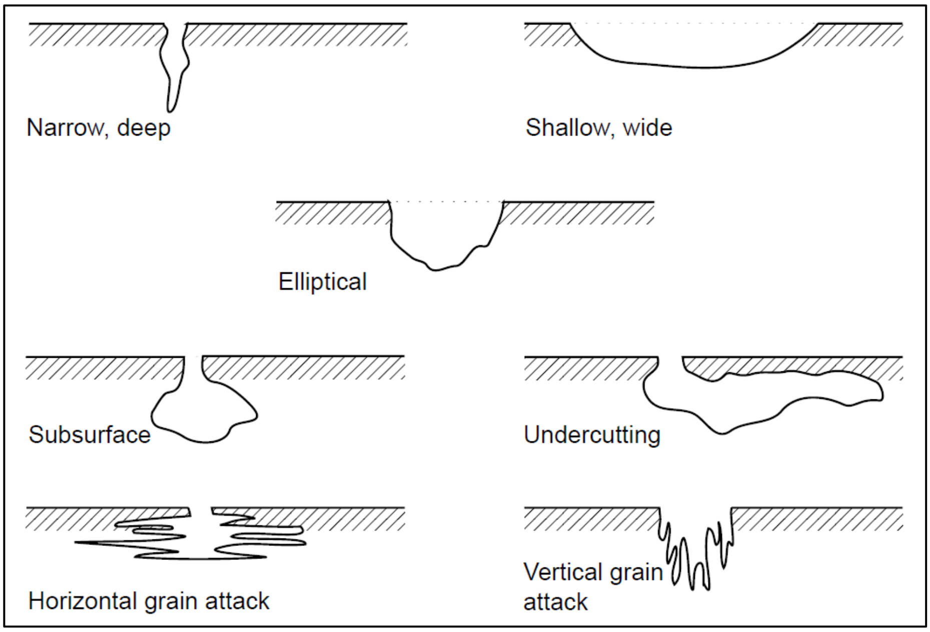

Figure 3-19: Different patterns of pitting corrosion [6]

In the study conducted by Pojtanabuntoeng et al. [50], the occurrence of pitting corrosion caused by CUI was described as "*a large opening with sharp edges and a flat bottom*." This description suggests that the pitting corrosion observed was characterized by a shallow and wide pit rather than a deep narrow cavity. The average pit depth base of the three samples was 69 μm.

3.5.3 Stress Corrosion Cracking (SCC)

Stress corrosion cracking (SCC), as shown in Figure 3-20, refers to a kind of engineering material failure that results from the gradual propagation of cracks caused by environmental factors such as a high temperature, high level of chloride content and a lower pH. This type of failure can occur very fast or very slowly at various kinetics ranging from as low as 10^{-11} m/s to as high as 10^{-2} m/s as discussed by Raja and Shoji [111], due to the combined and synergistic interactions of mechanical stress and corrosion reactions, which ultimately lead to crack propagation [112, 113].

Figure 3-20: An illustration of stress corrosion cracking that took place in type 316 stainless steel that was subjected to thermal insulation in the temperature range of 50 to 60°C. The cracking was initiated by the presence of rinsing water containing 60 mg/kg of chloride, coupled with pre-existing residual stresses [114]

The SCC depends on three factors; susceptible material, corrosive environment and applied or residual stress [10]. High chloride contents usually lead to what is known as chloride external stress corrosion cracking when applied or residual stresses are present and temperatures exceed 60°C [86]. After 10 years in service, an insulated 304 stainless steel pipe transporting H_2S at 110°C suffered from SCC failure, which was caused by the insulation becoming wet. The failure was determined to be due to chloride ions that had leached from the thermal insulation [37].

3.6 Corrosion products commonly encountered in CUI systems

In the context of CU, the primary corrosion mechanism occurs externally, where oxygen-rich atmospheres prevail, resulting in the formation of different oxides and oxyhydroxides. Corrosion products refer to substances that form as a result of the corrosion process. When steel is exposed to humid air, corrosion is initiated and gradually expands over time. Gaining a thorough understanding of the formation and progression of rust on iron-based materials is vital for the development of effective corrosion prevention and mitigation strategies across diverse industries effective corrosion prevention and mitigation strategies for various industries [115].

3.6.1 Morphology and crystal structure of various oxygenated corrosion products

Extensive research [116-119] has been carried out to characterise the various types of iron oxides that develop on steel surfaces under atmospheric conditions. However, there is limited research on the corrosion products that form beneath thermal insulation. It is reasonable to assume that the corrosion products formed under thermal insulation are similar to those formed on steel surfaces under atmospheric corrosion conditions, given that CUI occurs on the external surface of pipes and vessels. The corrosion process in both atmospheric corrosion and CUI is complex, resulting in the formation of a complex rust layer that consists of iron oxyhydroxides such as $\gamma - FeOOH$ (lepidocrocite), $\alpha - FeOOH$ (goethite), and iron oxides such as Fe_3O_4 (magnetite) and $\alpha - Fe_2O_3$ (hematite). Table 3-4 shows the chemical composition of corrosion products that are commonly found in atmospheric corrosion products.

In atmospheric corrosion, any of the oxides can form except for Wüstite, which only forms at temperatures above 570°C [42]. When low alloy steels are exposed to marine environments, the rust layers that develop are primarily composed of crystallized iron oxyhydroxides, such as $\gamma - FeOOH$ (lepidocrocite), $\alpha - FeOOH$ (goethite), $\beta - FeOOH$ (akaganeite), and amorphous oxyhydroxides like $\delta - FeOOH$ (feroxyhyte), as well as iron oxides like Fe_3O_4 (magnetite) [120, 121]. The electrical conductivity of magnetite, along with its higher nobility compared to carbon steel, enables the efficient transfer of electrons. Therefore, when magnetite forms on a surface, it facilitates the flow of electrons and can contribute to the occurrence of galvanic corrosion [122]. In contrast, weathering steel is protected from further corrosion by the formation of small goethite particles [117]. Lepidocrocite forms at the initial stage and makes up the majority of the outer layer.

When oxygen availability accelerates oxidation reactions, amorphous phases like feroxyhyte and ferrihydrite precipitate instead of crystalline phases (lepidocrocite, goethite, akageneite) [119].

Table 3-4: Corrosion product phases

Corrosion category	**Name**	**Formula**	**Crystallographic system**
Oxide	Wüstite	FeO	Cubic
	Hematite	$\alpha - Fe_2O_3$	Hexagonal
	Maghemite	$\gamma - Fe_2O_3$	Cubic-Tetragonal
	Magnetite	Fe_3O_4	Cubic
Hydroxides	Ferrous Hydroxide (white rust)	$Fe(OH)_2$	Rhombohedral
	Ferric Hydroxide (Bernalite)	$Fe(OH)_3$	Orthorhombic
Oxyhydroxides	Ferrihydrite	$5Fe_2O_3.9H_2O$	Hexagonal
	Goethite	$\alpha - FeOOH$	Orthorhombic
	Akaganeite	$\beta - FeOOH$	Monoclinic-tetragonal
	Lepidocrocite	$\gamma - FeOOH$	Orthorhombic
	Feroxyhyte	$\delta - FeOOH$	Hexagonal
Others	Ferrous chloride (lawrencite)	$FeCl_2$	-
	Ferric chloride (molysite)	$FeCl_3$	-
	Ferrous sulphate	$FeSO_4$	Orthorhombic

Lepidocrocite (γ-FeOOH), is a polymorph of ferric oxyhydroxides (-FeOOH) that exhibits an orthorhombic crystal structure [123]. This oxyhydroxide is characterized as semiconductor, electrochemically active and thermodynamic unstable which may lead to dissolution under certain conditions [124]. It can take on different shapes such as small crystalline globules, sandy crystals as shown in Figure 3-21 (a), fine plates that resemble flowery structures as depicted in Figure 3-21 (b), and clumps with a grass-like structure [103, 125, 126].

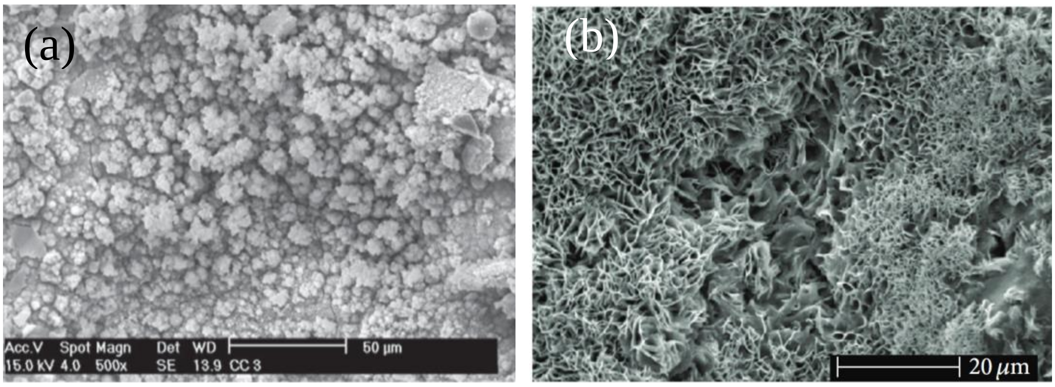

Figure 3-21: SEM micrographs showing (a) sandy crystals [126] and (b) flowery structure [127] of lepidocrocite

There is a consensus that lepidocrocite is the initial form of iron oxide that develops on steel upon exposure to atmospheric corrosion [119, 128]. Subsequently, this lepidocrocite transforms into goethite and magnetite. In the initial phase, the corrosion process involves the dissolution of steel into ferrous ions, which undergo eventual oxidation and subsequent precipitation to yield lepidocrocite, as depicted in equation 3-7 [128].

$$Fe \xrightarrow{dissolution} Fe^{2+} \xrightarrow{hydrolysis} FeOH^{+} \xrightarrow{Oxid.\ and\ precipitation} \gamma - FeOOH \tag{3-7}$$

Goethite ($\alpha - FeOOH$), is a ferric oxyhydroxide with an orthorhombic crystal structure. Different patterns of morphology were observed in $\alpha - FeOOH$ including sharp, needle-like formations and cotton ball-like aggregates shown in Figure 3-22 (a) and (b) respectively. Goethite is relatively less chemically reactive, less soluble, and has a lower electrical conductivity than other corrosion products [129]. These properties set it apart from other corrosion products and influence its role in the corrosion process positively. Most often, goethite appears on the outer layer of the corrosion film.

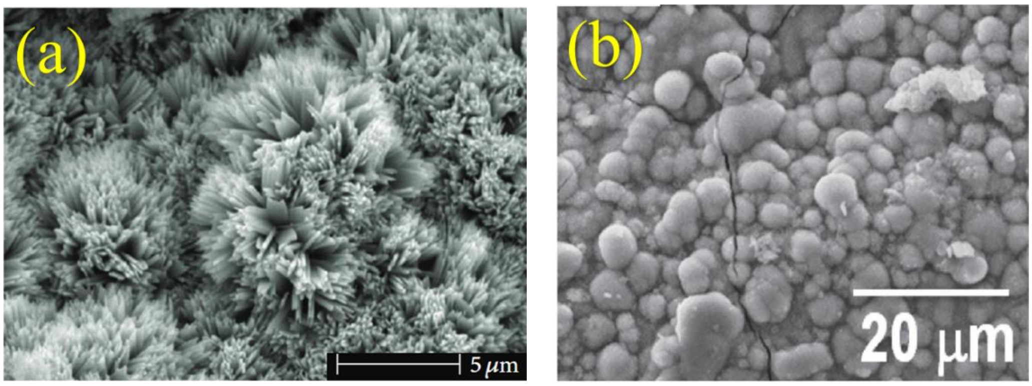

Figure 3-22: SEM micrographs of typical goethite reveal distinct structures: (a) a sharp (needle-like formation) [127] and (b) a cotton ball-like morphology [130].

Akaganeite $(\beta - FeOOH)$ is another type of ferric oxyhydroxide (-FeOOH) characterized by either monoclinic or tetragonal crystal structure [131]. Compared to $\alpha - FeOOH$ and $\gamma - FeOOH$, $\beta - FeOOH$ has the minimal density compered of 3.56 g/cm^3 [123]. $\beta - FeOOH$ exhibits two possible morphologies: rod-shaped structures resembling tubes, or intricate formations resembling rosettes as shown in Figure 3-23.

While a high chloride concentration is often associated with the formation of $\beta - FeOOH$, contributing to the stabilisation of its tunnel structure [133], recent studies suggest that it is not the sole condition necessary for its production. Studies indicate that a significant concentration of dissolved $Fe(II)$ in the medium is essential for facilitating the formation of $\beta - FeOOH$ [103, 134]. The formation of akageneite has been observed in various investigations, primarily on the metal-oxide interface

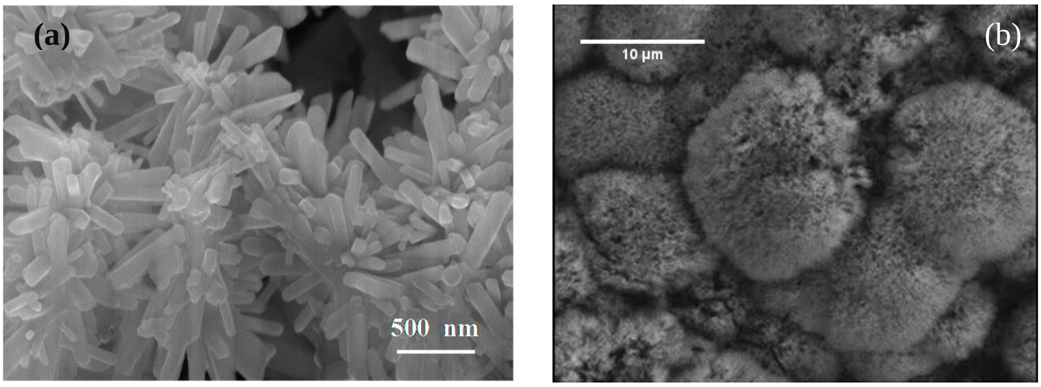

Figure 3-23: SEM view of akaganeite, (a) tubular [103] and (b) rosette [132]

of corroded artefacts [135, 136]. However, it has also been found on the external surfaces of rust deposits on carbon steel in coastal environments [137]. In marine settings, akageneite is widely regarded as one of the main products of atmospheric corrosion of carbon steel, primarily due to the availability of chloride ions [137, 138]. In relation to the mechanisms underlying the formation of akaganeite when steel is subjected to rich chloride ions (Cl^-) environment such as marine atmosphere, the process of akaganeite formation required the formation and then oxidization of the green rust (GR) [139]. The accumulation of Cl^- serves as a precursor to the creation of ferrous chloride $FeCl_2$. Consequently, this sequence initiates the gradual development of ferrous hydroxide ($\beta - Fe_2(OH)_3Cl)$, a precursor in the akaganeite formation process [103]. Subsequently, the $\beta - Fe_2(OH)_3Cl$ undergoes a series of oxidation stages, leading to the creation of GR, culminating in the ultimate formation of akaganeite, as represented in equation3-8.

$$FeCl_2 \rightarrow \beta\ - Fe_2(OH)_3Cl \rightarrow GR1(Cl^-) \rightarrow \beta - FeOOH \qquad 3\text{-}8$$

Among different iron oxyhydroxides, $\beta - FeOOH$ poses the greatest risk to the corrosion resistance of steel. Its strong reducibility and instability can accelerate the corrosion rate of carbon steel by increasing the active area of the cathode reaction and is consumed because it can serve as a reductant. The akaganeite reduction tendency is higher than lepidocrocite and goethite [140]. Furthermore, akageneite exhibits metastability under ambient conditions, indicating its tendency to transform into more stable iron oxide minerals like goethite or hematite over time [141].

Magnetite Fe_3O_4, is an iron oxide with an inverse spinel cubic crystal structure [123], which tends to concentrate in a region adjacent to the surface due to oxygen depletion [142, 143]. Magnetite exhibits a variety of morphologies, one of which is toroidal, resembling a doughnut shape, as illustrated in Figure 3-24. Corrosion may be affected by magnetite present in the inner part of the corrosion layer. The transfer of electron charges is one of the mechanisms by which magnetite increases the corrosion rate of carbon steels [144]. Nevertheless, according to Surnam et al.[124], the formation of magnetite could lead to a reduction in the corrosion rate due to its thermodynamic stability. The presence of chloride ions (Cl^-) in the environment can significantly influence the corrosion of steel and iron, leading to the formation of different corrosion products. One notable difference is the proportion of Fe_3O_4 in the corrosion products. Studies have shown that in the presence of Cl^-, the corrosion products of carbon steel contain a higher proportion of Fe_3O_4 compared to the products formed in the absence of Cl^-. This is likely due to the involvement of Cl^- in the corrosion process by promoting the formation of β-FeOOH [34, 145].

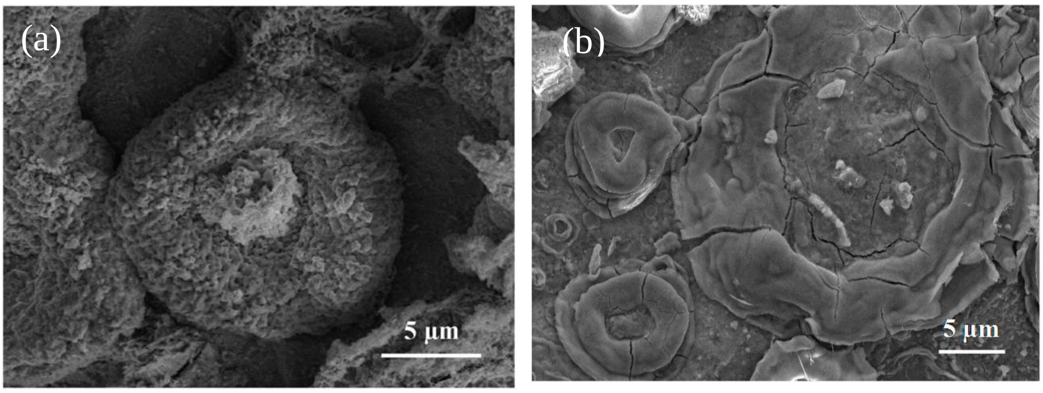

Figure 3-24: SEM image of magnetite formed on carbon steel (CS) sample reveals the presence of toroidal-shaped structures, resembling doughnuts [146]

The process of magnetite formation under wet conditions can be elucidated by considering the dissolution of steel, resulting in the generation of Fe^{2+} ions and electrons (e^-). The dissolved Fe^{2+} reacts with FeOOH rust, leading to the creation of magnetite, as depicted in equation 3-9 [143].

$$Fe^{+2} + 8FeOOH + 2e^- \rightarrow 3Fe_3O_4 + 4H_2O \qquad 3\text{-}9$$

3.6.2 Protective Ability Index of corrosion products (PAI)

The protective ability index (PAI) of a corrosion layer formed on a steel surface exposed to the atmospheric condition was first proposed by Yamashita et al. [147]. The PAI is a numerical value that represents the ratio between the mass fraction of goethite ($\alpha - FeOOH$) and lepidocrocite ($\gamma - FeOOH$) as shown in equation 3-10 [147]. This equation is applicable under the assumption that the corrosion film primarily consists of $\alpha - FeOOH$ and $\gamma - FeOOH$ [148].

$$PAI_1 = \frac{mass\ fraction\ of\ \alpha - FeOOH}{mass\ fraction\ of\ \gamma - FeOOH} = \frac{\alpha}{\gamma} \qquad 3\text{-}10$$

When a PAI_1 value greater than one indicates that the corrosion layer formed on the steel surface is protective and effective in reducing the corrosion rate, while a PAI_1 value less than one indicates that the protection is ineffective [148]. However, PAI_1 values exceeding 2 are considered necessary to achieve a lasting and stable corrosion layer [149].

The definition of PAI used in equation 3-103-1 differs depending on the environment to which the steel is exposed [150]. In a coastal environment, the presence of akageneite $\beta - FeOOH$ on the surface of steel is anticipated due to chloride deposition. Therefore, the determination of PAI_2 in equation 3-11 would encompass β-FeOOH and a spinal-type of iron oxide (S) (magnetite Fe_3O_4 or maghemite $\gamma - Fe_2O_3$) . A high value of PAI_2 for a rust layer indicates that the layer has insufficient ability to prevent corrosion. In contrast, a lower value of PAI_2 indicates a more effective rust layer that is capable of protecting against corrosion more effectively [150].

$$PAI_2 = \frac{mass\ fraction\ of\ (\beta + S)}{mass\ fraction\ of(\gamma + \beta + S)} \qquad 3\text{-}11$$

Semi-quantitative phase analysis methods can be used to determine the various mass fractions of a corrosion film using X-ray diffraction (XRD) and commercial software packages such as X'Pert HighScore [151] or EXPO2013 [152] software which are then used to calculate the PAI. These methods are capable of determining both the types and quantities of compounds in solid or powder systems. Reference intensity ratio (RIR) and Rietveld refinement are two semi-quantitative methods commonly used for this purpose. In the RIR method, the intensity ratio of the strongest Bragg peaks in the analysed phase is compared to the intensity ratio of a standard reference material [153]. The Rietveld refinement method is based on the principle that the area of the diffraction peak for each phase in a mixture is proportional to its content [154]. The accuracy of the Rietveld refinement is higher since this method refines the entire phase. This approach has been employed by researchers in the field [117].

A number of studies [147, 149, 150, 155, 156] have been conducted to evaluate the correlation between the corrosion rate of weathering steel as well as carbon steel and their PAI under several different environmental conditions, particularly in coastal areas. However, no studies have investigated the relationship between the PAI of the corrosion layer formed under thermal insulations and the corrosion rate.

3.7 Microcell techniques to evaluate corrosion phenomena

Studying corrosion through electrochemical techniques typically rely on the 3-electrode cell technique as described in section 2.4.1 with the working electrode usually having an active surface area ranging between ranging from square millimetres (mm^2) to square centimetres (cm^2) and assuming general corrosion mechanisms. While these approaches can effectively describe the overall electrochemical behaviour across the sample surface, they are limited in their ability to provide detailed, local electrochemical information that could enhance our understanding of corrosion mechanisms [157, 158]. The Scanning Vibrating Electrode Technique (SVET) was employed to study the localized corrosion of an aluminium matrix [159]. Additionally, the corrosion of carbon steel was characterized using the Scanning Reference Electrode Technique (SRET) to specifically examine pitting corrosion [160]. Regarding CUI, Cain et al. [109] utilized the ASTM G189 rig and integrated electrochemical noise (EN) to evaluate the pitting behaviour of CUI phenomena.

3.7.1 Microelectrode shapes

Microelectrodes have been produced in various forms, as depicted in Figure 3-25, using different approaches such as mechanical and lithographic techniques [161, 162].

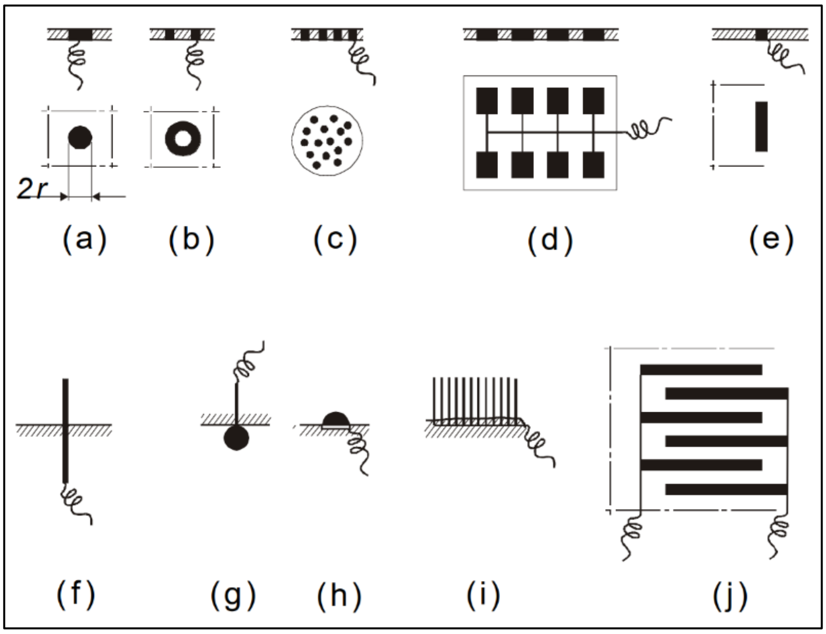

Figure 3-25: Different geometries of available microelectrodes (a) microdisk, (b) microring; (c) microdisk array (a composite electrode); (d) lithographically produced microband array; (e) microband; (f) microcylinder; (g) microsphere; (h) micro hemisphere; (i) fibre array; (j) interdigitated array[161]

For this study, the researcher utilized an embedded microcylinder as an innovative evaluation tool to investigate CUI. It involves the incorporation of a cylindrical structure of three electrodes (WE, RE and CE), within the experimental setup so that corrosion behaviour can be monitored and studied more precisely. Researchers in the corrosion field have adopted and explored embedded microcylinders in a wide variety of studies, not just this study. Its application has proven valuable in evaluating top-of-the-line corrosion [163].

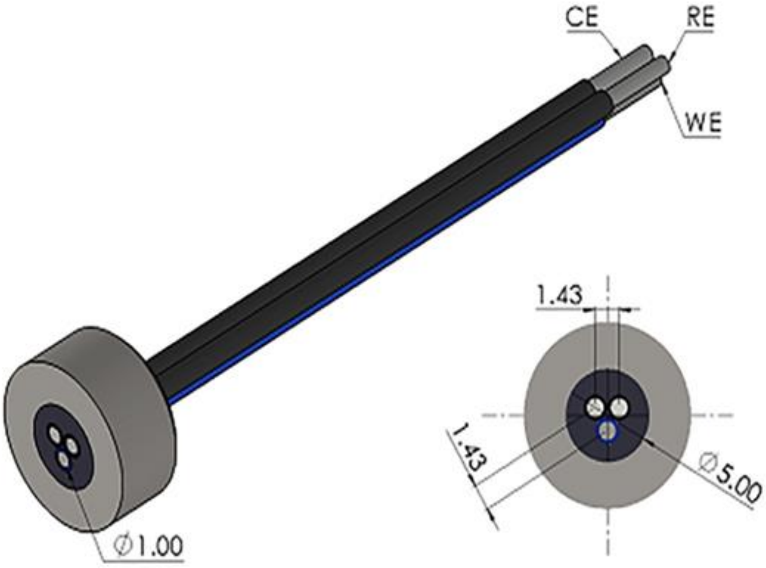

Figure 3-26: A three miniature electrodes cell composed of two wires, RE and CE, made from Hastelloy® c276 and a WE made of X65 carbon steel [163]

The following chapter explains the materials and methodology adopted for the evaluation of CUI, by utilizing a three microelectrodes cell setup. Additionally, the chapter outlines the techniques employed to analyse the corrosion layers that develop on the sample surfaces such as SEM-EDX and XRD.

Chapter 4: Materials and Experimental Procedures

This chapter focuses on providing an in-depth understanding of the methodologies used during the experimental work, along with the underlying theory behind each technique employed. Additionally, this chapter discusses the materials utilized throughout the research project, outlining their properties and characteristics. Furthermore, this chapter describes the various techniques, which are SEM-EDX-Raman and XRD, used to analyse the morphology and composition of the corrosion product obtained from the sample testing procedures.

4.1 Materials

4.1.1 Working electrode

Throughout the oil and gas industry, a number of metals and alloys are employed for downstream and upstream processes. There are at least 80% of all components used in this industry are constructed from carbon steel due to its affordability, widespread availability, and ease of fabrication [164].

In the context of electrochemical testing, the working electrode refers to one of the three electrodes present in the standard three-electrode cell setup as described in sections 2.4.1 and 2.4.1. The working electrode in this research is made of ASTM A 106 Grade B carbon steel. ASTM A106 grade B is a type of mild steel pipe material that is commonly employed in various industrial applications such as power refineries, gas refineries, power plants, boilers, ships, and chemical plants. Specifically designed to withstand high-temperature services, this type of pipe is highly coveted due to its versatility and reliability.

Compared to the other two grades in the ASTM A106 specification, grade B offers a balance of strength and cost-effectiveness. It possesses the necessary strength of minimum 415 MPa and yield strength of 240 MPa to transport high-temperature fluids and gases, up to 400 °C, but is not typically used for heavy-duty projects like grade C. Grade B has a carbon content that typically ranges around 0.30%, which is higher than grade A but not as strong as grade C.

The ASTM A106 Grade B is deemed equivalent to ASTM A53 Grade B and API 5L Grade, based on both chemical composition and mechanical properties. The chemical composition of the carbon steel is shown in Table 4-1 displays the micrograph of ASTM A106 Grade B, revealing a microstructure consisting of ferrite (light colour) and pearlite (dark colour).

Table 4-1:Chemical composition (wt%) of ASTM A 106 Gr B carbon steel [165]

C, max	Mn	P, max	S, max	Si, min	Cr, max
0.30	0.29-1.06	0.035	0.035	0.10	0.40
Cu, max	Mo, max	Ni, max	V, max	Fe	
0.40	0.5	0.4	0.08	Balance	

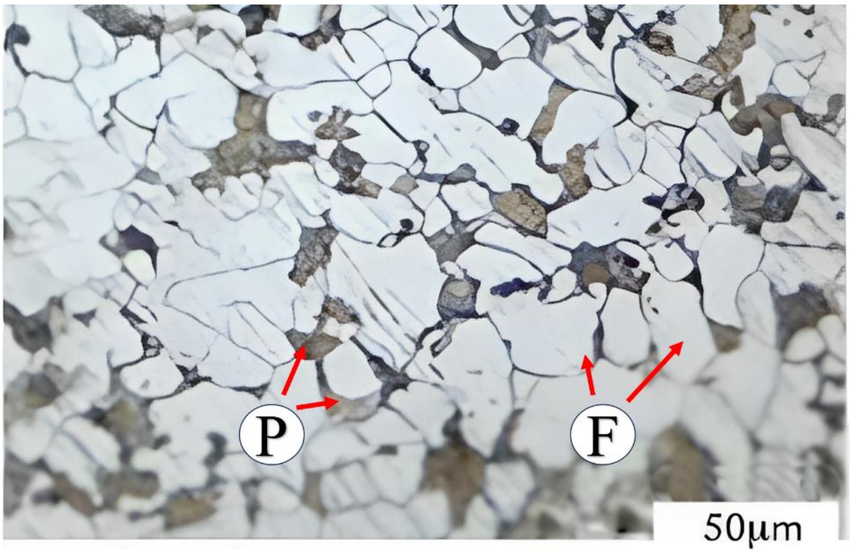

Figure 4-1: Normalized microstructure of the ASTM A106 Gr B steel shows ferrite (F) and pearlite (P) [166]

4.1.2 Reference and counter-electrode

The material utilized for the reference and counter electrodes in this research was Hastelloy C-276 (UNS-N10276), which is a high-performance nickel-based alloy. C-276 is known for its excellent resistance to corrosion in a range of environments, including hot and cold concentrated sulphuric acid, hydrochloric acid, and wet chlorine gas. It also has good resistance to stress corrosion cracking and excellent resistance to corrosion induced by high-velocity seawater and brine solutions [167]. Table 4-2 illustrates the composition of C-276, which includes nickel, molybdenum, chromium, and a small quantity of tungsten.

Table 4-2: Chemical composition of Hastelloy C-276 [168]

C	Si	Cr	Fe
0.001	0.03	15.88	5.35
Mo	Co	W	Ni
15.64	1.51	3.38	Balance

4.1.3 Thermal insulation

For the purpose of this study, a preformed pipe mineral wool thermal insulation, namely as Rockwool® RockLap H&V Pipe Sections, was utilized. The insulation was procured from ***Belgrade Insulations***, Leeds under the product code of BA2RW. It featured an internal diameter of 60 mm and a thickness of 20 mm, as depicted in Figure 4-2 (a). The insulation used in this work is provided with a foil-facing layer. The manufacturing process of this insulation involves combining fibres with an organic binder, like phenolic, to create the insulation material. The standard chemical composition of the thermal insulation is shown in Table 4-3.

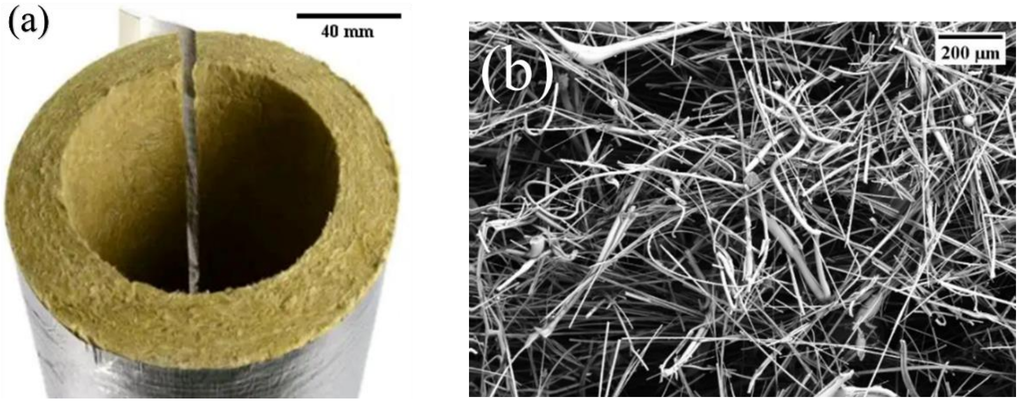

Figure 4-2: (a) Preformed pipe mineral wool insulation with a facing foil, (b) SEM of the insulation

Table 4-3: Standard chemical composition of a mineral wool thermal insulation [77]

Component	SiO_2	Al_2O_3	CaO	Na_2O	P_2O_5
Wt.%	30-45	8-15	30-35	0-1	0-1
Component	Fe_2O_3	TiO_2	ZrO_2	K_2O	MgO
Wt.%	2.5 max	2-4	0-17	0-1	6-12

Mineral wool insulation is a commonly utilized material in a range of industries, including the oil and gas sector, due to its beneficial properties. Its key features include high-temperature resistance of up to 250°C, a lightweight and porous structure, and ease of installation [77]. An SEM image of the thermal insulation used in this study is depicted in Figure 4-2 (b). The fibres of mineral wool insulation can possess varying degrees of curvature and may not be uniformly straight.

4.1.4 Heating oil

In this study, heat transfer oil 475 [169], produced by Millers Oils®, was used as a heat transfer facilitator. This oil is a premium solvent-refined mineral oil known for its exceptional quality. It is specifically designed for use in high-temperature applications due to its superior properties, such as a high flashpoint of 220°C and an auto-ignition temperature of 350°C. Its remarkable performance makes it ideal for use in applications that operate at temperatures up to 315°C, making it a suitable choice for this study.

4.1.5 The electrolyte solution

To create the electrolyte solution required for this study, 1L of deionised water was mixed with 35g of sodium chloride (NaCl) to produce a brine with a concentration of 3.5% NaCl. The resulting solution was then transferred into a 20L container and subsequently pumped into the thermal insulation at a flow rate of 40ml/min, utilizing a Reglo Analog dispensing peristaltic pump.

4.2 Working electrode preparation

The rig enables testing of both electrochemical and mass loss coupons, necessitating the preparation of both sample types.

4.2.1 Sample preparation for electrochemical measurements

A cylindrical working electrode (WE) with a circular diameter of 1 mm and a surface area of the circular face of 0.785 mm^2 was extracted from an ASTM A106 Grade B pipe. Each working electrode was attached to a wire and then immersed in a non-conductive resin assembled alongside RE and CE to form a three microelectrodes cell as shown in Figure 4-3. The assembled microelectrodes cell was then subjected to wet abrasion using silicon carbide (SiC) papers with P320, P600, and P800 grits. Then the microelectrode cell was subsequently degreased using acetone, rinsed with distilled water, and dried immediately using a heat gun.

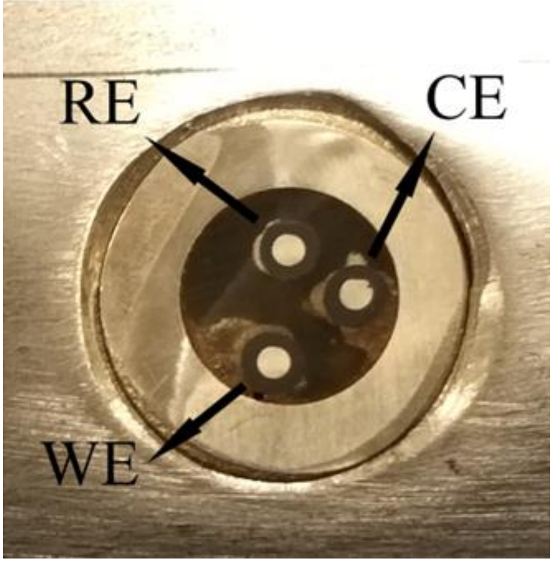

Figure 4-3: Three microelectrode cells used to evaluate CUI at 12 and 6 o'clock

4.2.2 Sample preparation for mass loss measurements and post-experiment analysis

The mass loss and surface analysis coupons were sectioned from the same pipe as the working electrode. The dimensions of the coupons were 24x14mm with an exposed surface area of around 3.45 cm^2. Prior to each test, the coupons were wet ground up to P800 grit, degreased with acetone, rinsed in distilled water, and then dried using a heat gun. Then, the coupons were electrically isolated by special shrink tape.

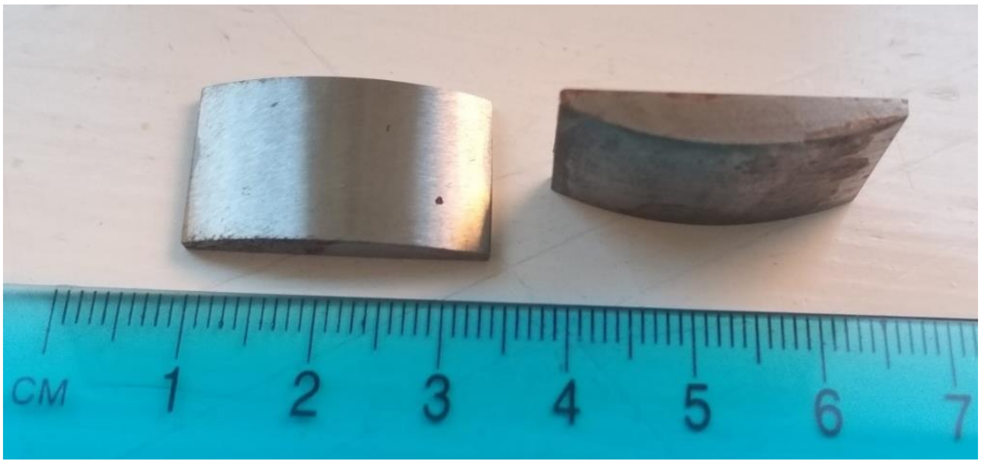

Figure 4-4: Mass loss and post-analysis coupons

4.3 Installation of the thermal insulation and positioning of the injection point

The preformed insulation was installed with consideration of its orientation relative to the pipe. Specifically, the split point was positioned at the 3 o'clock mark as per Figure 4-5 (a). This deliberate placement was chosen to mitigate the risk of brine being injected into the split section, where it could potentially move more swiftly throughout the gap between the insulation layers.

Further consideration was taken to avoid installing the split at the 6 o'clock position. This decision was made to optimize the insulation's ability to retain water over an extended period. By avoiding the 6 o'clock position, the insulation may effectively maintain water within its layers, enhancing the microelectrode wetting, hence improving electrochemical measurements.

Following the initial installation, the insulation was secured using the self-adhesive tape provided with the insulation material. Subsequently, the aluminium cladding was positioned around the insulation and fastened using two metal cable ties, as depicted in Figure 4-5 (e). Excessive tightening of the metal cable ties is avoided to prevent any unintended deformation of the thermal insulation material. This precaution helped maintain the integrity and effectiveness of the insulation layer surrounding the piping system.

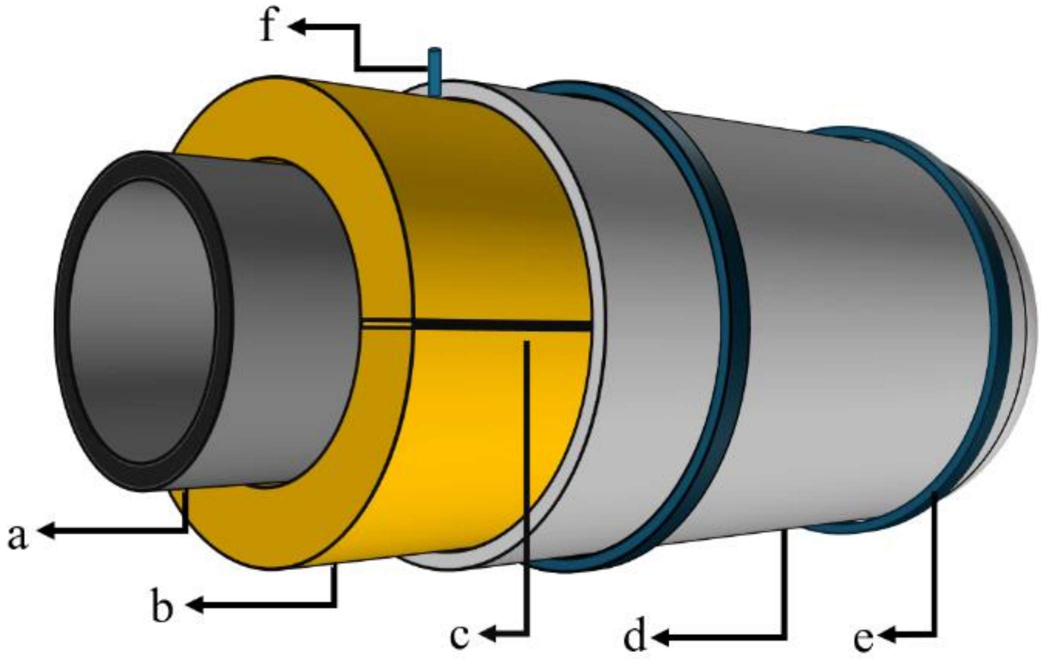

Figure 4-5: A section of CUI rig, (a) the pipe, (b) thermal insulation, (c) split section, (d) cladding, (e) metal cable ties, (f) the injection point

In the new system, the injection point consisted of a singular nozzle designated to deliver fluid consistently at a rate of 40 ml/hr. The injection point was positioned at the 12 o'clock orientation, situated above the thermal insulation layer and below the aluminium foil and the cladding, as shown in Figure 4-5 (f). It is essential to highlight that this particular placement diverges from the prescribed guidelines outlined within the ASTM G189-07 standard for the above-mentioned reasons.

After that, a series of potentiostatic tests were conducted on the microelectrode cell under the conditions shown in Table 4-4 to determine the corrosion rate under thermal insulation.

Table 4-4: Test matrix

pH	Temperature	Duration
7	Room temperature	168 hours
	80°C	
	150°C	
5	Room temperature	
	80°C	

4.4 Electrochemistry techniques and mass loss measurements

In this study, electrochemical responses were recorded using the LPR technique. This study employed three microelectrode cells. The WE was made of carbon steel, while the reference and auxiliary electrodes were made of Hastelloy C-276. Corrosion rate was measured using ACM GILL 4 potentiostat.

The LPR was performed by polarising the sample electrode from -15mV below the open circuit potential (OCP) to +15mV above the OCP at a scanning rate of 10mV/min to obtain a linear polarisation resistance measurement (R_p).

4.5 Mass loss measurement

In order to measure the mass loss of the coupons, a meticulous procedure was followed. The initial weights of each subject were recorded before each experiment using a sensitive balance of 1 milligram (mg) accuracy. As soon as the CUI test was completed, the coupons were removed from the rig with care. A corrosion layer formed on the coupon surface was removed chemically using Clarke's solution, its chemical composition is described in table 4-5. In accordance with ASTM G1 [170], this widely recognised method is specifically designed to remove corrosion products from steel. Thorough cleaning with acetone was performed after Clarke's solution was applied to the coupons. Afterwards, the coupons were washed with distilled water and carefully dried with a heat gun. An accurate balance with a sensitivity of 1 milligram (mg) was used to weigh the coupons after they had been cleaned and dried to obtain precise measurements. With this rigorous process, any mass loss caused by corrosion during the CUI test is accurately quantified.

able 4-5: Clarke's solution chemical composition

Compound	**Quantity**
Hydrochloric acid solution (HCl) SG 1.19	1L
Antimony trioxide (Sb_2O_3)	20g
Stannous chloride ($SbCl_2$)	50g

4.6 Post-experiment analysis techniques

An analysis of corrosion product layers formed under thermal insulation was carried out using some surface analysis techniques to determine their chemistry and morphology such as;

1. Scanning electron microscopy (SEM) and Energy dispersive X-ray analysis (EDX)
2. X-ray diffraction (XRD) spectroscopy
3. Raman spectroscopy
4. Ion chromatography (IC)

4.6.1 Surface analysis techniques

4.6.1.1 Scanning Electron Microscopy (SEM)

SEM was used for obtaining high-resolution images of materials and characterising their morphology. The SEM procedure involves radiating a low-energy electron beam, typically generated by tungsten filament lamps or field emission guns, onto the material and scanning its surface. Ultrahigh vacuum conditions are required for the field emission gun to work correctly. The electron beam is accelerated with a high voltage and narrowed after passing through apertures and electromagnetic lenses. When the beam reaches and enters the material, several different interactions occur, which result in the emission of photons and electrons. The images are generated using SEM signals produced from the interaction between the beam and specimen [171]. In this study, the corrosion film formed on the coupon was examined using a Carl Zeiss EVO MA15 (SEM). The Secondary Electron (SE) and Back Scattered Electron (BSE) images were obtained using a 20 kV accelerating voltage and an approximately 8 mm working distance.

4.6.1.2 X-ray diffraction (XRD) spectroscopy

X-ray diffraction analysis (XRD) is a non-destructive technique that allows for the analysis of materials at the molecular level and provides detailed information about their crystallographic structures, chemical composition, and physical properties. In this method, monochromatic X-rays interfere constructively with a crystalline sample. This technique involves collimating the generated X-rays and directing them toward the sample as shown in Figure 4-6. The incident rays interact with the sample to produce a diffracted X-ray when conditions satisfy Bragg's Law as shown in equation 4-1 [154]. Each material phase has a unique diffraction pattern due to its chemistry and atomic arrangement.

$$n\lambda = 2dsin\theta \qquad 4\text{-}1$$

Where d represents the spacing between the diffracting planes or lattice in A°, θ is the incident angle, n is an integer and λ is the wavelength of the X-ray beam.

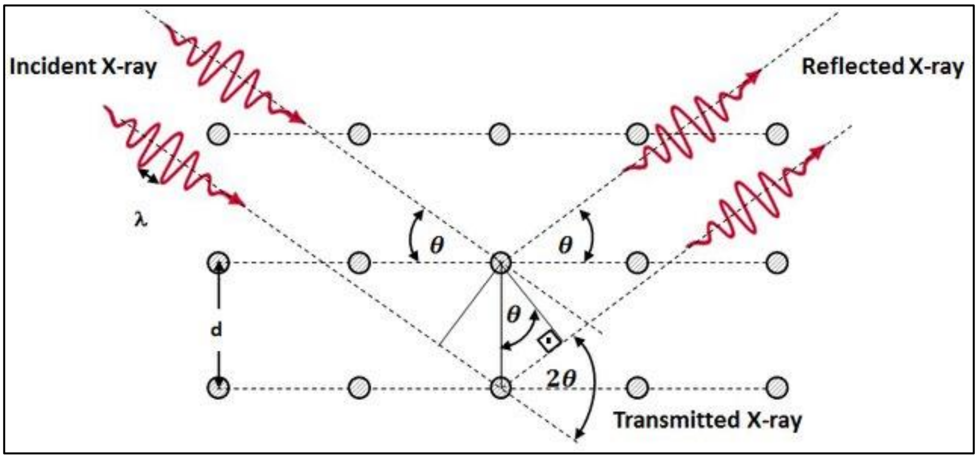

Figure 4-6: Schematic diagram of Bragg's law [172]

The XRD spectra for each sample were performed on Philips XPert XRD. The scans were performed at room temperature with the angular region of 2θ =10 to 90°, 0.03°

step size, 2s counting time, and filtered with Cu-Kα_{1+2} radiation. Then, the XRD diffraction patterns were compared to standard crystallographic databases using the International Centre for Diffraction Data (ICDD) with the assistance of HighScore Plus software version 5.0 to facilitate the phase identification of the corrosion products formed.

4.6.2 Chemical analysis techniques

4.6.2.1 Energy-Dispersive X-ray analysis (EDX)

Energy dispersive X-ray spectroscopy (EDX) is a chemical microanalysis technique commonly used in conjunction with scanning electron microscopy (SEM). The EDX analyses the elemental composition of a sample over a micro- or nanoscale by measuring the X-rays emitted from the area being excited by the electron beam. For this study, EDX analysis using an X-mas detector from Oxford Instruments with an area of 80 mm^2 was used to confirm the elemental composition of the corrosion layer on the surfaces of the sample coupon.

4.6.2.2 Raman Spectroscopy

The Raman spectrometry technique is used for non-destructive chemical analysis, which provides information regarding chemical structure, phase, polymorphism, crystallinity, and molecular interactions. This study utilised InVia Renishaw© Raman Spectroscopy. The Raman spectroscopy method involves scattering light by a vibrating molecule placed in front of a monochromatic light source and measuring its wavelength shift. The RENISHAW Raman spectroscopy uses a monochromatic laser to illuminate the vibrating molecules of a test sample.

4.6.3 Ion chromatography

This experiment aims to quantify the amount of ions leached from insulation that may promote or cause CUI. The primary focus of this experiment will be on chloride ions, fluorine ions, sodium ions, and silicate ions. As described in ASTM C 871-

08a and BS EN 13468-2001 [67, 81], Ion Chromatography (IC) and Atomic Absorption Spectroscopy (AAS) were utilised for quantitative measurement.

Ion chromatography is a technique that can be used to analyse the cations and anions present in many aqueous samples. Ion Chromatography separates ions based on their interaction with resin and eluent (stationary and mobile phases, respectively). This procedure has two columns: Anion columns, which attract anions, and Cation columns, which attract cations. However, as each column attracts only a specific type of ion, it can only measure the conductivity of those ions. Furthermore, according to the ions' affinity for the resin, ions move through the columns of an ion chromatographer at different speeds, and they separate from one another according to their charge and size. Therefore, those ions whose affinity for the resin is weaker will move through the column faster and be eluted first, while those whose affinity is stronger will move slower through it.

Chapter 5: Development of the CUI investigation rig

In order to replicate the CUI under controlled laboratory conditions, it was imperative to develop an appropriate laboratory rig. The foundational framework for designing this rig was drawn from the principles delineated in ASTM G189-07, which is the recognised standard guide for laboratory simulation of corrosion under insulation [110]. This standard serves as a comprehensive resource, offering directives on the structural and operational aspects of laboratory setups employed for simulating CUI.

While adhering to this standard, some studies in the literature have made slight alteration to further enhance the understanding of CUI phenomena. For instance, Caines [173] introduced the integration of the electrochemical potential noise method into the rig setup to monitor CUI. These adaptations did not deviate significantly from the fundamental design concept outlined in the standard.

In another approach, Pojtanabuntoeng et al. [174] conducted experiments by implementing CUI on both the top and bottom halves of the pipe through the use of ring specimens. Their findings indicated discernible differences in the corrosion rates between the top and bottom samples. These outcomes suggest that, at least during the initial stages of the experiment or even after prolonged exposure, as reported by[175], there exists an observable discrepancy in the corrosion rates between the top (12 o'clock position) and bottom (6 o'clock position) samples.

Despite being based on the concept of the ASTM G189-07 standard; certain alterations were made to the rig design in this research. The rig employed a three-microelectrode cell configuration instead of three rings as per the ASTM standard. These microelectrodes were in sets of 2 at the top (12 o'clock) and bottom (6 o'clock) of the pipework. Additionally, the mass loss coupons were manufactured to assess corrosion rates at two locations, aligning with the arrangement of the microelectrodes. As a result, the design and construction of the rig were primarily focused on identifying variations in CUI between the top and bottom positions.

5.1 CUI Laboratory rig design

To create the CUI rig for this particular study, SolidWorks 3D Cam software 2018 [176], was utilized. This advanced software package allowed for the creation of a detailed and accurate 3D model of the rig, which was then used to fabricate the actual rig components. The resulting rig design is represented in Figure 5-1, and it consists of various components.

In this study, the main pipe was constructed from a high-quality seamless pipe ASTM A106 Gr B with an outside diameter (OD) of 60.3mm and nominal diameter (ND) of 50mm. To construct the main pipe of the CUI rig, three separate pipe components were employed. The utilization of separate pipe components, as opposed to a single, continuous piece, offers some advantages. Firstly, it provides enhanced flexibility in machining and construction. Additionally, it simplifies the transportation and handling of the main pipe during the construction and assembly phases. Another noteworthy improvement is the incorporation of a tongue and groove configuration at both ends of each pipe, designed to accommodate O-rings as shown in Figure 5-1 detail C and D. This design choice streamlines assembly, ensures the alignment of the three pipe components, and effectively controls the potential for leaks. The main components of the CUI rig are as follows:

1. Immersion Heater: The immersion heater and thermostat are used to heat the heating oil and maintain a constant temperature throughout the testing process. The immersion heater is made of high-quality stainless steel by (Elmatic Cardiff Ltd). The thermostat is used to regulate the temperature of the immersion heater and ensure that the temperature remains constant.
2. Temperature Control and Thermostat Unit: are used to regulate the temperature of the heating oil and maintain a consistent temperature throughout the testing process with assist of the thermostat.
3. Mineral Wool Insulation.
4. Aluminium Cladding: is used to cover the mineral wool insulation and protect the thermal insulation.
5. Dispensing Peristaltic Pump: is used to deliver the brine to the test rig.

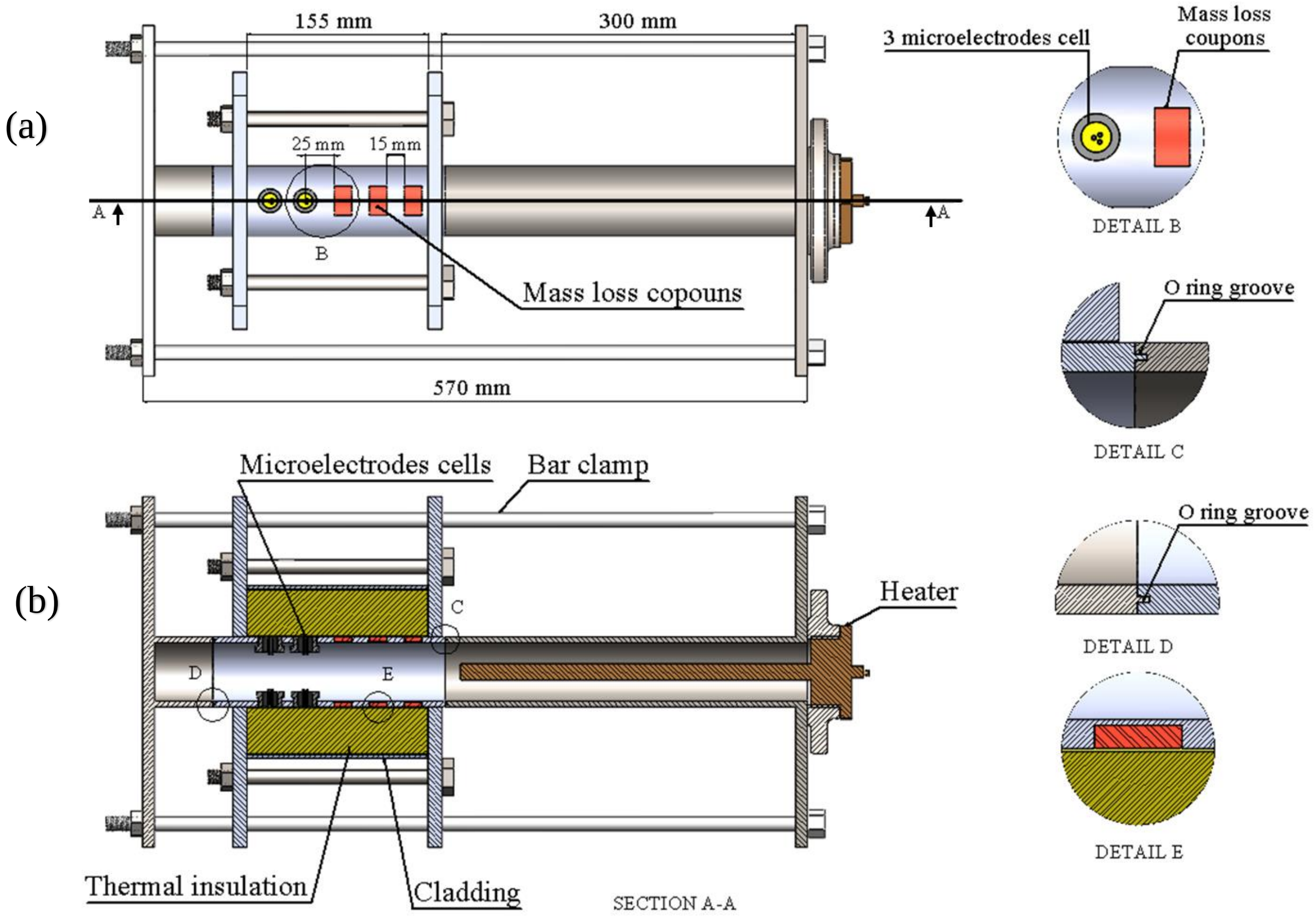

Figure 5-1: SolidWorks ® model of CUI laboratory test rig (a) top view; (b) cross-sectional

6. Aluminium Plates: are used to support the test specimen and provide a stable base for the CUI rig.
7. Bar Clamps: Bar clamps are used to secure the aluminium plates in place and ensure that the test specimen remains stable during the testing process. These clamps typically consist of a series of adjustable bars that can be tightened or loosened as needed.
8. Stainless Steel Water Tank.
9. A 20 L tank to hold the corrosive brine.

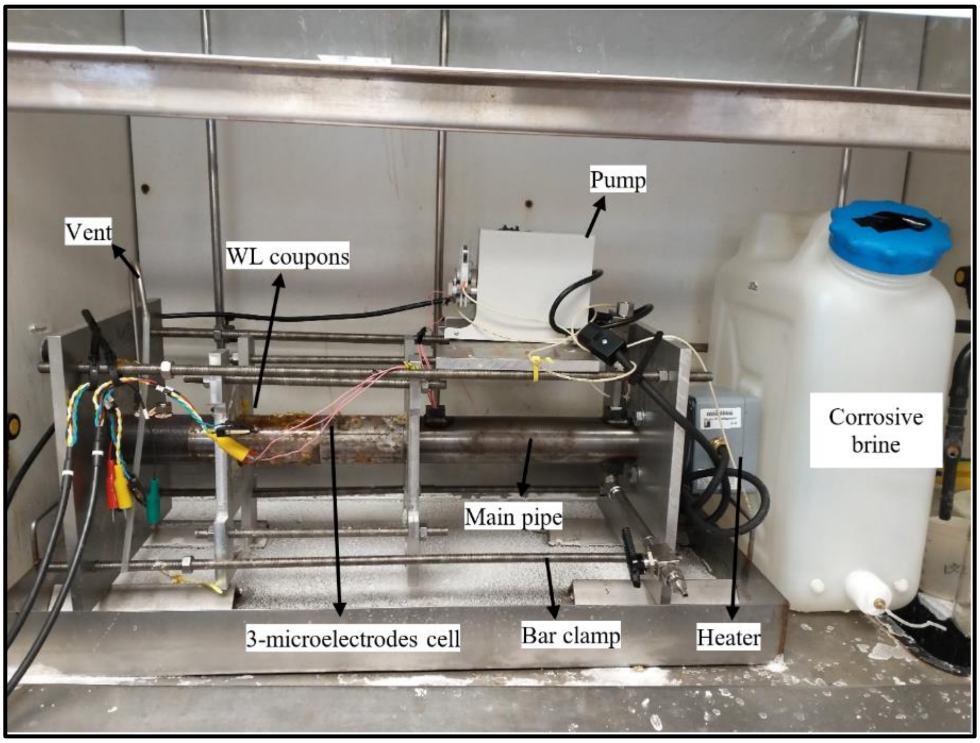

Figure 5-2: Image of final CUI rig

5.1.1 Three-microelectrodes cell

Three microelectrode cells were used to conduct the electrochemical measurements of CUI for this study, as shown in Figure 5-3. This cell was comprised of a working electrode (WE), a reference electrode (RE) and a counter electrode (CE). The sample electrode dimensions are 1mm in diameter and 3mm in length, as shown in Figure 5-4. The RE and CE were made of Hastelloy wire with a 1mm diameter. The WE was wired, and then each electrode was electrically isolated with shrink tape.

The material for the WE was carbon steel, and for RE and CE were Hastelloy, as described in sections 4.1.1 and 4.1.2, respectively.

Each experiment was conducted by twin-three microelectrodes’ cells at the top position (12 o'clock) and the other located at the bottom of the pipe (6 o'clock) for reproducibility and measuring corrosion rate at two different positions (top and bottom).

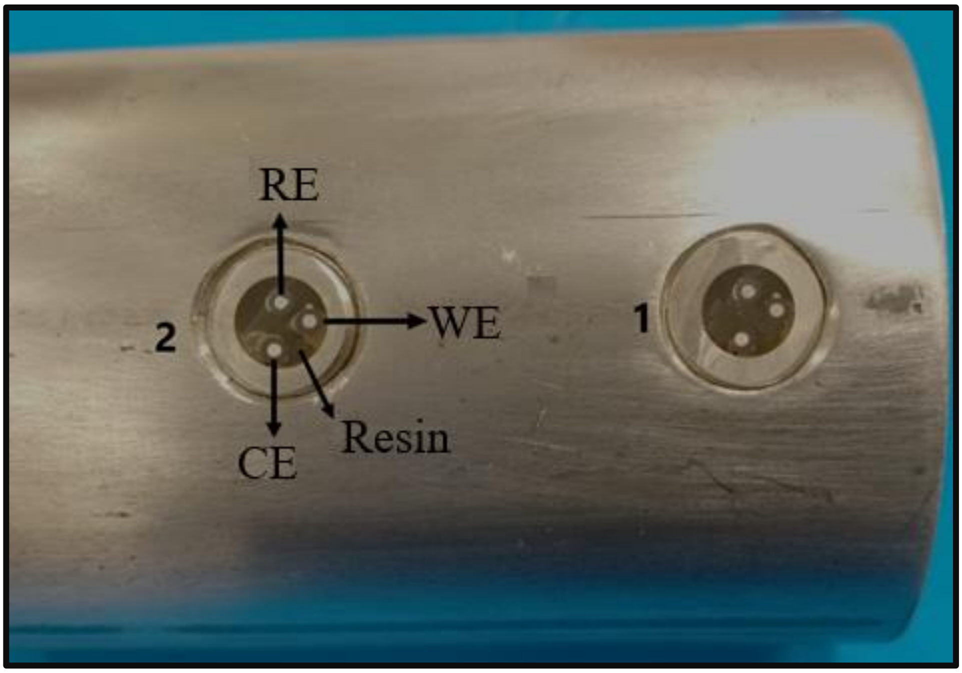

Figure 5-3: Image of the three microelectrodes cell

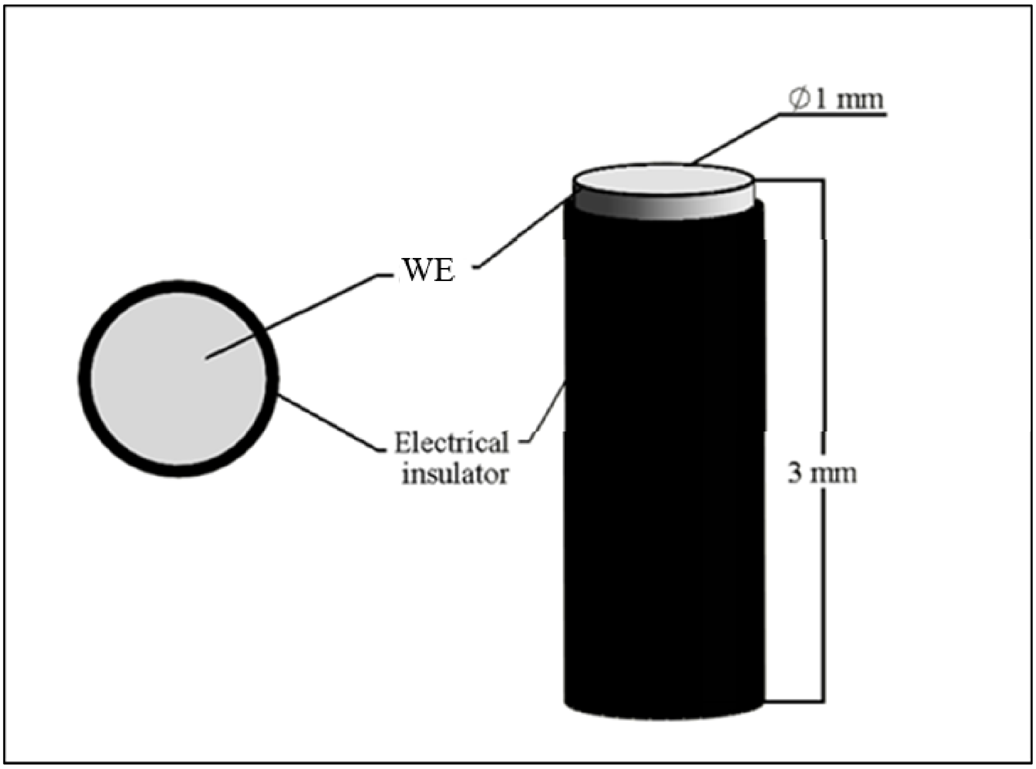

Figure 5-4: A SolidWorks® schematic represents ASTM A 106 Gr B working electrode (WE)

5.1.2 Mass loss and post-analysis coupons

In this study, each experiment involved the use of a total of six mass coupons, as depicted in Figure 5-1. Out of these, three coupons were positioned at the top (12 o'clock) as illustrated in Figure 5-5, while the remaining three were placed at the bottom (6 o'clock) of the rig. These coupons were standardized at dimensions of 14x24 mm and featured a radius of 30 mm on one side, as visually represented in Figure 5-6.

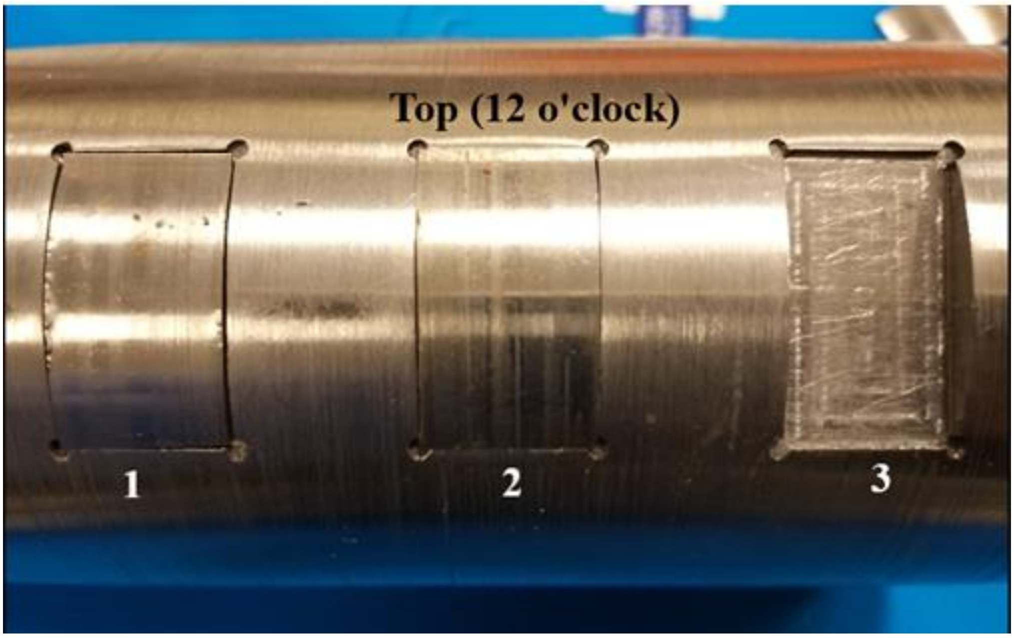

Figure 5-5: An image of mass loss coupons

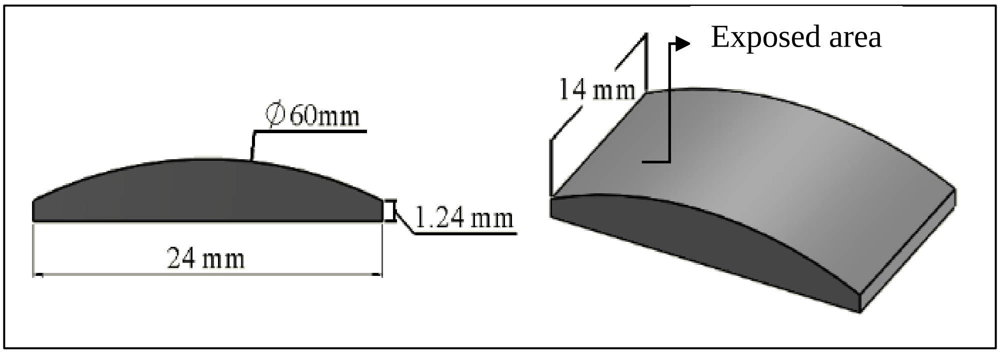

Figure 5-6: A SolidWorks ® schematic of mass loss coupons

Chapter 6: Results and discussion

6.1 Thermal insulation

6.1.1 Microscopic analysis of the thermal insulation

Figure 6-1 depicts the SEM image of thermal insulation fibres. The distribution of fibres in mineral wool and fibreglass insulation is random, which is a common feature of these types of thermal insulations. The fibres intertwine to form a three-dimensional network, creating a complex and heterogeneous profile. This arrangement generates a substantial volume of air voids, which act as thermal barriers, reducing heat transfer by conduction and improving energy efficiency. Moreover, the presence of air voids also makes thermal insulation materials lightweight and easy to handle, making them ideal for construction applications where insulation weight is essential.

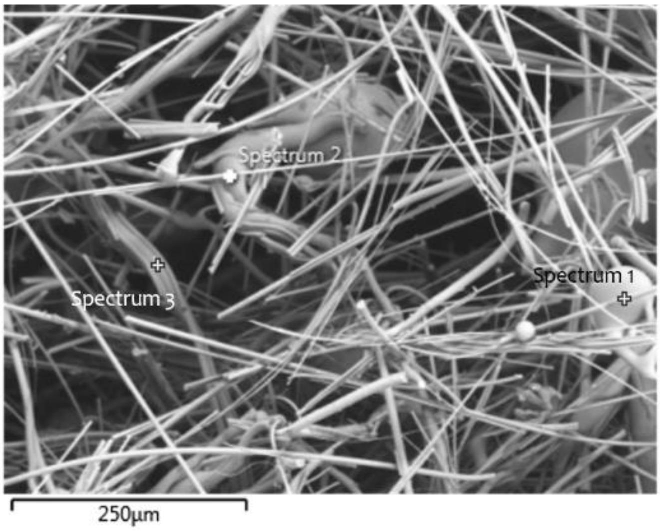

Figure 6-1: SEM micrograph for the mineral wool thermal insulation

The average diameter of the fibres is approximately 10 µm, a size that is suitable for achieving effective thermal insulation properties [177]. The small diameter of the fibres allows for a significant amount of air to be trapped within the fibre structure, which in turn reduces heat transfer and improves the insulation capabilities of the material [178].

The EDX mapping, per Figure 6-2, illustrates the anticipated elemental composition within the insulation material. A homogenous distribution of elements was observed on the fibres. The presence of gold (Au) in the mapping is attributed to its incorporation within the coating, which is essential in facilitating the SEM-EDX scanning procedure for such material.

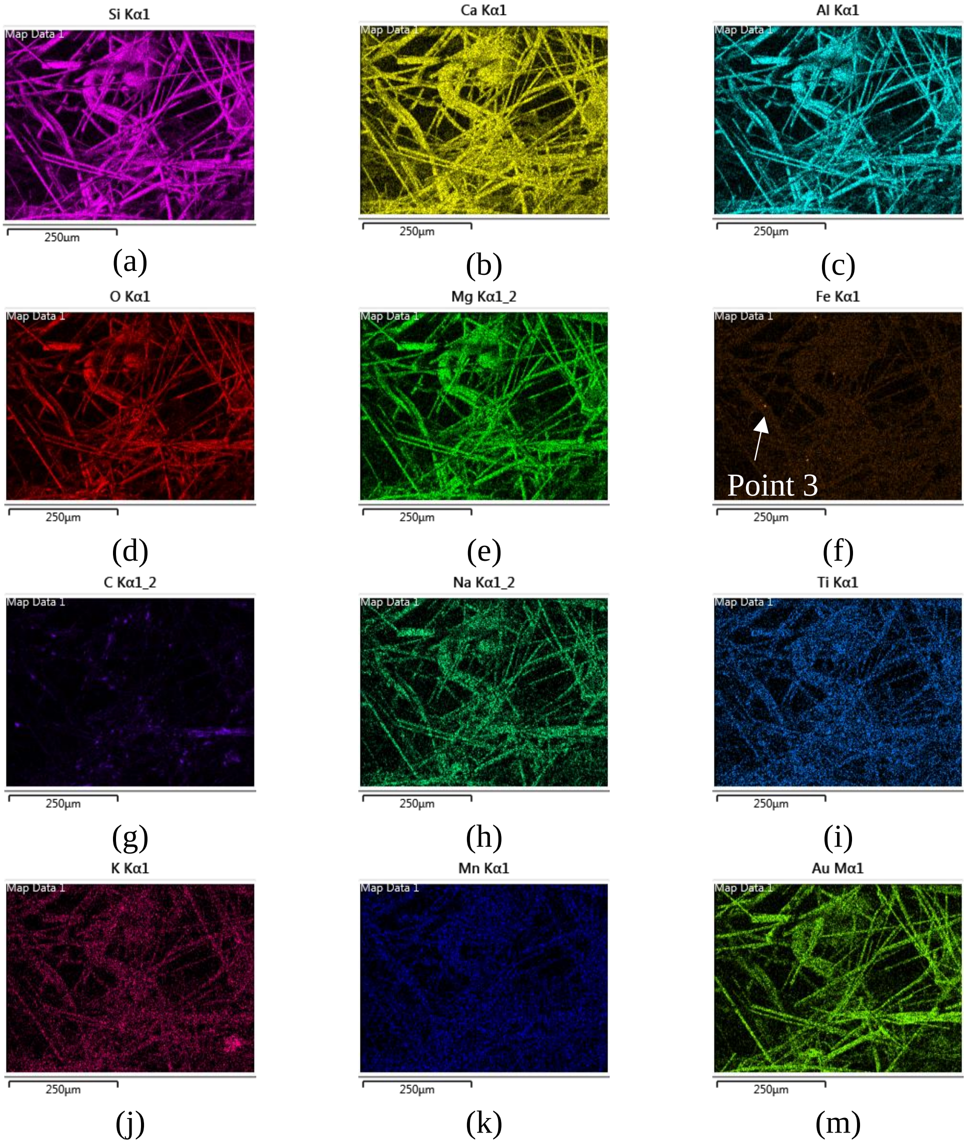

(a) (b) (c) (d) (e) (f) (g) (h) (i) (j) (k) (m)

Figure 6-2: EDX mapping for the thermal insulation showing the main elements, (a) silicon- Si, (b) calcium- Ca, (c) aluminium- Al, (d) oxygen- O, (e) magnesium- Mg, (f) iron- Fe, (g) carbon- C, (h) sodium- Na, (i) titanium- Ti, (j) potassium- K, (k) manganese- Mn, and (m) gold- Au

Figure 6-3 exhibits a point EDX analysis, accompanied by the corresponding elemental composition of the thermal insulation, presented in Table 6-1. The analysis discerns that oxygen, silicon, and calcium constitute the prevailing elements at points 1 and 2 (spectrum 1 and 2) of the insulation sample. Conversely, at point 3, a contrasting pattern emerges, with iron appearing as the dominant element. This observation suggests that this point contains a higher amount of iron compared to other points in the sample. In addition, carbon is also detected in the three scanned points, but its origin remains uncertain, possibly originating from contaminants present within the insulation material.

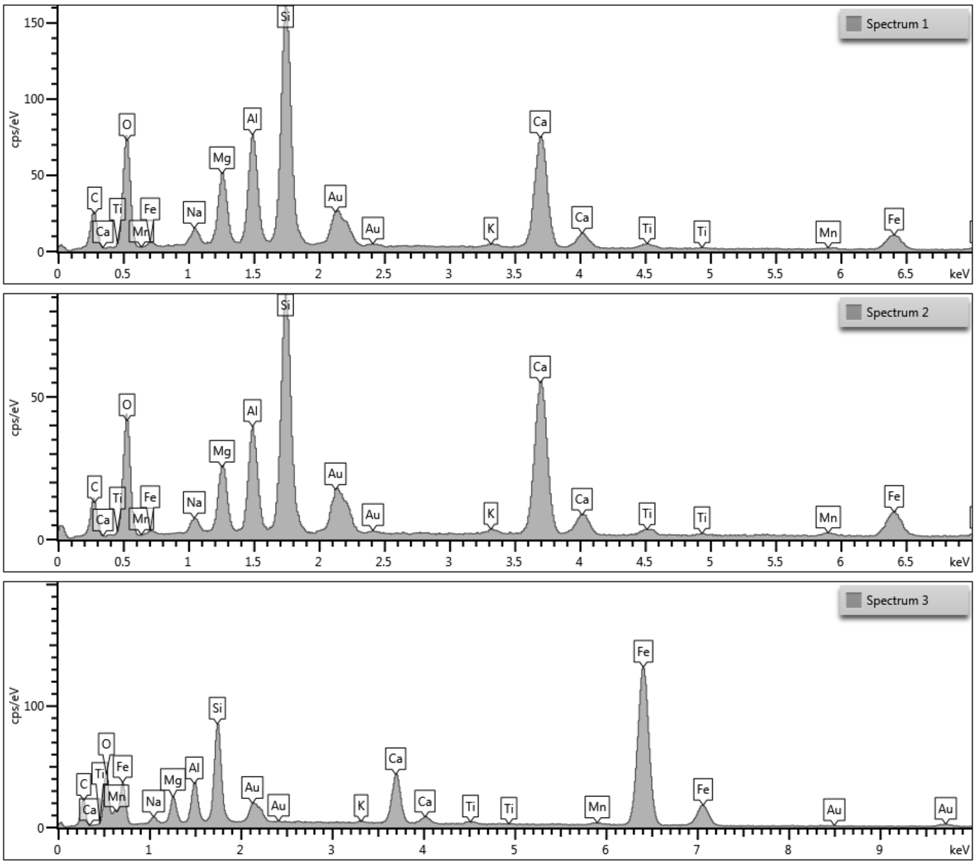

Figure 6-3: EDX spectra of the thermal insulation, points 1, 2 and 3 (spectrum 1, 2 and 3)

Table 6-1: Displays the weight percentage of elements identified in the thermal insulation using EDX as shown in Figure 6-1

Element	**Wt% (P1)**	**Wt% Sigma**	**Wt% (P2)**	**Wt% Sigma**	**Wt% (P3)**	**Wt% Sigma**
C	26.24	0.67	23.78	0.71	22.25	0.64
O	35.93	0.45	35.88	0.47	15.13	0.3
Na	1.33	0.06	1.19	0.07	0.98	0.07
Mg	4.15	0.08	3.79	0.08	2.6	0.07
Al	5.71	0.09	5.13	0.09	3.19	0.07
Si	12.1	0.15	10.99	0.14	6.8	0.09
K	0.25	0.03	0.29	0.03	0.14	0.03
Ca	9.83	0.13	12.3	0.16	4.84	0.08
Ti	0.56	0.04	0.76	0.05	0.32	0.04
Mn	0.28	0.05	0.56	0.07	0.4	0.06
Fe	3.61	0.09	5.34	0.13	43.34	0.41

The data from Table 6-1 can be used to estimate the weight percentage of oxides detected through EDX analysis by using equation 6-1. These estimations can then be compared with the standard chemical composition of the insulation, which is presented in Table 4-3.

$$Oxide\ percent = \frac{element\ percent}{converion\ number} \qquad 6\text{-}1$$

The conversion number can be calculated by using equation 6-2

$$Conversion\ number = \frac{molar\ mas\ of\ the\ element}{molar\ mass\ of\ the\ oxide} \qquad 6\text{-}2$$

For example, the conversion number of Al_2O_3 is 0.53 which is calculated by using equation 6-3. This particular example is based on data obtained specifically from point 1 of the analysis, focusing on the element aluminium (Al), as shown in Table 6-1.

$$Conversion\ number\ (Al_2O_3) = \frac{(2 \times 26.98)}{(2 \times 26.98) + (3 \times 16)} = 0.53 \qquad 6\text{-}3$$

By substituting the conversion number in equation 6-1, then the oxide percent can be calculated as shown in equation 6-4.

$$Oxide\ percent = \frac{5.71}{0.529} = 10.80 \qquad 6\text{-}4$$

Table 6-2: A comparison of the calculated and standard weight percentages of oxides in thermal insulation in points P1, P2 and P3,

Oxide	**Wt% Calculated (P1)**	**Wt% Calculated (P2)**	**Wt% Calculated (P3)**	**Wt% Standard**
Al_2O_3	10.8	9.7	6.0	8-15
CaO	13.8	17.2	6.8	30-35
Fe_2O_3	5.2	7.6	62.0	2.5 max
K_2O	0.3	0.3	0.2	0-1
MgO	6.9	6.3	4.3	6-12
Na_2O	1.8	1.6	1.3	0-1
SiO_2	25.9	23.5	14.5	30-45
TiO_2	0.9	1.3	0.5	2-4

Table 6-2 exhibits the weight percentages of various oxides detected in thermal insulation through EDX analysis at points 1, 2, and 3, along with their corresponding standard weight percentage ranges. Upon examination of the data, it is observed that certain oxides, like Al_2O_3, fall within the specified standard weight percentage range at points 1 and 2. This suggests that the concentration of Al_2O_3 in these regions of the thermal insulation is consistent and falls within the expected levels based on the standard range. However, contrasting results are found for other oxides, such as SiO_2, which weight percentage values are outside the specified standard range. Comparison of the actual chemical composition with standards of the mineral wool thermal insulation may not be conclusive based on the EDX point scan.

6.1.2 Leaching ions

Leaching of ions from thermal insulation materials can lead to the accumulation of corrosive species in the moisture beneath the insulation. The presence of corrosive agents can accelerate the CUI process and lead to equipment failure. The extent and rate of ion leaching can depend on various factors such as insulation material, environmental conditions, and exposure to chemicals and pollutants.

The study of ion leaching from insulation materials in the context of CUI is critical for developing effective corrosion prevention and mitigation strategies. This includes understanding the mechanisms and factors that contribute to ion leaching and how they interact with the corrosive agents present in the moisture. The development of new insulation materials with improved resistance to ion leaching can also help in the prevention of CUI.

Table 6-3 provides a quantitative analysis of the ion concentrations in both distilled water and leached ions from the thermal insulation at room and boiling temperatures. There are no significant differences in concentrations of leached ions between mineral wool thermal insulation and distilled water based on the results of the study. For instance, the concentration of leached chloride (Cl^-) ions from the insulation material was found to be 3.74 ppm and 3.84 ppm at room and boiling temperatures, respectively. This represents an increase of 1.6 ppm and 1.7 ppm, respectively, compared to the concentration of chloride ions in distilled water. Even so, the change in ion concentrations suggests that these ions are released by the insulation material.

Furthermore, the leached water contains detectable levels of phosphate and silica ions, which are likely to have originated from the insulation material. However, no detectable amounts of nitrite or sulphate ions were detected in either the distilled or leached water. The concentration of silica ions in the leached water at boiling temperature was higher than that measured at room temperature. This observation suggests that higher temperatures may lead to more significant leaching of silica ions from the insulation material.

Table 6-3: Chemical analysis of leached ions according to ASTM C871

Solution Ions	Distilled water/ ppm	Leached water at room temperature /ppm	Leached water at boiling temperature /ppm
Chloride (Cl^-)	2.127	3.74	3.843
Bromide (Br^-)	3.683	4.1	4.21
Fluoride (F^-)	-	0.91	1.293
Phosphate(PO_4^{3-})	-	0.08	0.117
Nitrite(NO^{2-})	-	-	0.617
Sulphate (SO_4^{2-})	-	-	-
Silica ($SiO_{4-x}^{4-2x})_n$	-	0.00164	0.02255
Sodium($Na+$)	0.00525	0.0117	0.0118

Overall, the concentrations of leached ions from the insulation material are found to be within the acceptable levels specified by CUI standards. However, it is important to note that even though the levels of leached ions may be within acceptable limits, their presence may accelerate CUI by increasing the brine conductivity.

6.2 Characterisation of CUI at pH 7

The evaluation of CUI for top and bottom samples at room temperature, 80 °C and 150 °C was performed by using three microelectrodes cells as described in section 5.1.1, in conjunction with the LPR technique. Furthermore, to establish a corrosion rate comparison with LPR results, the mass loss method was employed. The SEM technique was used to gain insights into the morphological structure of the corrosion layers formed on the top and bottom samples. The EDX, Raman and XRD were utilized to characterize the elemental distribution and the corrosion products formed on the steel surface.

6.2.1 Evaluation of CUI at pH 7 and room temperature

In this section, the CUI phenomena will be evaluated at room temperature, an extended exposure duration of 168 hours, and the application of a 3.5% NaCl brine solution, pH 7 with an injection rate of 40 ml/hour.

6.2.1.1 Visual observation

The macroscopic photos depicted in Figure 6-4 were captured at the end of the experiment carried out under room temperature conditions. Upon visual examination, it became evident that the insulation fibres had adhered to the steel surface for top and bottom samples following 7 days of exposure, signifying a degradation of the insulation throughout the experiment which was reported by Cao, et al. [179]. The presence of diverse colours, such as black and reddish brown, within the corrosion film suggests the development of various iron oxide compounds due to the corrosion process. Additionally, a discrepancy in the extent of corrosion coverage on the surfaces of the top and bottom samples was observed. It is important to highlight that, contrary to the guidelines stipulated in ASTM 189 standard, the injection point of the brine solution in this particular test was not directly on the steel surface. Instead, it was strategically positioned outside of the insulation and immediately beneath the cladding. This deliberate placement of the injection point was chosen to emulate real-world conditions, mirroring scenarios encountered in practical field environments. This positioning replicates the journey that water or moisture would undertake, traversing through the insulation layer to ultimately interact with the sample. This approach is designed to facilitate the potential leaching of ions from the insulation material, thus enhancing the test's representativeness. Hence, this variation in the corrosion surface coverage observed between the top and bottom samples, and even within the top and bottom samples themselves, could be attributed to this intentional selection of the brine solution injection point.

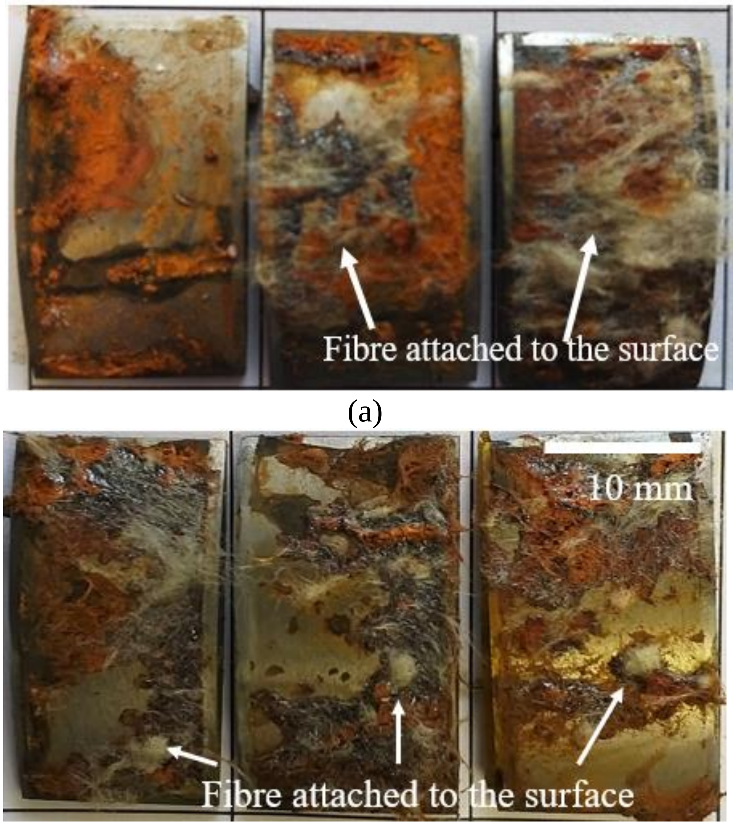

(a)

(b)

Figure 6-4: Photos of the corrosion coupons after 168 hours of exposure at room temperature(a) top samples, (b) bottom samples

The corrosion film surface coverage observed for this insulation material is consistent with results reported in a separate study by [92]. It is reported that the corrosion layer coverage under a mineral wool insulation is partial where it is less than 45% of the sample surface. Comparatively, PIR insulation exhibits extensive corrosion coverage, which encompasses the entire surface area.

6.2.1.2 Evaluating CUI mass loss and LPR

Table 6-4 shows the average corrosion rates measured by mass loss in mm/year for top and bottom samples that were exposed to a 3.5% NaCl environment with an initial pH of 7, at room temperature and for 7 days. The data reveals that the average corrosion rate for the top samples was 2.096 mm/year, which is almost twofold higher than the average corrosion rate of 1.064 mm/year for the bottom samples. The observed trend of higher corrosion rates at the top compared to the bottom is consistent with the explanation provided by Aspen Aerogels [180]. According to their analysis, the higher moisture content at the top of the insulated surface can be attributed to its proximity to the moisture source, resulting in a more humid environment.

Table 6-4: Corrosion rate calculated by mass loss at room temperature, pH 7 and 7 days of exposure for top and bottom samples

Sample position	**Initial mass (g)**	**Final mass (g)**	**Corrosion rate (CR) (mm/year)**	**Avg. CR (mm/year)**
Top	7.809	7.689	2.307	2.096
	8.820	8.731	2.711	
	8.019	7.901	2.268	
Bottom	8.642	8.579	1.212	1.064
	8.476	8.419	1.096	
	8.913	8.867	0.885	

Figure 6-5 presents the variation of corrosion rate at the top and bottom positions under the thermal insulation, as measured by LPR, in a 3.5% NaCl solution with an initial pH of 7 and at room temperature. The trend of corrosion rate over time was observed to vary between the top and bottom samples. In the initial 20-hour period of exposure to the corrosive environment, the top sample demonstrated a reduction in corrosion rate by 0.33 mm/year. However, subsequently, the corrosion rate gradually increased to 1.95 mm/year after 90 hours of exposure and remained relatively constant thereafter. In contrast, the corrosion rate of the bottom sample remained stable at slightly below 1 mm/year for the first 50 hours of exposure. Subsequently, the corrosion rate showed a gradual decrease and reached 0.58 mm/year at the end of the experiment. Similar studies are limited in the existing literature, which makes it challenging to compare the obtained results with those reported by others.

The corrosion rate determined by mass loss was generally higher than that obtained by LPR, as shown in Figure 6-6. However, the top samples exhibited a higher corrosion rate compared to the other samples, irrespective of the measurement technique used. This finding suggests that the top samples were exposed to a more aggressive environment, and this trend was consistently observed across both methods.

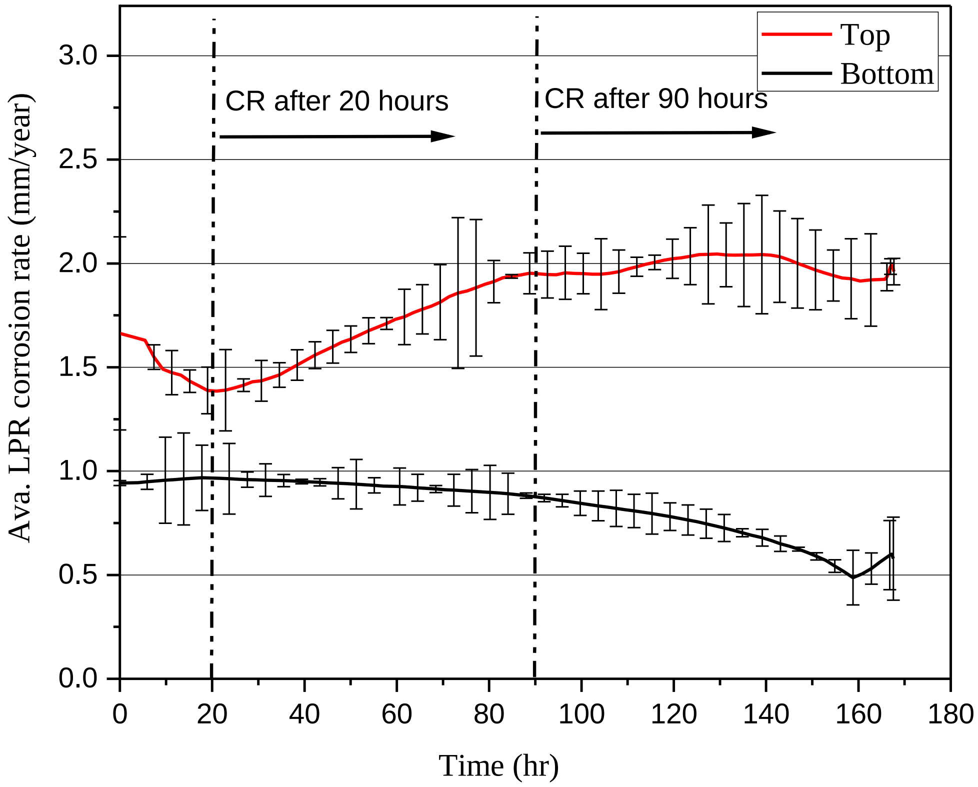

Figure 6-5: Corrosion rate variation of ASTM A 106 Gr B exposed to 3.5% NaCl brine at room temperature, initial pH 7 and for 168 hours for top and bottom microelectrodes, the Stearn-Geary coefficient is 26 mV/decade

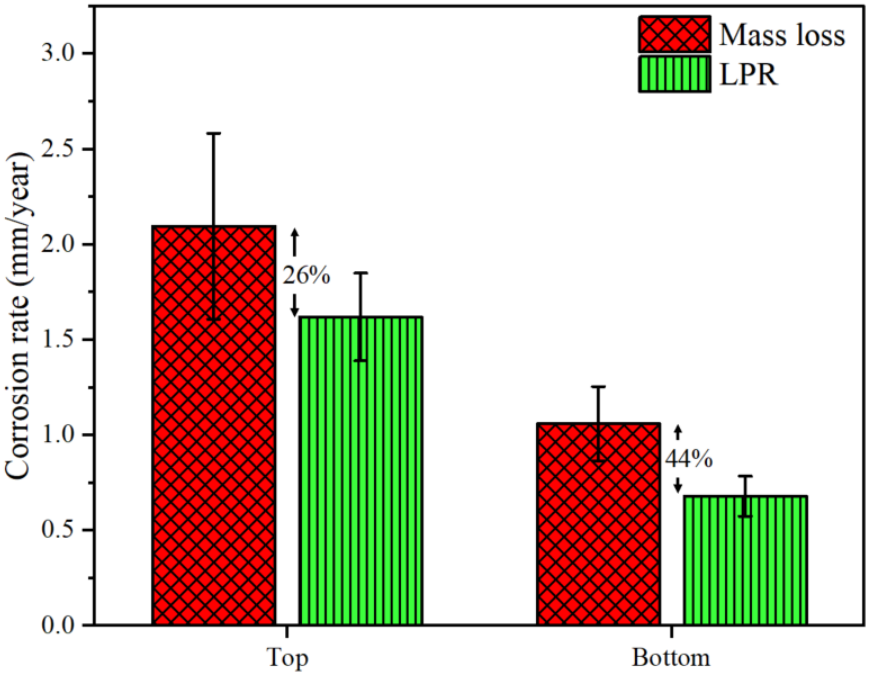

Figure 6-6: The average corrosion rate by mass loss and LPR for top and bottom samples exposed to 3.5 NaCl, initial pH 7 and at room temperature after 168 hours

6.2.1.3 Cross-sections and topography view of micrographs for CUI tests for the bottom and top samples

Figure 6-7 (a-d) depicts the SEM cross-sectional micrographs of ASTM A 106 Gr B top and bottom samples after being exposed to isothermal wet conditions for 7 days under thermal insulation. The red boxes in (a) and (c) indicate the designated regions for magnification, as depicted in micrographs (b) and (d). The micrographs reveal the existence of a continuous and irregular corrosion layer that covers the carbon steel surface.

For the top sample, the thickness of the corrosion layer varies significantly, ranging from 45 to 337 μm, as shown in Figure 6-8 (a). The non-uniform appearance of the corrosion layer indicates that the corrosion process was likely uneven or accelerated in certain areas. This variation in corrosion rate could be attributed to local fluctuations in the chemical environment, such as oxygen concentration, or the presence of corrosive agents. Owing to the inherent structure and hydrophobic nature of thermal insulation materials, the availability of water on the metal surface is expected to be non-uniform. In Figure 6-7 (b), distinct features of the corrosion layer formed on the top sample are evident, including a flowery structure, cotton ball-like formations, and interconnected nest structures. The presence of a flowery structure is typically associated with lepidocrocite. The cotton ball appearance is characteristic of semicrystalline goethite, which seems to interconnect with the nest formations [126]. Furthermore, there is a presence of cracks within the corrosion layer, this might be due to excessive corrosion film thickness.

However, Figure 6-7 (c-d) displays cross-sectional SEM micrographs of the bottom sample captured at different scale bar, 100 and 10 µm respectively. The analysis reveals that the thickness of the corrosion film varies, ranging from 67 to 195 µm, as depicted in the histogram graph in Figure 6-8 (b).

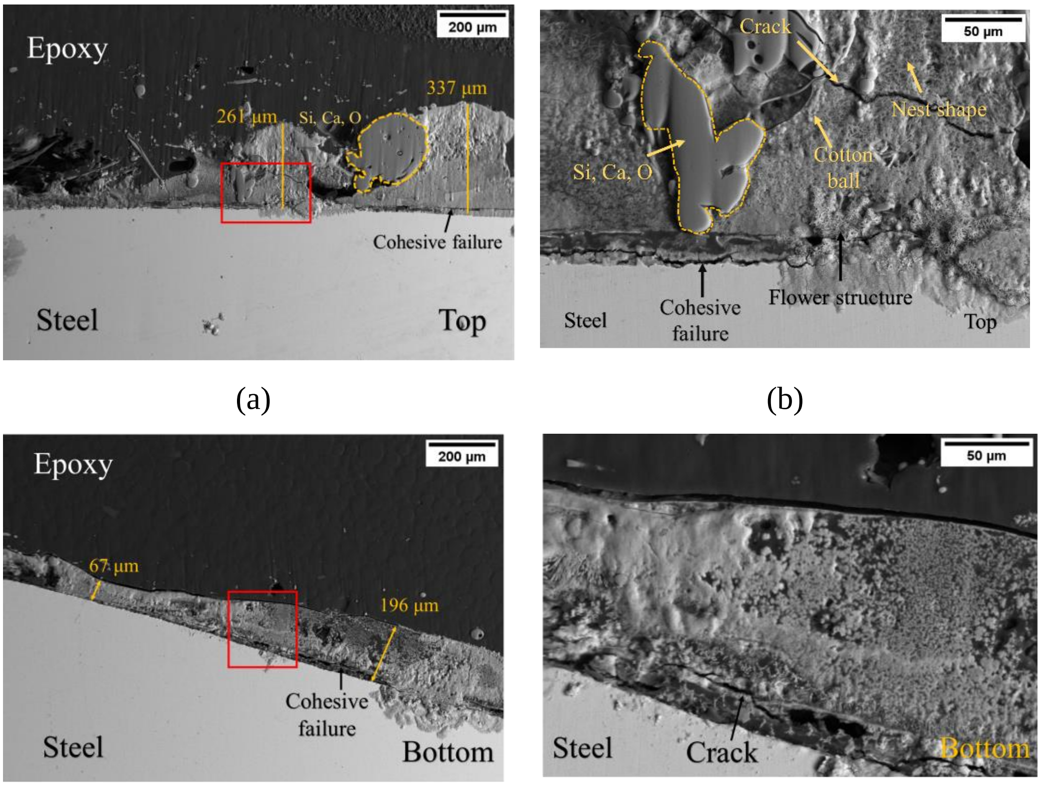

(a) (b)

(c) (d)

Figure 6-7: Cross-section SEM micrographs of the corrosion layer for the ASTM A 106 Gr B samples exposed to 3.5% NaCl, initial pH 7 at room temperature, (a and b) top sample, (c and d) bottom sample

In contrast to the top sample, the corrosion film in the bottom sample exhibits a more uniform appearance. Compared to the SEM micrographs of the top sample, the corrosion layer developed on the bottom sample surface exhibits an indistinctive appearance, and the characteristic morphology of expected iron oxyhydroxide is not discernible. Furthermore, the corrosion layer on the top and bottom samples displayed a cohesive failure pattern. This cohesive failure was observed both between the corrosion layer and the underlying metal surface and within the corrosion layer itself. The cohesive failure might be attributed to factors such as an excessive thickness of the corrosion layer or the presence of internal stress within the film.

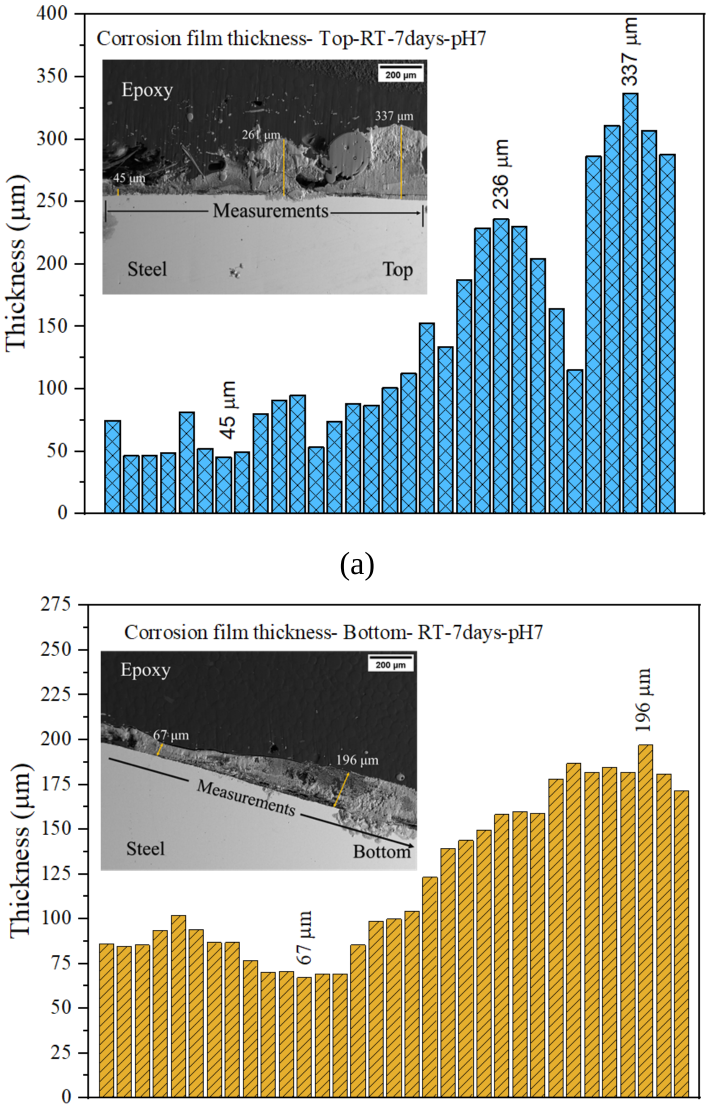

(a)

(b)

Figure 6-8: A histogram shows the thickness distribution of a corrosion film form on the sample (a) top and (b) the bottom after 168 hours of exposure to room temperature, pH 7 brine

Figure 6-9 displays the SEM micrographs topography view of the corrosion film formed on both the top and bottom samples after 7 days of exposure at room temperature and pH 7. The red boxes in micrographs (a) and (c) represent the designated area for further magnification as depicted in (b) and (d). The surface morphology of the corrosion products on the top and bottom samples exhibits notable differences. For the top sample, Figure 6-9 (a-b) reveals the presence of sandy structure on the surface as well as insulation fibres. In addition, the SEM micrographs showed a loose and sandy structure. Conversely, the SEM images of the bottom sample, illustrated in Figure 6-9 (c-d), reveal a more complex and non-homogeneous corrosion film. The presence of at least four distinct areas, labelled as (1, 2, 3, and 4). The corrosion layer is characterized by a cohesive appearance, exhibiting an absence of structural looseness. In addition, there is an absence of discernible cracks within the observed corrosion layer. Furthermore, some sections

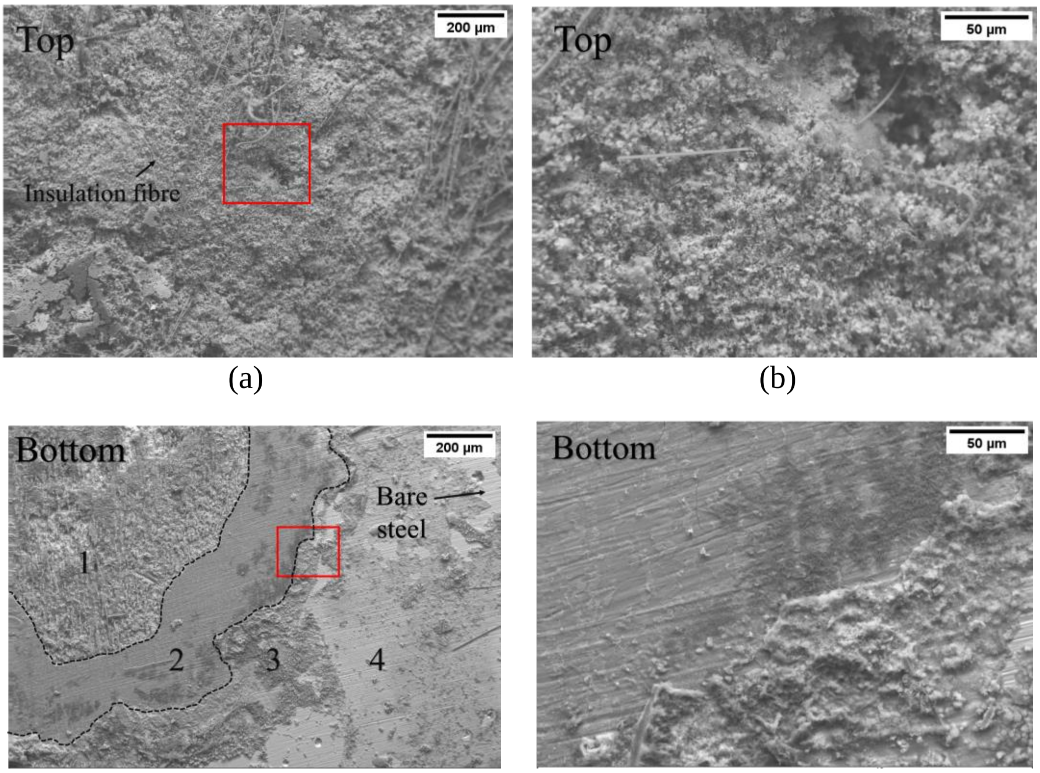

(a) (b)

(c) (d)

Figure 6-9: SEM micrographs topography view of the corrosion layer for the surface of the ASTM A 106 Gr B coupons being exposed to 3.5% NaCl, initial pH 7 at room temperature: (a-b) top sample, (c-d) bottom sample appear to be unaffected by corrosion, indicating localized variations in the corrosion process within the bottom sample.

The following section involved a chemical analysis of the corrosion products by using the EDX analysis technique. The main focus of this analysis was to elucidate the distribution of elements within the oxide formations that have evolved on the surface due to the corrosion process. This analysis encompassed both the cross-sectional examination and the topographical assessment of both the top and bottom samples.

6.2.1.4 EDX analysis

The EDX analysis was performed on the cross-section and on the surface of the top and bottom samples. The resultant findings are highlighted in the form of elemental distribution mapping.

Cross-sectional EDX analysis

EDX analysis for cross-section was performed on both the top and bottom samples. Figure 6-10 presents the EDX map illustrating the elemental distribution on the surface of the steel top sample subjected to 3.5% NaCl brine for 168 hours, resulting in the formation of an iron oxide layer. The EDX map identifies the presence of iron (Fe) and oxygen (O), which are the primary constituents expected in the iron oxide layer under the CUI oxidation conditions. Furthermore, there are localized depositions of chloride (Cl^{-}) on the steel surface. The Cl^{-} are primarily concentrated in regions where the corrosion film thickness is relatively thin or disrupted by segments containing silicon and calcium. However, the EDX map provides additional insight by revealing distinct localized areas rich in calcium (Ca) and silicon (Si) within the grown corrosion layer. The undeniable origin of these elements lies within the insulation material, as no alternative source exists apart from the insulation fibres themselves. The observed presence of calcium and silicon can be attributed to their gradual leaching from the thermal insulation material during the experiment, subsequently traversing their way to the steel surface. Over time, these elements become seamlessly integrated into the evolving iron oxide layer as an intrinsic outcome of the oxidation process.

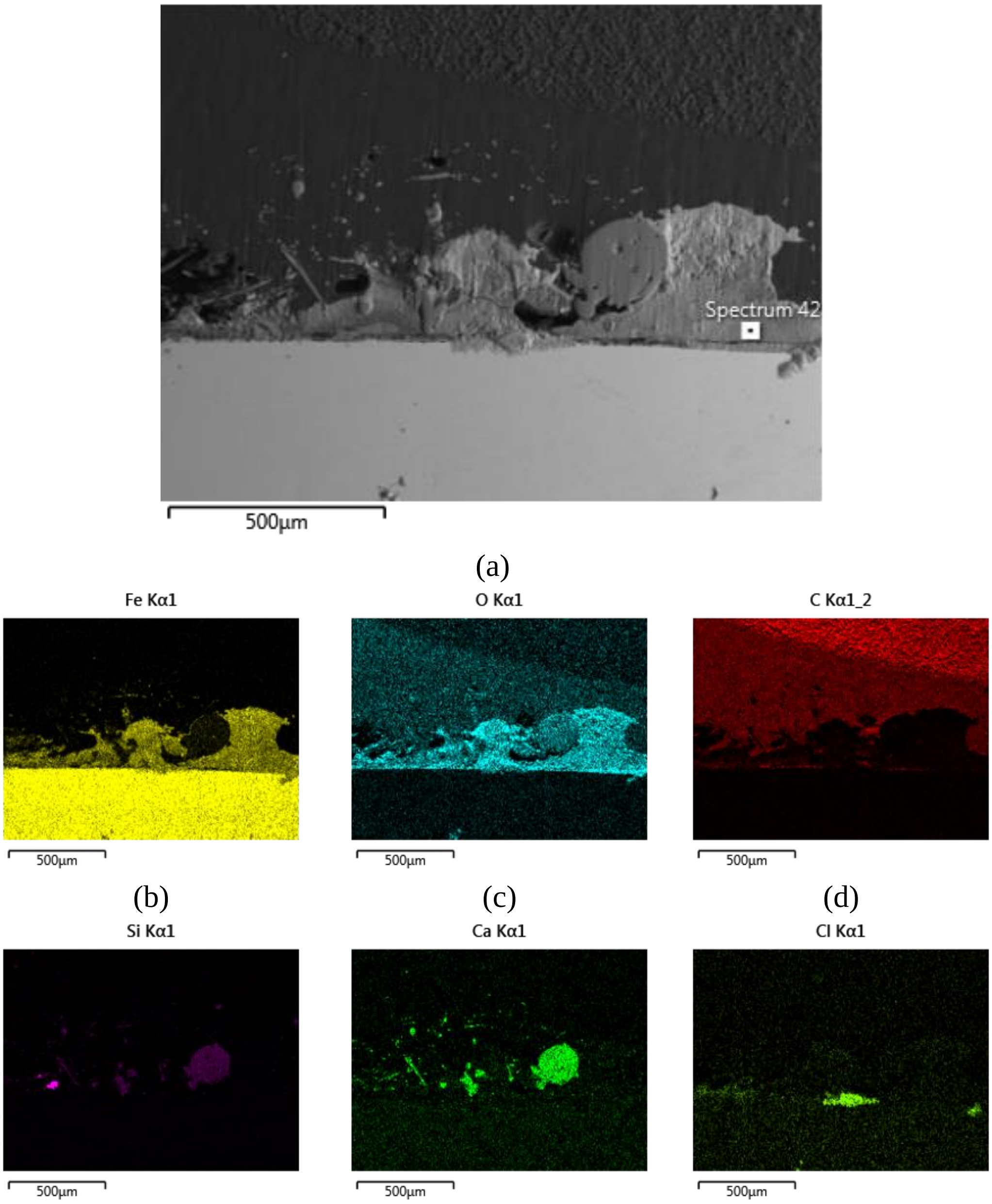

(a)

(b) (c) (d)

(e) (f) (g)

Figure 6-10: EDX map analysis of a cross-section of the corrosion layer formed on the top sample after exposure to 3.5 NaCl, pH 7 and for 168 hours, (a) the micrograph of the scanned area, (b) iron-Fe, (c) oxygen-O, (d) carbon-C, (e) silicon-Si, (f) calcium-Ca and (g) chloride-Cl

In Figure 6-11, an EDX map depicts the distribution of elements on the surface of the steel bottom sample subjected to oxidation and the formation of iron oxide. It is evident from the map that iron (Fe) and oxygen (O) are the primary constituents of iron oxide under such oxidation conditions. Additionally, the EDX map reveals the presence of silicon (Si) distributed as a thin layer both inside and outside the corrosion layer. The simultaneous presence of silicon (Si) and oxygen (O) strongly suggests the formation of silicon dioxide (SiO_2), which is a primary constituent of mineral wool thermal insulation.

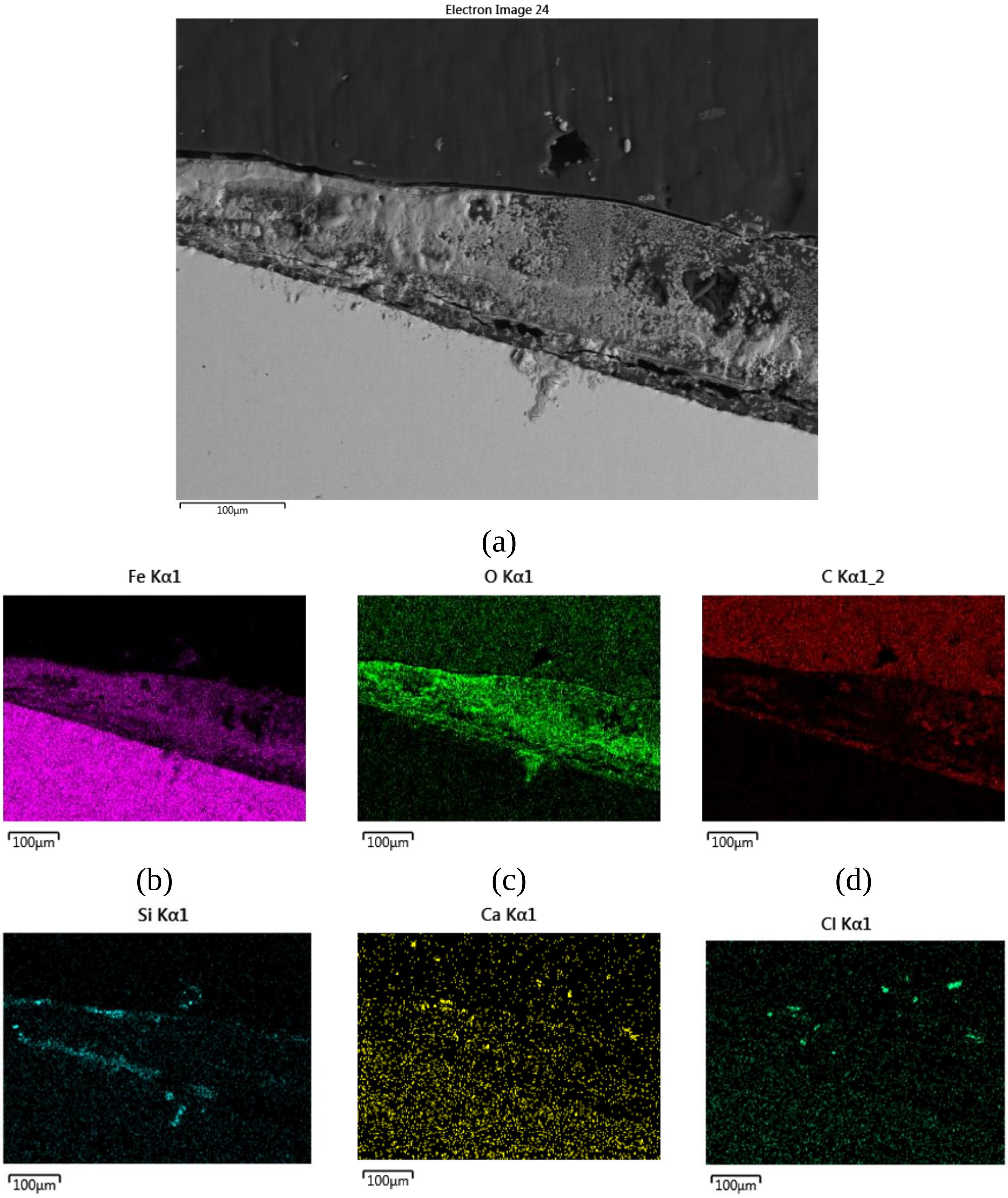

(a)

(b) (c) (d)

(e) (f) (g)

Figure 6-11: EDX reconstructed map of corrosion layer grown on bottom samples at room temperature, initial pH 7 after 168 hours of exposure, (a) SEM micrograph, (b) iron-Fe, (c) oxygen-O, (d) carbon-C, (e) silicon-Si, (f) calcium-Ca and (g) chloride-Cl

The inclusion of silicon in the corrosion film indicates that it has been incorporated into the film during the corrosion process, potentially originating from the surrounding environment or adjacent materials. Furthermore, carbon was identified close to the steel surface and also found to be dispersed within the formed corrosion layer. The carbon's origin might stem from potential sources such as contaminants or coatings applied to the material.

The EDX map reveals that the amount of chloride ions Cl^-in the corrosion film of the bottom sample is small. This observation suggests that the bottom sample experienced minimal incorporation of chloride ions during the corrosion process. The positioning of the bottom sample in relation to the injection point during the experiment might be a contributing factor to this finding.

EDX elemental mapping on the surface of the corrosion layers

The EDX analysis performed on the top and bottom samples under room temperature and pH 7 conditions revealed the simultaneous presence of iron, oxygen, chloride, sodium, silicon, and calcium. This occurrence is visually depicted in both Figure 6-12 and Figure 6-13 for top and bottom samples respectively. Iron and oxygen emerged as the prevailing constituents in both the top and bottom samples, aligning with anticipated outcomes in this experimental context.

Both chloride and sodium were identified in both the top and bottom samples. However, a disparity was observed in the distribution of chloride on the two surfaces. The bottom sample exhibited a chloride presence that aggregated in clusters, in contrast to the top sample where chloride was dispersed across the developed corrosion layer.

The origin of silicon and calcium detected on the corrosion layer can be attributed to fibres attached to the surface of the top sample. This connection is evident due to their coexistence with insulating fibres.

.

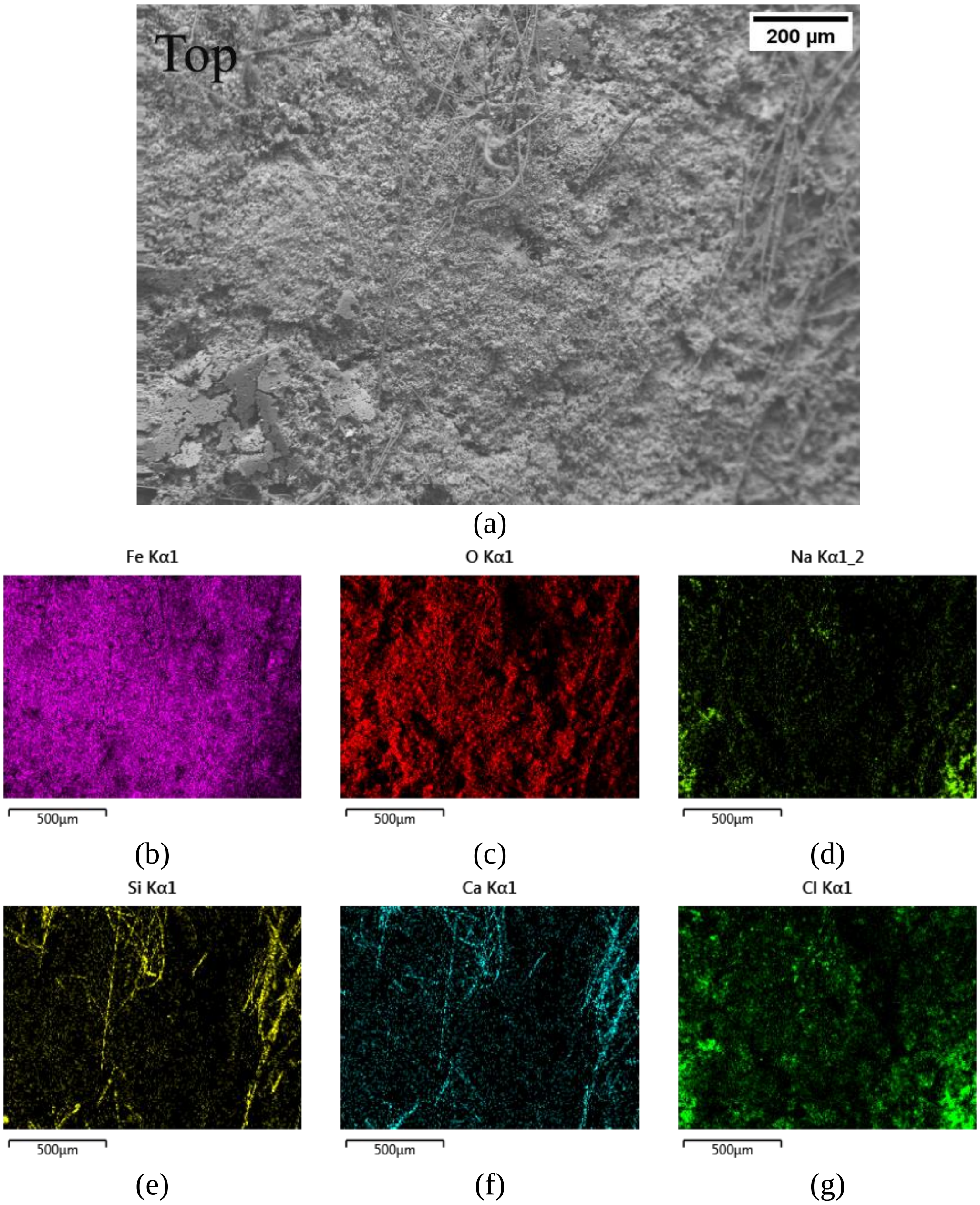

(a)

(b) (c) (d)

(e) (f) (g)

Figure 6-12-EDX elemental mapping analysis on the surface of the corrosion film grown on the top sample after 168 hours of exposure at room temperature and pH 7, (a) SEM micrograph, (b) iron-Fe, (c) oxygen-O, (d) sodium-Na, (e) silicon-Si, (f) calcium-Ca and (g) chloride-Cl

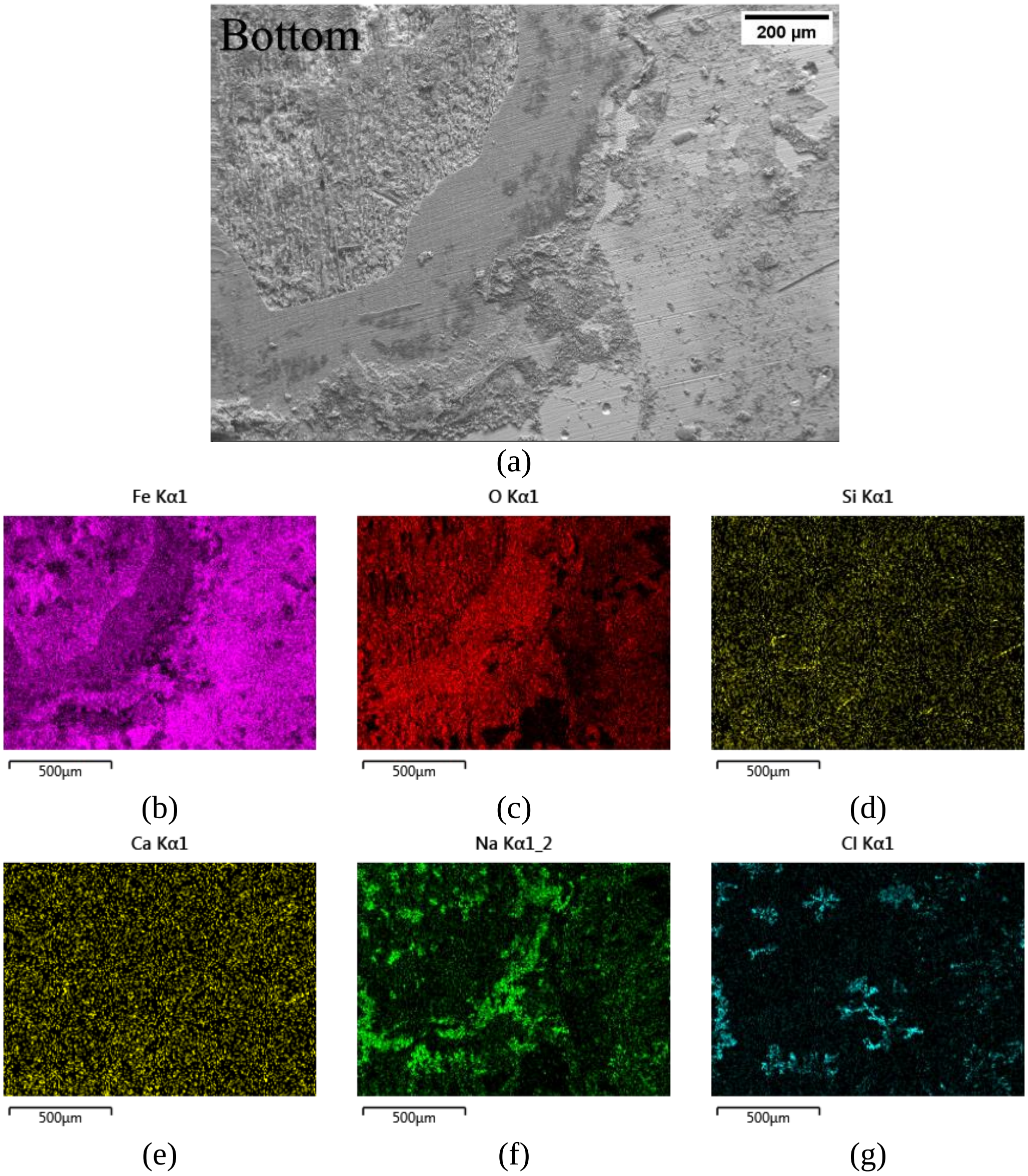

(a)

(b) (c) (d)

(e) (f) (g)

Figure 6-13: EDX elemental mapping analysis on the surface of the corrosion film grown on the bottom sample after 168 hours of exposure at room temperature and pH 7, (a) SEM micrograph, (b) iron-Fe, (c) oxygen-O, (d) silico-Si, (e) calcium-Ca, (f) sodium-Na and (g) chloride-Cl

In summary, the cross-sectional EDX analysis demonstrated that chloride distribution was adjacent to the steel surface in the top sample, while this proximity was not observed in the bottom sample. The surface-level EDX assessment indicated uniform chloride distribution for the top sample, while the bottom sample displayed a clustered distribution. The primary source of silicon and calcium was identified as the insulation fibres. Additionally, both iron and oxygen were detected in both the top and bottom samples as the main constituents.

6.2.1.5 Characterizing the corrosion lay by Raman spectroscopy

Raman spectra were collected from both the top and bottom of the corroded steel samples using a Renishaw Raman spectrometer. The samples were carefully handled and stored in plastic bags after being removed from the rig. In the case of steel exposed to such conditions, Raman spectra for the corrosion products typically fall within the range of 100 to 800 cm^{-1}. Figure 6-14 illustrates the Raman spectra obtained from both the top (a) and bottom (b) samples exposed to a corrosive environment containing 3.5% NaCl, an initial pH of 7, and at room temperature. The x-axis represents the Raman shift in $cm^{-1,}$ while the y-axis is the intensity in arbitrary unit (a.u).

From Figure 6-14 (a), the main constituent of the corrosion film formed on the top sample appears to be akageneite, as indicated by the strongest peaks observed at 331 cm^{-1}. In contrast, the Raman spectra indicate the predominant presence of lepidocrocite on the surface of the bottom sample, as evidenced by the strongest peak observed at 252 cm^{-1} as depicted in Figure 6-14 (b) [121, 181, 182].

In Figure 6-14 (a), the Raman spectra for the corrosion film formed on the top sample exhibit peaks corresponding to akageneite at 331, 389, 494, and 725 cm^{-1}. Lepidocrocite peaks are observed at 219 and 522 cm^{-1}, while Goethite peaks are detected at 299 and 331 (overlap with akageneite), and 546 cm^{-1} [181, 183-185].

However, the Raman spectra for the corrosion film formed on the bottom sample indicate the presence of akageneite, with distinct peaks observed at 307, 334, and 724 cm^{-1}. Lepidocrocite peaks are observed at 218, 252, 378, 527 and 647 cm^{-1}, while goethite peaks are detected at 307 and 348 cm^{-1}. The weak intensity of the observed goethite peaks suggests that the concentration of goethite in the scanned area is relatively low.

Magnetite was not detectable in both the top and bottom regions of the scanned area. However, this lack of detection does not necessarily imply that magnetite was not formed on the surface. Magnetite can still form in environments with low oxygen levels, especially close to the steel surface.

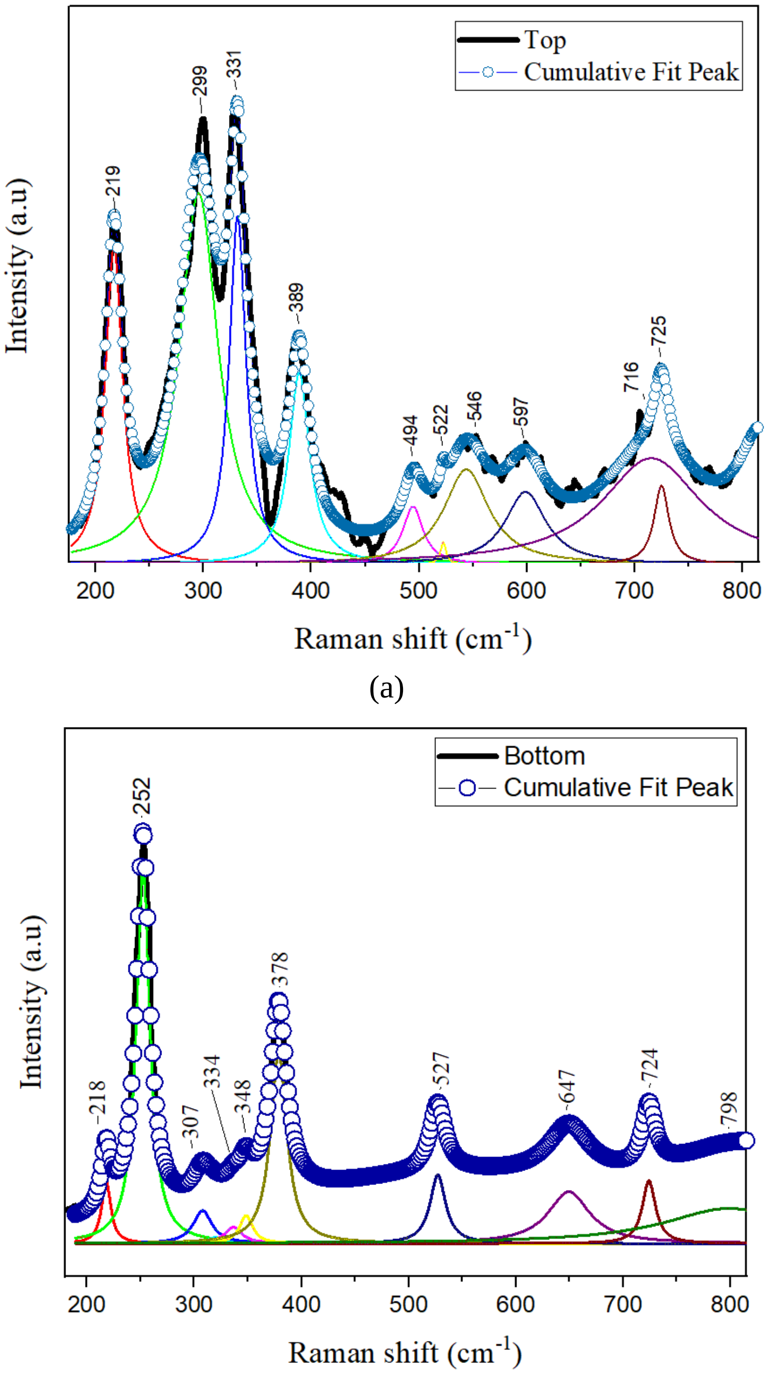

(a)

(b)

Figure 6-14: Raman spectra for (a) top and (b) bottom samples exposed to 3.5% NaCl, initial pH7 and at room temperature for 168 hours

6.2.1.6 XRD diffraction pattern for test ran at room temperature

Figure 6-15 displays the XRD pattern of both the top and bottom samples exposed to a 3.5% NaCl solution at room temperature and pH 7. The XRD peaks obtained from the analysis of both samples verify the presence of iron oxyhydroxides. The identified iron oxyhydroxides are characterized as akageneite, goethite, and lepidocrocite, indicating their prevalence in both the top and bottom samples. Remarkably, the XRD analysis did not detect any magnetite peaks in either of the samples. This observation suggests the absence of magnetite within the examined regions of the materials under the specified environmental conditions. In a separate experimental setup involving thermal insulation and a duration of 7 days at an elevated temperature of 80°C, magnetite was identified through XRD analysis [50]. In contrast, during experimentation at a lower temperature of 30°C, only a minimal quantity of magnetite was observed [186]. Furthermore, the average XRD penetration depth is constrained to approximately 20 µm [187]. This limitation curtails its capability to thoroughly scan the surface, potentially resulting in an inability to detect magnetite growing in the vicinity of the steel surface.

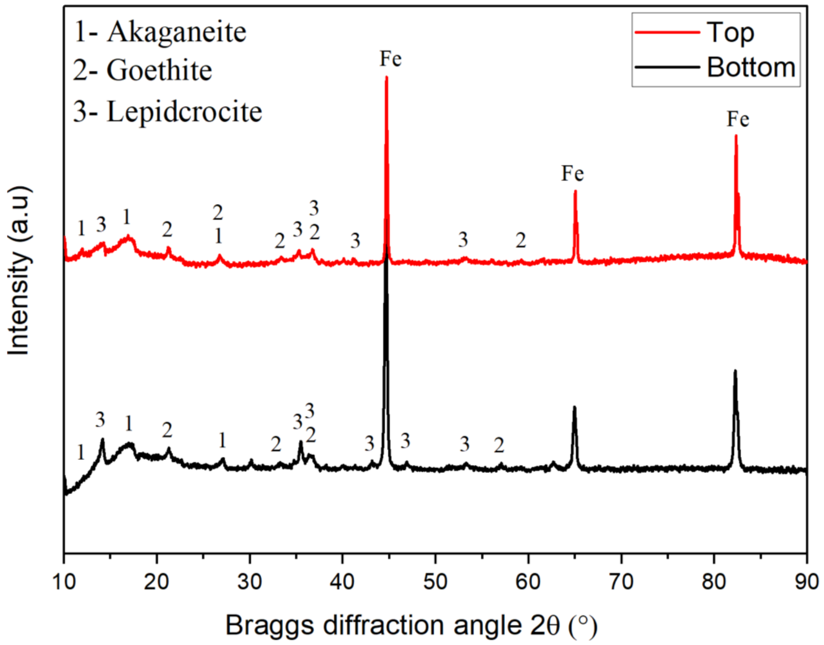

Figure 6-15: XRD pattern for corrosion products formed on the top and the bottom samples after exposure to a 3.5% NaCl solution for 7 days at room temperature

The XRD technique was employed to assess the relative proportion of different corrosion products formed on the carbon steel sample, utilizing a semi-quantitative approach. The analysis was performed using the X'Pert HighScore Plus software, employing the Retriveld fitting method. The results are visually presented in the form of a bar graph, depicted in Figure 6-16. From the bar graph, it can be observed that the relative content of iron oxyhydroxides appears to be comparable in the top sample. However, in contrast, lepidocrocite is predominant in the bottom sample. The relative abundance of goethite (α-FeOOH) seems to be consistent for both the top and bottom samples.

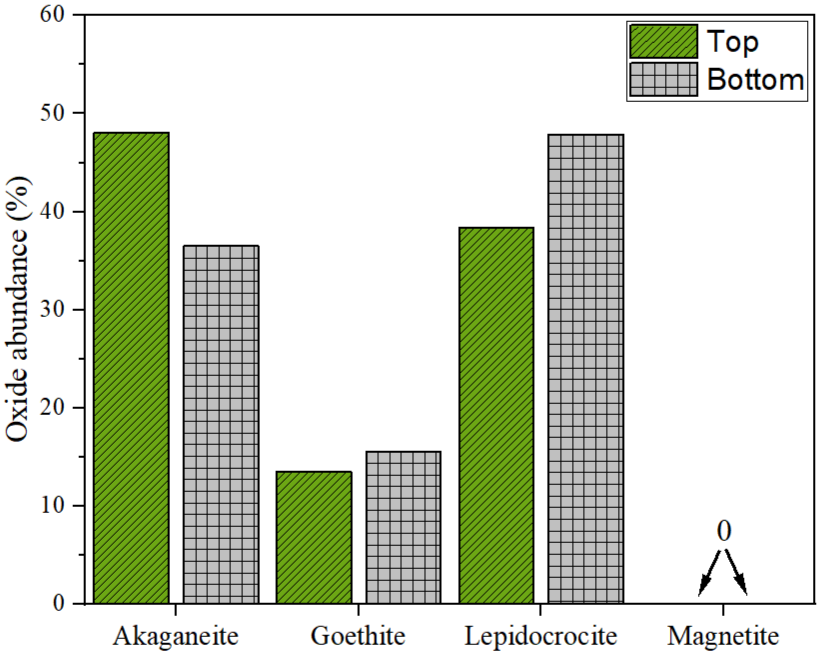

Figure 6-16: Relative content of corrosion products formed on top and bottom samples, quantified using XRD results from Figure 6-15

The bottom sample exhibits a higher proportion of lepidocrocite (γ-FeOOH) compared to the top sample, while akageneite (β-FeOOH) appears to be more prevalent in the top sample. The observed differences in akageneite content may be attributed to potential variations in chloride deposition on the sample surfaces, potentially influenced by their respective locations (top sample) relative to the injection point [117].

6.2.2 Evaluation of CUI at pH 7 and 80°C

6.2.2.1 Visual inspection

The surface morphology of the corrosion layer formed on steel coupons exposed to 3.5% NaCl at 80°C for 168 hours was captured using a mobile phone camera at a macro level. Figure 6-17 shows the top and bottom samples, labelled as (a) and (b) respectively. By visual observation, it was noted that the corrosion layer coverage has not achieved its full extent for either the top or bottom samples. In addition, the insulation fibres were attached to the surfaces of both samples. Furthermore, a compelling aspect to consider is the heterogeneity observed within the corrosion layers. The emergence of distinct colour variations implies the formation of diverse iron oxide compounds on the surface of the samples. The corrosion layers manifest red-brown hues on their external surfaces, while the lower layers exhibit a black colour. Compared to the red-brown layer, the black layer appears to be more attached to the surface.

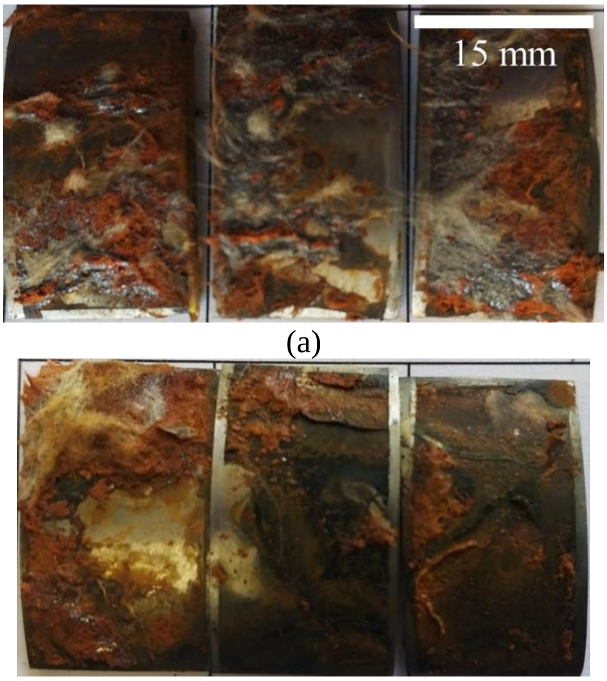

(a)

(b)

Figure 6-17: Digital photos of corrosion products developed on coupon surfaces after being exposed to 3.5% NaCl, pH 7 at 80°C for 168 hours. (a) the top sand (b) the bottom samples

In the following section, the corrosion rate is computed using the LPR technique, followed by a comparative assessment of these results with corrosion rates determined through mass loss measurement.

6.2.2.2 Evaluation of CUI rate by LPR and mass loss

In Figure 6-18, the corrosion rate data determined by LPR for both the bottom and top samples are presented. The corrosion rate of the bottom sample showed a different behaviour over the 168 hour exposure period to 3.5% NaCl and pH 7 brine at 80°C. During the initial 70 hours, the corrosion rate was observed to be slightly above 1.5 mm/year. However, as time progressed, the corrosion rate decreased below 1.5 mm/year.

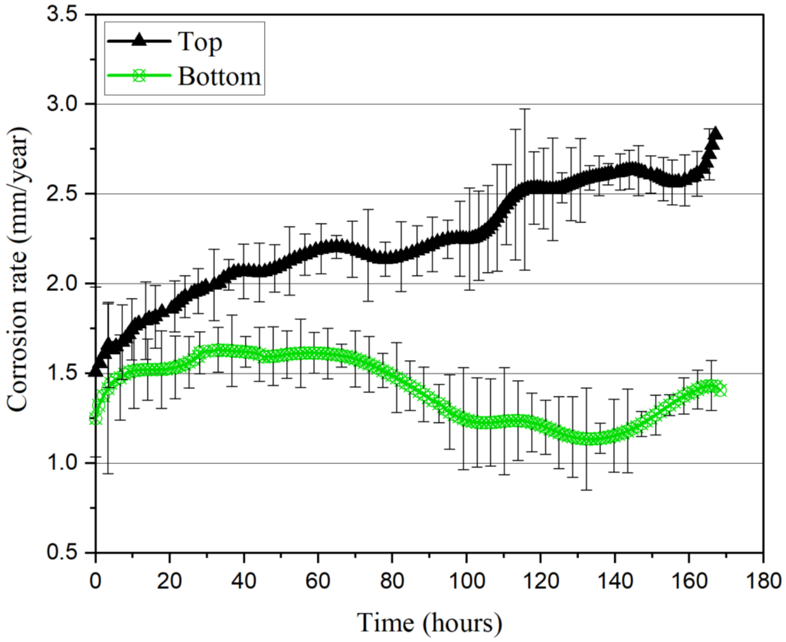

Figure 6-18: Avarga corrosion rate from LPR measurements for ASTM A 106Gr B exposed to 3.5% NaCl and pH7 brine after 80°C over 168 hours of exposure

On the other hand, the corrosion rate for the top sample demonstrated a different trend. Unlike the bottom sample, the corrosion rate of the top sample exhibited a continuous increase throughout the entire 168 hour test duration. Starting at 1.5 mm/year at the beginning of the experiment, the corrosion rate steadily rose, reaching 2.8 mm/year by the end of the test. These results indicate that the corrosion behaviour of the two samples under thermal insulation in the given brine solution was distinct. The bottom sample showed a reduction in its corrosion rate after the initial period, while the top sample experienced a progressive increase in its corrosion rate over time, this might be due to the chemical composition of the brine deposited on the surface.

Table 6-5 summarises the corrosion rates of top and bottom samples exposed to a 3.5% NaCl brine at 80°C for 168 hours using the mass loss method. The table presents the initial and final masses of the samples in grams (g), along with the corresponding corrosion rates in mm/year. Additionally, it includes the average corrosion rate calculated for each location. The results demonstrate that the average corrosion rate for the top sample is higher than that of the bottom sample, with values of 4.622 mm/year and 2.385 mm/year, respectively.

Table 6-5: The corrosion rate by mass loss for top and bottom samples exposed to 3.5% NaCl and pH 7 brine at 80°C over 168 hours of exposure

Sample position	Initial mass (g)	Final mass (g)	Corrosion rate (CR) (mm/year)	Avg. CR (mm/year)
Top	7.618	7.349	5.173	4.622
	8.165	7.988	3.404	
	7.971	7.696	5.289	
Bottom	8.012	7.921	1.750	2.385
	7.895	7.561	2.577	
	8.136	7.989	2.827	

Figure 6-19 displays the general corrosion rates obtained from the CUI test at 80°C and pH 7 using mass loss and LPR techniques. The data indicates that, on average, the corrosion rate evaluated by mass loss is higher than that by LPR for both the top and bottom samples. The corrosion rate for the top samples is 4.62 mm/year using mass loss and 2.89 mm/year using LPR. Conversely, for the bottom sample, the corrosion rate is 2.38 mm/year with mass loss and 1.41 mm/year with LPR. The corrosion rate measurements exhibit a 46% percentage difference from those obtained using mass loss and LPR techniques for the top sample, while the bottom sample demonstrates an even more substantial 51% variance. However, the acquired findings substantiate the comparability of the three microelectrode techniques with mass loss measurements, thus affirming their applicability for investigating CUI.

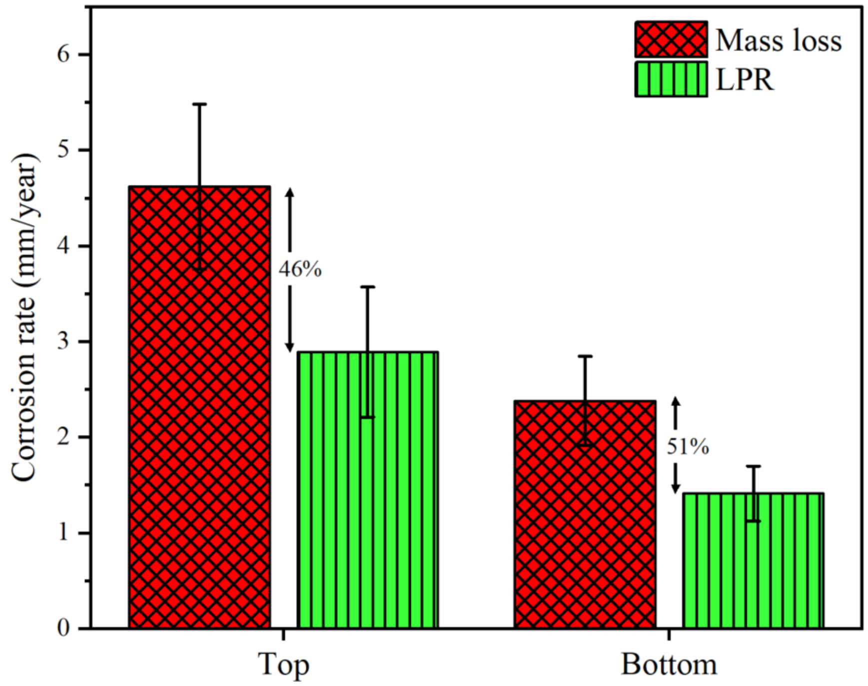

Figure 6-19: Corrosion rate comparison using LPR and mass loss techniques for top and bottom samples after 168 hours of exposure to 3.5% NaCl and pH 7 brine at 80°C

6.2.2.3 SEM micrographs for cross-section and topography view

Figure 6-20 and Figure 6-21 present SEM micrographs of the corrosion film formed on the surface of ASTM A 106 Gr B for the top and bottom samples for test ran at 80°C and pH 7 for 168 hours. Figure 6-20 depicts the topography of the corrosion film, while Figure 6-21 shows the cross-section view. In both Figure 6-20 (a and c) and Figure 6-21 (a and c), the highlighted red boxes delineate the designated areas chosen for further magnification.

The topographical morphology of the corrosion products formed on the top and bottom samples displays distinct differences as shown in Figure 6-20. The top samples show signs of greater loss of material and contain visible loose flakes of corrosion products, per Figure 6-20 (a and b). The morphology of the corrosion layer on the top formed on the top sample seems to show a sandy structure which is referred to as lepidocrocite [126]. In contrast, the bottom samples appear more uniform, and there is no clear evidence of flakes as shown in Figure 6-20 (c-d). It can be seen in Figure 6-20 (d) that there is a doughnut shape, flowery structure and cotton ball, which represent magnetite [146], lepidocrocite [127] and goethite [130] respectively.

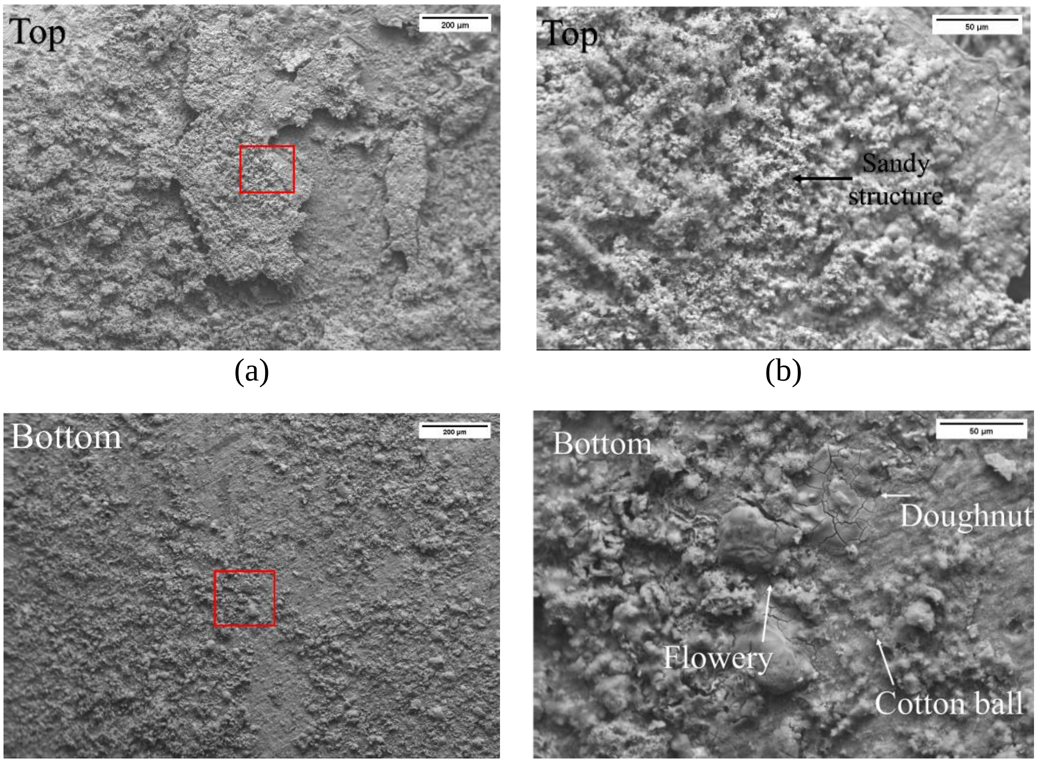

(a) (b)

(c) (d)

Figure 6-20: SEM micrographs topography view of corrosion film grown on ASTM A 106 Gr B exposed to 3.5% NaCl and pH 7 brine at 80°C for 168 hours (a-b) top and (c-d) bottom

The cross-sectional SEM images of the top sample, as shown in Figure 6-21 (a and b), reveal a cohesive failure in the corrosion film layer located approximately 16 µm from the steel surface. This failure is manifested as a continuous crack within the corrosion layer. This occurrence could be attributed to internal stresses that have developed within the corrosion layer itself [188], or it might suggest the possibility of the corrosion film having formed as a dual-layer structure [186, 189]. Conversely, in the case of the bottom sample, the corrosion layer experienced a mix of adhesive and cohesive failure as shown in Figure 6-21 (b). The adhesive failure might be attributed to the heat generated during the epoxy casting process [190].

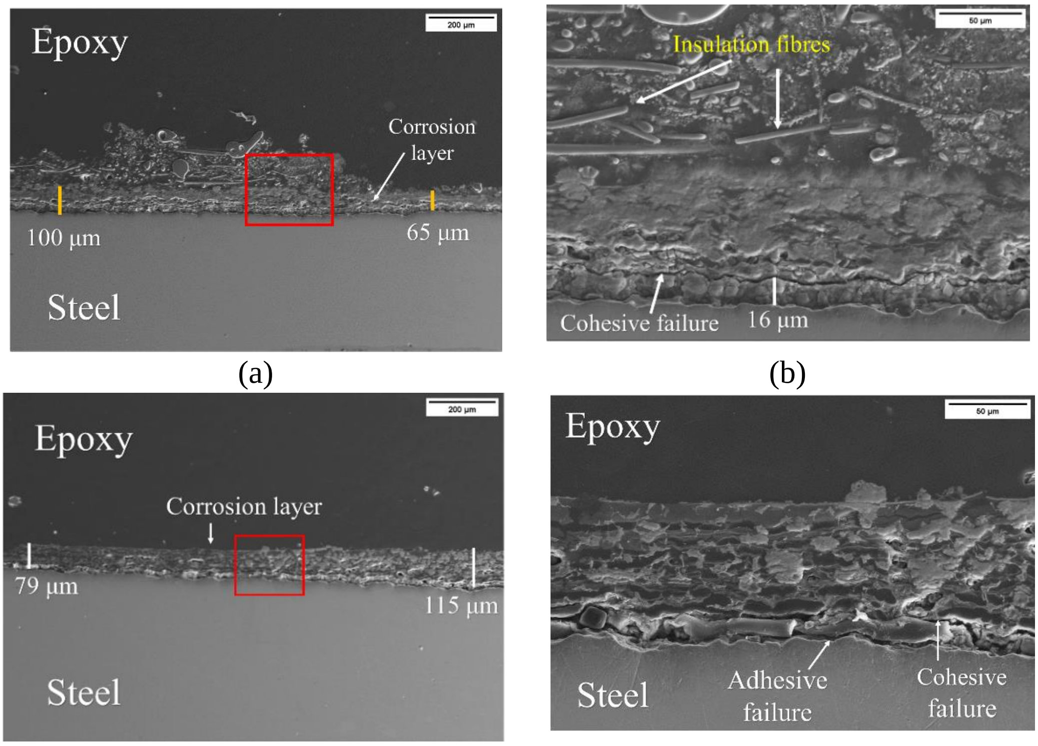

(a) (b)

(c) (d)

Figure 6-21: Cross-section SEM micrographs of corrosion film growing over ASTM A 106 Gr B top and bottom samples at various magnifications as shown by corresponding scale bar at pH 7, 80°C and 3.5% NaCl for 168 hours, (a-b) top sample, (c-d) bottom sample

The corrosion film thickness was measured by using ImageJ software. The corrosion film formed on both the top and bottom maintains a uniform thickness, as depicted in Figure 6-22. The analysis highlights this uniformity, with the average corrosion film thickness measured at 81µm for the top sample and slightly greater at 86 µm for the bottom samples. It is important to acknowledge that the measurement of corrosion layer thickness, especially for the top sample, may be subject to inaccuracies. This is primarily due to the presence of insulation fibres adhering to the corrosion film, which can lead to the removal of some corrosion when disassembling the insulation from the test rig.

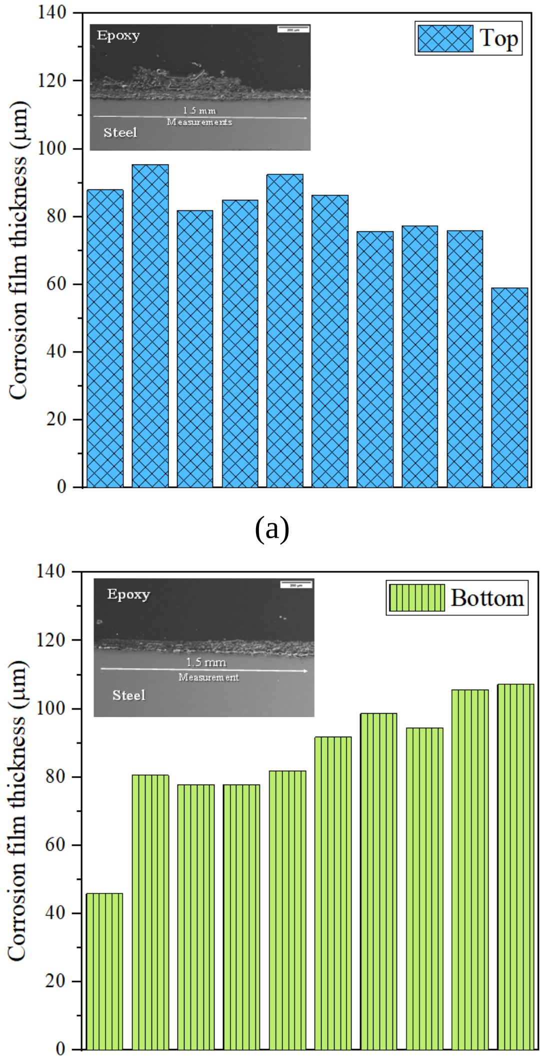

(a)

(b)

Figure 6-22: A histogram shows the thickness distribution of a corrosion film form on the sample (a) top and (b) the bottom after 168 hours of exposure to 80°C and a pH 7 brine

6.2.2.4 EDX analysis

This section delves into the comprehensive EDX elemental mapping of the corrosion layer's evolution on both the top and bottom sample surfaces. The elucidation commences with an exposition of the EDX analysis from a topographical view, followed by the cross-sectional EDX analysis.

EDX of the topography view of the corrosion layer.

Figure 6-23 depicts the EDX topography detailing the characteristics of the corrosion film that has formed on the surface of the top sample. Meanwhile, Figure 6-24 provides a comparable analysis of the corrosion film grown on the surface of the bottom sample. The degree of element concentration within the examined region correlates directly with the intensity of the corresponding colouration. Both samples contain a substantial amount of iron and oxygen, in addition, the chloride ion presence is evident. However, the distribution pattern of sodium ions is comparatively different to the distribution pattern observed for chloride ions.

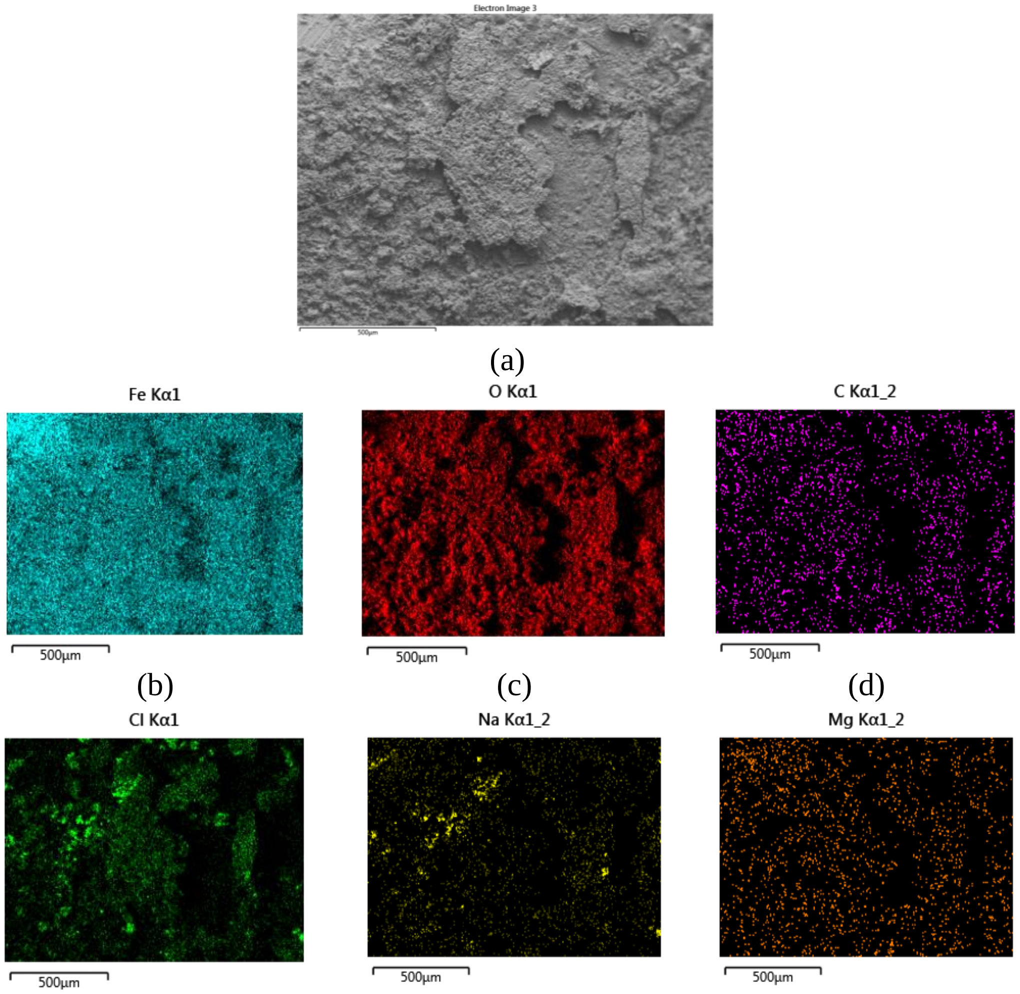

(a)

(b) (c) (d)

(e) (f) (g)

Figure 6-23: EDX elemental mapping analysis on the surface of the corrosion film grown on the top sample after 168 hours of exposure at 80°C and pH 7, (a) SEM micrograph, (b) iron-Fe, (c) oxygen-O, (d) carbon-C, (e) chloride-Cl, (f) sodium-Na and (g) magnesium-mg

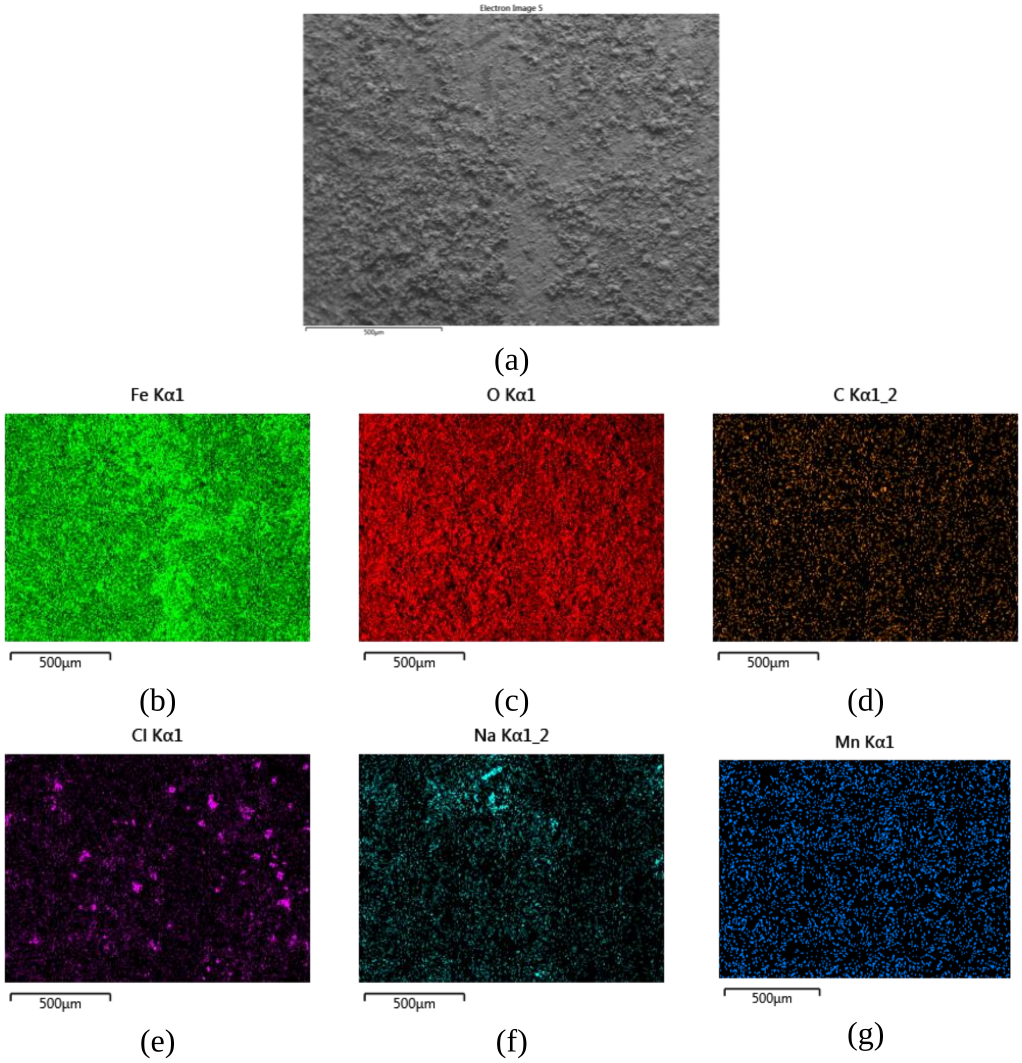

Figure 6-24: EDX elemental mapping analysis on the surface of the corrosion film grown on the top sample after 168 hours of exposure at 80°C and pH 7, (a) SEM micrograph, (b) iron-Fe, (c) oxygen-O, (d) carbon-C, (e) chloride-Cl, (f) sodium-Na and (g) manganese-Mn

EDX mapping for cross-section

Figure 6-25 and Figure 6-26 display the cross-sectional morphologies and element distribution maps of the top and bottom samples, respectively, after being exposed for 168 hours at 80°C and pH 7. The EDX map reveals the elemental composition of each sample which are iron, oxygen, carbon, silicon, chloride, and sodium. Both the top and bottom samples predominantly consist of iron and oxygen, which are the main elements in the corrosion products formed on their surfaces. However, a substantial amount of carbon is observed in the bottom sample compared to the top sample, yet its origin remains unclear. Chloride is present in both the top and bottom samples, but there are noticeable differences in its distribution. In the top sample, chloride is dispersed across the corrosion layer, whereas in the bottom sample, it mainly forms clusters within the corrosion layer. Furthermore, the corrosion layer of the bottom sample contains a substantial amount of silicon, especially on the outer side.

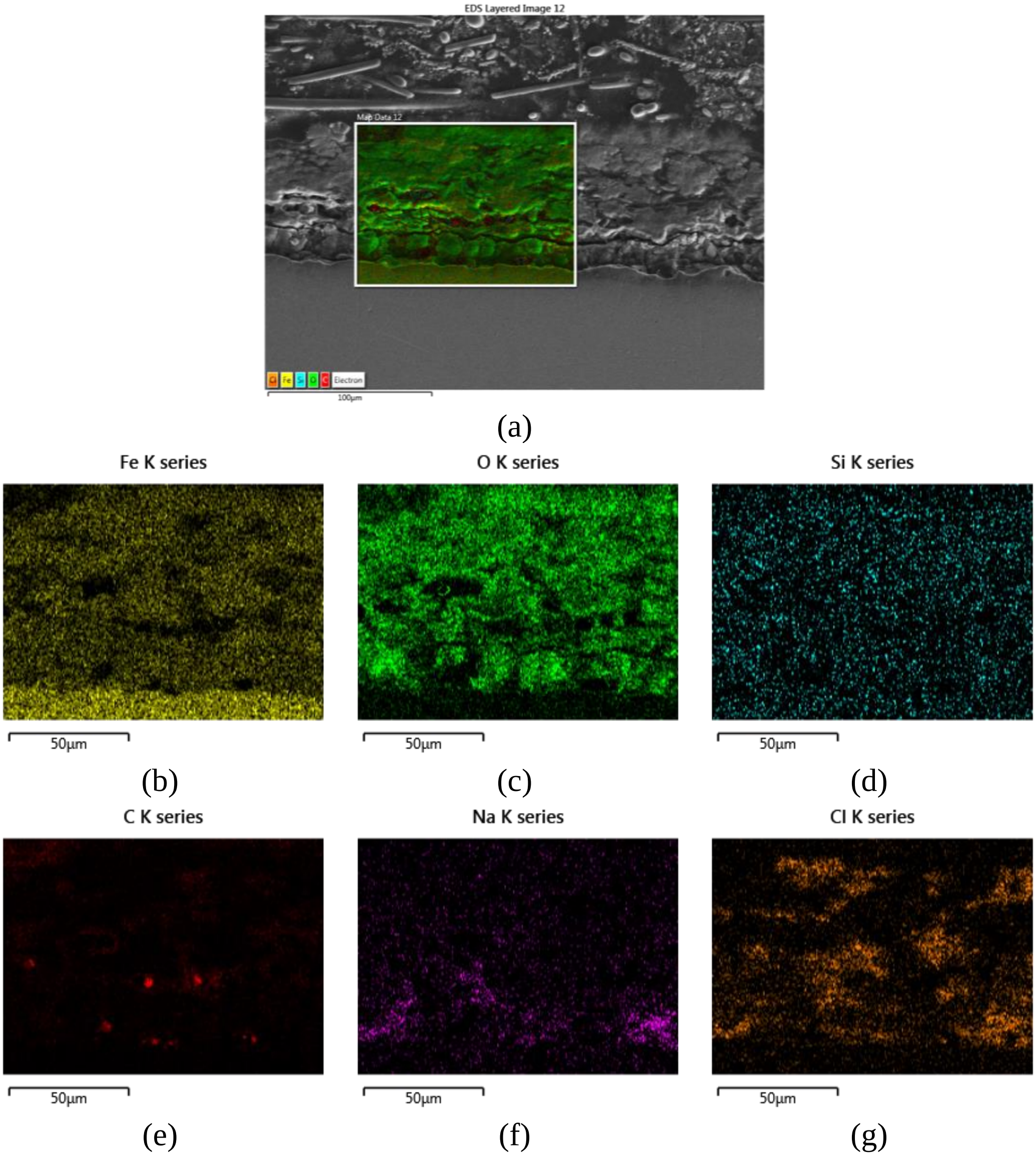

(a)

(b) (c) (d)

(e) (f) (g)

Figure 6-25: EDX elemental mapping analysis on the surface of the corrosion film grown on the top sample after 168 hours of exposure at room temperature and pH 7, (a) SEM micrograph, (b) iron-Fe, (c) oxygen-O, (d) silicon-Si, (e) carbon-C, (f) sodium-Na and (g) chloride-Cl

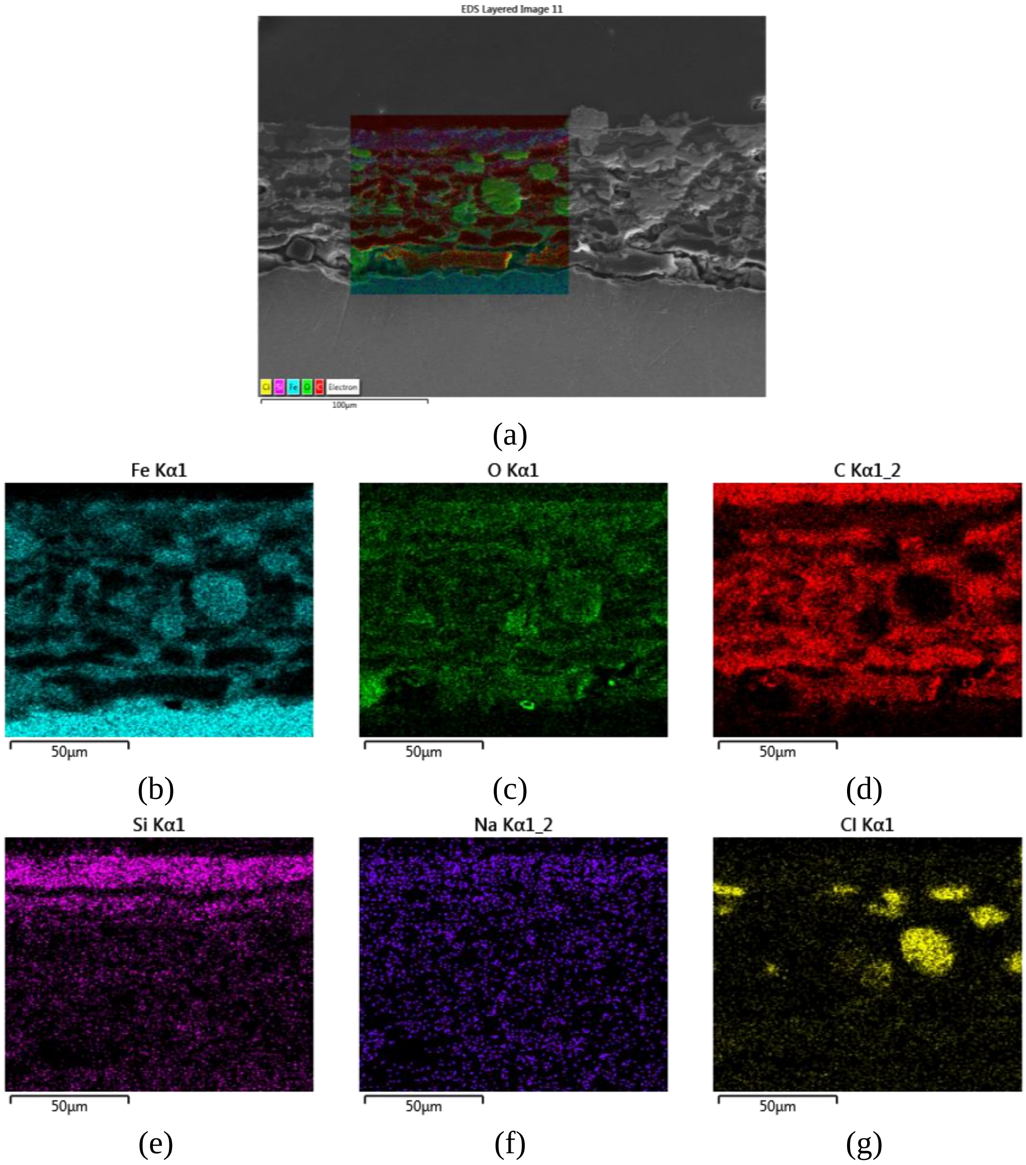

(a)

(b) (c) (d)

(e) (f) (g)

Figure 6-26: EDX elemental mapping analysis on the surface of the corrosion film grown on the top sample after 168 hours of exposure at room temperature and pH 7, (a) SEM micrograph, (b) iron-Fe, (c) oxygen-O, (d) carbon-C, (e) silicon-Si, (f) sodium-Na and (g) chloride-Cl

6.2.2.5 Characterisation of corrosion layer by Raman spectroscopy

Figure 6-27 illustrates the Raman spectra obtained from the top (outer) layer of the corrosion film grown on the surfaces of both the top (a) and bottom (b) samples at 80°C. Lorentzian fitting was executed to validate and discern the Raman peaks, and the outcomes are highlighted as a cumulative fit peak in Figure 6-27.

In the top sample, the strong peak at 588 cm^{-1} is likely to correspond to either magnetite or maghemite [191], both of which are iron oxides. The peaks at 249 cm^{-}

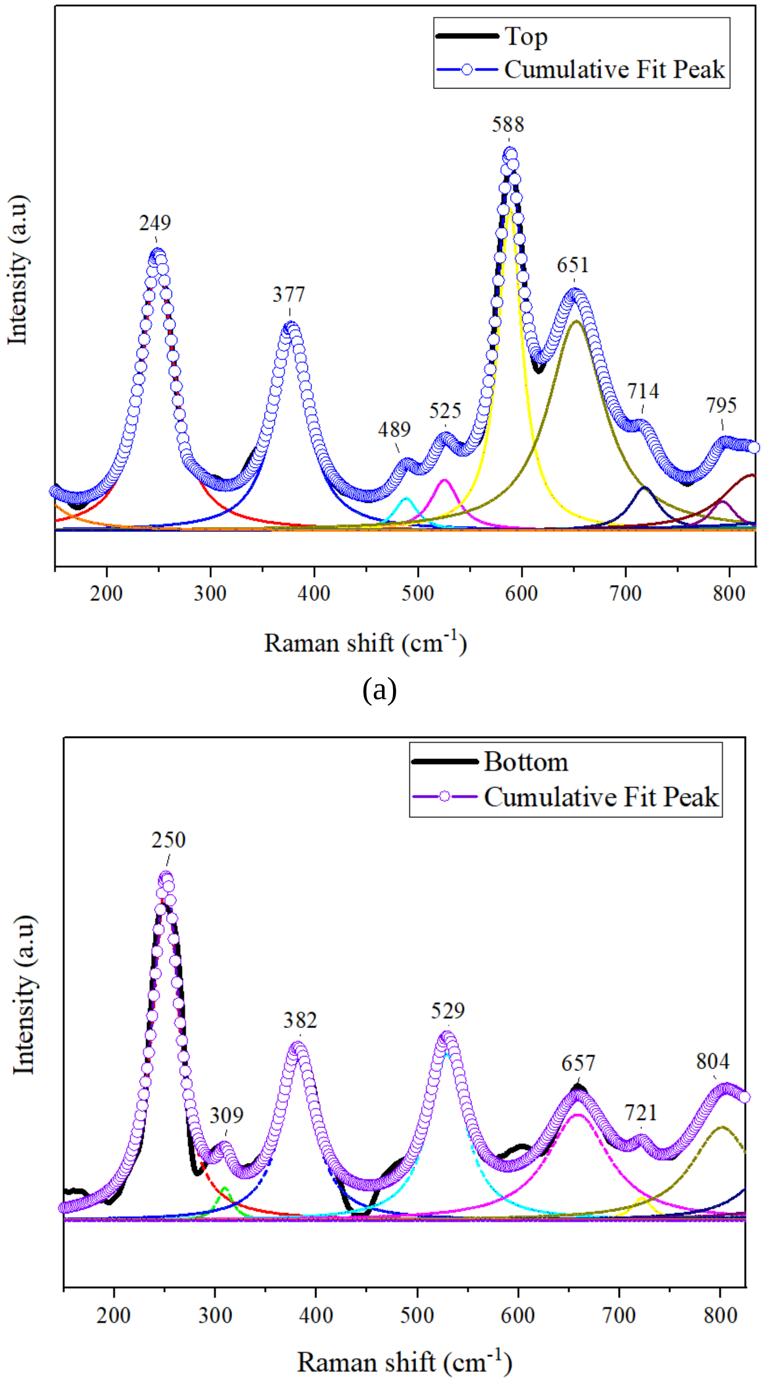

(a)

(b)

Figure 6-27: Raman spectra of corrosion film grown on the steel surface at 80°C, pH and 3.5% NaCl (a) top and (b) bottom

^{1}, 377 cm^{-1}, and 651 cm^{-1} are indicative of lepidocrocite. Akageneite is suggested by peaks at 489 cm^{-1} and 714 cm^{-1}, with a shared peak at 377 cm^{-1} with lepidocrocite [121]. Notably, the goethite peaks are not visible in this spectrum.

On the other hand, the bottom sample primarily exhibits the presence of lepidocrocite as the dominant phase, indicated by the peak at 250 cm^{-1}. Additionally, peaks at 529 cm^{-1} and 657 cm^{-1} further confirm the presence of lepidocrocite. Akaganeite is also observed with peaks at 382 cm^{-1} and 721 cm$_{-1}$. Moreover, peaks at 309 cm^{-1} and 657 cm^{-1} suggest the presence of magnetite [124].

6.2.2.6 XRD diffraction patterns

As depicted in Figure 6-28, the phase composition variation of the corrosion film formed on the surfaces of the top and bottom samples is presented. The XRD data was employed to obtain semi-quantitative values representing the phase distribution in the corrosion film, as shown in Figure 6-29. The results reveal the presence of several compounds in the corrosion film, including akageneite, lepidocrocite, goethite, and magnetite. However, the main compounds identified in both the top and bottom samples are akageneite and magnetite. These two phases are found to be the primary constituents of the corrosion film on both surfaces.

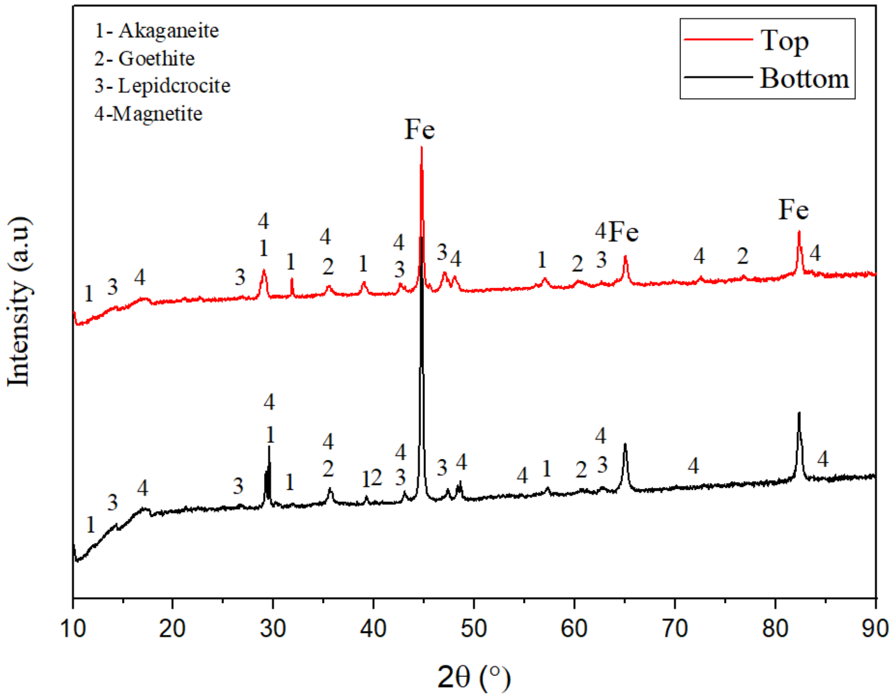

Figure 6-28: XRD pattern of the composition of the corrosion film grown on the surface of the top and the bottom samples at 80°C, pH 7 for 168 hours

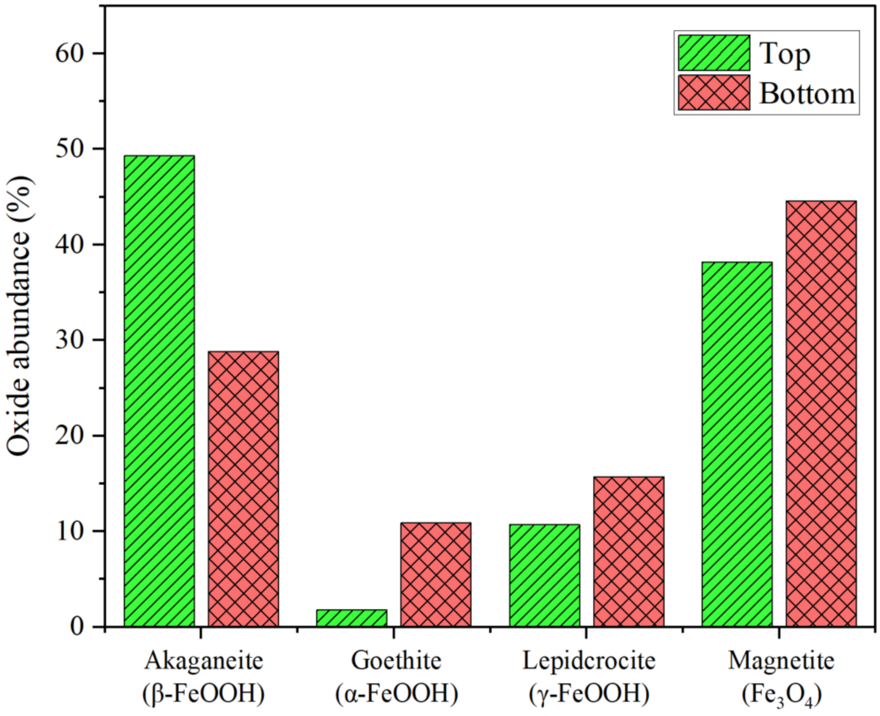

Figure 6-29: Semi-quantitative analysis of the corrosion film formed on the surface of the top and the bottom samples

6.2.3 Evaluation of CUI at pH 7 and 150°C

6.2.3.1 Visual inspection

Figure 6-30 (a and b) present the visual observation of CUI for top and bottom samples respectively. There is a distinct difference between the surface coverage of corrosion on the top sample and the bottom sample. In contrast to the bottom samples, the top samples exhibit less corrosion coverage, particularly the middle sample, sample 2. In addition, there are insulation fibres attached to the surface of the steel.

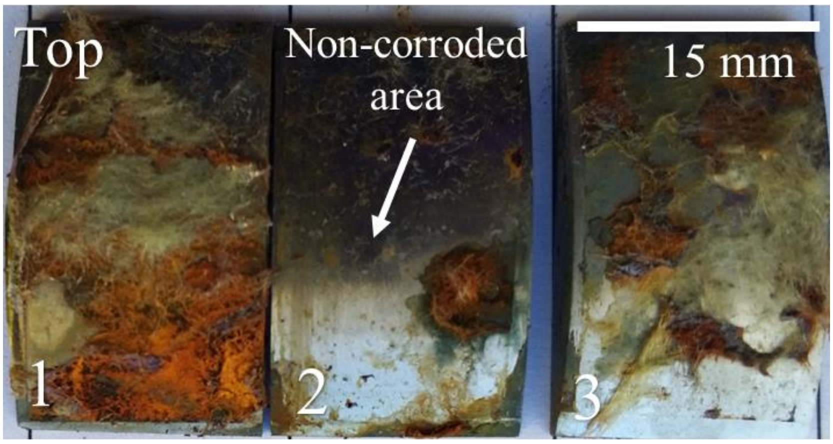

(a)

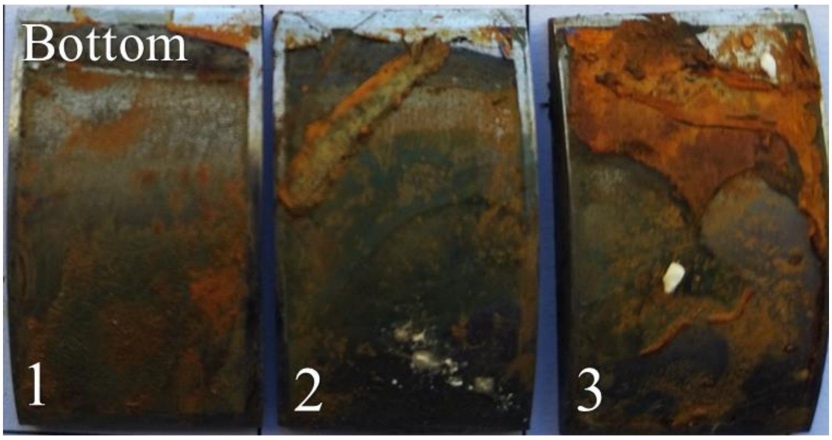

(b)

Figure 6-30: Digital photos of corrosion products developed on coupon surfaces after being exposed to 3.5% NaCl, pH 7 and 150°C for 168 hours. (a) the top sand (b) the bottom samples

Conversely, the corrosion layer that developed on the bottom sample encompassed nearly the entirety of its surface area. Nonetheless, it appears that the corrosion layer is relatively thin. In addition, no traces of insulation fibres were detected on the surface.

6.2.3.2 Characterisation of the CUI at 150°C and pH 7

Figure 6-31 graphically represents the corrosion rates measured at an elevated temperature of 150°C by LPR technique, for both the top and bottom samples. The error bars were derived from linear segments of repeated LPR measurements. No clear trend is evident for the initial corrosion rate, which ranges from 0.5 to 1.6 mm/year for the bottom and top samples, respectively. Over the testing duration, the corrosion rate of the bottom sample consistently rises from 0.51 to 0.82 mm/year. Conversely, the top sample displays an initial decline in corrosion rate for the initial 43 hours, followed by an increase, culminating in an average corrosion rate of 1.9 mm/year after the test. Overall, the corrosion rate for both top and bottom samples has consistently shown a slightly stable pattern.

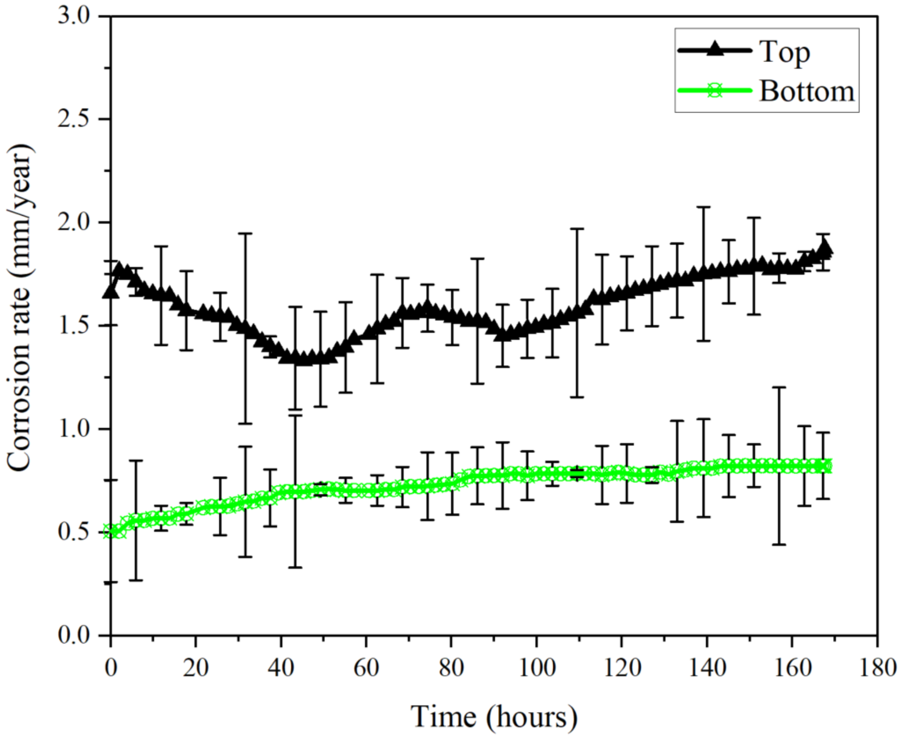

Figure 6-31: Average corrosion rate vs time for ASTM A 106 Gr B steel at the top and bottom sample at 3.5% NaCl, pH 7 fat 150°C for 168 hours

The corrosion rates, determined through mass loss, for both top and bottom samples, are presented in Table 6-6. The initial and final masses are provided in grams (g), along with the corresponding corrosion rates in mm/year. The findings indicate that the average corrosion rate, as computed using the mass loss method, is greater for the top sample compared to the bottom, with values of 2.8 mm/year and 1.5 mm/year, respectively.

Figure 6-32 elucidates the comparison between the corrosion rate obtained through mass loss and the time-averaged corrosion rate determined by LPR. The error bars for the mass loss represent data from three samples exposed in a single experiment. The percentage difference for the corrosion rate calculated via mass loss and LPR for both the top and bottom are 47% and 49% respectively. Nevertheless, a notable level of agreement is observed overall. This serves as evidence that the overarching trend observed in LPR measurements remains valid under these specific conditions.

Table 6-6: Corrosion rate by mass loss method calculated from top and bottom sample in 150°C, pH 7 for 168 hours

Sample position	Initial mass (g)	Final mass (g)	Corrosion rate (CR) (mm/year)	Avg. CR (mm/year)
Top	8.019	7.901	2.086	2.841
	7.881	7.690	3.377	
	7.267	7.094	3.059	
Bottom	8.031	7.937	1.663	1.611
	8.349	8.248	1.856	
	7.545	7.842	1.314	

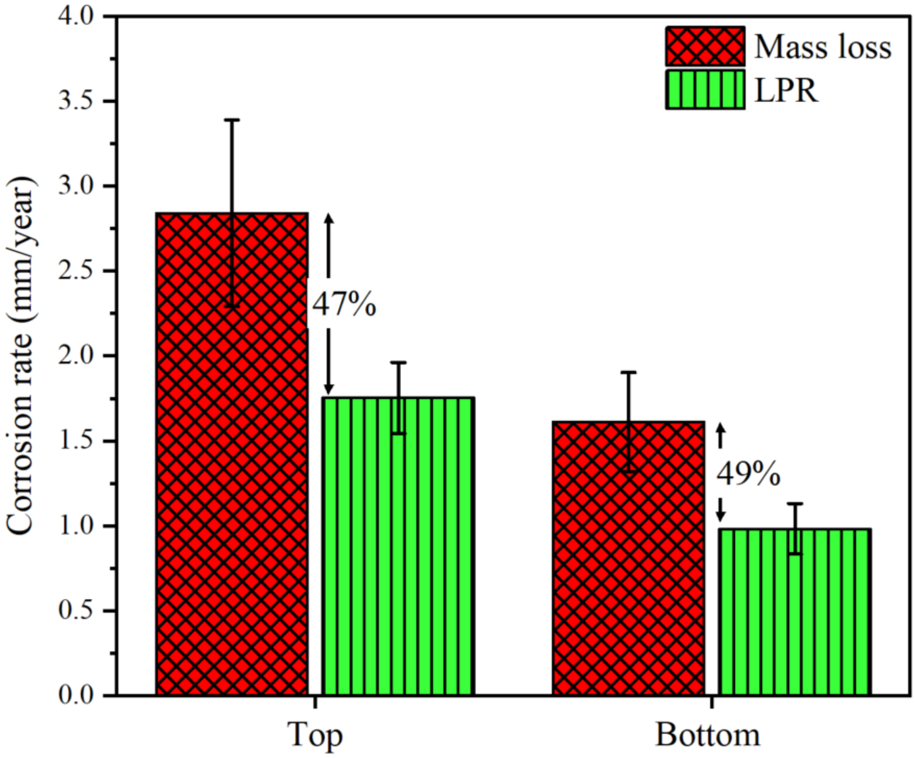

Figure 6-32: Comparison of corrosion rates measured by LPR average and mass loss at 150°C and pH 7 for 168 hours

6.2.3.3 SEM micrograph for, cross-section and topography view of the corrosion layer

Figure 6-33 displays the SEM images depicting the surface morphology of the corrosion layer that developed on the steel surfaces of both the upper and lower samples at 150°C. In the SEM image, per Figure 6-33 (a), of the corrosion layer formed on the top sample, insulation fibres can be observed adhering to the surface. Upon further magnification, the corrosion layer exhibits characteristics resembling a cotton ball and a flowery structure, which are indicative of the presence of goethite and lepidocrocite. However, the surface micrographs of the corrosion layer formed on the bottom sample, as shown in Figure 6-33 (c and d), revealed that some cohesive failure might have formed within the corrosion layer due to internal stress.

Figure 6-34 displays the cross-sectional SEM micrographs of both the top and bottom samples. In the case of the top sample, the corrosion layer appears to be devoid of adhesive failure. However, a distinct manifestation of cohesive failure is evident, as depicted in Figure 6-34 (a and b). Furthermore, the corrosion layer on the top sample is comparatively thin when compared to the thickness of the corrosion thickness of bottom sample as depicted in Figure 6-35 with average thicknesses of 35 µm and 81 µm, respectively.

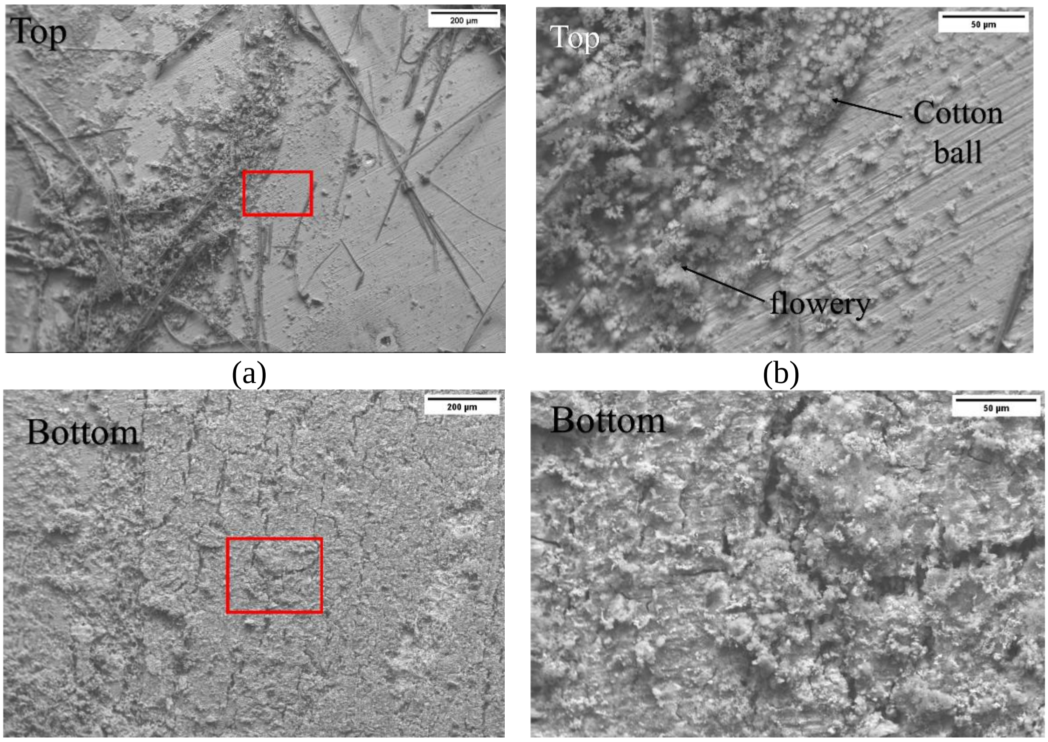

(a) (b)

(c) (d)

Figure 6-33: SEM micrographs for topography view for (a and b) top samples and (c and d) bottom samples exposed to 3.5%NaCl for 168 hours at 150°C

Conversely, the corrosion layer that has developed on the bottom sample exhibits greater thickness, and higher density, and does not show observable indications of cohesive or adhesive failures, per Figure 6-34 (c and d). This characteristic might contribute to its effectiveness in reducing the corrosion rate by blocking the diffusion of corrosive elements such as chloride from reaching the substrate.

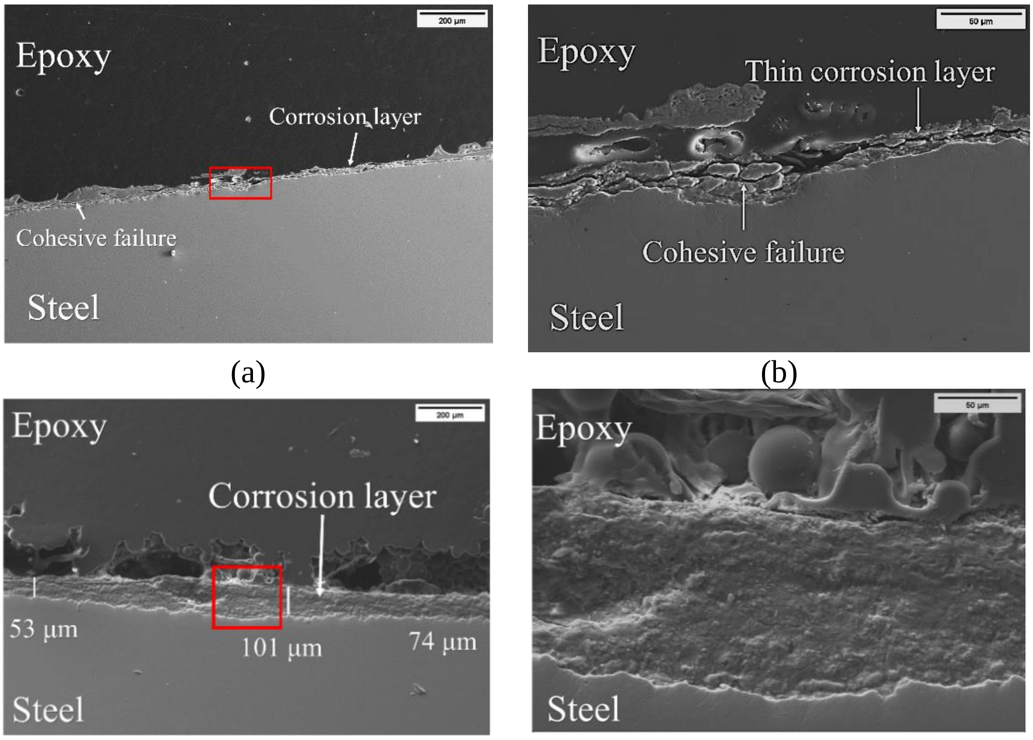

(a) (b)

(c) (d)

Figure 6-34: Cross-sectional SEM micrographs for (a and b) top samples and (c and d) bottom samples exposed to 3.5%NaCl for 168 hours at 150°C

6.2.3.4 EDX analysis

Figure 6-36 and Figure 6-37 provide insights into the elemental distribution within the corrosion layer on the top surface. Among the elements analysed, iron (Fe) and oxygen (O) are prominently identified, underscoring their significant presence in both the top surface and the cross-section of the corrosion layer. Silicon (Si) is primarily associated with thermal insulation fibre, given its role as a major constituent of mineral wool.

The presence of chlorine (Cl) and sodium (Na) is also observed on the top surface. However, their identification in the cross-section presented challenges. To ascertain their existence within the corrosion layer, an EDX point scan technique was employed, focusing on a selected point labelled as "Sp" in Figure 6-37 (a). The EDX point analysis successfully confirmed the presence of Na and Cl in the corrosion layer.

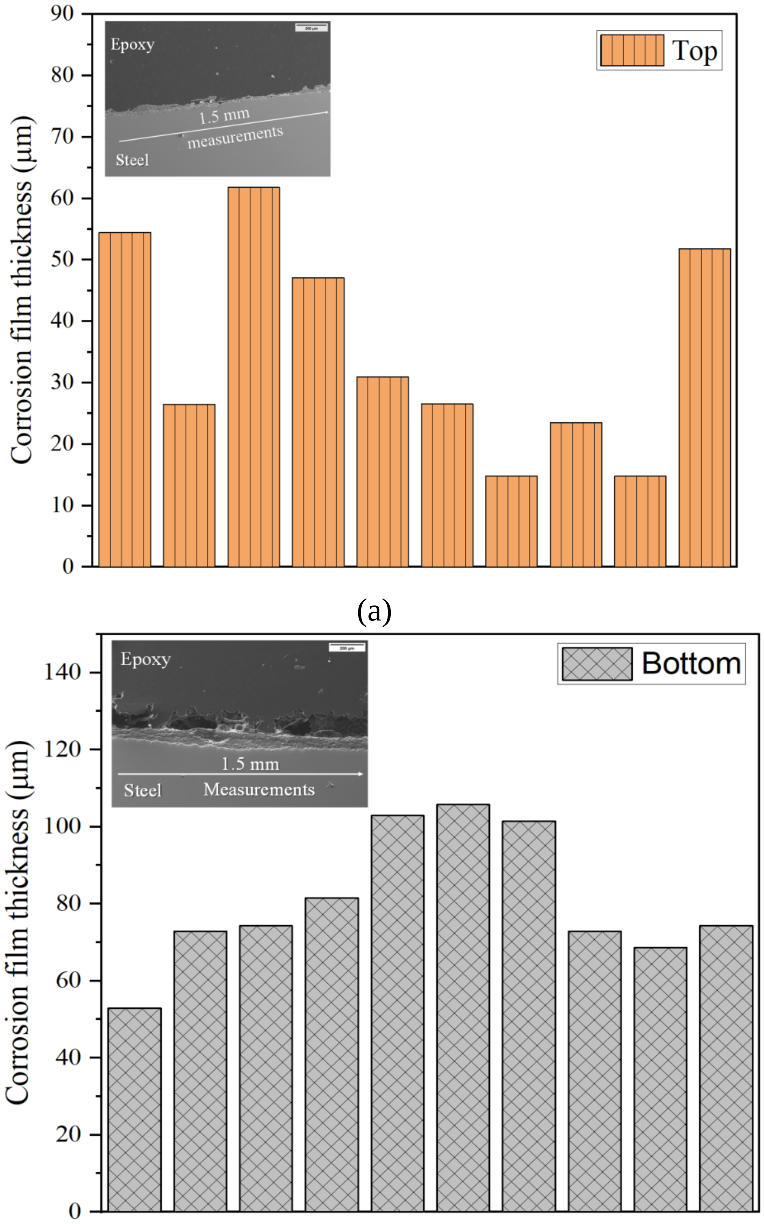

(a)

(b)

Figure 6-35: Corrosion layer thickness of (a) top and (b) bottom samples, exposed to 3.5 %NaCl for 168 hours at 150°C

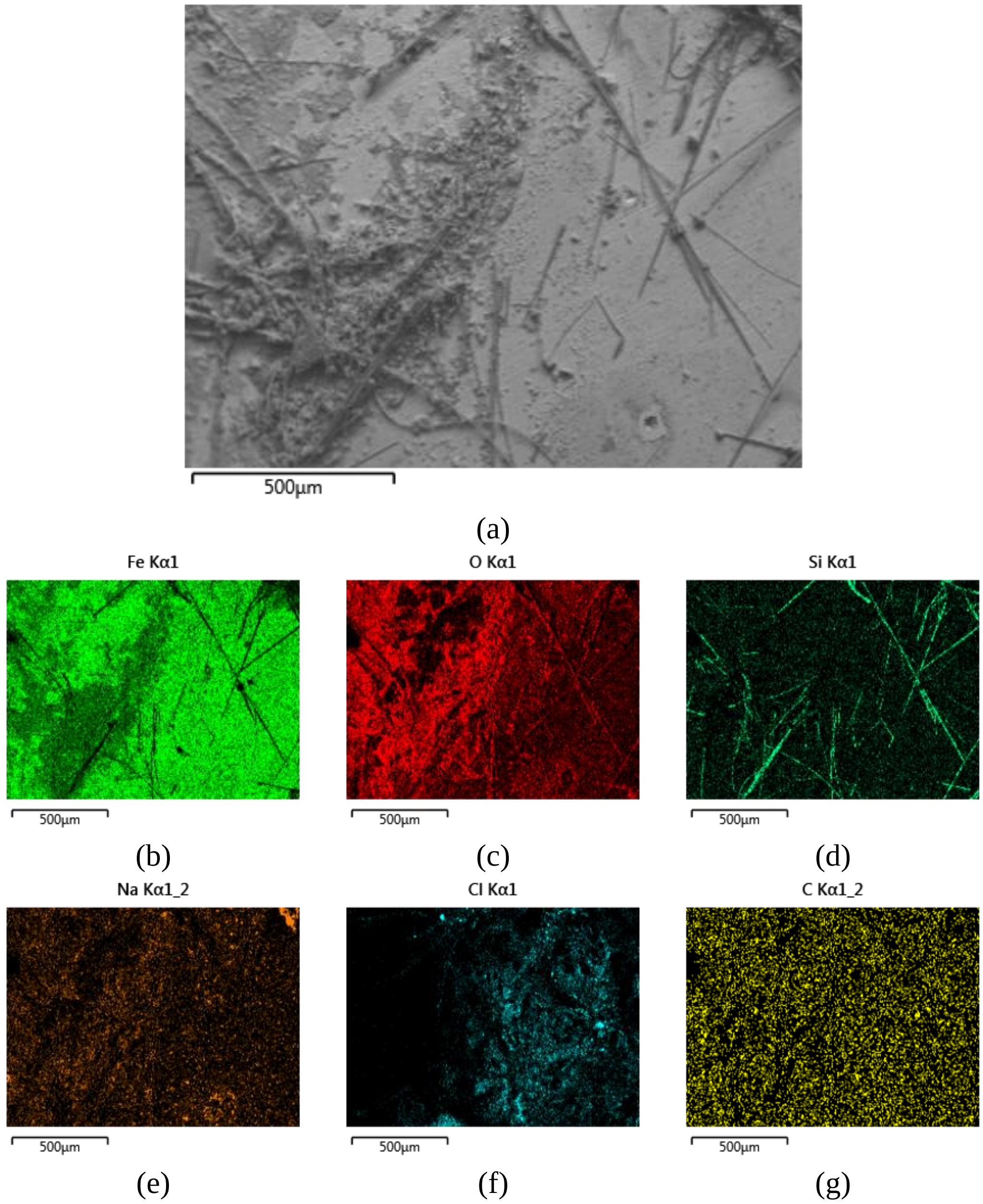

(a)

(b) (c) (d)

(e) (f) (g)

Figure 6-36: SEM micrographs and the corresponding elemental distribution for the surface of the corrosion layer grown on the top sample after being exposed to 3.5% NaCl, pH 7 at 150°C for 168 hours, (a) SEM micrograph, (b) iron-Fe (c) oxygen-O, (d) silicon-Si, (e) sodium-Na, (f) chloride-Cl and (g) carbon-C

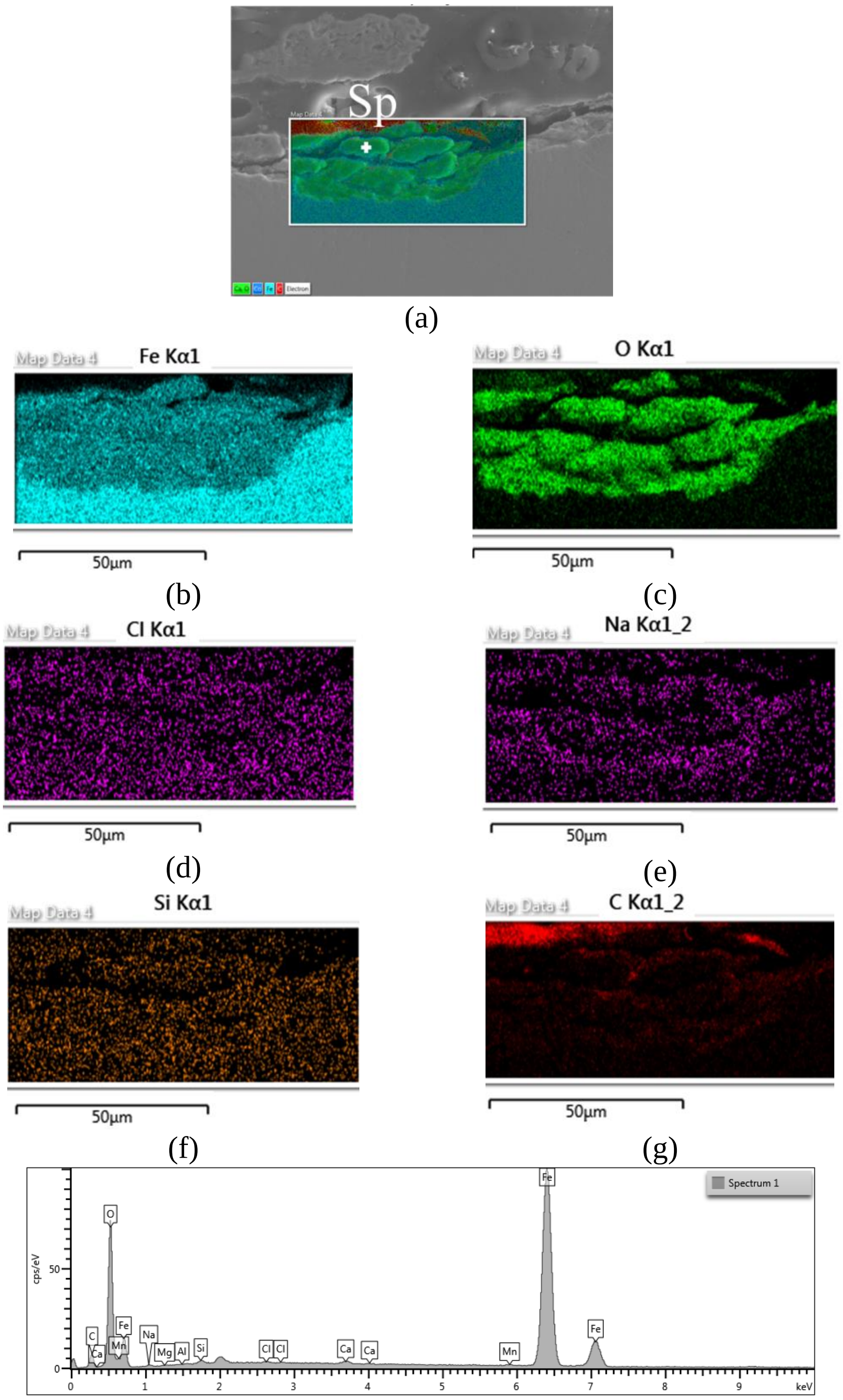

(a)
(b)
(c)
(d)
(e)
(f)
(g)
(h)

Figure 6-37: SEM micrographs and the corresponding elemental distribution for the cross-sectional of the corrosion layer grown on the top sample after being exposed to 3.5% NaCl, pH 7 at 150°C for 168 hours, (a) SEM micrograph, (b) iron-Fe (c) oxygen-O, (d) chloride-Cl, (e) sodium-Na, (f) silicon-Si, (g) carbon-C and (h) EDX point analysis of the selected point (Sp)

Figure 6-38 and Figure 6-39 offer insights into the elemental distribution within the corrosion layer, both on the top surface and in the cross-sectional view. These images reveal the presence of chloride (Cl) and sodium (Na) alongside iron (Fe) and oxygen (O) within the corrosion layer.

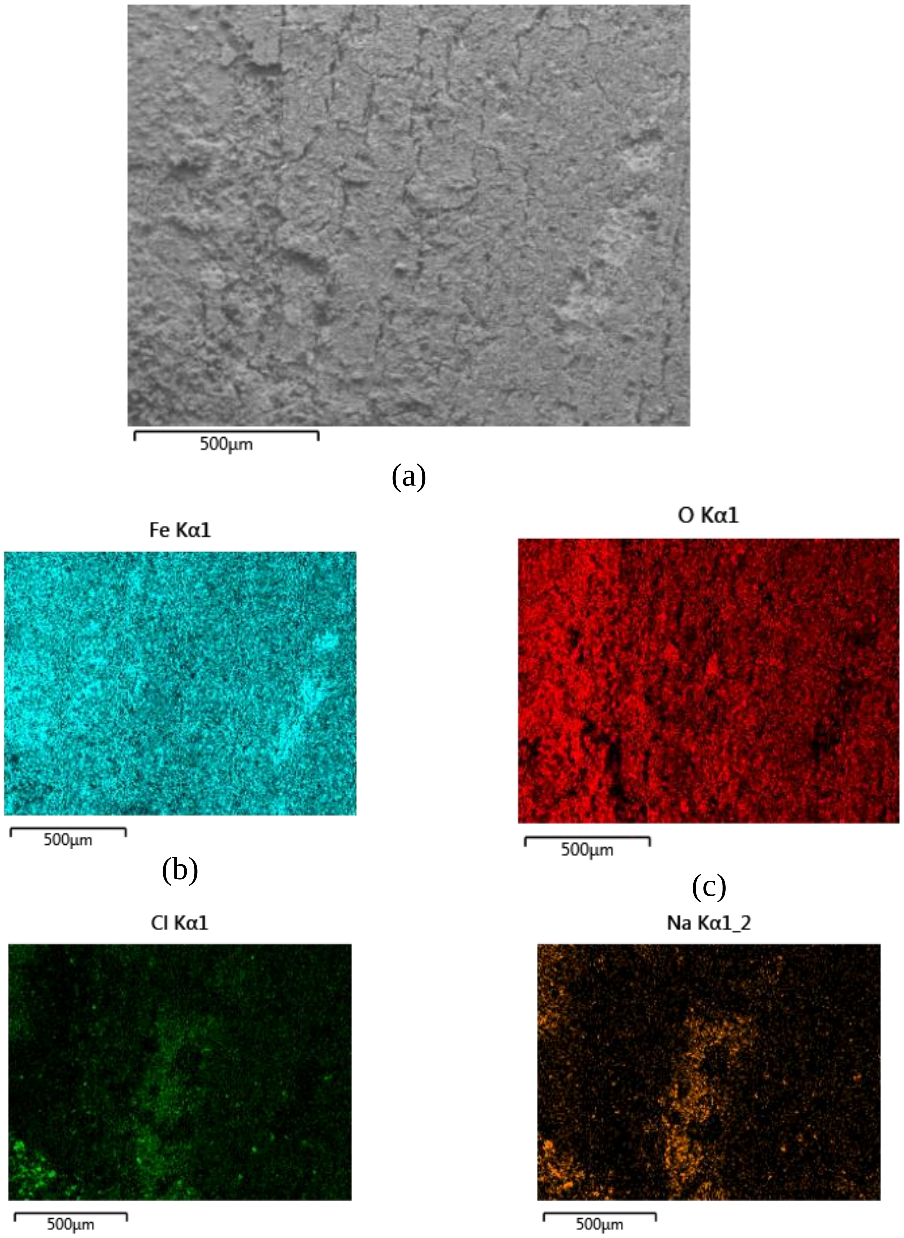

(a)

(b)

(c)

(d)

(e)

Figure 6-38: SEM micrograph for surface view and the elemental distribution on the bottom sample after being exposed to 3.5% NaCl, pH 7 at 150°C for 168 hours, (a) SEM micrograph, (b) iron-Fe (c) oxygen-O, (d) chloride-Cl, (e) sodium-Na

However, the distribution of both chloride and sodium is not uniform throughout the corrosion layer, whether observed from the top surface or in cross-sectional views. This non-uniform distribution highlights the complex and heterogeneous nature of the corrosion layer, indicating variations in the composition and concentration of these elements at different locations within the layer.

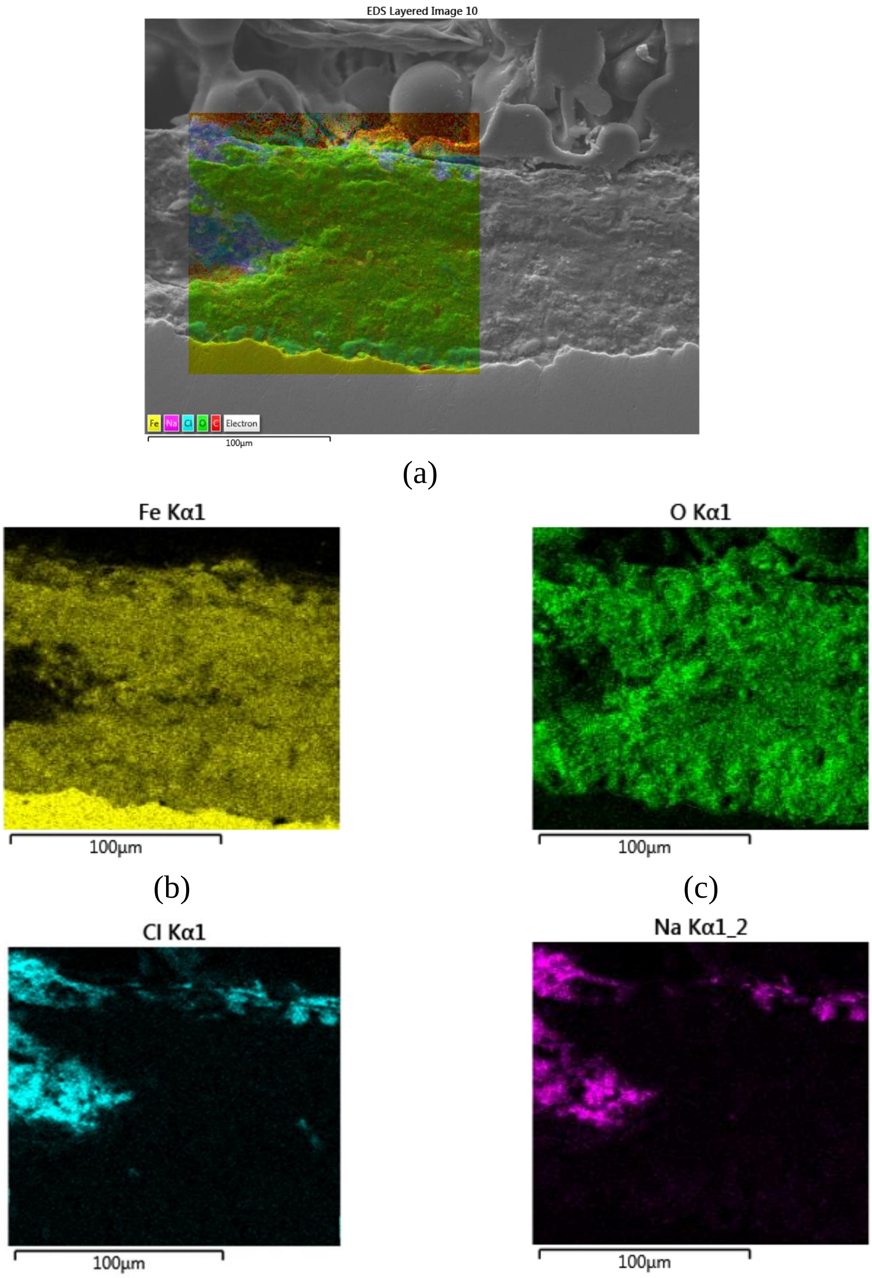

(a)

(b)

(c)

(d)

(e)

Figure 6-39: SEM micrograph for cross-sectional view and the elemental distribution on the bottom sample after being exposed to 3.5% NaCl, pH 7 at 150°C for 168 hours, (a) SEM micrograph, (b) iron-Fe (c) oxygen-O, (d) chloride-Cl, (e) sodium-Na

6.2.3.5 Raman spectroscopy analysis for the corrosion layer

Figure 6-40 presents a detailed analysis of the composition of the corrosion film that develops on the surfaces of the carbon steel samples taken from both the top and bottom samples by Raman spectroscopy. In the context of the top sample (as shown in sub-figure a), discernible peaks are observed within the spectral range. Notably, the most prominent peak resonates at 295 cm^{-1}, which corresponds to the presence of goethite. Additional notable peaks are identified at 243 cm^{-1} and 541 cm^{-1}. Further examination of the spectral data reveals the presence of lepidocrocite, manifested through discernible peaks at 378 and 663 cm^{-1}. Meanwhile, akageneite, another discernible component of the corrosion film, manifests its presence through peaks at 322, 411 1, 541, and 714 cm^{-1}. An additional noteworthy observation pertains to the presence of magnetite, evidenced by peaks at 541 and 663 cm^{-1}.

Regarding the bottom samples, the primary constituents comprising the corrosion film are successfully discerned. The principal Raman peaks corresponding to the corrosion products manifest at distinct wavenumbers, specifically at 226, 297, 339, 364, 405, 665, and 730 cm^{-1}. These distinctive peaks are indicative of the presence of goethite, lepidocrocite, and akageneite within the corrosion film.

It is worth noting, however, that the characteristic peaks corresponding to magnetite are notably absent in the acquired spectra. It is crucial to emphasize that the absence of magnetite peaks does not necessarily imply the non-existence of magnetite within the corrosion film. Rather, it signifies that magnetite may not have formed at the specific scan point under consideration.

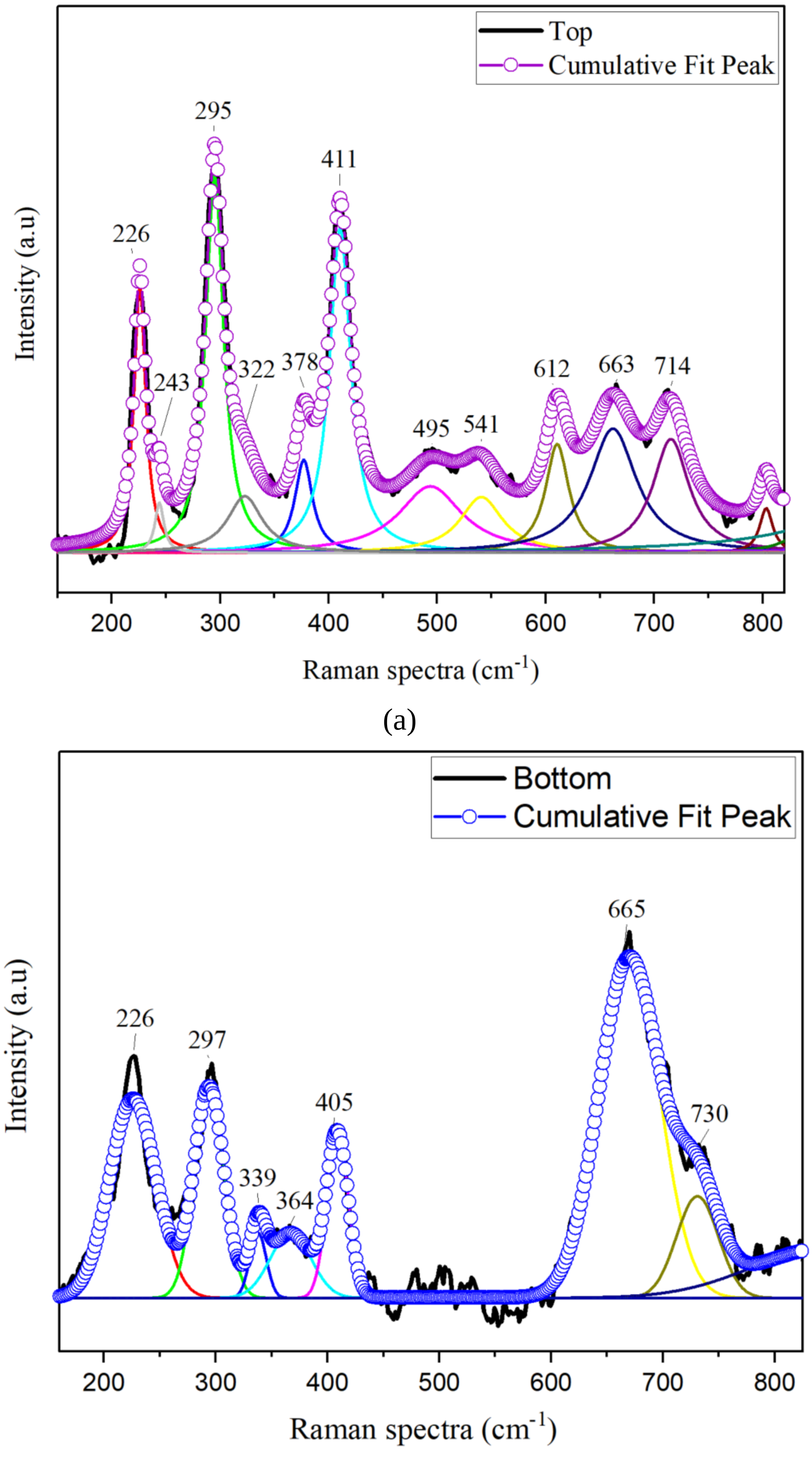

(a)

(b)

Figure 6-40: Raman spectra results of the corrosion film grown on ASTM A 106 Gr B after 168 hours, in a 3.5% NaCl, pH7 brine at 150°C, (a) top, (b) bottom

6.2.3.6 Characterisation of the corrosion layer by XRD

The XRD was utilized to analyse the chemical composition of the corrosion layers grown on both the top and bottom samples, as illustrated in Figure 6-41. The XRD analysis revealed the presence of akaganeite, goethite, lepidocrocite, and magnetite in both samples, highlighting a consistent composition across the corrosion layers. Nonetheless, it is noteworthy that the content of each corrosion product varies between the top and bottom samples.

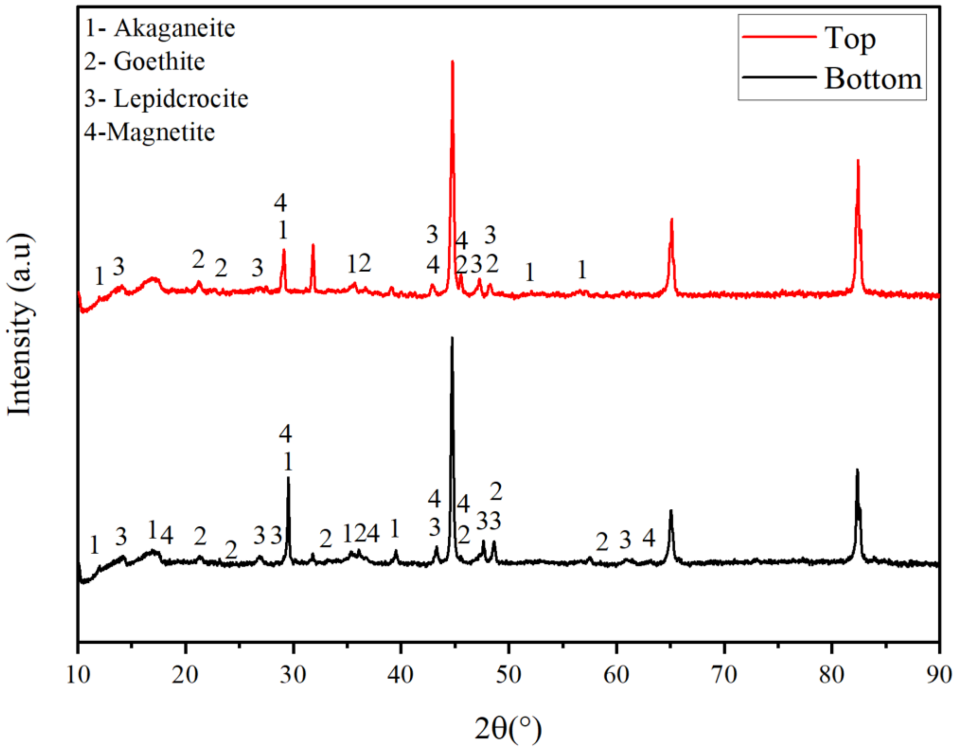

Figure 6-41: XRD patterns of corrosion layer grown on the surface of the top and the bottom samples

6.2.4 Discussion

By examining the CUI rates at two specific positions, 12 o'clock (top) and 6 o'clock (bottom), notable differences were observed, as illustrated in sections 6.2.1 to 6.2.3. These differences were observed when samples were exposed to a 3.5% NaCl brine solution at a pH level of 7, at room temperature, 80°C, and 150°C. In order to establish these discernible variations in corrosion rates, the use of both LPR and mass loss measurements was employed. In addition, a thorough examination of the corrosion layers developed on top and bottom samples using SEM-EDX and XRD analysis provided additional insight into their distinctive characteristics.

The corrosion assessment by LPR was conducted under three different temperatures and a constant initial pH of 7, and the difference in corrosion rates at each temperature is depicted in Figure 6-42. At room temperature, top microelectrodes exhibited an initial decrease in corrosion rate from a value as high as 1.7 mm/year to a value as low as 1.3 mm/year within the first 24 hours followed by a gradual increase before stabilisation at approximately a corrosion rate around 1.9 mm/year. Nonetheless, the corrosion rate observed on the bottom samples remained consistently at approximately 0.9 mm/year for the initial 120 hours, after which it declined, ultimately reaching 0.5 mm/year by the end of the test.

At 150°C, the corrosion rate determined from the top sample follows a similar pattern of corrosion rate evolution as the one recorded at room temperature but remains consistently below the observed corrosion rate value at room temperature across most of the experimental duration up to 150 hours before it becomes more corrosive. On the contrary, the bottom samples exposed to a temperature of 150°C demonstrated the most minimal corrosion rate in the context of CUI at pH 7. The corrosion rate commenced at a value of 0.5 mm/year and gradually increased to reach a maximum of 0.8 mm/year by the end of the test. Notably, during the initial 100 hours of the experiment, the corrosion rate consistently maintained its lowest levels, subsequently surpassing the corrosion rate observed in the bottom samples subjected to room temperature conditions.

In contrast, at 80°C, the environment exhibits a continuous and progressive rise in the corrosion rate of top samples, starting at 1.5 mm/year and culminating at 2.6 mm/year. This trend was observed by Yang and Liu [100], wherein the calculated polarisation resistance decreased from approximately 0.4 KΩ·cm² at the commencement of the test to roughly 0.16 KΩ·cm² after a 7-day exposure period. In the context of the bottom samples, the corrosion rate displayed a notably consistent behaviour. It remained nearly constant, at approximately 1.5 mm/year, during the initial 80 hours of exposure. Following this phase, a gradual reduction was observed, reaching its lowest point at 1.1 mm/year around 140 hours. Subsequently, there was a slight increase in the corrosion rate value, leading to a final corrosion rate of 1.4 mm/year by the end of the testing duration. These findings underscore the significant influence of temperature on corrosion kinetics under thermal insulation.

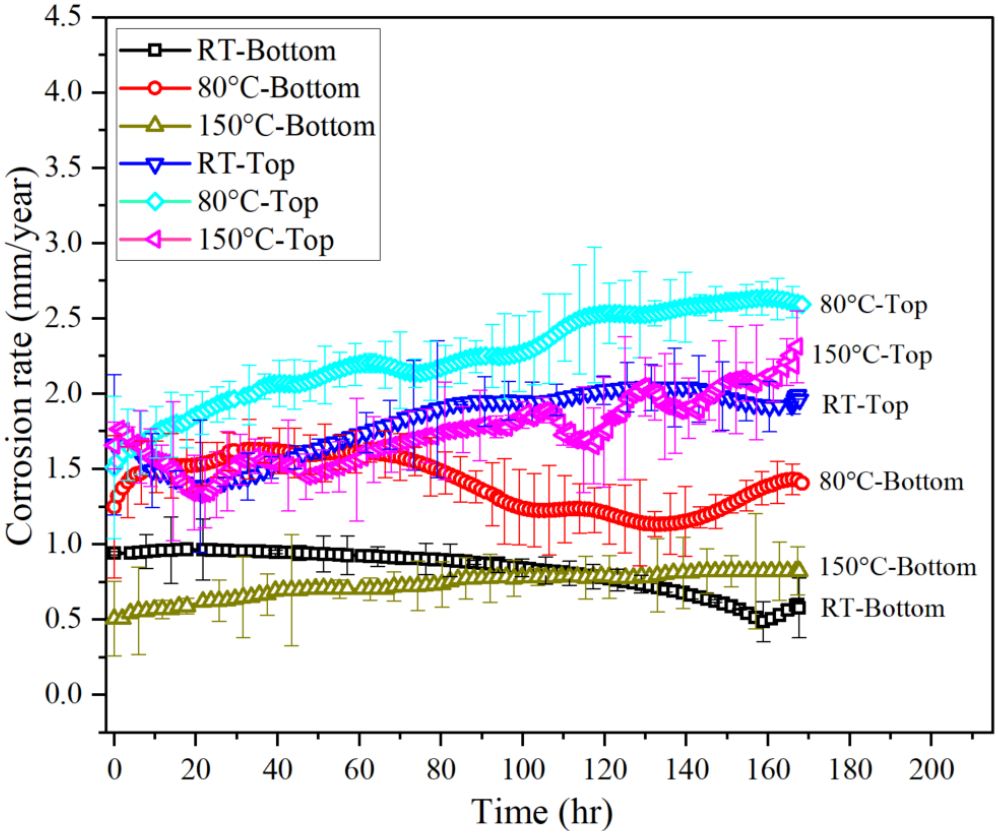

Figure 6-42: Corrosion rate under thermal insulation by LPR for samples exposed to 3.5% NaCl, pH 7 for 168 hours at room temperature (RT), 80C and 150C for top and bottom samples

In summary, regardless of the temperature, it appears that the rate of CUI recorded in the bottom samples is consistently lower than that recorded in the top samples. The higher corrosion rate observed at the top can be attributed to several factors. Firstly, in this research, the brine solution was directed onto the top of the insulation, differing from the ASTM G189 standard. This deliberate variation aimed to replicate real-world conditions encountered in the field, where the brine must traverse the insulation before reaching the substrate. This process could lead to the leaching of ions from the insulation or potential ion adsorption by the insulation during conveyance. Furthermore, pumping the brine directly onto the steel surface of the pipe facilitates the circulation of the brine around the pipe's circumference, ensuring a uniform chemical composition of the brine on the top and the bottom samples. Additionally, the bottom samples are situated at a slight distance from the injection point, which may influence the initial chemical composition of the brine near the bottom samples. The depletion in oxygen within the bottom sample could potentially explain the reduced corrosion rate, as it is anticipated that in CUI, the primary cathodic reaction would involve the reduction of oxygen [50].

The rate of CUI at the top and the bottom samples (12 and 6 o'clock, respectively) at 150°C is lower than the one recorded at room temperature which in turn is lower than CR recorded at 80°C. Raising the operational temperature, specifically within the interval of 49 to 93°C, has been posited to accelerate electrochemical reactions, resulting in an exacerbation of the ensuing mass loss [192]. The mechanism driving the accelerated corrosion rates in substrate materials at 80°C is proposed to be linked to the accumulation of corrosive species on the metal surface, occurring as a result of water evaporation and the subsequent reduction in brine thickness which would increase the path for the diffusion of corrosive species such as chloride and oxygen [193, 194]. Furthermore, it is noteworthy that the CUI rate is predominantly controlled by the diffusion of oxygen. This phenomenon is intricately linked to the key electrochemical processes underlying CUI, specifically, the oxidation of iron (anodic reaction) and the reduction of oxygen (cathodic reaction) [50].

In Figure 6-43 the corrosion rates determined by mass loss are depicted. Notably, irrespective of the temperature conditions, the corrosion rate calculated from the top samples consistently surpasses that of the bottom samples. The highest recorded corrosion rate was observed at 80°C on the top samples, with a corrosion rate value reaching 4.6 mm/year, while the lowest corrosion rates were found to be approximately 1.1 mm/year for the bottom samples at room temperature.

The corrosion rate, as determined by mass loss measurements under thermal insulation, consistently surpasses the corrosion rate calculated via the LPR technique across various temperature conditions and positions. The percentage difference between the corrosion rate values varies, ranging from as low as 26% for the top sample at room temperature to as high as 51% for the bottom sample at 80°C. In a study conducted by Yang and Lui [100], a 36% difference was observed for CUI experiments at 93°C, assuming a Stearn-Geary constant of 0.026 V/decade. Additionally, Martinelli-Orlando and Angst [195], reported a corrosion percentage difference of 42% for carbon steel exposed to artificial seawater, assuming a Tafel constant of 0.026 V/decade. These variations can likely be attributed to underlying assumptions associated with Tafel constants.

In a broader context, the corrosion rates calculated through LPR, when employing microelectrodes, closely align with those obtained through mass loss coupon experiments.

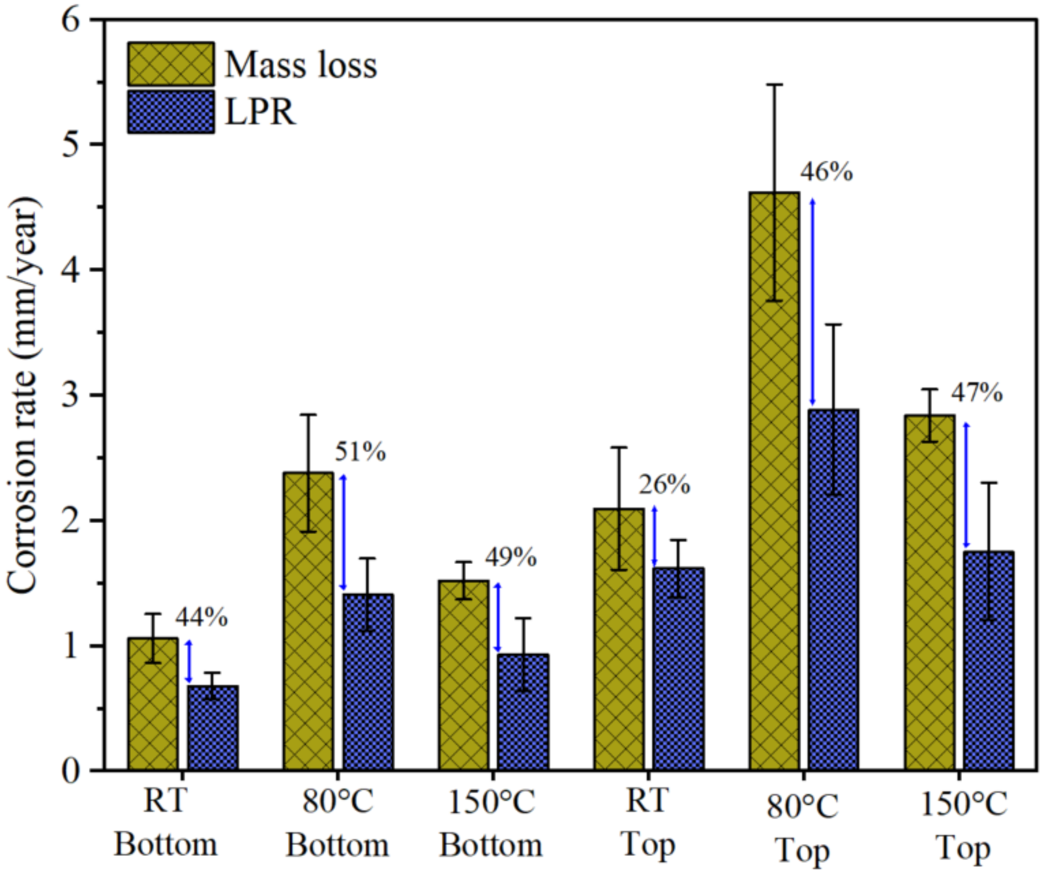

Figure 6-43: Comparison of corrosion rate by mass loss and LPR for top and bottom samples exposed to 3.5% NaCl brine, pH 7 at room temperature (RT), 80°C and 150°C

Summary of characteristics of corrosion layer formed on the steel surface at pH 7

Figure 6-44 and Figure 6-45 depict the elemental distribution of chloride within the cross-sectional corrosion layers, for the top and bottom samples, respectively, that developed on steel surfaces exposed to 3.5% NaCl at pH 7 for 168 hours. The exposure occurred under varying conditions: room temperature, 80°C, and 150°C.

Regarding the chemical composition of the formed corrosion layers on the top samples, the EDX maps reveal distinct patterns, per Figure 6-44. At room temperature, the elemental distribution maps indicate a minor presence of chloride within the inner layer, particularly at the interface between the corrosion layer and the steel surface. This aligns with previous studies, which suggested that β-FeOOH (akageneite) tends to form in this region during the slow oxidation of iron complexes containing chlorine [104, 186].

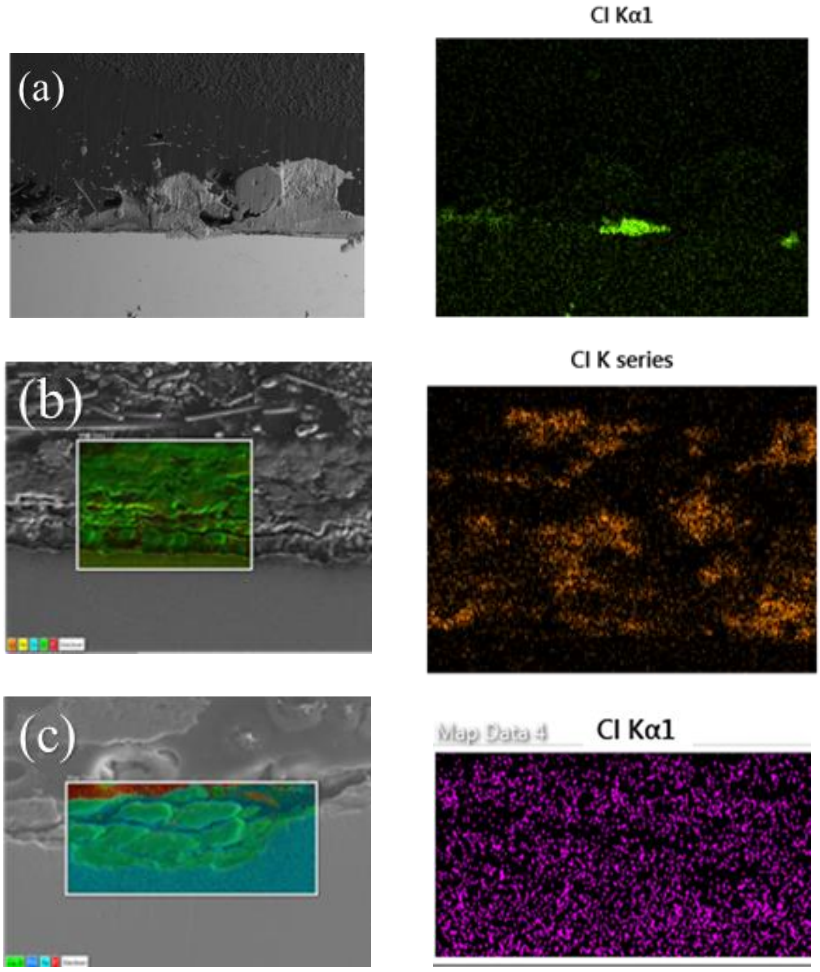

Figure 6-44: The distribution of iron-Fe, oxygen-O, chloride-Cl and carbon-C in the corrosion layer formed on the bottom samples exposed to 3.5% NaCl, pH7 at (a) room temperature, (b) 80°C and (c) 150°C by EDX mapping

Furthermore, as the temperature increases, there is a noticeable increase in chloride concentration within the corrosion layer, specifically at 80°C. This observation provides compelling evidence that elevated temperatures enhance the diffusion of Cl^- contributing to altered corrosion layer compositions as suggested by Pan, et al.

[186]. In the context of CUI, chloride's influence encompasses multiple mechanisms. Firstly, chloride ions can initiate phase transformations within the corrosion layer, potentially altering its protective properties [196]. Secondly, certain rust phases that contain chlorides are soluble, resulting in a notable enhancement of electrolyte conductivity [197]. Lastly, hygroscopic chlorides have the capacity to absorb moisture from the atmosphere, thereby facilitating the generation of electrolytes [198].

Nonetheless, the EDX mapping of the bottom samples unveiled a notable escalation in chloride content within the corrosion layer as temperature increased, as illustrated in Figure 6-45. Interestingly, at 150°C, the corrosion layer formed was dense and exhibited strong adhesion to the surface, potentially explaining the reduced corrosion of steel under this condition compared to the one observed at 80°C. It's worth noting that chloride presence was scarcely detected at room temperature, which could account for the lower concentration of β-FeOOH and, consequently, the reduced corrosion rate observed.

It is important to note that the constant experimental parameters, such as the thermal insulation thickness, the position of the injection point, and the rate of brine injection, are constant whatever the temperature. Therefore, the only variable that distinguishes these conditions is the internal pipe temperature. Consequently, chloride behaviour is solely affected by temperature. As the temperature increases, the rate of chloride diffusion increases. However, when the temperature exceeds the boiling point, there may be less brine reaching the steel surface than at 80°C, thereby decreasing the amount of chloride available for diffusion. Thus, there is a direct relation between the corrosion rate and the chloride deposition.

The XRD patterns of the corrosion layers that formed on both the top and bottom samples, after exposure to 3.5% NaCl at pH 7 and under varying temperature conditions (room temperature, 80°C, and 150°C), are presented in Figure 6-46. In essence, the temperature rise has had no notable impact on the predominant composition of the corrosion products. Four distinct crystalline phases were identified, including α-FeOOH (01-084-8280), γ-FeOOH (01-074-6247), β-FeOOH (04-008-9457) and Fe_3O_4 (04-021-0451).

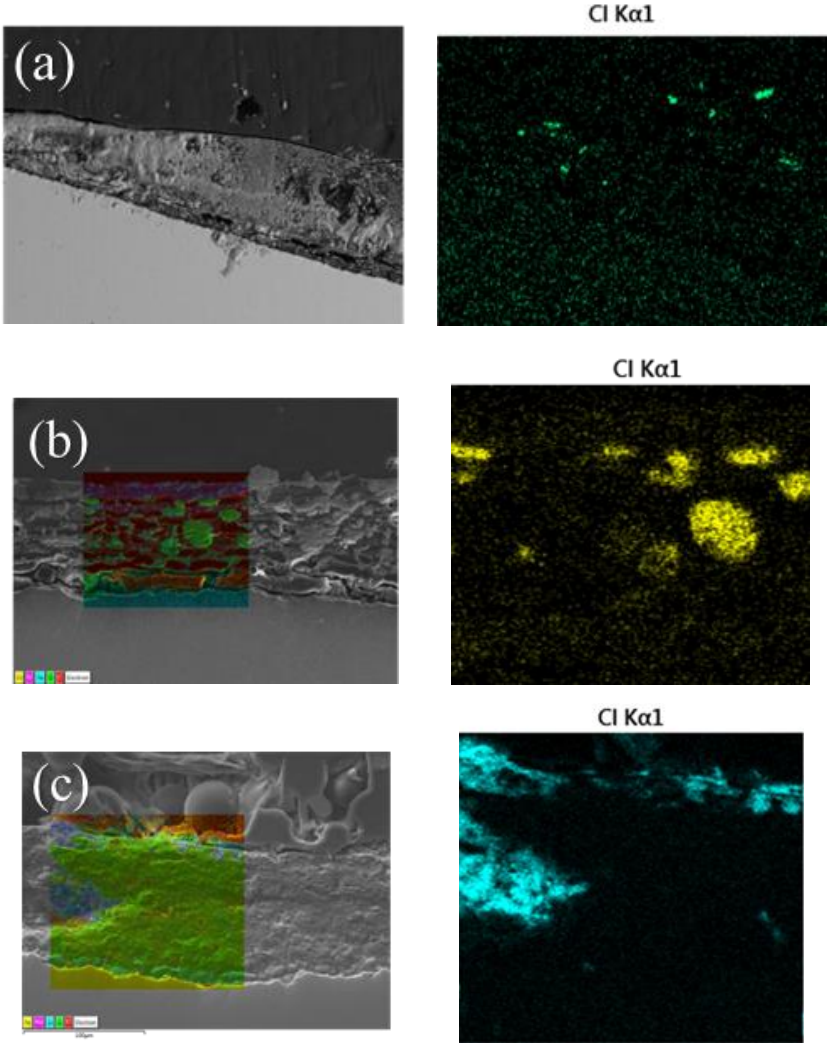

Figure 6-45: The distribution of chloride-Cl corrosion layer formed on the bottom samples exposed to 3.5% NaCl, pH7 at (a) room temperature, (b) 80°C and (c) 150°C by EDX mapping

While the possibility of maghemite's presence as a phase was considered, due to its structural similarity to magnetite [150], it was assumed that the phase identified in this analysis is indeed magnetite. This assumption was made because the XRD peaks of these two phases would overlap, making it challenging to distinguish them accurately.

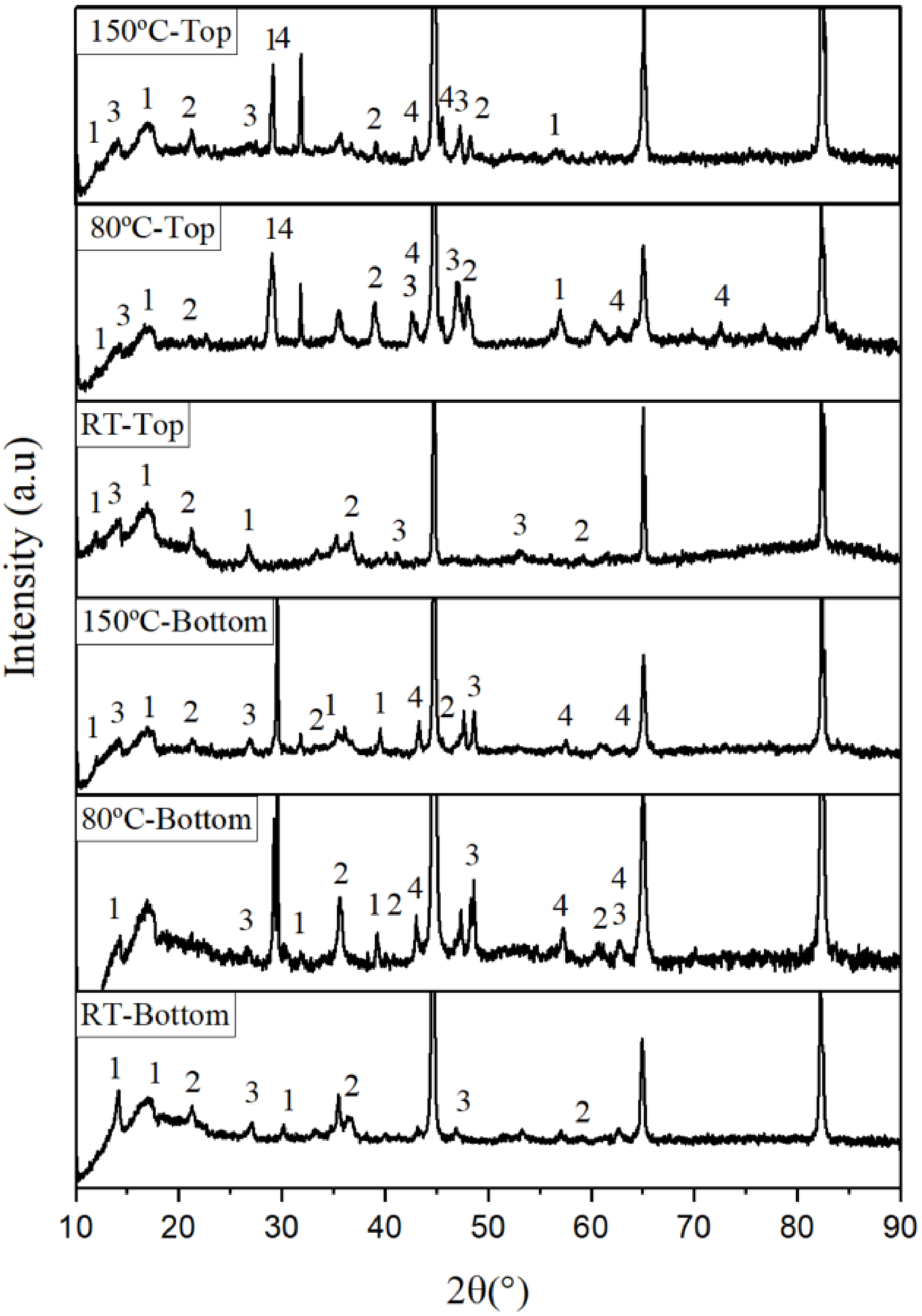

Figure 6-46: The XRD patterns of the phase composition of the corrosion layer formed on the surfaces of both the top and bottom samples exposed to 3.5%NaCl, pH 7 and at room temperature, 80°C and 150°C

Figure 6-47 presents the relative oxide content within the corrosion layers formed on both the top and bottom samples. Notably, the composition of each oxide varies between the top and bottom samples. The akaganeite content is higher in the top samples compared to the bottom samples, with the highest levels recorded at 80°C for both sets. This increase in temperature, from room temperature to 80°C, enhances chloride diffusion [186], consequently elevating the relative content of akaganeite. However, as the temperature reaches 150°C, the relative content of akaganeite diminishes. This can be attributed to reduced dissolved oxygen, resulting in a decrease in OH^- concentration and subsequently a decline in the relative content of akaganeite. Additionally, at 150°C, there may be minimal brine reaching the substrate, due to brine evaporation and the entrapment of chloride within the insulation material. The presence of akaganeite within the corrosion layer tends to increase the corrosion rate due to its high reactivity, as well as when combined with lepidocrocite [199].

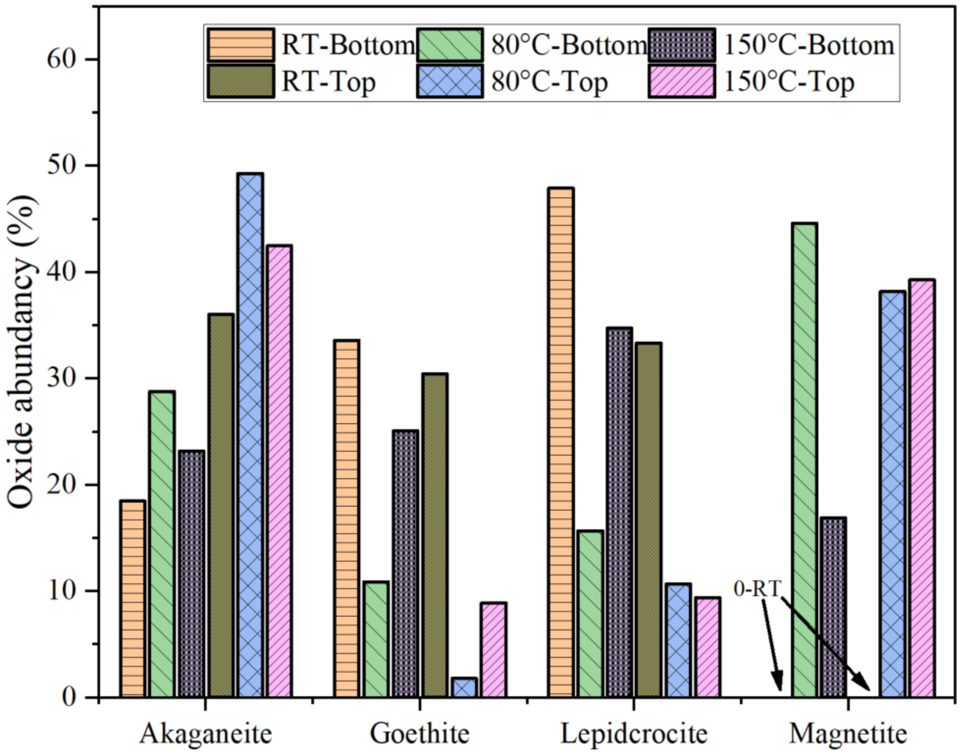

Figure 6-47: A semi-quantitative analysis of the corrosion layers formed on the steel surfaces for both the top and bottom samples at room temperature (RT), 80°C, and 150°C reveals the presence and relative amounts of akaganeite, goethite, lepidocrocite, and magnetite

In addition, the relative content of lepidocrocite decreases with increasing temperature, while the relative content of magnetite, especially in the top samples, rises. Magnetite stands out as the sole conductive corrosion product among oxyhydroxide corrosion products [200]. Consequently, having magnetite in the corrosion layer can accelerate the corrosion rate through galvanic coupling.

In contrast, goethite is considered a thermodynamically stable and protective corrosion product [201]. Notably, the lowest goethite content was observed at 80°C in the top samples, which corresponded to the highest corrosion rate in this case.

The Protective Ability Index (PAI_2) of the corrosion layer formed on the steel surface under thermal insulation is determined using equation 3-11. This calculation relies on the mass ratio of akaganeite, lepidocrocite, and magnetite, with the condition that this ratio remains below 1. A lower PAI_2 value indicates a more protective corrosion layer [150]. In Figure 6-48 the PAI_2 values are presented as a function of operating temperature for both the top and bottom samples. It is evident that for both the bottom and top samples, the highest PAI_2 was noted at 80°C, while conversely, the lowest PAI_2 value was determined at room temperature for both sets of samples. These findings align with the corrosion rate results obtained through the mass loss technique as depicted in Figure 6-48. In a separate study [202], it was

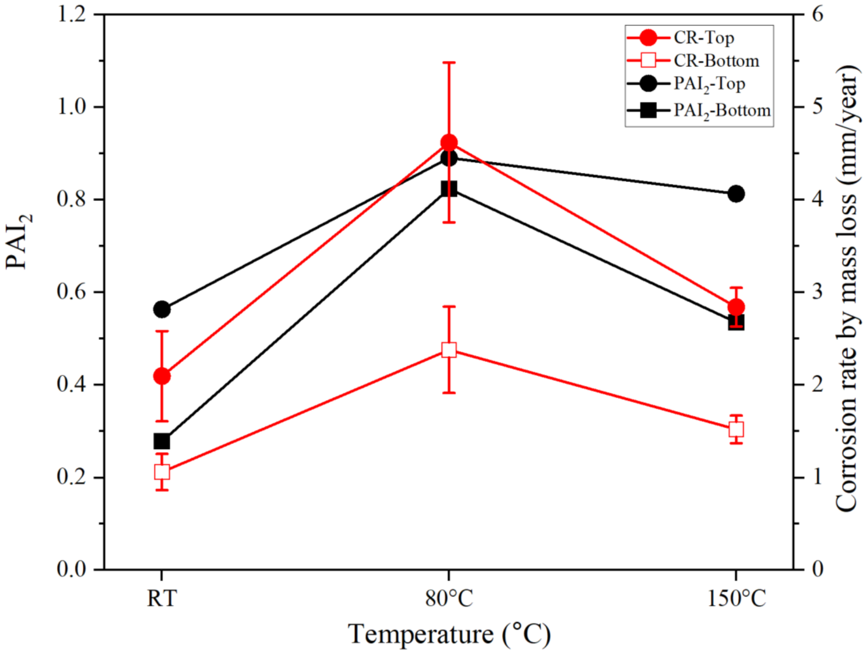

Figure 6-48: Variation of PAI_2 and corrosion rate with temperature for top and bottom samples

observed that higher values of PAI_2 were directly correlated with the presence of soluble chloride ions in the environment.

The Raman spectra of the corrosion layers grown on both the top and bottom samples, subjected to different temperatures (room temperature, 80°C, and 150°C) at pH 5, are depicted in Figure 6-49. The peaks corresponding to lepidocrocite and akageneite are consistently detected in all samples. Specifically, common peaks associated with lepidocrocite are observed in the range of 219-225 and 250 cm^{-1}, while akageneite exhibits characteristic peaks in the range of 714-730 cm^{-1}.

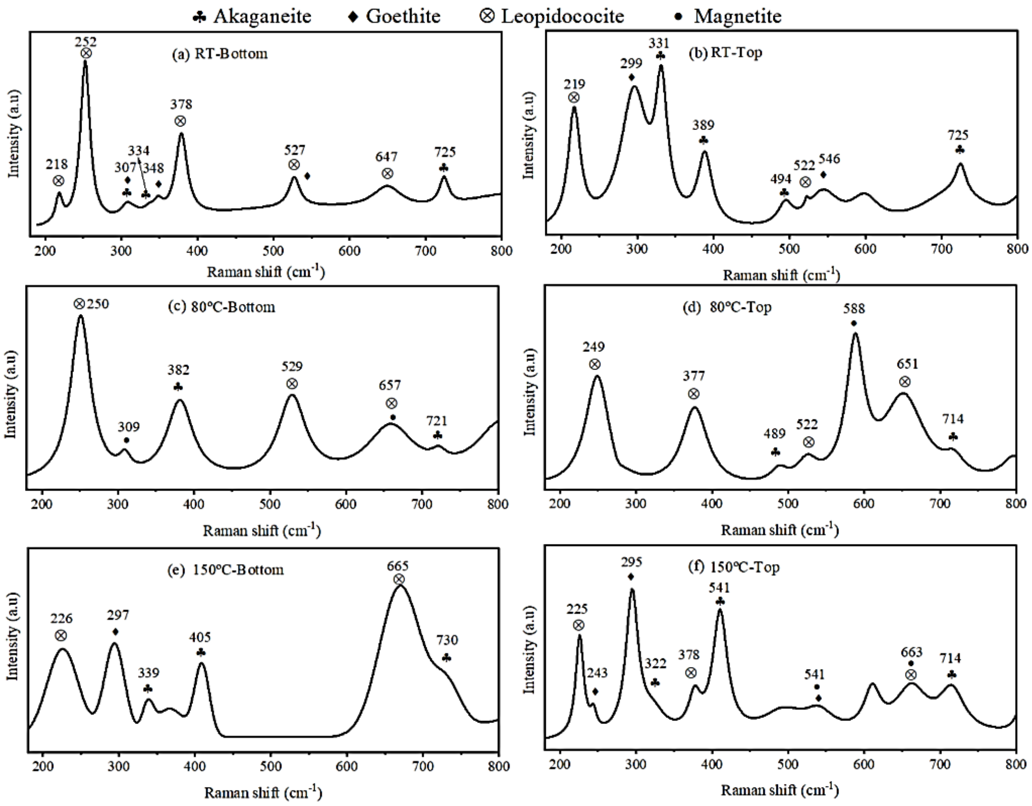

Figure 6-49: Raman spectra of corrosion layers grown on the surface of both top and bottom samples after being exposed to 3.5 NaCl, pH 5 for 168, (a)room temperature-bottom, (b) room temperature- top, (c)80°C-bottom, (d) 80°C-top, (e) 150°C-bottom, and (f) 150°C-top

Notably, the absence of goethite peaks is observed at 80°C for both the top and bottom samples. Furthermore, magnetite peaks are not detected at room temperature for either the top or bottom samples. Additionally, at 150°C, the bottom sample does not exhibit detectable magnetite peaks.

These findings emphasize the impact of temperature on the composition of the corrosion layers, as certain iron oxide phases such as goethite and magnetite appear to be influenced by temperature variations.

6.3 Characterisation of CUI at pH 5

6.3.1 Evaluation of CUI at pH 5 and room temperature

6.3.1.1 Visual inspection

Upon the completion of the experiment, the coupons were carefully extracted from the test rig, and the developed corrosion layers were documented using a mobile phone camera. Figure 6-50 visually presents the corrosion layers that formed on both (a) the top samples and (b) the bottom samples.

From the captured images, it is evident that the top samples exhibited a different feature: thermal insulation fibres appear to be adhering to their surfaces. In contrast, no such fibres were observed on the bottom samples. In terms of corrosion surface coverage, both the top and bottom samples are notably covered by the corrosion layer across almost their entire surfaces.

The corrosion layer on the bottom sample exhibits a distinctive two-colour appearance, featuring black as the representation of the inner layer and light brown as the external colouration. In addition, this corrosion layer appears to have a relatively weak attachment to the steel substrate, as it could be easily removed from the surface. Conversely, the corrosion layer on the top samples primarily comprises two distinct colours, black and reddish brown.

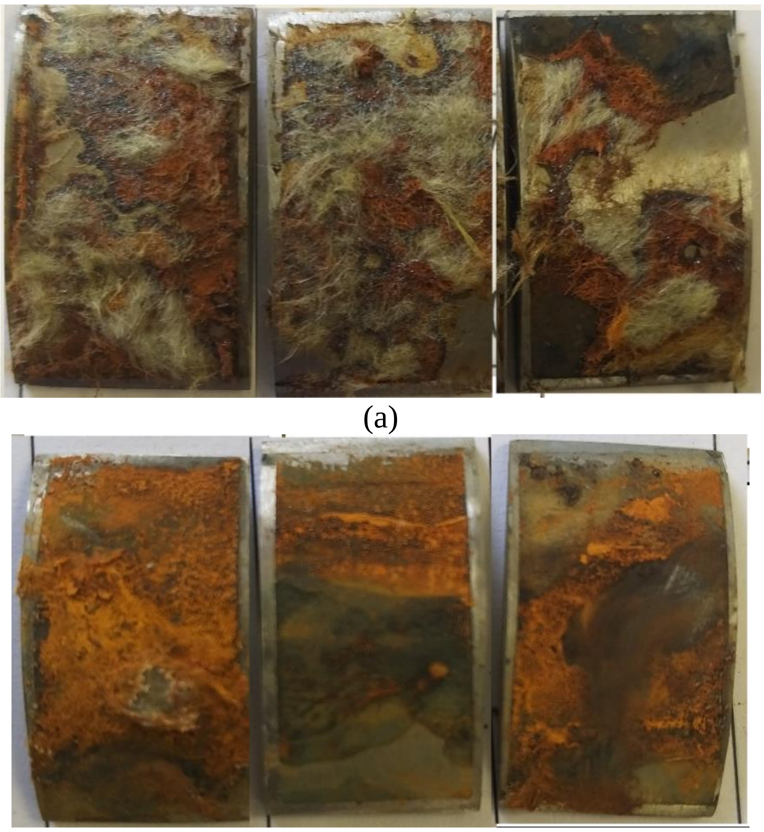

(a)

(b)

Figure 6-50: Digital images of mass loss coupon after being exposed to 3.5% NaCl for 168 hours at room temperature, (a) top samples, and (b) bottom samples

6.3.1.2 Characterisation of the CUI rate at room temperature and pH 5

Figure 6-51 illustrates the variation in corrosion rates, as determined by LPR, for both top and bottom samples exposed to a 3.5% NaCl solution for 168 hours. During the initial 60 hours, both samples displayed nearly constant corrosion rates, with values of approximately 1.9 mm/year for the top sample and 1.4 mm/year for the bottom sample. Subsequently, the corrosion rates began to rise before stabilizing. After 93 hours of exposure, the corrosion rate for the bottom sample reached a steady level of 1.9 mm/year, while the top sample took 125 hours to reach a stable corrosion rate of 2.7 mm/year. This observed change in corrosion rate is likely attributable to alterations in the chemical properties of the brine solution over time.

Table 6-7 presents the corrosion rates determined through mass loss measurements for both the top and bottom samples following a 168 hour exposure to a 3.5% NaCl solution with a pH of 5. Interestingly, the average corrosion rate for the top samples exceeds that of the bottom samples by approximately 1 mm/year.

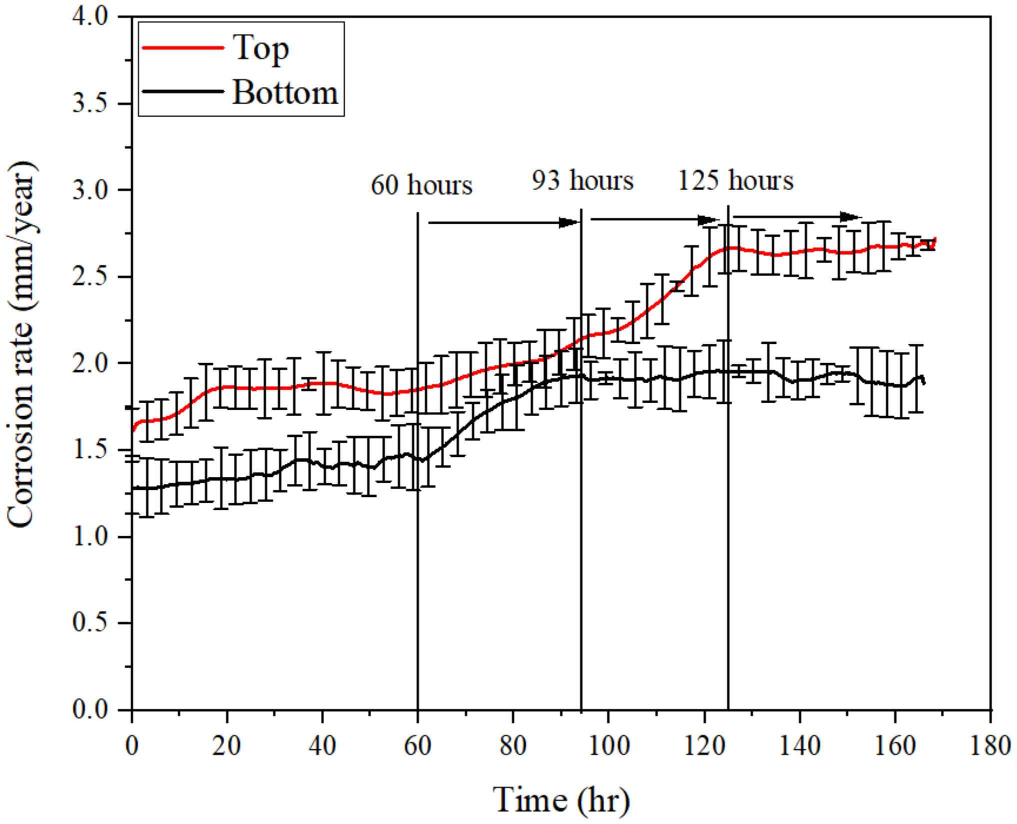

Figure 6-51: Corrosion rate determined by LPR for top and bottom microelectrodes samples after exposure to 3.5%NaCl, room temperature for 168 hours

Table 6-7: The corrosion rate by mass loss for top and bottom samples exposed to 3.5% NaCl and pH 5 brine at room temperature over 168 hours of exposure

Sample position	Initial mass (g)	Final mass (g)	Corrosion rate (CR) (mm/year)	Avg. CR (mm/year)
Top	7.429	7.268	3.096	3.237
	8.092	7.918	3.346	
	7.719	7.549	3.269	
Bottom	8.513	8.401	2.154	2.205
	8.119	7.996	2.365	
	7.588	7.479	2.096	

In Figure 6-52 a comparison of corrosion rate measurements was obtained through the utilization of two distinct techniques: mass loss and LPR. These methodologies were employed to evaluate the rate of CUI exhibited by both the top and bottom samples, which were subjected to 168 hours within a corrosive brine, consisting of a 3.5% NaCl solution at room temperature. The dataset unveils disparities in the corrosion rate values discerned between the two measurement methodologies. For the top sample, the corrosion rate determined via mass loss analysis was quantified at 3.23 mm/year, whereas the LPR technique yielded a lower value of 2.72 mm/year. However, in the case of the bottom sample, the mass loss approach rendered a corrosion rate of 2.20 mm/year, while the LPR technique yielded a reduced rate of 1.89 mm/year. Nevertheless, the differences in corrosion rate values between the mass loss and LPR measurements are minimal, indicating that both techniques can be regarded as comparable.

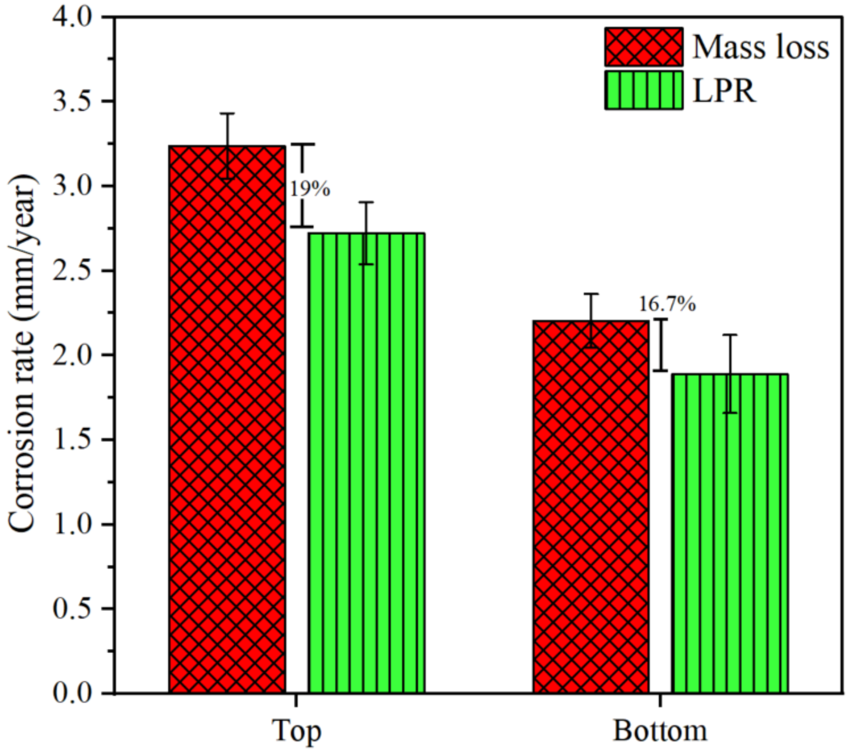

Figure 6-52: Comparison corrosion rate calculated by LPR and mass loss techniques for top and bottom samples after being exposed to 3.5% NaCl brine at room temperature for 168 hours

6.3.1.3 SEM micrographs

Figure 6-53 presents SEM topographic micrographs of the corrosion layers developed on the steel surfaces of both the top and bottom samples. A detailed examination of the corrosion layer formed on the top samples (a-b) reveals a notable observation: insulation fibres are visibly adhered to the surface, with subsequent corrosion growth occurring around these fibres. This observation not only underscores the presence of insulation material but also suggests a significant level of insulation deterioration. Conversely, when examining the corrosion layers on the bottom samples (c-d), there is an absence of apparent insulation fibres adhering to the surface. However, it is worth noting the existence of microcracks within the corrosion layer. In a broader context, the SEM micrographs do not distinctly display characteristic features of corrosion products on either the top or bottom samples.

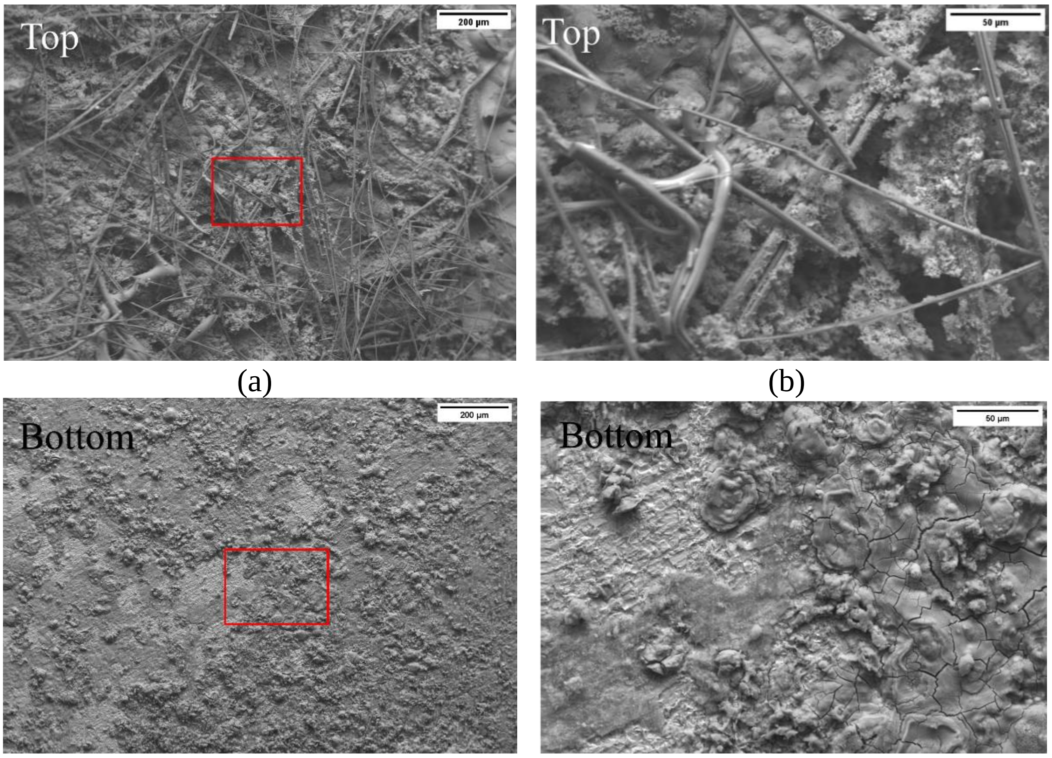

(a) (b)

(c) (d)

Figure 6-53: SEM micrographs of corrosion layer grown on the surface of steel exposed to 3.5% NaCl brine, pH 5 at room temperature for 168 hours, (a-b) top samples, (c-d) bottom sample

Figure 6-54 provides cross-sectional scanning electron microscope (SEM) micrographs detailing the corrosion characteristics of both the top and bottom samples. In the SEM micrographs of the top samples (a-b), it is discernible that the corrosion layer exhibits instances of cohesive failure in certain regions. Additionally, the corrosion film's thickness exhibits a range between approximately 41 and 75 µm, as illustrated in Figure 6-55 (a). The average thickness of the corrosion layer is calculated to be 55 µm. Nevertheless, it is essential to acknowledge a potential source of inaccuracy in the thickness measurement of the top sample. This measurement was carried out after the removal of the insulation fibres from the corrosion layer, which could have inadvertently taken some corrosion products with them during the removal process.

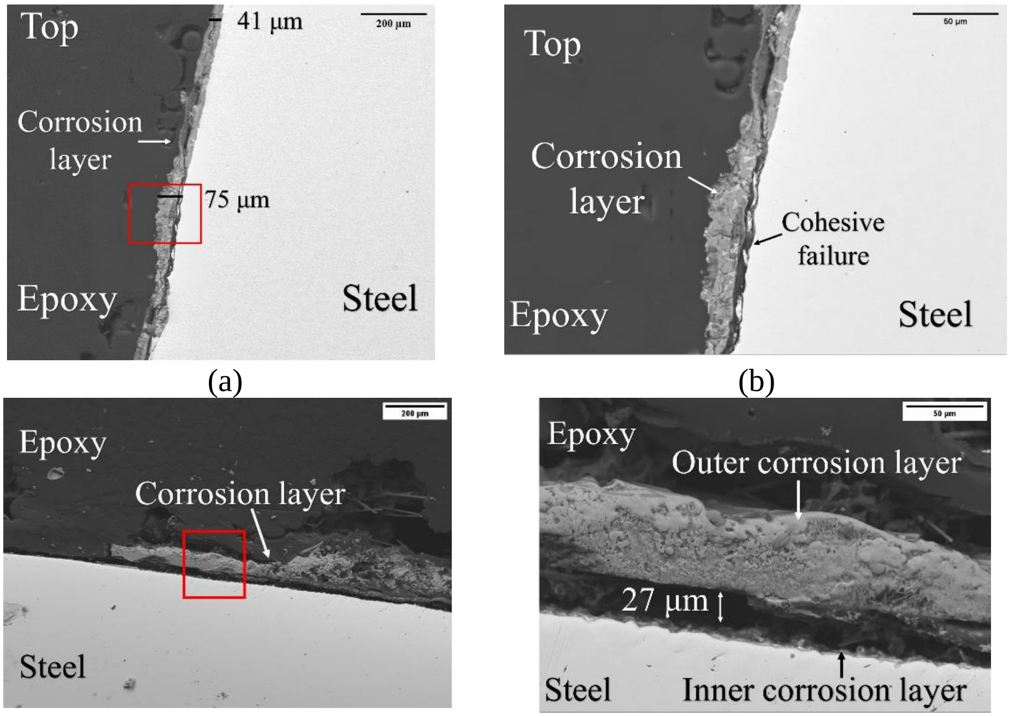

(a) (b)

(c) (d)

Figure 6-54: SEM micrographs for cross-section corrosion layer grown on the surface of (a-b) top sample, and (c-d) bottom samples, after being exposed to 3.5% NaCl, pH 5 for 168 hours at room temperature

Conversely, the corrosion film formed on the bottom samples displays a distinctive structure, consisting of inner and outer corrosion layers. Notably, there exists an adhesion gap measuring 27 µm between these two layers as shown in 6-48 (d). Furthermore, the corrosion layer on the bottom samples demonstrates a notably greater thickness when compared to the top samples, with measurements ranging from 45 to 195 µm, as depicted in Figure 6-55 (b). The average thickness of the corrosion layer on the bottom samples is calculated to be 105 µm.

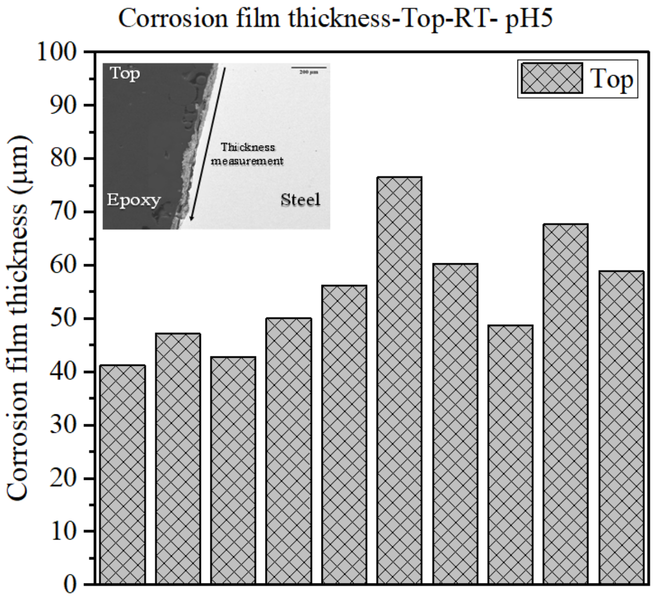

(a)

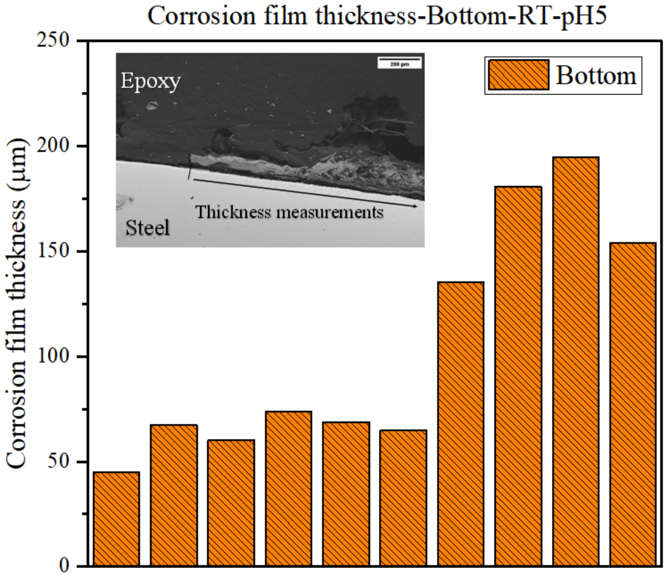

(b)

Figure 6-55: Corrosion film thickness grown on steel surface after being exposed to 3.5%NaCl, pH5, for 168 hours at room temperature, (a) top and (b) bottom

6.3.1.4 EDX analysis

Figure 6-56 and Figure 6-57 display the results of the EDX analysis conducted on the surface of the corrosion layers that formed on the top and bottom samples. In both instances, the presence of chloride is evident, suggesting its significant role within the composition of the corrosion layer. Notably, the top samples reveal the presence of silicon and calcium, which are likely to facilitate the adsorption of chloride ions (Cl^{-}) onto the surface. Such heightened chloride ion adsorption has the potential to accelerate the corrosion rate in this context.

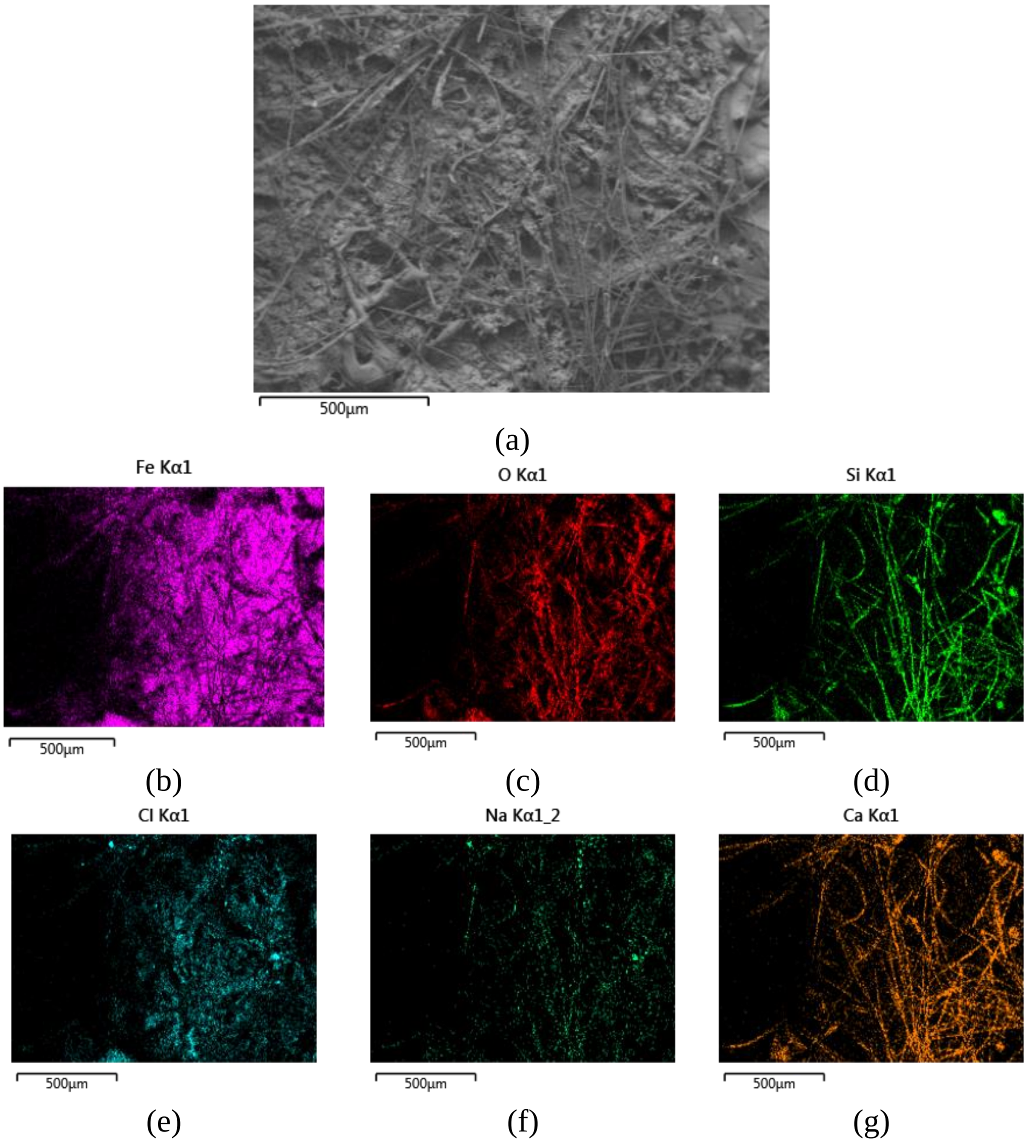

(a)

(b) (c) (d)

(e) (f) (g)

Figure 6-56: The distribution of elements in the corrosion layer grown on top after 168 hours of exposure to 3.5% NaCl, pH at room temperature brine, (a) micrograph image, (b) iron-Fe, (c) oxygen-O, (d) silicon-Si, (e) chloride-Cl, (f) sodium-Na and (g) calcium-Ca

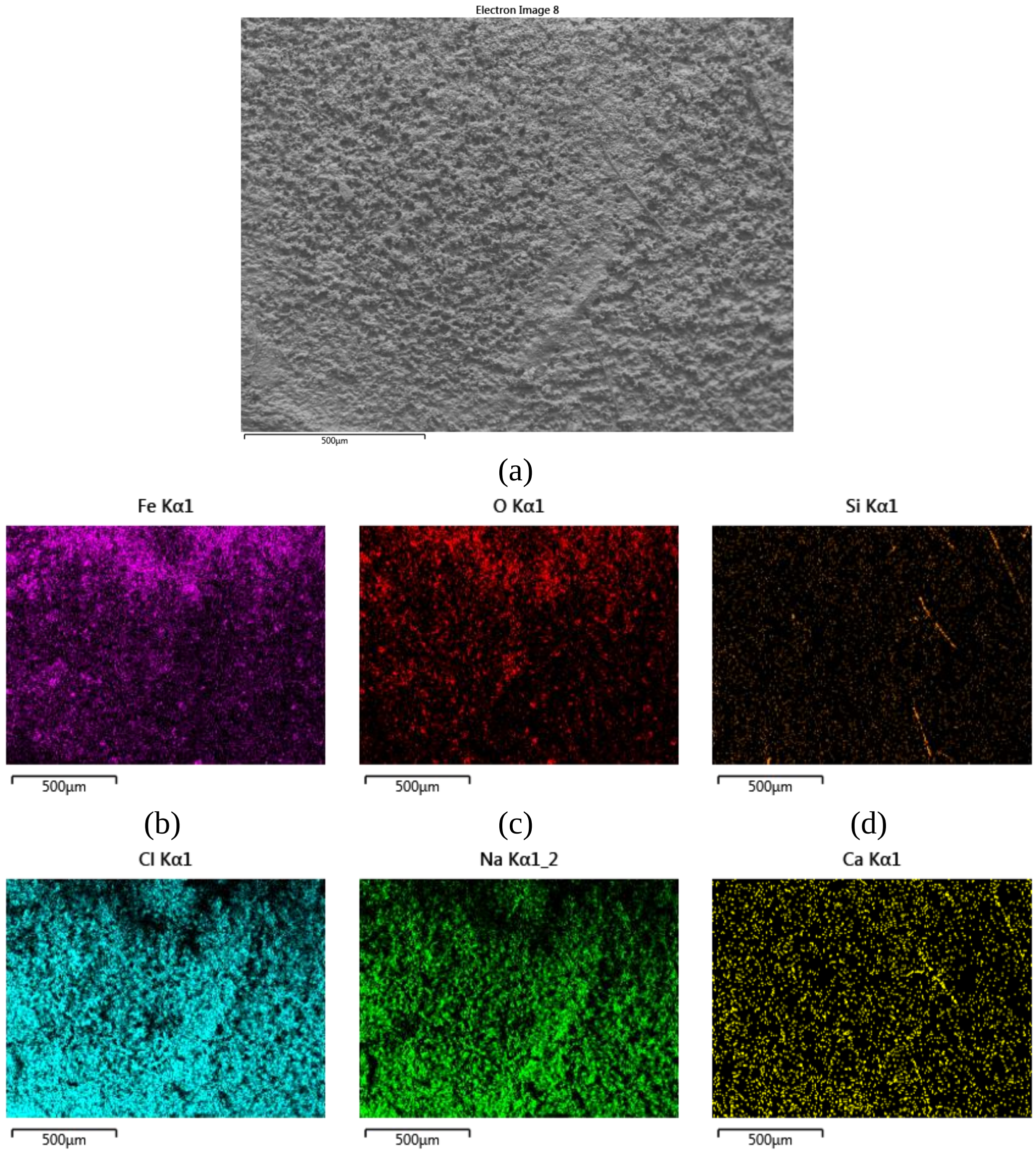

(a)

(b) (c) (d)

(e) (f) (g)

Figure 6-57: The distribution of elements in the corrosion layer grown on the bottom after 168 hours of exposure to 3.5% NaCl, pH at room temperature brine, (a) micrograph image, (b) iron-Fe, (c) oxygen-O, (d) silicon-Si, (e) chloride-Cl, (f) sodium-Na and (g) calcium-Ca

Furthermore, a detailed analysis was conducted using EDX mapping on the cross-sectional for both the top and bottom samples, as illustrated in Figure 6-58 and Figure 6-59. The findings from this analysis confirm the diffusion of chloride ions into the corrosion layer for both sets of samples. The chloride distribution within these layers appears to exhibit a uniform and consistent pattern.

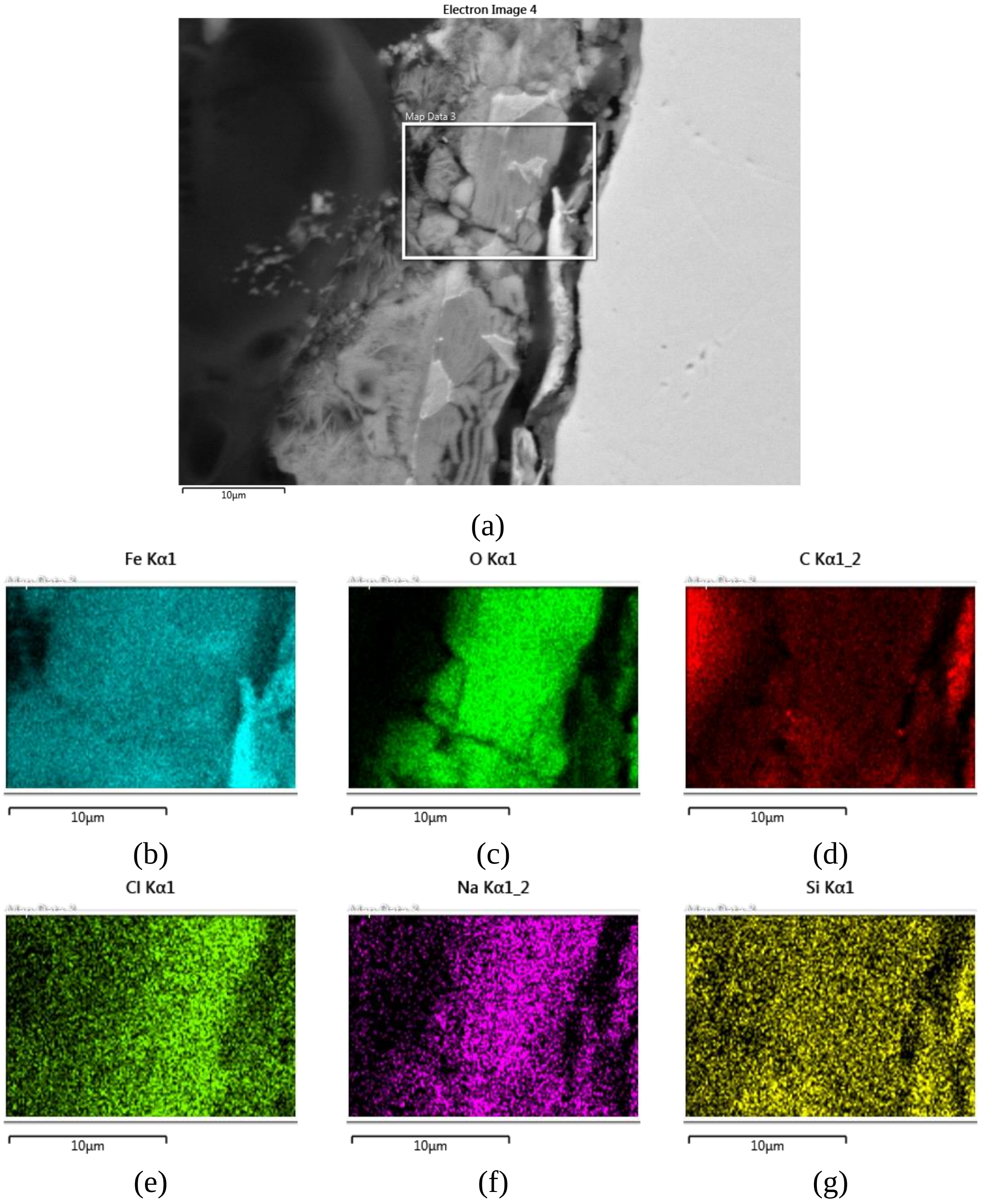

(a)

(b) (c) (d)

(e) (f) (g)

Figure 6-58: Cross-section of the distribution of elements in the corrosion layer grown on the top sample after 168 hours of exposure to 3.5% NaCl, pH at room temperature brine, (a) micrograph image, (b) iron-Fe, (c) oxygen-O, (d) carbon-C, (e) chloride-Cl, (f) sodium-Na and (g) silicon-Si

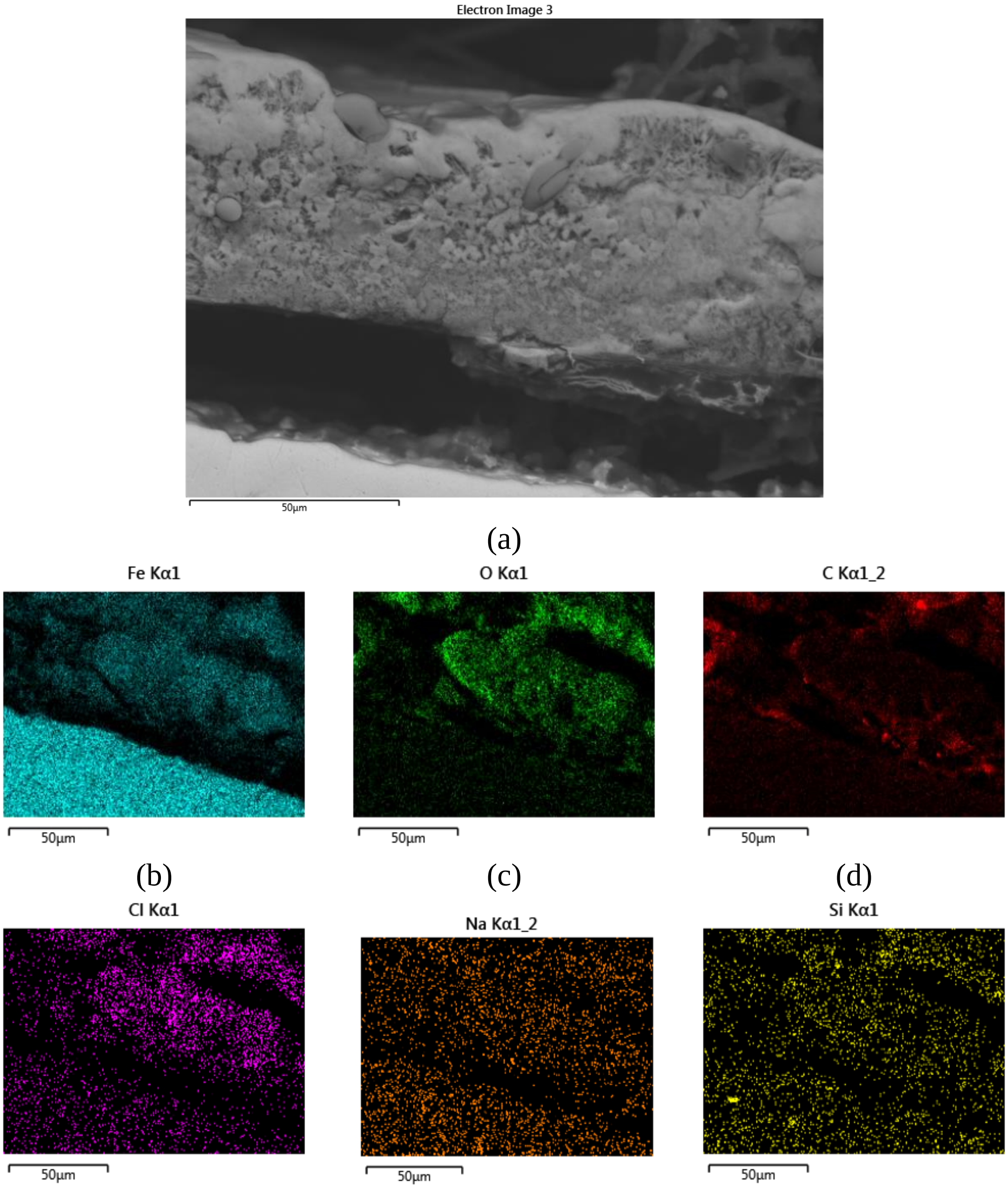

(a)

(b) (c) (d)

(e) (f) (g)

Figure 6-59: Cross-section of the distribution of elements in the corrosion layer grown on the bottom sample after 168 hours of exposure to 3.5% NaCl, pH at room temperature brine, (a) micrograph image, (b) iron-Fe, (c) oxygen-O, (d) carbon-C, (e) chloride-Cl, (f) sodium-Na, and (g) silicon-Si

6.3.1.5 Raman spectroscopy analysis of the corrosion layer

Figure 6-60 presents the Raman spectra obtained from the corrosion layers of both the top and bottom samples after being exposed to 3.5% NaCl brine with pH 5 for 168 hours at room temperature. Lepidocrocite: the top sample displays a higher band intensity at 246 cm^{-1} [121, 184], indicating a higher concentration of lepidocrocite

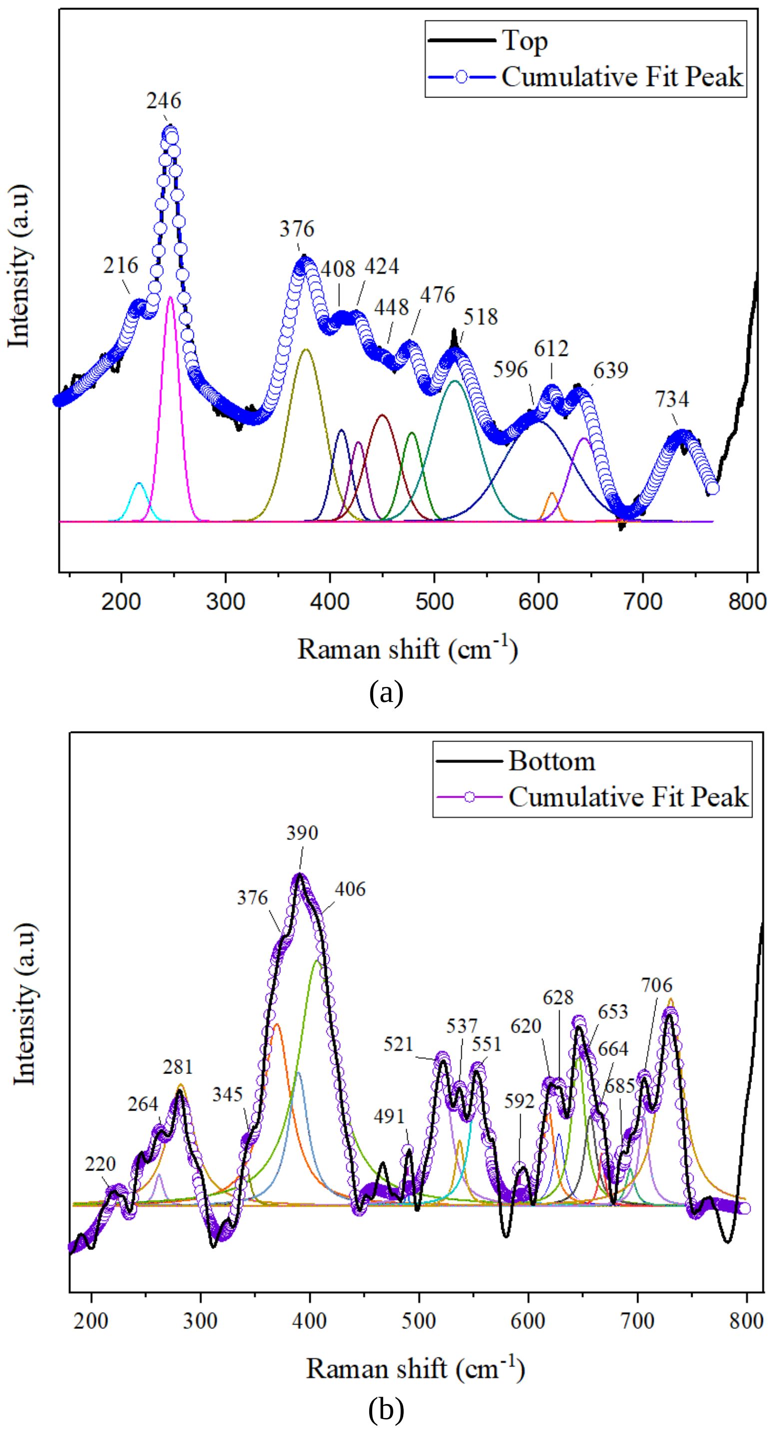

Figure 6-60: Raman spectra for corrosion layer grown on the surface of steel after being exposed to 3.5NaCl, pH 5 at room temperature for 168 hours, (a)top and (b) bottom

in comparison to the bottom sample. Lepidocrocite is further characterized by the presence of four distinct peaks at 216, 246, 380, and 518 cm^{-1} in the top sample [124, 203]. In the bottom sample, lepidocrocite is identified through four peaks at 220, 376, 521, and 653 cm^{-1} [203, 204]. The strongest peak at 390 cm^{-1} in the bottom sample suggests the presence of goethite in a high concentration (345, 390, 491, 551, 685 cm^{-1}). In the top sample, goethite is characterized by peaks at 424 and 476 cm^{-1}. Akageneite is identified by the presence of peaks at 408, 424, and 734 cm^{-1} in the top sample, and peaks at 406, 491, 537, and 685 cm^{-1} in the bottom sample. Peaks at 551, 653, and 664 cm^{-1} in the bottom sample are indicative of magnetite [121]. However, magnetite peaks were not detected in the top sample.

6.3.1.6 XRD analysis

Figure 6-61 displays the XRD pattern for both top and bottom samples, revealing the presence of akaganeite ($\beta - FeOOH$), lepdicrocite ($\gamma - FeOOH$), and magnetite (Fe_3O_4) within the corrosion layers grown on both samples. In particular, a slight increase in lepidocrocite peaks, specifically at 29° and 45.6°, is observed in the bottom sample. However, there are no notable alterations in the peaks associated with akaganeite and magnetite for either sample. Notably, goethite was absent in both samples.

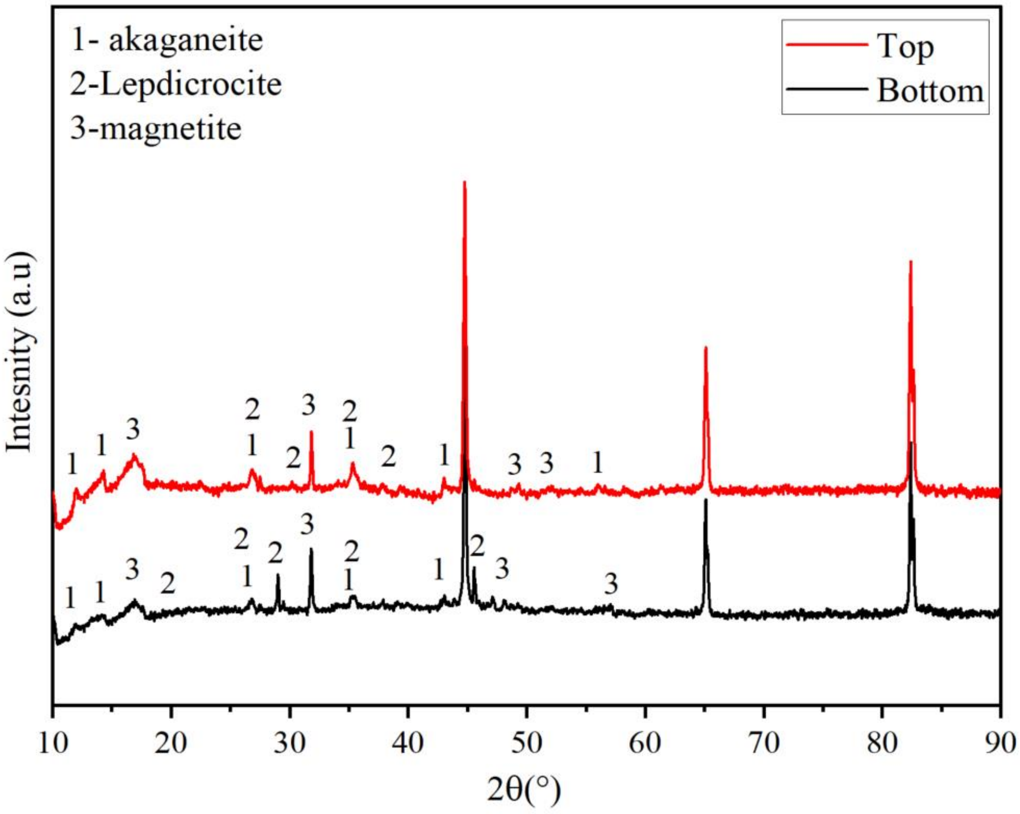

Figure 6-61: Corrosion phase composition for top and bottom samples by XRD after being exposed to 3.5 % NaCl, pH 5, for 168 hours at room temperature

The proportion of akaganeite in the top sample is marginally higher than in the bottom sample, attributable to the chloride presence within the corrosion layer with values of 45 and 40%, respectively. Conversely, the lepidocrocite proportion in the top sample is significantly lower compared to the bottom sample, with values of 19% and 34%, respectively. This divergence can be attributed to the increased deposition and diffusion of chloride in the corrosion process [150]. Magnetite exhibits an inverse trend, with abundance values of 36% for the top sample and 25% for the bottom sample. PAI_2 values are 0.72 for the top sample and 0.65 for the bottom sample. These values suggest that the corrosion layer developed on the top sample offers relatively less protection compared to the layer on the bottom sample.

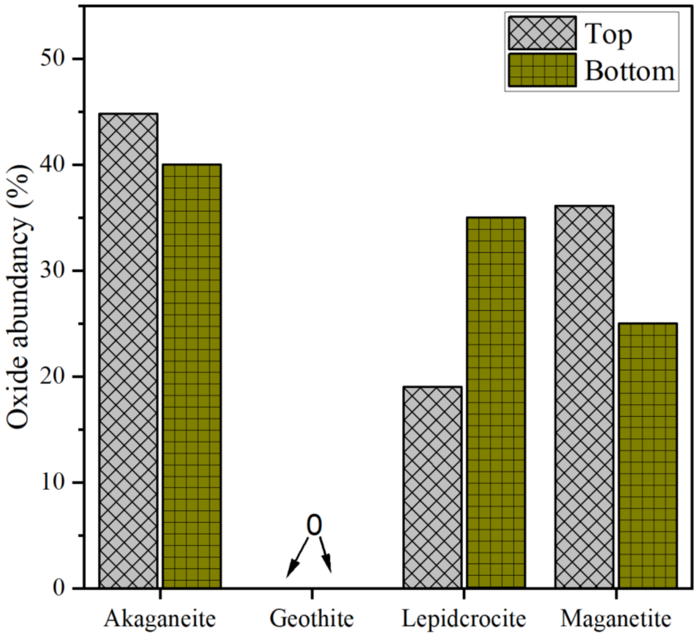

Figure 6-62: Semi-quantitative analysis of corrosion layer formed on the surface of top and bottom samples

6.3.2 Evaluation of CUI at pH 5 and 80°C

6.3.2.1 Characterizing the rate of CUI by LPR and mass loss

Figure 6-63 presents the corrosion rate data obtained through the LPR technique for both the top and bottom samples during their exposure to a 3.5% NaCl solution at a pH of 5, maintained at 80°C for 168 hours.

In the case of the top sample, the corrosion rate initially commences at approximately 2.1 mm/year and experiences an increase within the first 35 hours of exposure. Subsequently, the corrosion rate stabilises, maintaining a steady value of around 3.25 mm/year for the remainder of the test.

For the bottom sample, the initial corrosion rate is noted at 1.75 mm/year, followed by an increase to approximately 2.3 mm/year after 30 hours of exposure. Subsequently, the corrosion rate exhibits a sustained plateau for an additional 70 hours. However, after 100 hours of exposure, a slight upward trend in the corrosion rate is observed, culminating in a final value of 2.6 mm/year at the end of the test.

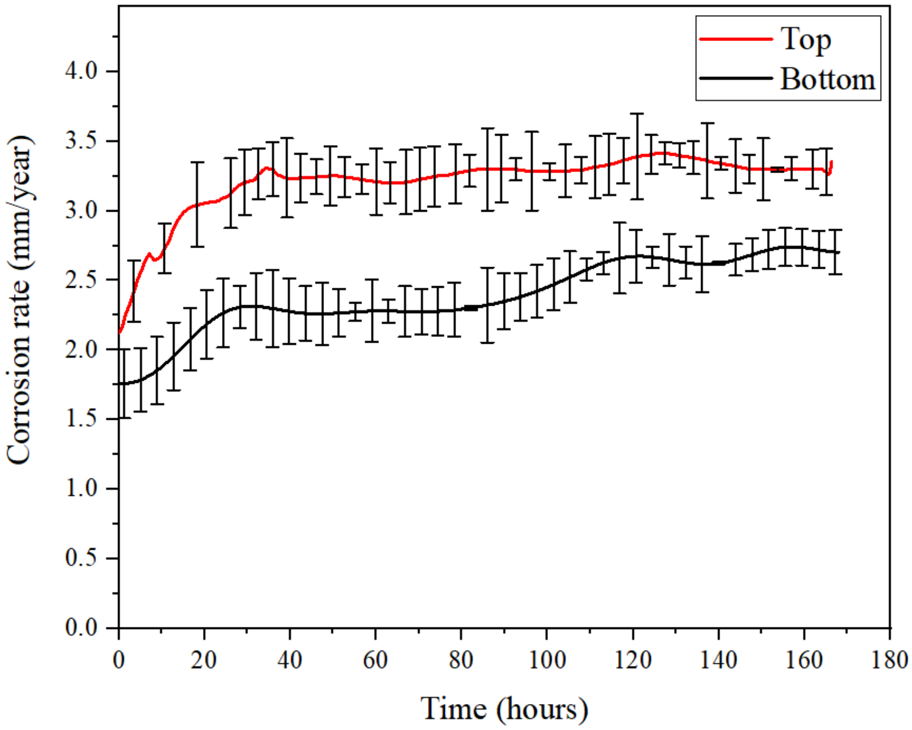

Figure 6-63: Corrosion rate determined by LPR for top and bottom samples exposed to 3.5% NaCl, pH5 for 168 hours at 80°C.

Table 6-8 provides a comprehensive overview of the average corrosion rates determined through the mass loss technique for both the top and bottom samples. The results indicate that the top samples exhibit a significantly higher corrosion rate, quantified at 4.013 mm/year, in contrast to the bottom samples, which display a marginally lower corrosion rate of 2.930 mm/year.

Moreover, a detailed comparison between the corrosion rates obtained through the LPR technique and the mass loss method is presented in Figure 6-64. This comparative analysis reveals that, for the top samples, the average corrosion rate, as determined by mass loss, stands at 4.013 mm/year, surpassing the corresponding LPR-derived rate of 3.3 mm/year. In addition, for the bottom samples, the corrosion rate calculated via mass loss is marginally higher, measuring approximately 2.930 mm/year, compared to the LPR-derived rate of approximately 2.75 mm/year.

Table 6-8: Corrosion rate calculated by mass loss technique for top and bottom samples

Sample position	Initial mass (g)	Final mass (g)	Corrosion rate (CR) (mm/year)	Avg. CR (mm/year)
Top	7.81	7.599	4.058	4.013
	7.614	7.416	3.808	
	7.902	7.685	4.173	
Bottom	8.447	8.317	2.500	2.930
	8.117	7.926	3.673	
	7.663	7.527	2.615	

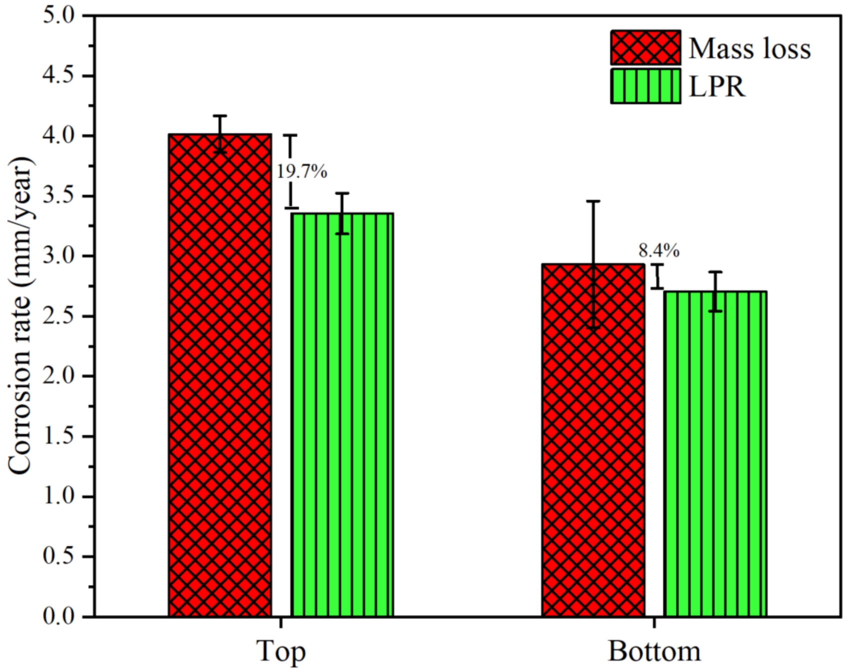

Figure 6-64: Comparison of corrosion rate determined by mass loss and LPR for top and bottom samples

6.3.2.2 Surface morphology of the corrosion layer

Figure 6-65 presents SEM micrographs offering a detailed examination of the surface morphology of the corrosion layers that have developed on both the top and bottom samples. The red box represents the selected area for further magnification.

In the top sample, as shown in Figure 6-65 (b), a rosette-like structure has been identified. Such a formation is typically associated with the presence of akageneite, an iron oxyhydroxide mineral. This finding suggests that the presence of chloride on the surface yielded the formation of akageneite.

Conversely, the bottom sample, per Figure 6-65 (d), exhibits a markedly different structural pattern, resembling a flowery arrangement. This structure bears a resemblance to lepidocrocite, another iron oxyhydroxide mineral commonly encountered in corrosion processes in such conditions. Specific points on the corrosion layers, denoted as Sp 1 and Sp 2, have been selected for further elemental analysis through EDX point analysis.

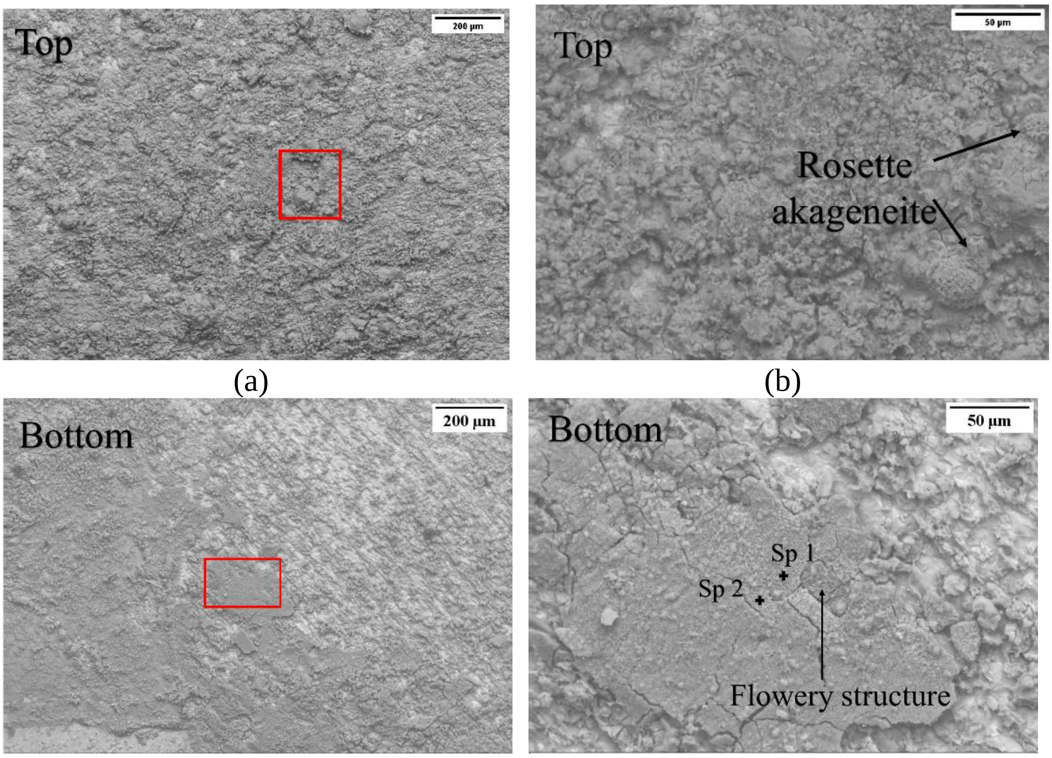

(a) (b)

(b) (d)

Figure 6-65: SEM of topography view of the corrosion layer grown on steel surface after being exposed to 3.5% NaCl, pH 5 at 80°C for 168 hours, (a-b) top samples, (b-c) bottom samples

Figure 6-66 provides cross-sectional SEM micrographs for both the top and bottom samples after being exposed to 3.5% NaCl, pH 5 at 80c for 168 hours. In the context of the top samples, the corrosion layer is notably observed to be firmly adhered to the steel surface. This adherence might contribute to the uniformity in corrosion layer thickness, as depicted in Figure 6-67 (a), where the average thickness measures 55 µm. Furthermore, there is a substantial amount of NaCl in proximity to the steel surface within certain regions of the corrosion layer. This observation is validated through EDX mapping analysis, as illustrated in Figure 6-68 (e-f).

In contrast, the corrosion layer formed on the surface of the bottom samples presents a more intricate and heterogeneous structural profile, as illustrated in Figure 6-66 (a). The thickness of this corrosion layer exhibits significant variability from one point to another, with measurements ranging from a minimum of 12 µm to a maximum of 192 µm with an average corrosion rate of 105 µm, per Figure 6-67 (b).

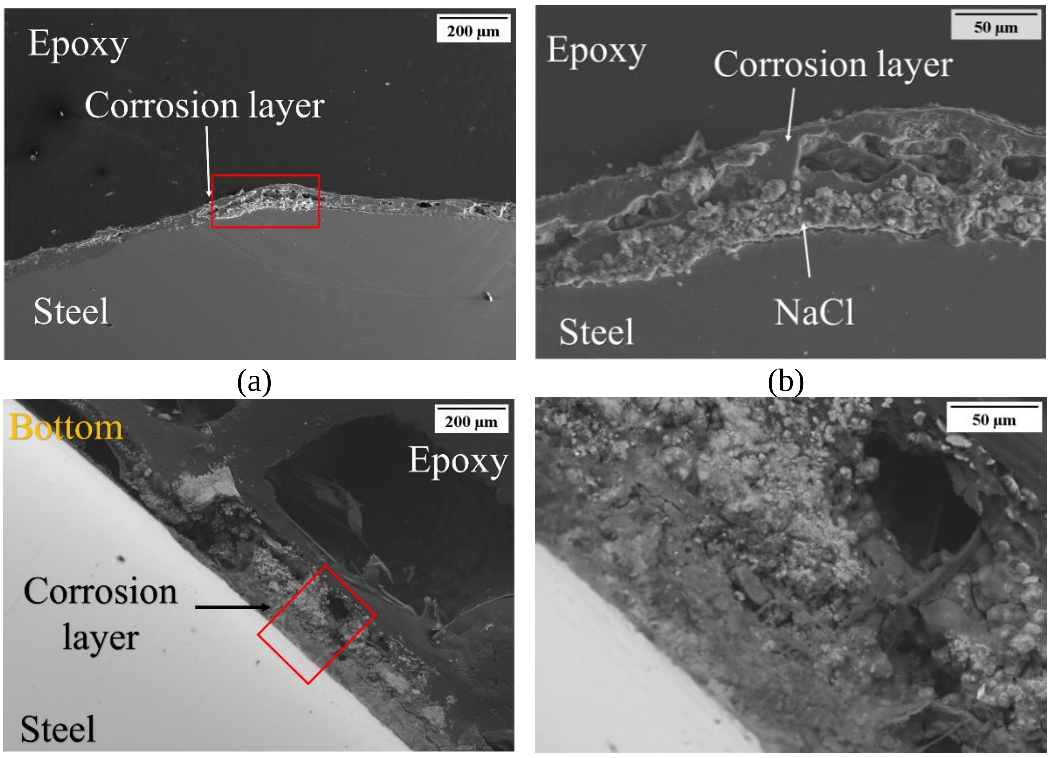

(a) (b)

(c) (d)

Figure 6-66: Cross-section SEM for the top (a-b) and bottom samples (c-d) after being exposed to 3.5% NaCl, pH 5 at 80°C for 168

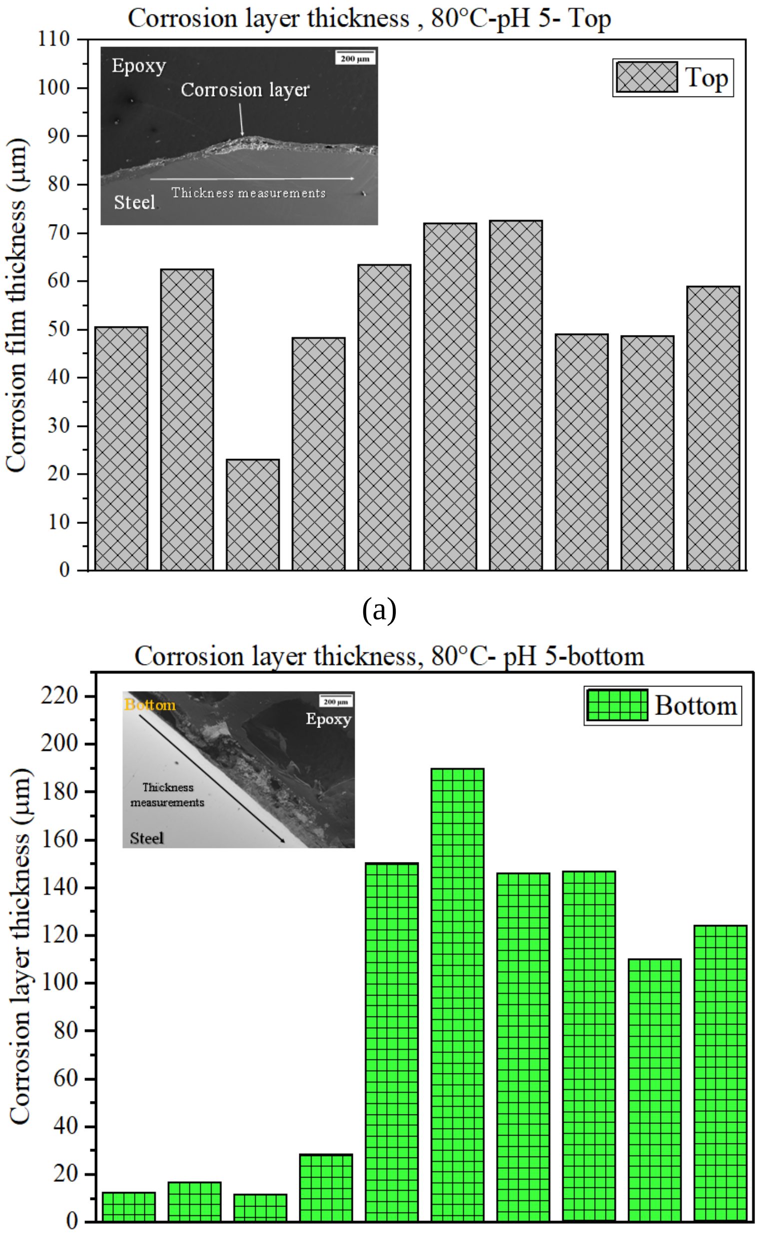

(a)

(b)

Figure 6-67: Corrosion film thickness for, (a) top sample and (b) bottom sample after being exposed to 3.5 %NaCl, pH 5 at 80°C for 168 hours

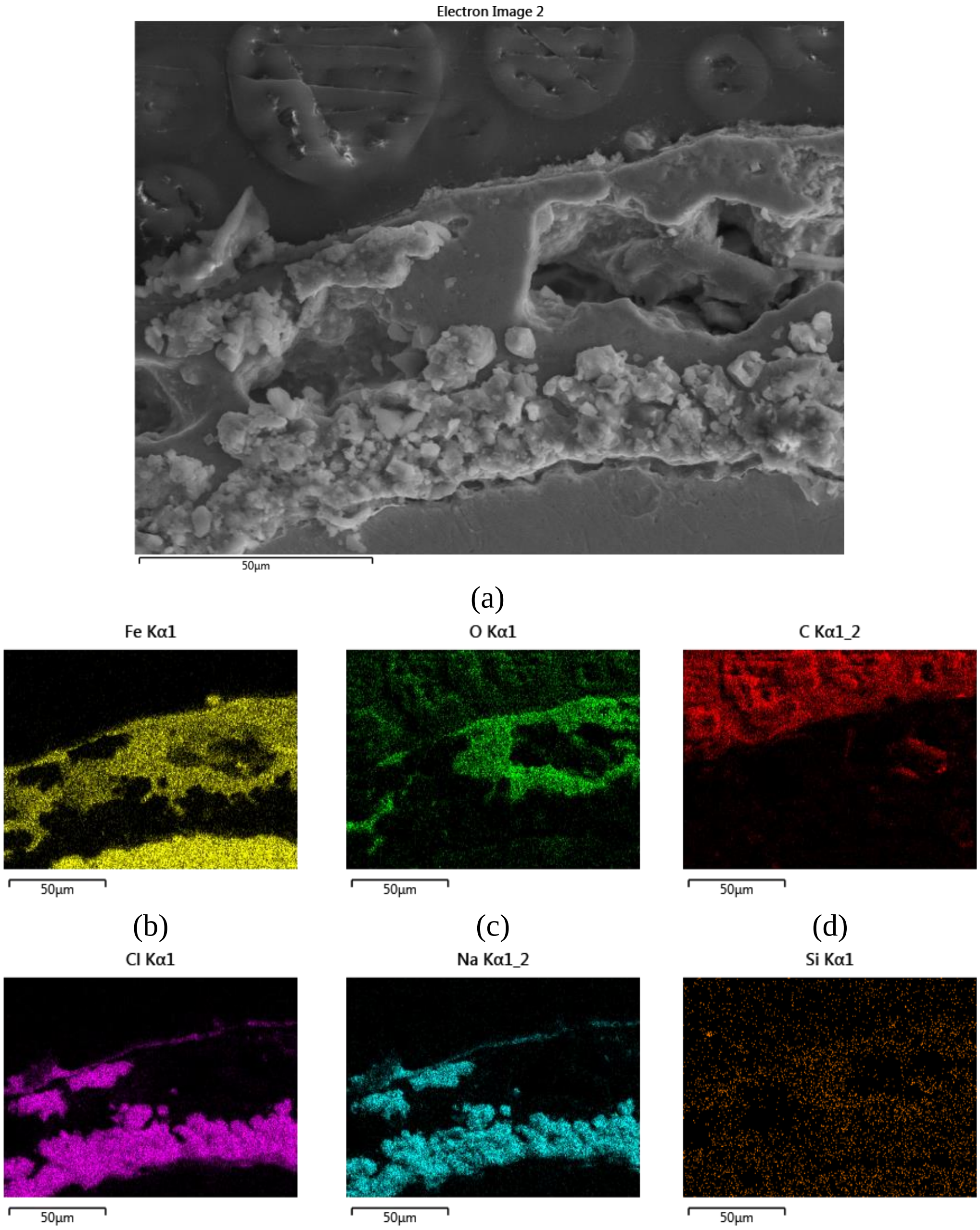

(a)

(b) (c) (d)

(e) (f) (g)

Figure 6-68: Element distribution within the corrosion layer formed on the surface of the top sample, (a) micrograph image, (b) iron-Fe, (c) oxygen-O, (d) carbon-C, (e) chloride-Cl, (f) sodium-Na and (g) silicon-Si

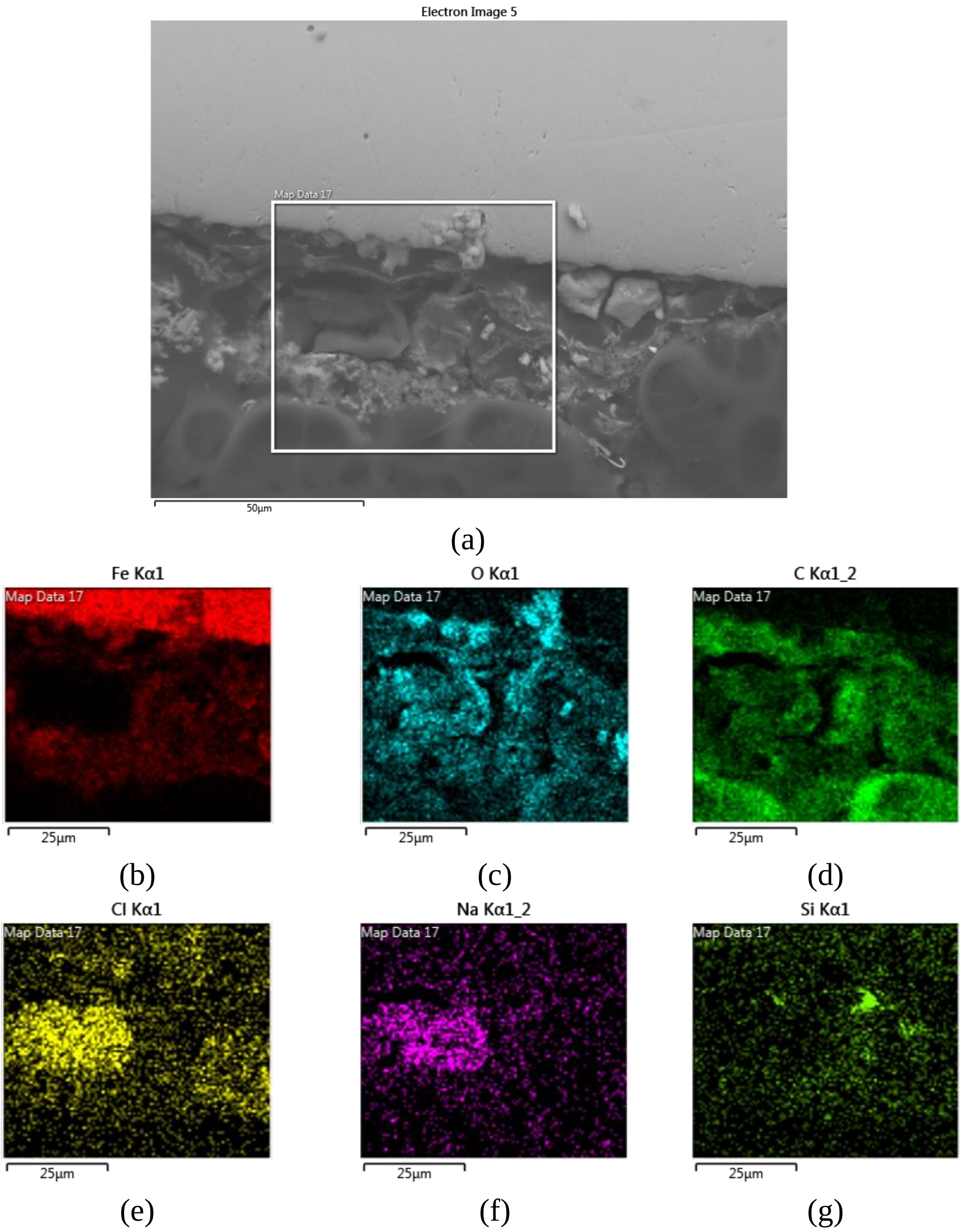

(a)

(b) (c) (d)

(e) (f) (g)

Figure 6-69: The elemental distribution within the corrosion layer that formed on the bottom sample following 168 hours of exposure to a 3.5% NaCl solution at 80°C and pH 5, (a) micrograph image, (b) iron-Fe, (c) oxygen-O, (d) carbon-C, (e) chloride-Cl, (f) sodium-Na and (g) silicon-Si

6.3.2.3 Raman spectroscopic characterisation of the corrosion layer

The Raman spectra, as illustrated in Figure 6-70, provide a detailed analysis of the corrosion layers formed on both the top and bottom samples. The strongest peak in the top sample appears at 224 cm^{-1}, indicative of lepidocrocite [124, 203]. Additional lepidocrocite peaks are observed at 643 cm^{-1}. Furthermore, goethite peaks are noted at 293 and 411 cm^{-1}, and akaganeite is identified through peaks at 411 and 607 cm^{-1}. Magnetite is detected at 665 cm^{-1}[121, 134].

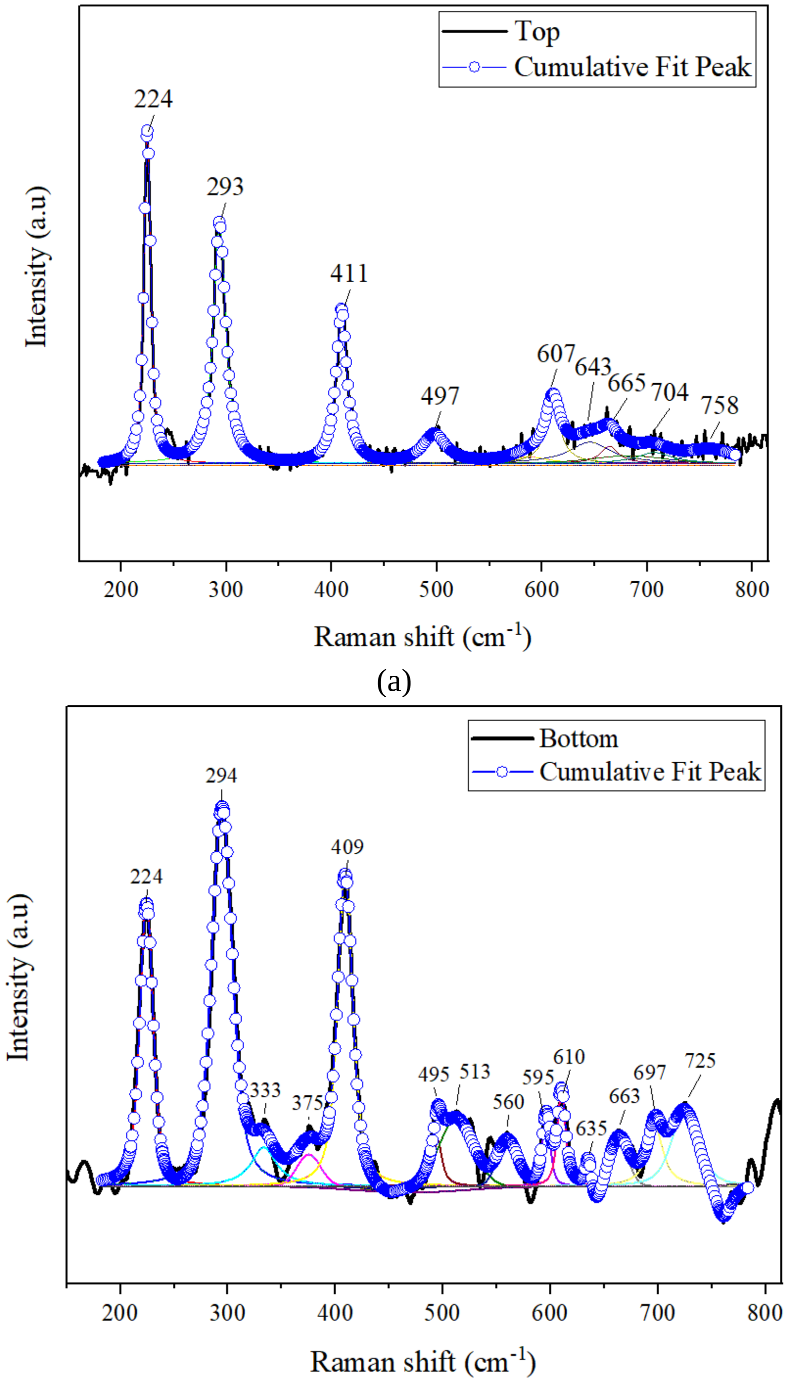

(a)

(b)

Figure 6-70: Raman spectra for the corrosion layer grown on the surface of the (a) top, and (b) bottom sample

In the bottom sample, the most prominent peak occurs at 294 cm^{-1}, corresponding to goethite [121, 134]. Lepidocrocite peaks are observed at 224, 375, and 663 cm^{-1}.

Goethite is also represented by peaks at 560 and 697 cm^{-1}. Akaganeite is identified through peaks at 333, 409, and 725 cm^{-1}. Additionally, magnetite is detected at 663 and 697 cm^{-1}.

6.3.2.4 Characteristic of the corrosion later by the XRD

The XRD analysis was employed to characterize the chemical composition of the corrosion layers developed on both the top and bottom samples, as depicted in Figure 6-71. were all identified within the corrosion layers of both samples. o assess the oxide content within the corrosion layers quantitatively, a semi-quantitative approach was adopted and the results are presented in Figure 6-72. the top sample is predominantly composed of akaganeite, accounting for nearly 49% of the oxide content. Following magnetite, lepidocrocite, and goethite are present, with abundance percentages of 30%, 17%, and 4%, respectively. These findings suggest that the corrosion layer on the top sample may offer less protection, as akaganeite and magnetite are known to promote corrosion rate through reduction and galvanic coupling mechanisms, respectively.

Conversely, in the bottom sample, lepidocrocite emerges as the primary oxide component, constituting approximately 38% of the oxide content. It is followed by akaganeite at 32%, magnetite at 24%, and goethite at 6%. Interestingly, the reduced proportions of both akaganeite and magnetite in the bottom sample suggest a potential enhancement in the corrosion resistance of the corrosion layer. This shift in oxide composition may contribute to improved protective properties.

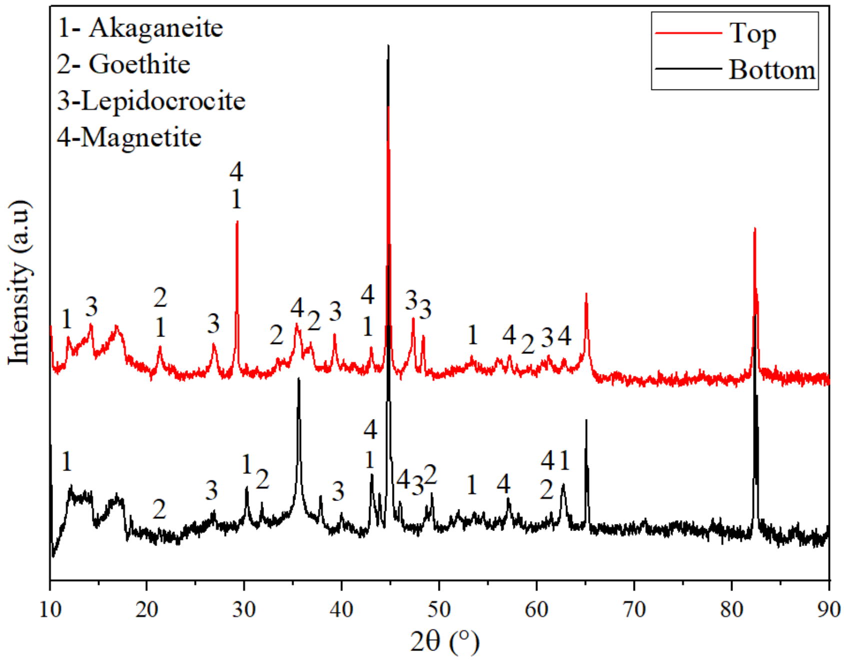

Figure 6-71: XRD pattern for corrosion layer grown on the top and the bottom samples after being exposed to 3.5% NaCl, pH 5 for 168 hours at 80°C

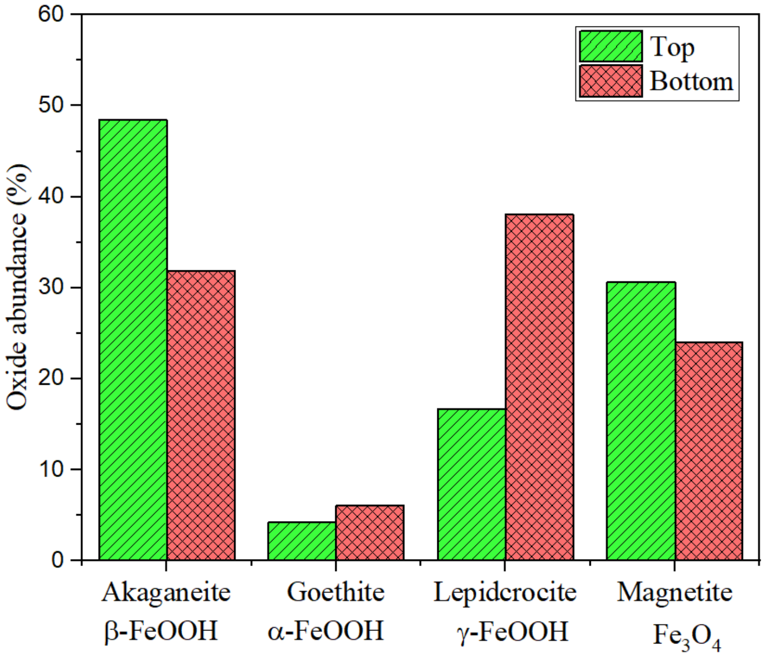

Figure 6-72: Semi-quantitative approach for determining the percentage of the oxides abundance in the corrosion layer formed on the surface of steel exposed to 3.5% NaCl, pH 5 for 168 hours at 80°C

6.3.3 Discussion

Figure 6-73 illustrates the corrosion rate, as measured by LPR, for both top and bottom microelectrode samples following exposure to 3.5% NaCl at pH 5 for 168 hours at two different temperatures: room temperature (RT) and 80°C. The corrosion of steel under thermal insulation, regardless of the temperature, can be explained as follows. The anodic process of ASTM A 106 Gr B involves the dissolution of steel, as depicted in equation 6-5. The cathodic reaction may entail the reduction of hydrogen, as shown in equation 6-6 or oxygen reduction, as per equation 6-7

$$Fe \rightarrow Fe^{2+} + 2e \qquad 6\text{-}5$$

$$2H^{+} + 2e \rightarrow H_2 \qquad 6\text{-}6$$

$$O_2 + 4H^{+} + 4e \rightarrow 2H_2O \qquad 6\text{-}7$$

Comparatively, at 80°C, the corrosion rate is higher than that observed at room temperature for both top and bottom samples. Specifically, at room temperature, the corrosion rate maintained a steady level, registering at 1.25 mm/year for the bottom sample and 1.81 mm/year for the top sample during the initial 60 hours. Subsequently, the corrosion rate increased before stabilizing once more. In contrast, when the temperature was elevated, the corrosion rate experienced an initial rise during the first 30 hours before reaching a relatively stable state. This temperature rise appears to influence the corrosion rate by potentially promoting the formation and dissolution of corrosion products [205]. Additionally, the increase in temperature may favour the transformation of lepidocrocite into more protective goethite within the corrosion layer. This was confirmed through the utilization of a semi-quantitative approach in conjunction with the XRD method, as depicted in Figure 6-76. Nonetheless, the proportion of formed goethite may be insufficient to generate a protective layer. As observed in Figure 6-76, the abundance of both akageneite and magnetite exhibited an increase with rising temperatures, and notably, their prevalence within the top sample appears to surpass that of the bottom samples. This increase in their presence within the corrosion layer is directly associated with an increase in the corrosion rate. However, it is worth noting that despite lepidocrocite being a reduction-favouring iron oxide, its reduction activity is comparatively lower than that of akageneite and magnetite [206].

In addition, it is important to note that the elevated temperature also enhances ion mobility, thereby promoting the dissolution of the substrate [206]. As a result, the corrosion rate is influenced by the combined action of these two mechanisms, temperature and type of the formed iron oxide.

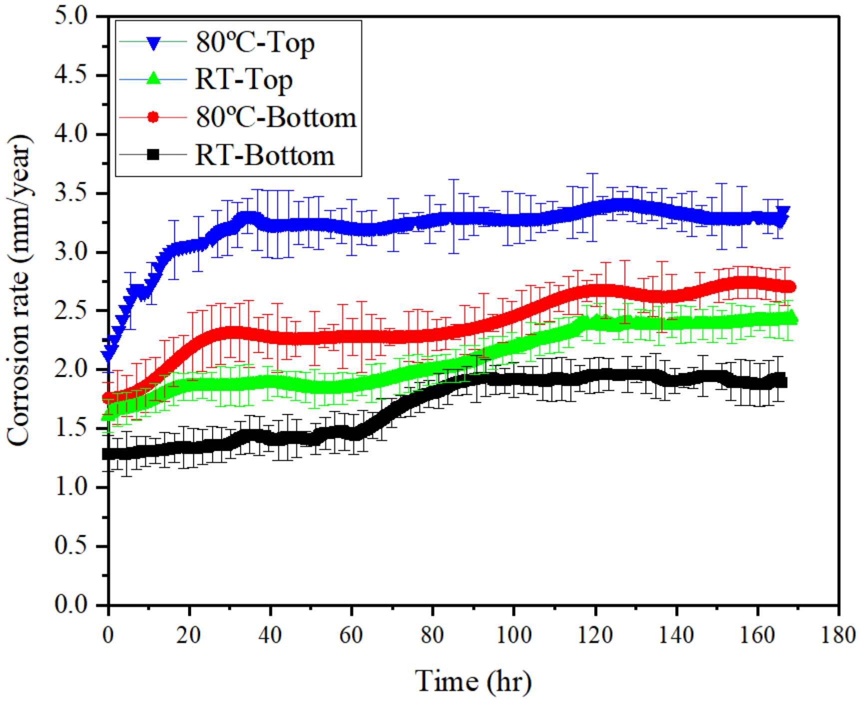

Figure 6-73: Corrosion rate determined by LPR technique for top and bottom microelectrodes after being exposed to 3.5% NaCl, pH 5 for 168 hours at room temperature and 80°C

Figure 6-74 presents a comparison of corrosion rates determined by both mass loss and LPR techniques for both top and bottom samples exposed to brine with a pH of 5 at room temperature and 80°C. The analysis reveals that the highest corrosion rate among all conditions is observed for the top sample at 80°C when measured by the mass loss technique, reaching a value of 4.01 mm/year. Conversely, the lowest corrosion rate is recorded for the bottom sample at room temperature when assessed by the LPR technique, with a rate of 2.21 mm/year. This observed trend remains consistent even at pH 7, further reinforcing the patterns in corrosion rates between the two techniques for both sample positions. The percentage difference between the corrosion rates calculated through mass loss and LPR techniques exhibits an exponential relationship, with values ranging from as low as 8% to as high as 18%. This trend suggests that the chosen value of the Tafel constant at 26 mV/decade aligns well with the experimental conditions, supporting its suitability for accurate corrosion rate determination under these circumstances.

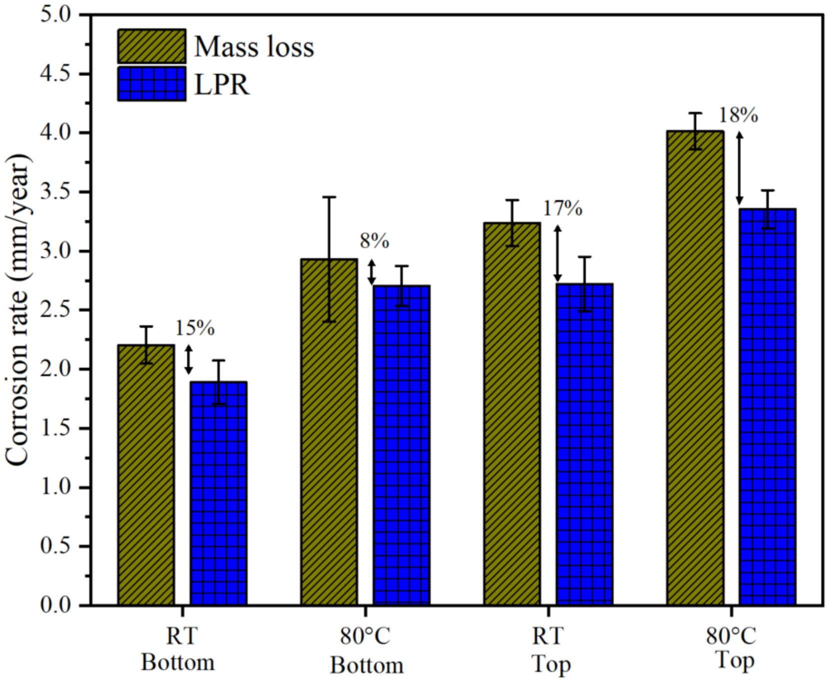

Figure 6-74: Comparison of corrosion rate by mass loss and LPR for top and bottom samples exposed to 3.5% NaCl brine, pH 5 at room temperature (RT) and 80°C

The cumulative fit peaks of Raman spectroscopy analysis of the chemical composition of the corrosion layers developed on steel surfaces at pH 5, under varying temperature conditions, are presented in Figure 6-75 and summarized in Table 6-9. At room temperature, the lepidocrocite exhibits distinct peaks at 216 and 220 cm^{-1}, which appear to correspond to the characteristic peak observed at 224 cm^{-1} when the temperature is elevated to 80°C. Notably, the peaks at 246, 247, 518, and 521 cm^{-1} are absent at 80°C for both the top and bottom samples. Additionally, while the 376 cm^{-1} peak is detected at room temperature for both samples, it is notably absent in the top sample at 80°C and is relatively weak in the bottom sample under the same conditions.

Furthermore, akaganegaite is detected in all four corrosion layers, indicated by the presence of peaks at 406, 408, 409, and 411 cm^{-1}. Several other characteristic peaks are also observed, including those at 491, 607, 612, 620, 725, 730, and 734 cm^{-1}. The goethite phase is characterized by its strongest peaks at 293 and 390 cm-1, while magnetite is identified by peaks at 653 and 663 cm^{-1}.

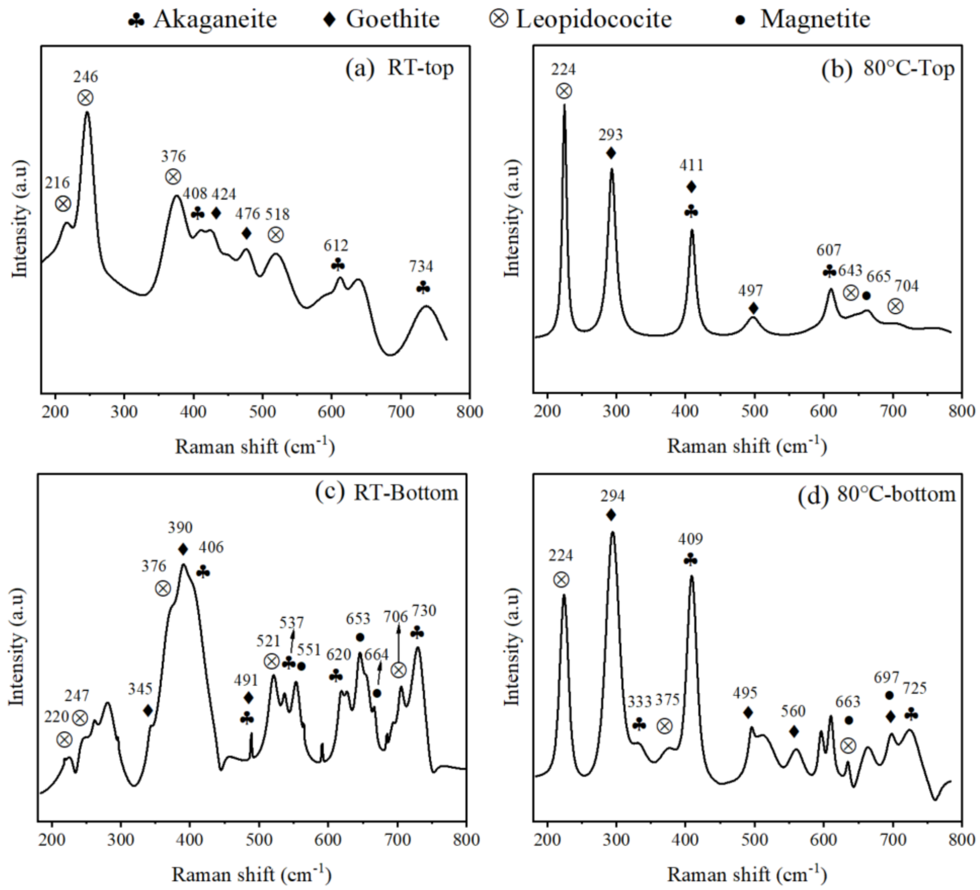

Figure 6-75: Raman spectra of corrosion layer grown on the surface of carbon steel after being exposed to 3.5% NaCl, pH 5 for 168 hours at, (a) room temperature - top, (b) 80°C- top, (c) room temperature- bottom, (d) 80°C- bottom

The disappearance of certain peaks and the emergence of new ones in the Raman spectra analysis serve as clear indicators that the chemical composition of the corrosion layers is influenced by temperature. These spectral changes suggest that temperature variations play a pivotal role in altering the composition and structure of the corrosion products, highlighting the dynamic nature of corrosion processes under different thermal conditions.

Table 6-9: Raman spectra peaks corresponding to the phases detected in the corrosion layers (main peaks are in bold)

Phase	Peaks	Reference
Akaganeite	333, **406-411**, 607-620, **725-734**	[124, 185, 207]
Goethite	**293**, 345, **390**, 411, 424, 491-497, 650, 697	[124, 185, 208]
Lepidocrocite	216-224, **246**, **376**, 518,521,706	[117, 119, 209]
Magnetite	551, 653, 663-665	[121, 207, 210]

The correlation between PAI_2 and the corrosion rate is visually represented in Figure 6-77. It is evident from the figure that an escalation in PAI value corresponds to an increase in corrosion rate, both for the top and bottom samples, whether at room temperature or 80°C. Consequently, PAI_2 can be used to evaluate the protective efficacy of the corrosion layer under thermal insulation conditions.

Temperature	Room temperature	80°C
Top	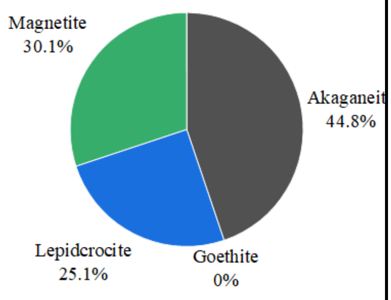	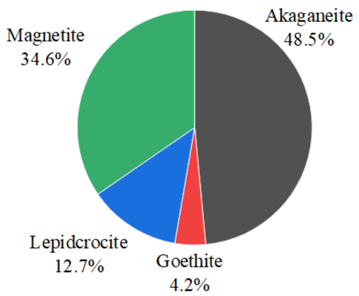
Bottom	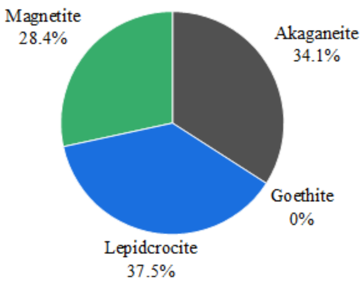	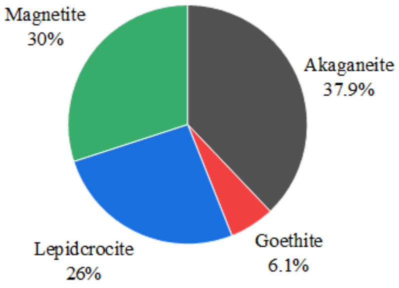

Figure 6-76: Iron oxide abundance in the corrosion layer grown on the surface for top and bottom samples at pH 5 as a function of temperature

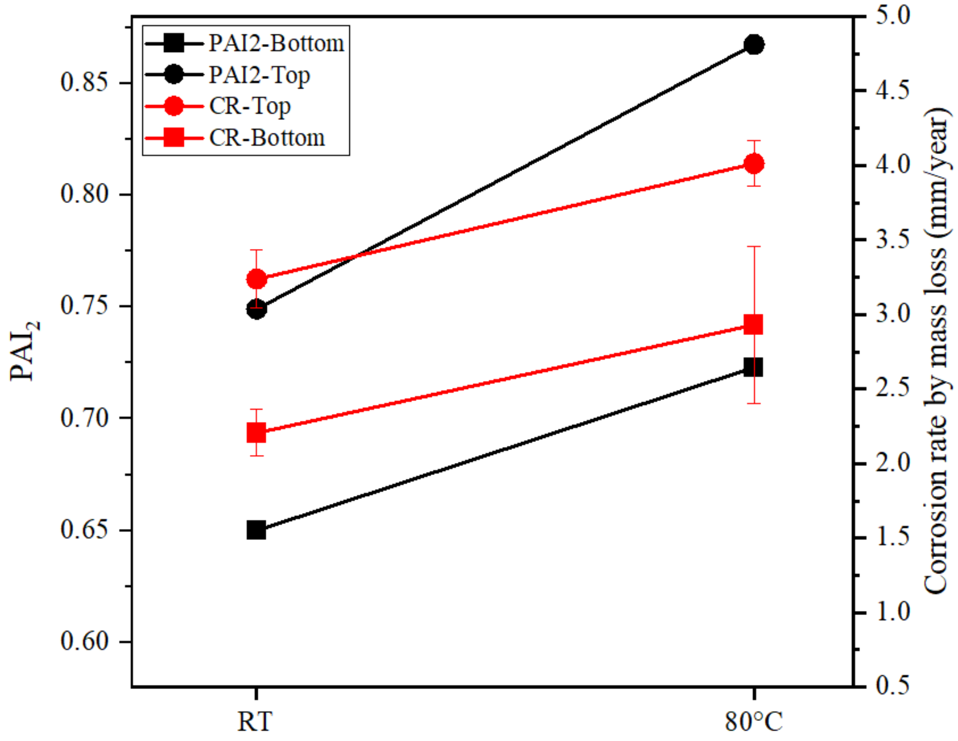

Figure 6-77: The variation of PAI2 and corrosion rate with temperature for both the top and bottom samples

6.4 Additional observations

Throughout the course of this research, some relevant findings have emerged that have not been incorporated into the results section. These findings primarily related to the type of thermal insulation used and the concept of thermal insulation water retention. These observations are elaborated upon in the following sub-sections.

6.4.1 Early phase insulation selection

During the initial phase of this study, a preformed Knauf Insulation Rock Mineral Wool, specifically identified as the Power-Tek PS 680 variant, was chosen for experimentation. This insulation material possessed an inner diameter of 60 mm and a thickness of 40 mm, procured from *Belgrade Insulations*, Leeds under the product code BD1115KN. Subsequently, the insulation underwent an aging process within a controlled furnace environment, enduring a period of 24 hours at a temperature of 150°C.

However, this particular insulation material was later excluded from further investigation due to its pronounced water repellent properties. The significant hydrophobicity posed considerable challenges in maintaining consistent wetting of the microelectrodes and mass loss coupons essential for the research objectives. Furthermore, the 40 mm thickness likely impacted the movement of water through the insulation, potentially hindering the wetting of the microelectrodes, thus rendering it unsuitable for fulfiling the intended experimental objectives (i.e. determination of the ability of micro-electrodes to provide real-time corrosion data in CUI systems). However, it is important to highlight that this particular insulation may prove a favourable choice with respect to mitigation of CUI, though

6.4.2 Water retention within the thermal insulation

During the experiments, the insulation water retention was monitored to find the effect of temperature and brine pH on water absorption by the insulation. The thermal insulation was weighted pre- and post-experiment. The difference between the measurements is the amount of water retained within the thermal insulation, as indicated by the “water absorption” column in Table 6-10.

Table 6-10 presents the impact of temperature and pH on the water absorption of the insulation material. The calculation of water absorption by mass utilizes the percentage increase formula. The data illustrates that as the temperature rises from room temperature to 80°C, there is a tendency for water adsorption to increase for both pH levels. Furthermore, there is a discernible discrepancy in water adsorption between pH levels 7 and 5, with pH 5 consistently demonstrating higher water adsorption compared to pH 7 at both room temperature and 80°C.

While this research has not directly investigated the specific reasons behind the disparity in water retention with respect to temperature and pH, the findings put forth compelling evidence that both operating temperature and brine composition influence the hydrophobic properties of thermal insulation. This suggests that alterations in temperature and brine composition directly diminish the insulation's ability to repel water.

Table 6-10: The effect of temperature and pH on the water absorption

pH	Temperature (°C)	Water absorption (g)	Water absorption by weight
7	Room temperature	24.3	31%
	80	75.5	94%
	150	19.0	24%
5	Room temperature	30.2	38%
	80	81.0	101%

In terms of CUI results, there appears to be a direct relationship between water adsorption and the corrosion rate. However, to obtain a more comprehensive understanding of these phenomena, further investigation is imperative. Additional research efforts are required to elucidate the underlying mechanisms governing the interaction between temperature, pH, and the hydrophobic characteristics of thermal insulation.

6.5 Summary

Table 6-11 presents, under different sample positions, temperatures, and pH conditions, a comprehensive overview of corrosion rates (CR) extracted from both mass loss and LPR techniques. The table also shows CR’s percentage difference, and the percentage of abundance of various iron oxides. The dominant corrosion layers’ oxides discovered were (β-FeOOH, α-FeOOH, γ-FeOOH, and Fe_3O_4). Additionally, the table includes the Protective Ability Index (PAI2) for each set of conditions.

- **Sample position influence:** The data indicates that the corrosion rates for the top samples are consistently higher than those for the bottom samples under the same conditions. This trend is observed across all temperature and pH variations.

- **Temperature effect:** Higher temperatures generally accelerate corrosion, in the CUI system, but this effect may stabilise or become less pronounced at extremely high temperatures like 150°C, per Figure 6-78. For instance, with a constant pH of 7, the temperature's influence on corrosion rates is evident. As the temperature increases from RT to 80°C, both the bottom and top samples experience higher corrosion rates. The CR for the top sample increased from 2.09 to 4.62 mm/year, while for the bottom sample, it rose from 1.06 to 2.09 mm/year. However, at 150°C, the effect is less pronounced, with corrosion rates being relatively lower. The CR decreased by 1.78 and 0.77 mm/year for the top and the bottom samples respectively.
- **pH impact:** The influence of pH is also evident, with more acidic conditions (pH 5) resulting in higher corrosion rates compared to neutral conditions (pH 7). This effect is particularly pronounced for the bottom samples, as depicted in Figure 6-78.
- **Percentage differences:** The percentage difference was only varying between 8-18% at pH5 between the different temperatures and sample positions, which hints at anodic and cathodic Tafel values adjustments. But for other acidities, the trend was lost and the percentage differences between corrosion rates determined by mass loss and LPR are more scattered. These differences can range from as low as 26% to as high as 51%.
- **Protective Ability Index**: PAI_2 values provide insights into the effectiveness of the corrosion layer in protecting the underlying material. Higher PAI_2 values are generally associated with lower corrosion protection, per Figure 6-78. For instance, "Bottom RT-pH 7" has a PAI_2 of 0.29 and a mass loss corrosion rate of 1.06 mm/year, while "Bottom 80°C-pH 7" has a higher PAI_2 of 0.82 but a higher mass loss corrosion rate of 2.38 mm/year.
- **Iron oxide abundance:** The abundance of iron oxides within the corrosion layer is influenced by factors such as sample position, pH, and temperature as depicted in Figure 6-79 and Table 6-11. The abundance of $\beta - FeOOH$ generally increases with rising temperature for both bottom and top samples. In addition, it increases as pH decreases from 7 to 5 for both positions, except at 80°C for the top sample. Consistently higher in the top sample position at each temperature. The $\alpha - FeOOH$ is more dominant at RT and

pH 7 for both sample positions. However, its presence becomes nearly negligible when the pH is lowered to 5 for both positions. Furthermore, as the temperature escalates to 80°C, there is a notable reduction in its abundance, indicating that elevated temperatures may promote the formation of alternative iron oxides or corrosion byproducts. The $\gamma - FeOOH$ is more abundant at RT and under pH 7 conditions, with a notable presence in the bottom sample. As the pH level becomes more acidic (pH 5), there is a decrease in the abundance of γ-FeOOH for both sample positions. At higher temperatures, such as 80°C and 150°C, the percentage of γ-FeOOH varies, generally showing lower proportions compared to RT and pH 7 conditions. Nevertheless, at 80°C and pH 7, the bottom sample has the highest abundance percentage of Fe_3O_4 with 44.6%. The top sample shows inconsistent trends, with varying percentages depending on conditions.

In summary, the composition of iron oxides within the corrosion layer is complex and dependent on sample position, pH, and temperature. Higher temperatures tend to promote the presence of $\beta - FeOOH$. $\alpha - FeOOH$ is more prevalent at RT and pH 7 but diminishes with increased temperature. $\gamma - FeOOH$ is influenced by both pH and temperature, with higher temperatures generally resulting in lower percentages. The presence of Fe_3O_4 exhibits variations depending on sample position and conditions.

Overall, these observations illustrate how temperature and pH affect corrosion rates and corrosion layer composition, as well as the specific positions of sample samples. The presence of such multifaceted dynamics is of paramount importance as part of a comprehensive evaluation and mitigation of CUI under a variety of environmental conditions

Table 6-11: Summary of CUI experiments includes corrosion rates determined by mass loss and LPR, along with the percentage difference, as well as the abundance of iron oxides under various temperature and pH conditions

Sample position. Temperature and pH	CR mass loss^{1} (mm/year)	CR LPR^{2} (mm/year)	Percentage difference between 1 and 2	β-FeOOH %	α-FeOOH %	γ-FeOOH %	Fe_3O_4 %	PAI_2
Bottom-RT-pH 7	1.06	0.68	44%	18.5	33.6	47.9	-	0.29
Bottom-RT-pH 5	2.21	1.89	15%	34.1	-	37.5	28.4	0.63
Bottom-80°C-pH 7	2.38	1.41	51%	28.8	10.9	15.7	44.6	0.82
Bottom-80°C-pH 5	2.93	2.70	8%	37.9	6.07	26.02	30.01	0.72
Bottom-150°C-pH 7	1.61	0.98	49%	32.2	25.1	34.8	16.9	0.54
Top-RT-pH 7	2.09	1.62	26%	43.1	23.5	33.4	-	0.56
Top-RT-pH 5	3.24	2.72	17%	44.8	-	25.1	30.1	0.75
Top-80°C-pH 7	4.62	2.89	46%	49.3	1.8	10.7	38.2	0.89
Top-80°C-pH 5	4.01	3.35	18%	48.5	4.2	12.7	34.6	0.88
Top-150°C-pH 7	2.84	1.75	47%	42.5	8.9	9.4	39.2	0.89

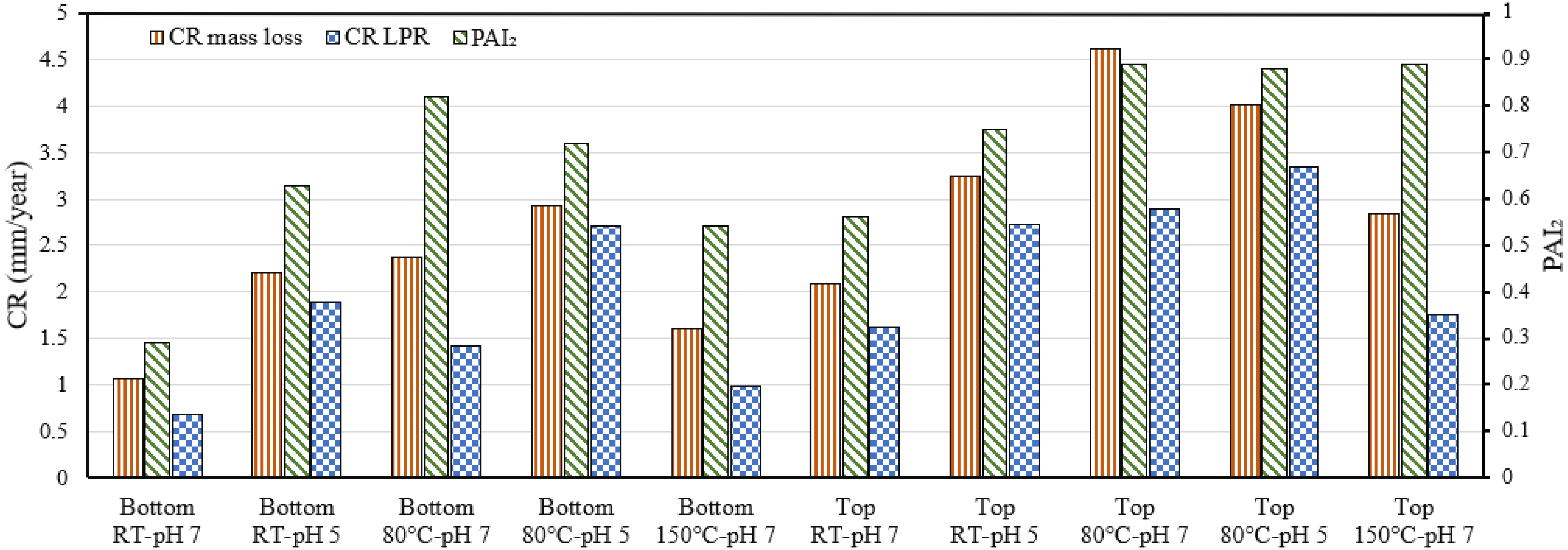

Figure 6-78: Corrosion rates for top and bottom samples after exposure to 3.5% NaCl brine for 168 hours at different temperatures (room temperature, 80°C, and 150°C) and pH levels (7 and 5), the Stearn Geary constant is 26 mV/decade

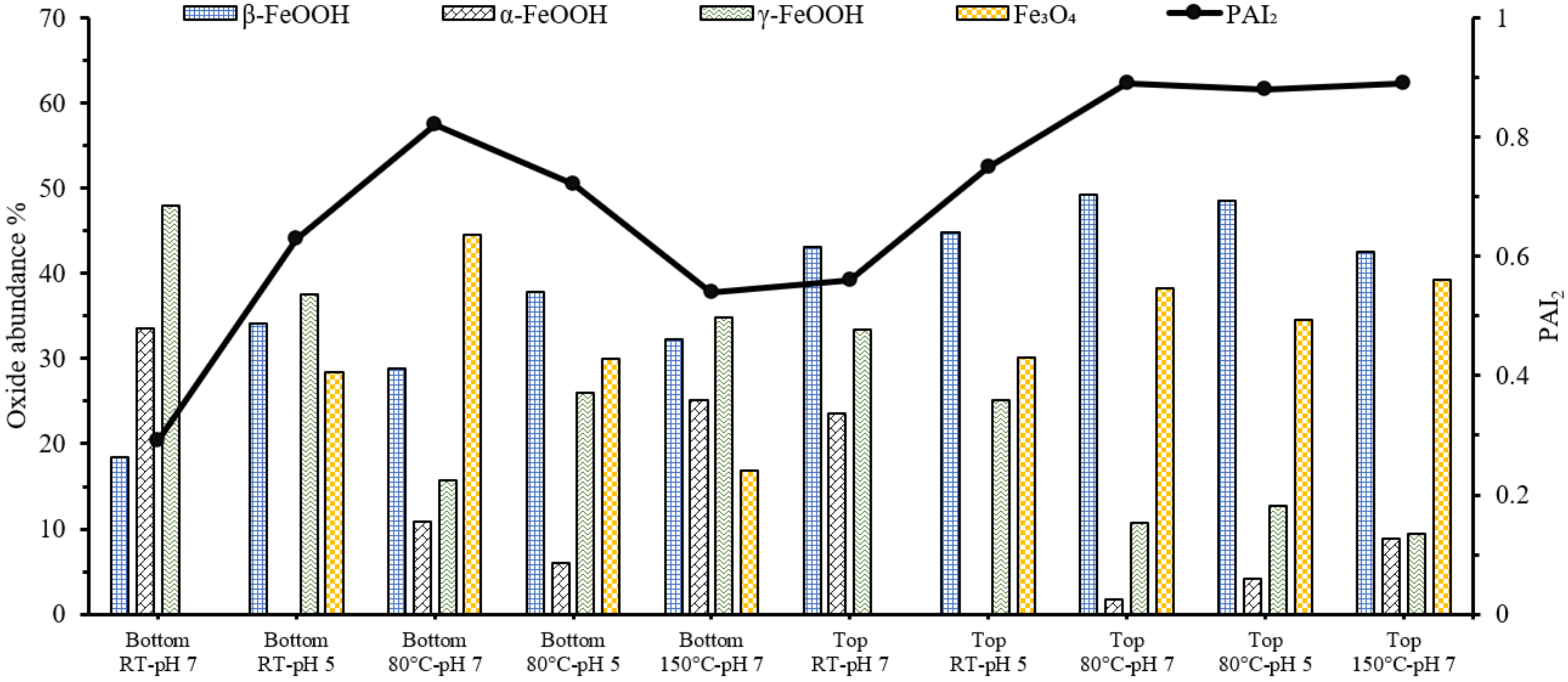

Figure 6-79: Iron oxides abundance and the PAI_2 for corrosion layer grown on steel surface for the top and bottom samples after being exposed to 3.5% NaCl brine at different temperatures (room temperature-RT, 80°C, and 150°C) and pH levels (7 and 5)

Chapter 7: Conclusion, recommendation and future work

7.1 Conclusion

This research investigated the CUI through the application of a novel research rig employing three microelectrodes, focusing on the top (12 o'clock) and bottom (6 o'clock) of the pipe, subjected to varying experimental conditions, including temperature and pH, for an extended period of 168 hours. Key findings derived from this extensive investigation are as follows:

- The innovative rig design for probing CUI effectively ensured that electrochemical cells and mass loss coupons remained free from any disruptions, such as wires, that would interact with the brine movement within the insulation.
- The utilization of three microelectrodes demonstrated a promising opportunity for CUI investigation, offering a potential approach for general corrosion assessment, particularly in select areas of interest.
- In the same conditions and positions, it has consistently been observed that corrosion rates calculated from mass loss measurements exceed those calculated using the LPR.
- The study revealed that CUI is influenced by temperature and pH variations. These factors are likely to impact the hygroscopic properties of thermal insulation materials, potentially leading to increased moisture retention within the insulation material.
- Regardless of the technique employed, the corrosion rate for the top sample consistently exceeded that of the bottom sample under the same temperature and pH conditions. This phenomenon can be attributed to the proximity of the injected brine to the samples, resulting in distinct chemical compositions of the brine on the surfaces of the top and bottom specimens. Furthermore, differential aeration cell conditions may exist between these regions.
- At a pH of 7, the corrosion rate at the top sample tends to continuously increase throughout the test duration, irrespective of the temperature. In contrast, the bottom sample demonstrates an almost steady corrosion rate over the same period.

- The absence of magnetite at room temperature and pH 7 for both the top and bottom samples suggests that higher temperatures are likely required to facilitate the formation of magnetite within the corrosion layer. This observation underscores the influence of temperature on the chemical composition and corrosion processes occurring within the insulation environment.
- The research demonstrated that the corrosion rate reached its highest levels at 80°C compared to both room temperature and 150°C, as depicted in Figure 6-42. High temperatures contributed to an increased concentration of corrosion species and enhanced the kinetics of corrosion reactions.
- The detection discrepancy between XRD and Raman spectroscopy for goethite presence at pH 5 adds a layer of complexity to the characterisation of corrosion products under thermal insulation environments. This inconsistency implies that the probing depth of the XRD beam may not extend deep enough into the corrosion layer to identify the goethite phase accurately. This observation underscores the importance of utilizing multiple analytical techniques with complementary probing depths to comprehensively assess the chemical composition and structural characteristics of corrosion layers formed under such intricate conditions.
- It was observed that the measurement of the actual corrosion film thickness formed beneath thermal insulation could be challenging due to the integration of the corrosion film with insulation fibres. Upon insulation removal, some of the corrosion film may become dislodged.
- The presence of akageneite and magnetite within the corrosion layer emerged as influential factors affecting CUI rates. These compounds contributed to increased corrosion rates by enhancing reduction activity and the galvanic coupling effect.
- The Protective Ability Index (PAI) emerged as a valuable indicator for assessing the protective properties of corrosion layers formed beneath thermal insulation.
- Deterioration of the thermal insulation material was observed under all experimental conditions. Significantly, more insulation fibres adhered to the top sample compared to the bottom, attributed to the influence of gravity,

which led to firm attachment of insulation from above, creating an annular gap beneath.

7.2 Recommendations and future work

This research used three microelectrode cells combined with an electrochemical to investigate the behaviour of CUI under different conditions. The outcome of this study opens the way to further investigations of CUI using microelectrodes under different scenarios. Specific recommended suggestions for future work include:

- Integrate supplementary electrochemical methods, such as Electrochemical Impedance Spectroscopy (EIS), into the research framework to offer comprehensive insights into the interfacial behaviour between the working electrode and the electrolyte. Additionally, EIS can provide valuable data on solution resistance dynamics, enhancing the overall understanding of the corrosion processes under thermal insulation.
- Conduct an experimental determination of the Tafel constant to enhance the precision of corrosion rate comparisons between the mass loss and LPR methodologies. This approach will help reduce the discrepancies observed in previous studies and provide more accurate insights into corrosion behaviour under thermal insulation conditions.
- Enhance the grinding and polishing methodology to achieve consistent surface roughness, particularly for the semi-circular mass loss coupons. Consistency in surface preparation is crucial for accurate and reliable data collection.
- Evaluate the CUI using both real-world and artificially aged thermal insulation materials. This approach will provide a comprehensive understanding of CUI behaviour under various insulation ageing conditions, allowing for more robust conclusions and insights. Considering that CUI development requires a certain duration, this extended investigation will yield more robust conclusions and insights into the phenomenon.
- Investigate the potential for ‘smart-insulation’ whereby inhibitory chemicals are incorporated into the insulation and released or leached –out of the insulation upon contact with water to provide inhibition at the insulation-

steel interface. This process could then be evaluated in real-time through the implementation of the three microelectrode cells.

- Develop hygrothermal models to simulate moisture transport and thermal performance in insulation materials used in CUI-prone environments. Investigate the effects of insulation thickness, material properties, environmental conditions, and design factors on moisture accumulation, condensation risk, and thermal insulation effectiveness, with implications for CUI risk assessment and prevention strategies

References

1. Fontana, M., *Corrosion engineering'3rd edn, 39: 1986*. McGraw-Hill.
2. Marcus, P., *Corrosion mechanisms in theory and practice*. 2011: CRC press.
3. Jones, D., *Principles and prevention of corrosion.* Macmillan Publishing Company(USA), 1992, 1992: p. 568.
4. Grabke, H., R. Krajak, and J.N. Paz, *On the mechanism of catastrophic carburization:'metal dusting'.* Corrosion Science, 1993. **35**(5-8): p. 1141-1150.
5. Javaherdashti, R., C. Nwaoha, and H. Tan, *Corrosion and Materials in the Oil and Gas Industries*. 2016: CRC Press.
6. Roberge, P.R., *Handbook of corrosion engineering*. 2019: McGraw-Hill Education.
7. Alkazraji, D., *A Quick Guide to Pipeline Engineering*. 2008: Elsevier Science.
8. Roberge, P.R., *Corrosion engineering*. 2008: McGraw-Hill Education.
9. Agala, A., M. Khan, and A. Starr, *Degradation mechanisms associated with metal pipes and the effective impact of LDMs and LLMs in water transport and distribution.* Proceedings of the Institution of Mechanical Engineers, Part C: Journal of Mechanical Engineering Science, 2023. **237**(8): p. 1855-1876.
10. Caines, S., et al., *Experimental design to study corrosion under insulation in harsh marine environments.* Journal of Loss Prevention in the Process Industries, 2015. **33**: p. 39-51.
11. Pojtanabuntoeng, T., et al., *Influence of drain holes in jacketing on corrosion under thermal insulation.* 2015. **71**(12): p. 1511-1520.
12. Winnik, S., *Corrosion under insulation (CUI) guidelines*. 2014: Elsevier.
13. Thermaxx, J., *Corrosion under insulation (CUI)*. 2018.
14. Fitzgerald, B.J., et al. *Strategies to prevent corrosion under insulation in petrochemical industry piping*. in *CORROSION 2003*. 2003. OnePetro.
15. Simpson, J., *The application of risk based inspection to pressure vessels and aboveground storage tanks in petroleum fuel refineries.* 2007.
16. Gouda, H., *Interview: Cloud Solution Promises to Drive Down CUI Maintenance Costs in O&G Industry*, in *Offshore Engineering*, B. Tomic, Editor. 2021.
17. Brown, R. *Promoted: What lies beneath? Tackling the challenge of corrosion under insulation*. 2016 [cited 2022 19/01/2022]; Available from: https://www.energyvoice.com/promoted/120819/promoted-lies-beneath-tackling-challenge-corrosion-insulation/.
18. White, T., *The Cost of Corrosion*, in *ZERUST EXCOR*. 2019.
19. Jacobson, G., *International Measures of Prevention, Application and Economics of Corrosion Technology (IMPACT).* 2016, Materilas Performance.
20. Javaherdashti, R., F.J.I.J.o.E.T. Akvan, and M. Research, *ON THE LINK BETWEEN FUTURE STUDIES AND NECESSITY OF INCLUDING CORROSION IN A "DESIRED FUTURE" SCENARIO: PRESENTING A MODEL.* 2015. **2**(4): p. 1-8.
21. Hou, B., *The Cost of Corrosion in China*. 2019: Springer Nature Singapore.

22. Swift, M., *Corrosion Under Insulation on Industrial Piping - a Holistic Approach to Insulation System Design*, in *CORROSION 2019*. 2019, NACE International: Nashville, Tennessee, USA. p. 15.
23. Hou, B., et al., *The cost of corrosion in China.* 2017. **1**(1): p. 1-10.
24. Sastri, V.S., *Challenges in Corrosion: Costs, Causes, Consequences, and Control*. 2015: Wiley.
25. Powertherm. *Corrosion under insulation expertise*. 30/10/2022]; Available from: https://www.powertherm.co.uk/cui-corrosion-under-insulation-expertise/.
26. Sampaio, R.a.L., A, L, *More Lessons "Re-Learned" from Corrosion Under Insulation.* 2009.
27. Cramer, S.D. and B.S. Covino, *Corrosion: Environments and industries*. 2006: ASM International.
28. Anderson, S.A., *Out of sight, out of mind.* 2010. **15**: p. 64-69.
29. 0198, N.S., *Control of Corrosion Under Thermal Insulation and Fireproofing Materials—A Systems Approach*. 2010, NACE: Houston.
30. Winnik, S., *Corrosion-Under-Insulation (CUI) Guidelines (Second Edition)*, in *Corrosion-Under-Insulation (CUI) Guidelines (Second Edition)*, S. Winnik, Editor. 2016, Woodhead Publishing. p. 1-9.
31. G193-12d, N.A., *Standard Terminology and Acronyms Relating to Corrosion.* 2012.
32. Papavinasam, S., *Corrosion control in the oil and gas industry*. 2013: Elsevier.
33. Ahmad, Z., *Principles of Corrosion Engineering and Corrosion Control*. 2006: Elsevier Science.
34. Schweitzer, P.A., *Fundamentals of Corrosion: Mechanisms, Causes, and Preventative Methods*. 2009: CRC Press.
35. Perez, N., *Electrochemistry and Corrosion Science*. 2016: Springer International Publishing.
36. Bodsworth, C., *The Extraction and Refining of Metals*. 2018: CRC Press.
37. Elayaperumal, K. and V.S. Raja, *Corrosion Failures: Theory, Case Studies, and Solutions*. 2015: Wiley.
38. Stansbury, E.E. and R.A. Buchanan, *Fundamentals of electrochemical corrosion*. 2000: ASM international.
39. Pedeferri, P. and M. Ormellese, *Corrosion science and engineering*. 2018: Springer.
40. Cicek, V., *Corrosion engineering*. 2014: John Wiley & Sons.
41. McCafferty, E., *Introduction to corrosion science*. 2010: Springer Science & Business Media.
42. Talbot, D.E.J. and J.D.R. Talbot, *Corrosion Science and Technology*. 2018: CRC Press.
43. Laidler, K.J., *transition-state theory*, in *Encyclopedia Britannica*. 2019.
44. Kelly, R.G., et al., *Electrochemical Techniques in Corrosion Science and Engineering*. 2002: CRC Press.
45. PE, P.A.S., *Fundamentals of Metallic Corrosion: Atmospheric and Media Corrosion of Metals*. 2006: CRC Press.
46. Revie, R.W., *Corrosion and corrosion control: an introduction to corrosion science and engineering*. 2008: John Wiley & Sons.
47. Hansen, P.F. and O.M. Jensen, *The Science of Construction Materials*. 2009: Springer Berlin Heidelberg.

48. Sato, N., *Basics of corrosion chemistry*. Green Corrosion Chemistry and Engineering, 2012. **1**.
49. Townsend, H.E., *Outdoor Atmospheric Corrosion*. 2002: ASTM.
50. Pojtanabuntoeng, T., et al., *Influence of Drain Holes in Jacketing on Corrosion Under Thermal Insulation*. Vol. 71. 2015. 150907155222005.
51. Ohtsuka, T., et al., *Electrochemistry for Corrosion Fundamentals*. 2017: Springer Singapore.
52. Peabody, A.W. and R.L. Bianchetti, *Peabody's Control of Pipeline Corrosion*. 2001: NACE International, The Corrosion Society.
53. Prabhu, S., *8 Things to Know and Understand About Iron Corrosion*. 2021, CorrosionPedia.
54. Craig, B.D., *Fundamental aspects of corrosion films in corrosion science*. 1991: Springer Science & Business Media.
55. Scully, J.C., *The Fundamentals of Corrosion*. 1975: Elsevier Science & Technology Books.
56. Zoski, C.G., *Handbook of Electrochemistry*. 2007: Elsevier Science.
57. Curioni, M., A. Balaskas, and G. Thompson, *An alternative to the use of a zero resistance ammeter for electrochemical noise measurement: Theoretical analysis, experimental validation and evaluation of electrode asymmetry*. Corrosion science, 2013. **77**: p. 281-291.
58. Mohammed, S.A., *Investigating pitting corrosion on X65 carbon steel in sweet oil and gas environment*. 2018, University of Leeds.
59. Pessu, F.O., *Investigation of pitting corrosion of carbon steel in sweet and sour oilfield corrosion conditions: a parametric study*. 2015, University of Leeds.
60. Vetter, K.J., *Electrochemical kinetics: theoretical aspects*. 2013: Elsevier.
61. Bockris, J.O.M. and A.K.N. Reddy, *Modern Electrochemistry: An Introduction to an Interdisciplinary Area*. 2012: Springer US.
62. Revie, R.W., *Uhlig's corrosion handbook*. Vol. 51. 2011: John Wiley & Sons.
63. ASTM-C692, *Evaluating the Influence of Wicking Type Thermal Insulations on the Stress Corrosion Cracking Tendency of Austenitic Stainless Steels*. 1971, ASTM: Pennsylvania.
64. International, I. *Thermal insulation*. 2020; Available from: https://www.iogs.org/post/blog-thermal-insulation#:~:text=The%20insulation%2C%20or%20more%20correctly,a%20refinery%20or%20process%20plant.
65. Cao, Q., et al., *A Review of Corrosion under Insulation: A Critical Issue in the Oil and Gas Industry*. Metals, 2022. **12**(4): p. 561.
66. Kane, R.D., M. Chauviere, and K. Chustz, *Evaluation Of Steel And Tsa Coating In A Corrosion Under Insulation (Cui) Environment*, in *CORROSION 2008*. 2008, NACE International: New Orleans, Louisiana. p. 20.
67. Miyashita, J., *Performance of Three Types of Coatings in a Simulated Corrosion under Insulation Condition*, in *CORROSION 2017*. 2017, NACE International: New Orleans, Louisiana, USA. p. 11.
68. Pedersen, L.T., *Corrosion Under Insulation Technologies - High Performance Solutions*, in *Abu Dhabi International Petroleum Exhibition and Conference*. 2015, Society of Petroleum Engineers: Abu Dhabi, UAE. p. 14.

69. Houben, J., et al. *Deployment of CUI prevention strategies and TSA implementation in projects*. in *CORROSION 2012*. 2012. OnePetro.

70. Wilds, N. and S. Williams. *Performance of Next Generation CUI Mitigation Systems*. in *NACE International Corrosion Conference Proceedings*. 2017. NACE International.

71. Bernad, P.L., U. Bork, and J. McDonald. *Lessons from Development of a Coating for CUI protection*. in *CORROSION 2016*. 2016. OnePetro.

72. Pollock W, B.J., *Corrosion of metal under thermal insulation*. 1985, West Conshohocken, PA: ASTM International.

73. Bahadori, A., *Thermal Insulation Handbook for the Oil, Gas, and Petrochemical Industries.* Thermal Insulation Handbook for the Oil, Gas, and Petrochemical Industries, 2014: p. 1-394.

74. C168-10, A., *Standard Terminology Relating to Thermal Insulation*. 2010, ASTM International. p. 6.

75. Delahunt, J.F., *Corrosion Under Thermal Insulation and Fireproofing-An Overview.* CORROSION 2003, 2003.

76. TESS, *Everything There Is To Know About Marine Insulation*, in *Everything There Is To Know About Marine Insulation*. 2019, TESS.

77. Bahadori, A., *Thermal insulation handbook for the oil, gas, and petrochemical industries*. 2014: Gulf Professional Publishing.

78. 583, A.R., *Corrosion Under Insulation and Fireproofing* 2014, American Petroleum Institute: Washington.

79. Wilds, N., *17 - Corrosion under insulation*, in *Trends in Oil and Gas Corrosion Research and Technologies*, A.M. El-Sherik, Editor. 2017, Woodhead Publishing: Boston. p. 409-429.

80. Ashkenazi, D., *How aluminum changed the world: A metallurgical revolution through technological and cultural perspectives.* Technological Forecasting and Social Change, 2019. **143**: p. 101-113.

81. Vargel, C., *Corrosion of aluminium*. 2020: Elsevier.

82. Zupanič, F., *Structure and Properties of Aluminium Alloys*. 2021: MDPI AG.

83. API, *API RP583 Corrosion Under Insulation and Fireproofing*. 2014, API Publishing Services: Washington DC.

84. Javaherdashti, R., *Corrosion under insulation (CUI): A review of essential knowledge and practice*. 2014.

85. Rana, A.R.K., et al. *Corrosion Under Insulation Performance of Insulation Stand-Offs and Non-Metallic Membranes*. in *AMPP Annual Conference+ Expo*. 2022. OnePetro.

86. Winnik, S., *Corrosion Under Insulation (CUI) Guidelines: Revised*. 2015: Woodhead Publishing.

87. Geary, W., *Analysis of a corrosion under insulation failure in a carbon steel refinery hydrocarbon line.* Case studies in engineering failure analysis, 2013. **1**(4): p. 249-256.

88. Change, D.o.E.a.C., *Review of the Refining and Fuel Import Sectors in the UK*, D.o.E.a.C. Change, Editor. 2014: London. p. 44.

89. Racfoundation. *UK fuel market review refining*. 2012 [cited 2023 25-04-2023]; Available from: https://www.racfoundation.org/assets/rac_foundation/content/downloadables/racf_deloitte-refineries-jan13.pdf.

90. IBP, I., *Libya Oil, Gas Sector Business and Investment Opportunities Yearbook - Strategic Information and Regulations*. 2018: International Business Publications, USA.
91. Schütze, M., M. Roche, and R. Bender, *Corrosion Resistance of Steels, Nickel Alloys, and Zinc in Aqueous Media: Waste Water, Seawater, Drinking Water, High-Purity Water*. 2016: John Wiley & Sons.
92. Zwaag, C. and S.N. Rasmussen. *Cyclic CUI testing of Insulation materials*. in *CORROSION 2017*. 2017. OnePetro.
93. Schindelholz, E., et al., *Comparability and accuracy of time of wetness sensing methods relevant for atmospheric corrosion.* Corrosion Science, 2013. **67**: p. 233-241.
94. Peter, W.T., et al., *Engineering Asset Management-Systems, Professional Practices and Certification: Proceedings of the 8th World Congress on Engineering Asset Management (WCEAM 2013) & the 3rd International Conference on Utility Management & Safety (ICUMAS)*. 2014: Springer.
95. NACE, *NACE SP0198-98 Control of Corrosion Under Thermal Insulation and Fireproofing Materials–A Systems Approach*. 2010.
96. Pollock, W.I., *Corrosion of Metals Under Thermal Insulation: A Symposium Sponsored by ASTM Committees C-16 on Thermal Insulation...[et Al.]*. 1985: ASTM International.
97. Haga, G. *Corrosion Under Insulation CUI Management on Idle LNG Process Train*. in *SPE/IATMI Asia Pacific Oil & Gas Conference and Exhibition*. 2017. OnePetro.
98. Swift, M. *Corrosion Under Insulation on industrial piping-a holistic approach to insulation system design*. in *CORROSION 2019*. 2019. OnePetro.
99. Roffey, P. and E. Davies, *The generation of corrosion under insulation and stress corrosion cracking due to sulphide stress cracking in an austenitic stainless steel hydrocarbon gas pipeline.* Engineering Failure Analysis, 2014. **44**: p. 148-157.
100. Yang, M. and J.J.I.J.o.C. Liu, *In Situ Monitoring of Corrosion under Insulation Using Electrochemical and Mass Loss Measurements.* 2022. **2022**.
101. Williams, J. and O. Evans, *The influence of insulation materials on corrosion under insulation.* 2010.
102. Pojtanabuntoeng, T., et al. *Comparison of insulation materials and their roles on corrosion under insulation*. in *CORROSION 2017*. 2017. OnePetro.
103. Alcántara, J., et al., *Marine atmospheric corrosion of carbon steel: A review.* Materials, 2017. **10**(4): p. 406.
104. Alcántara, J., et al., *Airborne chloride deposit and its effect on marine atmospheric corrosion of mild steel.* Corrosion Science, 2015. **97**: p. 74-88.
105. ASTM, *ASTM C 795 Standard Specification for Thermal Insulation for Use in Contact with Austenitic Stainless Stee*. 2018: West Conshohocken.
106. ASTM, *ASTM C 871-18 Standard Test Methods for Chemical Analysis of Thermal Insulation Materials for Leachable Chloride, Fluoride, Silicate, and Sodium Ions*. 2018: West Conshohocken, PA.
107. BSI, B.S.I., *BS EN ISO 12624 Thermal Insulating Products For Building Equipment And Industrial Installations. Determination Of Trace Quantities Of Water-Soluble Chloride, Fluoride, Silicate, Sodium Ions And PH* 2022: Brussels.

108. Caines, S., F. Khan, and J. Shirokoff, *Analysis of pitting corrosion on steel under insulation in marine environments.* Journal of Loss Prevention in the process Industries, 2013. **26**(6): p. 1466-1483.
109. Caines, S., et al., *Demonstration of increased corrosion activity for insulated pipe systems using a simplified electrochemical potential noise method.* Journal of Loss Prevention in the Process Industries, 2017. **47**: p. 189-202.
110. ASTM, *Standard Guide for Laboratory Simulation of Corrosion under Insulation*, in *ASTM G189-07*. 2007.
111. Raja, V. and T. Shoji, *Stress corrosion cracking: theory and practice*. 2011: Elsevier.
112. Cheng, Y.F., *Stress corrosion cracking of pipelines*. 2013: John Wiley & Sons.
113. Ali, B. and A. Saud. *Under insulation stress corrosion cracking of process piping*. in *Corrosion 2006 Conference & Expo*. 2006. HT: NACE.
114. Rudling, P., *Welding of Zirconium alloys.* Skultuna Adv. Nucl. Technol. Int. Eur. AB, 2007: p. 8-9.
115. Schwertmann, U. and R.M. Cornell, *Iron oxides in the laboratory: preparation and characterization*. 2008: John Wiley & Sons.
116. Wang, Y., et al., *Insight into atmospheric corrosion evolution of mild steel in a simulated coastal atmosphere.* Journal of Materials Science & Technology, 2021. **76**: p. 41-50.
117. Fan, Y., et al., *Evolution of rust layers on carbon steel and weathering steel in high humidity and heat marine atmospheric corrosion.* Journal of Materials Science & Technology, 2020. **39**: p. 190-199.
118. Kamimura, T., et al., *The role of chloride ion on the atmospheric corrosion of steel and corrosion resistance of Sn-bearing steel.* Corrosion Science, 2012. **62**: p. 34-41.
119. Xiao, K., et al., *Corrosion Products and Formation Mechanism During Initial Stage of Atmospheric Corrosion of Carbon Steel.* Journal of Iron and Steel Research, International, 2008. **15**(5): p. 42-48.
120. Dillmann, P., F. Mazaudier, and S. Hœrlé, *Advances in understanding atmospheric corrosion of iron. I. Rust characterisation of ancient ferrous artefacts exposed to indoor atmospheric corrosion.* Corrosion Science, 2004. **46**(6): p. 1401-1429.
121. Li, S. and L. Hihara, *A micro-Raman spectroscopic study of marine atmospheric corrosion of carbon steel: the effect of akaganeite.* Journal of The Electrochemical Society, 2015. **162**(9): p. C495.
122. Chan, E.W.L., *Magnetite and its galvanic effect on the corrosion of carbon steel under carbon dioxide environments*. 2011, Curtin University.
123. Cornell, R.M. and U. Schwertmann, *The Iron Oxides: Structure, Properties, Reactions, Occurrences and Uses*. 2006: Wiley.
124. Surnam, B.Y.R., et al., *Investigating atmospheric corrosion behavior of carbon steel in coastal regions of Mauritius using Raman Spectroscopy.* Matéria (Rio de Janeiro), 2016. **21**: p. 157-168.
125. Seechurn, Y., B.Y. Surnam, and J.A. Wharton, *Marine atmospheric corrosion of carbon steel in the tropical microclimate of Port Louis.* Materials and Corrosion, 2022. **73**(9): p. 1474-1489.
126. Antunes, R.A., I. Costa, and D.L.A.d. Faria, *Characterization of corrosion products formed on steels in the first months of atmospheric exposure.* Materials research, 2003. **6**: p. 403-408.

127. Antunes, R.A., et al., *Characterization of corrosion products on carbon steel exposed to natural weathering and to accelerated corrosion tests.* 2014. **2014**.
128. Morcillo, M., I. Díaz, and H. Cano, *Atmospheric corrosion of mild steel.* 2011.
129. Waseda, Y., S. Suzuki, and Y. Waseda, *Characterization of corrosion products on steel surfaces*. Vol. 1. 2006: Springer.
130. Periyathambi, D., et al., *Weathering Steel in Industrial-Marine-Urban Environment: Field Study.* MATERIALS TRANSACTIONS, 2016. **57**.
131. Cai, J., et al., *Synthesis and anion exchange of tunnel structure akaganeite.* Chemistry of Materials, 2001. **13**(12): p. 4595-4602.
132. To, D., T. Shinohara, and O. Umezawa, *A study on the initial atmospheric corrosion behaviors of carbon steel exposed to urban and marine atmospheres in Cambodia.* Zairyo-to-Kankyo, 2017. **66**(4): p. 131-135.
133. Asami, K., *Characterization of rust layers on a plain-carbon steel and weathering steels exposed to industrial and coastal atmosphere for years.* Characterization of corrosion products on steel surfaces, 2006: p. 159-197.
134. Remazeilles, C. and P. Refait, *On the formation of β-FeOOH (akaganeite) in chloride-containing environments.* Corrosion Science, 2007. **49**(2): p. 844-857.
135. Selwyn, L.S., P. Sirois, and V. Argyropoulos, *The corrosion of excavated archaeological iron with details on weeping and akaganeite.* Studies in conservation, 1999. **44**(4): p. 217-232.
136. Neff, D., et al., *Corrosion of iron archaeological artefacts in soil: characterisation of the corrosion system.* Corrosion science, 2005. **47**(2): p. 515-535.
137. Asami, K. and M. Kikuchi, *In-depth distribution of rusts on a plain carbon steel and weathering steels exposed to coastal–industrial atmosphere for 17 years.* Corrosion Science, 2003. **45**(11): p. 2671-2688.
138. Rodrıguez, J.S., F.S. Hernández, and J.G. González, *XRD and SEM studies of the layer of corrosion products for carbon steel in various different environments in the province of Las Palmas (The Canary Islands, Spain).* Corrosion Science, 2002. **44**(11): p. 2425-2438.
139. Xiao, H., et al., *Evolution of akaganeite in rust layers formed on steel submitted to wet/dry cyclic tests.* Materials, 2017. **10**(11): p. 1262.
140. Lair, V., et al., *Electrochemical reduction of ferric corrosion products and evaluation of galvanic coupling with iron.* Corrosion Science, 2006. **48**(8): p. 2050-2063.
141. Li, Z.-l., et al., *Atmospheric corrosion behavior of low-alloy steels in a tropical marine environment.* Journal of Iron and Steel Research International, 2019. **26**: p. 1315-1328.
142. Lyon, S., *Corrosion of carbon and low alloy steels*, in *Shreir's Corrosion| Shreir's Corrosion: Volume 3: Corrosion and Degradation of Engineering Materials*. 2010, Elsevier BV. p. 1693-1736.
143. Morcillo, M., et al., *Marine atmospheric corrosion of carbon steels.* Revista de Metalurgia, 2015. **51**: p. e045.
144. Cambier, S.M.N., *Atmospheric corrosion of coated steel; relationship between laboratory and field testing*. 2014: The Ohio State University.
145. Ishikawa, T., et al., *Formation of magnetite in the presence of ferric oxyhydroxides.* Corrosion Science, 1998. **40**(7): p. 1239-1251.

146. Alcántara, J., et al., *An attempt to classify the morphologies presented by different rust phases formed during the exposure of carbon steel to marine atmospheres.* Materials Characterization, 2016. **118**: p. 65-78.
147. Yamashita, M., et al., *The long term growth of the protective rust layer formed on weathering steel by atmospheric corrosion during a quarter of a century.* Corrosion Science, 1994. **36**(2): p. 283-299.
148. Aramendia, J., et al., *Protective ability index measurement through Raman quantification imaging to diagnose the conservation state of weathering steel structures.* Journal of Raman Spectroscopy, 2014. **45**(11-12): p. 1076-1084.
149. Yamashita, M. and T. Misawa, *Recent progress in the study of protective rust-layer formation on weathering steel.* CORROSION 98, 1998.
150. Chen, H., et al., *Influence of chloride deposition rate on rust layer protectiveness and corrosion severity of mild steel in tropical coastal atmosphere.* Materials Chemistry and Physics, 2021. **259**: p. 123971.
151. Degen, T., et al., *The HighScore suite.* Powder Diffraction, 2014. **29**.
152. Altomare, A., et al., *EXPO2013: a kit of tools for phasing crystal structures from powder data.* Journal of Applied Crystallography, 2013. **46**(4): p. 1231-1235.
153. Sardela, M., *Practical materials characterization*. 2014: Springer.
154. Pecharsky, V.K. and P.Y. Zavalij, *Fundamentals of diffraction*. 2003: Springer.
155. Hara, S., et al., *Taxonomy for protective ability of rust layer using its composition formed on weathering steel bridge.* Corrosion Science, 2007. **49**(3): p. 1131-1142.
156. Krivy, V., V. Urban, and K. Kreislova, *Development and failures of corrosion layers on typical surfaces of weathering steel bridges.* Engineering Failure Analysis, 2016. **69**: p. 147-160.
157. Marcus, P.M., F, ed. *Analytical methods in corrosion science and engineering*. 2006, CRC Press: New York.
158. Andreatta, F. and L. Fedrizzi, *The use of the electrochemical micro-cell for the investigation of corrosion phenomena.* Electrochimica Acta, 2016. **203**: p. 337-349.
159. Ding, H. and L. Hihara, *Localized Corrosion Currents and pH Profile over B4C, SiC, and Al2O3 Reinforced 6092 Aluminum Composites: I. In Solution.* Journal of the Electrochemical Society, 2005. **152**(4): p. B161.
160. Cui, N., et al., *Use of scanning reference electrode technique for characterizing pitting and general corrosion of carbon steel in neutral media.* Electrochemistry communications, 2001. **3**(12): p. 716-721.
161. Stulík, K., et al., *Microelectrodes. Definitions, characterization, and applications (Technical report).* Pure and Applied Chemistry, 2000. **72**(8): p. 1483-92.
162. Montenegro, M.I., M.A.M. Queiros, and J.L. Daschbach. *Microelectrodes : theory and applications*. 1991.
163. Folena, M.C., et al., *CO2 top-of-line-corrosion; assessing the role of acetic acid on general and pitting corrosion.* Corrosion, 2021. **77**(3): p. 298-312.
164. Burkle, D.P., *Understanding the Formation of Protective FeCO3 on to Carbon Steel Pipelines during CO2 Corrosion*. 2017, University of Leeds.
165. ASTM, A.A.M.-a., *Standard specification for seamless carbon steel pipe for high temperature service*. 2006, ASTM International Ann Arbor (MI).

166. Felipe, G.B.U., et al., *Heat treatment analysis of ASTM A106 steel spheroidization and erosive wear at high temperatures.* REM-International Engineering Journal, 2020. **73**: p. 539-546.
167. Philip A. Schweitzer, P.E., *Encyclopedia Of Corrosion Technology*. 2004: CRC Press.
168. Zhang, Q., et al., *Corrosion behavior of Hastelloy C-276 in supercritical water.* Corrosion Science, 2009. **51**(9): p. 2092-2097.
169. oils, M. *Heat Transfer Oil 475-Solvent refined mineral oil for heat transfer applications*. 2019 22/04/2023]; Available from: https://www.millersoils.co.uk/products/heat-transfer-oil-475/.
170. G1-03, A., *Standard practice for preparing, cleaning, and evaluation corrosion test specimens*. 2017, ASTM international.
171. Kumar, S.S., et al., *Structure, morphology, and optical properties of amorphous and nanocrystalline gallium oxide thin films.* The Journal of Physical Chemistry C, 2013. **117**(8): p. 4194-4200.
172. Kot, M., *In-operando hard X-ray photoelectron spectroscopy study on the resistive switching physics of HfO2-based RRAM*. 2014.
173. Caines, S., *Development of a simplified electrochemical noise method to monitor assets under insulation*. 2016, Memorial University of Newfoundland.
174. Pojtanabuntoeng, K., et al., *New experimental rig to investigate corrosion under insulation at different climate conditions.* Corrosion and Materials, 2015. **40**(6): p. 46-51.
175. Marquez, A., J. Singh, and C. Maharaj, *Corrosion under insulation examination to prevent failures in equipment at a petrochemical plant.* Journal of Failure Analysis and Prevention, 2021. **21**(3): p. 723-732.
176. Soildworks, *Soildworks-student edition*. 2018.
177. Marmoret, L., et al., *Anisotropic Structure of Glass Wool Determined by Air Permeability and Thermal Conductivity Measurements.* Journal of Surface Engineered Materials and Advanced Technology, 2016. **06**: p. 72-79.
178. Dieckmann, E., et al., *Valorization of waste feathers in the production of new thermal insulation materials.* Waste and Biomass Valorization, 2021. **12**: p. 1119-1131.
179. Cao, Q., et al., *Corrosion of mild steel under insulation–the effect of dissolved metal ions.* 2020. **55**(4): p. 322-330.
180. *The Influence of Insulation Materials on Corrosion Under Insulation*. 2020 [cited 2023 08/05/2023]; Available from: https://fluidhandlingpro.com/fluid-process-technology/piping-systems/the-influence-of-insulation-materials-on-corrosion-under-insulation/.
181. Li, S. and L. Hihara, *In situ Raman spectroscopic study of NaCl particle-induced marine atmospheric corrosion of carbon steel.* Journal of the Electrochemical Society, 2012. **159**(4): p. C147.
182. Bellot-Gurlet, L., et al., *Raman studies of corrosion layers formed on archaeological irons in various media.* Journal of Nano Research, 2009. **8**: p. 147-156.
183. Li, S. and L. Hihara, *In situ Raman spectroscopic identification of rust formation in Evans' droplet experiments.* Electrochemistry communications, 2012. **18**: p. 48-50.

184. De Faria, D.L., S. Venâncio Silva, and M. De Oliveira, *Raman microspectroscopy of some iron oxides and oxyhydroxides.* Journal of Raman spectroscopy, 1997. **28**(11): p. 873-878.

185. Cambier, S., D. Verreault, and G. Frankel, *Raman investigation of anodic undermining of coated steel during environmental exposure.* Corrosion, 2014. **70**(12): p. 1219-1229.

186. Pan, C., et al., *Effect of temperature on corrosion behavior of low-alloy steel exposed to a simulated marine atmospheric environment.* Journal of Materials Engineering and Performance, 2020. **29**(2): p. 1400-1409.

187. Fry, A., *Residual stress measurement: XRD depth profiling using successive material removal.* 2002.

188. Prieto, C., et al. *Adhesion of Corrosion Product Layers Formed in Dewing Conditions*. in *NACE CORROSION*. 2021. NACE.

189. Díaz, I., et al., *Some Clarifications Regarding Literature on Atmospheric Corrosion of Weathering Steels.* International Journal of Corrosion, 2012. **2012**.

190. Taleb, W., *Nanotechnology for corrosion control Silsesquioxane based nanofillers for iron carbonate film enhancement*. 2016, University of Leeds.

191. Dwivedi, D., K. Lepková, and T. Becker, *Carbon steel corrosion: a review of key surface properties and characterization methods.* RSC advances, 2017. **7**(8): p. 4580-4610.

192. Mizushima, K., et al. *Factors for selecting thermal insulation materials to prevent corrosion under insulation*. in *NACE CORROSION*. 2019. NACE.

193. Li, W., et al., *Numerical simulation of carbon steel atmospheric corrosion under varying electrolyte-film thickness and corrosion product porosity.* npj Materials Degradation, 2023. **7**(1): p. 3.

194. Abayarathna, D., et al. *Measurement of corrosion under insulation and effectiveness of protective coatings*. in *NACE CORROSION*. 1997. NACE.

195. Martinelli-Orlando, F. and U. Angst, *Monitoring corrosion rates with ER-probes – a critical assessment based on experiments and numerical modelling.* Corrosion Engineering, Science and Technology, 2022. **57**(3): p. 254-268.

196. Ma, Y., Y. Li, and F. Wang, *The atmospheric corrosion kinetics of low carbon steel in a tropical marine environment.* Corrosion Science, 2010. **52**(5): p. 1796-1800.

197. Tamura, H., *The role of rusts in corrosion and corrosion protection of iron and steel.* Corrosion Science, 2008. **50**(7): p. 1872-1883.

198. D'Angelo, L., et al. *Effect of hygroscopic atmospheric particles deposition on the corrosion reliability of electronics*. in *European Corrosion Congress, EUROCORR 2016*. 2016.

199. Antony, H., et al., *Electrochemical study of indoor atmospheric corrosion layers formed on ancient iron artefacts.* Electrochimica Acta, 2007. **52**(27): p. 7754-7759.

200. Kim, Y. and M. Oliveria, *Magnetic properties and texture of sputtered Fe/Fe/sub 3/O/sub 4/multilayer films.* IEEE transactions on magnetics, 1994. **30**(3): p. 1316-1323.

201. He, S., et al., *Corrosion behaviour of carbon steel in Beibu Gulf tidal zone.* Corrosion Engineering, Science and Technology, 2023. **58**(2): p. 116-123.

202. Hara, S., et al., *Protective Ability Index of Rust Layer Formed on Weathering Steel Bridge.* Corrosion Science and Technology, 2007. **6**(3): p. 128-132.

203. Nieuwoudt, M., J. Comins, and I. Cukrowski, *The growth of the passive film on iron in 0.05 M NaOH studied in situ by Raman micro-spectroscopy and electrochemical polarisation. Part I: near-resonance enhancement of the Raman spectra of iron oxide and oxyhydroxide compounds.* Journal of Raman Spectroscopy, 2011. **42**(6): p. 1335-1339.
204. Crespo, A., et al., *Effect of sulfuric acid Patination treatment on atmospheric corrosion of weathering steel.* Metals, 2020. **10**(5): p. 591.
205. Hœrlé, S., et al., *Advances in understanding atmospheric corrosion of iron. II. Mechanistic modelling of wet–dry cycles.* Corrosion Science, 2004. **46**(6): p. 1431-1465.
206. Wang, Z., et al., *Study of the corrosion behavior of weathering steels in atmospheric environments.* Corrosion Science, 2013. **67**: p. 1-10.
207. Balasubramaniam, R., A.R. Kumar, and P. Dillmann, *Characterization of rust on ancient Indian iron.* Current Science, 2003: p. 1546-1555.
208. De la Fuente, D., et al., *Characterisation of rust surfaces formed on mild steel exposed to marine atmospheres using XRD and SEM/Micro-Raman techniques.* Corrosion Science, 2016. **110**: p. 253-264.
209. Li, C., et al., *Insight to atmosphere corrosion behavior of Q345NH steel in Wenchang tropical marine environment.* Journal of Materials Research and Technology, 2023. **24**: p. 5755-5768.
210. Colomban, P., *Potential and drawbacks of Raman (micro) spectrometry for the understanding of iron and steel corrosion*. 2011: INTECH Open Access Publisher.